

Studies of Numerical Algorithms for
Gyrokinetics and the Effects of Shaping
on Plasma Turbulence

Emily Ann Belli

A DISSERTATION
PRESENTED TO THE FACULTY
OF PRINCETON UNIVERSITY
IN CANDIDACY FOR THE DEGREE
OF DOCTOR OF PHILOSOPHY

RECOMMENDED FOR ACCEPTANCE
BY THE DEPARTMENT OF
ASTROPHYSICAL SCIENCES

JUNE 2006

© Copyright 2006 by Emily Ann Belli.

All rights reserved.

Abstract

Advanced numerical algorithms for gyrokinetic simulations are explored for more effective studies of plasma turbulent transport. The gyrokinetic equations describe the dynamics of particles in 5-dimensional phase space, averaging over the fast gyromotion, and provide a foundation for studying plasma microturbulence in fusion devices and in astrophysical plasmas. Several algorithms for Eulerian/continuum gyrokinetic solvers are compared. An iterative implicit scheme based on numerical approximations of the plasma response is developed. This method reduces the long time needed to set-up implicit arrays, yet still has larger time step advantages similar to a fully implicit method. Various model preconditioners and iteration schemes, including Krylov-based solvers, are explored. An Alternating Direction Implicit algorithm is also studied and is surprisingly found to yield a severe stability restriction on the time step. Overall, an iterative Krylov algorithm might be the best approach for extensions of core tokamak gyrokinetic simulations to edge kinetic formulations and may be particularly useful for studies of large-scale ExB shear effects.

The effects of flux surface shape on the gyrokinetic stability and transport of tokamak plasmas are studied using the nonlinear GS2 gyrokinetic code with analytic equilibria based on interpolations of representative JET-like shapes. High

shaping is found to be a stabilizing influence on both the linear ITG instability and nonlinear ITG turbulence. A scaling of the heat flux with elongation of $\chi \sim \kappa^{-1.5}$ or κ^{-2} (depending on the triangularity) is observed, which is consistent with previous gyrofluid simulations. Thus, the GS2 turbulence simulations are explaining a significant fraction, but not all, of the empirical elongation scaling. The remainder of the scaling may come from (1) the edge boundary conditions for core turbulence, and (2) the larger Dimits nonlinear critical temperature gradient shift due to the enhancement of zonal flows with shaping, which is observed with the GS2 simulations.

Finally, a local linear trial function-based gyrokinetic code is developed to aid in fast scoping studies of gyrokinetic linear stability. This code is successfully benchmarked with the full GS2 code in the collisionless, electrostatic limit, as well as in the more general electromagnetic description with higher-order Hermite basis functions.

Acknowledgments

I foremost thank my thesis advisor Greg Hammett, whose guidance made this thesis possible and whose insight, wisdom, and integrity has inspired me. Thanks also to Bill Dorland, who has been an influential and inspiring mentor, and to the many teachers and researchers who have inspired and guided me throughout my graduate years at Princeton University, particularly Bill Tang, Steve Jardin, and John Krommes. I am also grateful to the coordinators of the PICASso program at Princeton, particularly J. P. Singh and Steven Kleinstein, for giving me the opportunity to pursue broader computational efforts. Thanks also to my readers, Steve Jardin and Bill Dorland, for their advice and suggestions.

I would like to thank the original developers of the GS2 code, specifically Mike Kotschenreuther, Peter Liu, and Bill Dorland, on which much of the work in this thesis is based. I am also grateful to Robert Budny for providing TRANSP analysis of the JET data, as well as to David Mikkelsen and Martha Redi for their invaluable GS2 help. The 3D visualizations of GS2 data were made possible via collaborations with Scott Klasky.

Finally, I extend personal thanks to my family, particularly my parents Lou and Judy, my sister Jenine, and my grandfather Richard Goff, for encouraging me every step along the way. Special thanks also to Enes Dedovic, whose dedicated support

and encouragement has helped me to be a better person and whose non-ending intellectual curiosity has inspired me to be a better scientist.

This work was supported by U.S. DOE contract # DE-AC02-76CH03073 and in part by a U.S. Department of Energy OFES Fusion Energy Sciences Graduate Fellowship and by a fellowship through the PICASso Program at Princeton, funded by National Science Foundation IGERT grant # DGE-9972930. Use of computer resources at PPPL, the LBL National Energy Research Scientific Computing Center, and the ORNL Center for Computational Sciences is gratefully acknowledged.

Contents

Abstract	iii
Acknowledgments	v
1 Introduction	1
1.1 Background	3
1.1.1 The Gyrokinetic Equation	3
1.1.2 Drift Wave Microinstabilities	11
1.1.3 Advances of Nonlinear Gyrokinetic Simulations	20
1.1.4 Turbulent Transport Models	24
1.2 Motivation	28
1.3 Overview of this Thesis	29
2 Semi-Implicit and Iterative Implicit Algorithms for Eulerian Gyrokinetic Solvers	31
2.1 Implicit Schemes	36
2.1.1 Kotschenreuther’s Implicit Solution	41
2.2 Semi Implicit-Explicit Schemes	45
2.3 Iterative Implicit Schemes	59

2.3.1	Simple Iteration	60
2.3.2	Preconditioners	65
2.3.3	Initializers	90
2.3.4	Iteration Schemes	100
2.4	Summary	121
3	An ADI Algorithm for Gyrokinetics	124
3.1	Motivation	126
3.2	Kinetic Alfvén Wave Test Problem	128
3.3	Implementing and Testing an ADI Algorithm	131
3.4	Simpler Illustration of the Difficulties	137
3.5	Comparison with Adams-Bashforth Schemes	140
3.6	Summary	147
4	Effects of Shaping on Gyrokinetic Plasma Turbulence	149
4.1	The Equilibrium	153
4.1.1	JET-based Plasmas	154
4.2	Linear Gyrokinetic Stability	158
4.3	Nonlinear ITG Turbulence	167
4.4	Electromagnetic Effects	180
4.4.1	Linear Results	180
4.4.2	Nonlinear Results	188
4.5	Summary	193
5	Trial Function-Based Methods	195
5.1	Formulation of the Model	198
5.2	The Algorithm	208

5.3	Benchmarks in the Local Limit	214
5.3.1	Electrostatic Results	216
5.3.2	Electromagnetic Results	217
5.4	Test Cases for Shaped Flux Surfaces	222
5.4.1	Electrostatic Results	222
5.4.2	Electromagnetic Results	236
5.5	Higher-Order Models	244
5.6	Summary	254
6	Conclusions	256
6.1	Summary	257
6.1.1	Studies of Numerical Algorithms for Gyrokinetics	257
6.1.2	Studies of the Effects of Shaping on Plasma Turbulence	259
6.2	Future Directions	261
6.2.1	Subgrid Models of Turbulence	262
6.2.2	Equilibrium-Scale ExB Shear Effects	266
A	The GS2 Algorithm	269
B	Templates of Iterative Algorithms	274
B.1	Simple Iteration	275
B.2	Steepest Descent and Conjugate Gradient	275
B.3	Bi-CGSTAB	276
B.4	GMRES(m)	277
C	Unsaturated Transport in Finite β GS2 Simulations	279

List of Figures

2.1	Illustration of the grid differencing for the Beam-Warming 2nd order compact finite differencing algorithm	39
2.2	Mode frequency and growth rate vs. Δt with adiabatic electrons comparing single-step semi implicit-explicit schemes	50
2.3	Mode frequency and growth rate vs. Δt with adiabatic electrons and with upwind biasing comparing single-step semi implicit-explicit schemes	51
2.4	Mode frequency and growth rate vs. Δt with adiabatic electrons and no particle trapping comparing single-step semi implicit-explicit schemes	52
2.5	Mode frequency and growth rate vs. Δt with adiabatic electrons, no particle trapping, and self-periodic boundary conditions with $\hat{s} = 0$ comparing single-step semi implicit-explicit schemes	53
2.6	Mode frequency and growth rate vs. Δt with gyrokinetic electrons comparing single-step semi implicit-explicit schemes	54
2.7	Mode frequency and growth rate vs. Δt with adiabatic electrons comparing predictor-corrector semi implicit-explicit schemes	57

2.8	Mode frequency and growth rate vs. Δt with gyrokinetic electrons comparing predictor-corrector semi implicit-explicit schemes	58
2.9	Real frequency and growth rate vs. $k_y \rho_i$ for ITG test case parameters for iterative implicit schemes	61
2.10	Electrostatic response rows M_{ij}^1 vs. Δt comparing analytic approximations to the plasma response	71
2.11	Illustration of the multiM preconditioner	74
2.12	Electrostatic response rows M_{ij}^1 vs. θ_i comparing various preconditioners	76
2.13	Max error eigenvalue of M and num of GK solves vs. Δt comparing various preconditioners	77
2.14	Electromagnetic response rows M_{ij}^1 and M_{ij}^2 vs. θ_i comparing multiM preconditioners of varying resolution	79
2.15	Electromagnetic response rows M_{ij}^3 and M_{ij}^4 vs. θ_i comparing multiM preconditioners of varying resolution	80
2.16	Max error eigenvalue of M and num of GK solves vs. Δt in the electrostatic limit with adiabatic electrons comparing multiM preconditioners of varying resolution	82
2.17	Max error eigenvalue of M and num of GK solves vs. Δt in the electrostatic limit with gyrokinetic electrons comparing multiM preconditioners of varying resolution	83
2.18	Max error eigenvalue of M and num of GK solves vs. Δt with electromagnetic dynamics comparing multiM preconditioners of varying resolution	85

2.19	Max error eigenvalue of M and num of GK solves vs. Δt with electromagnetic dynamics at various β using multiM preconditioners . . .	86
2.20	Max error eigenvalue of M and num of GK solves vs. Δt with electromagnetic dynamics at various $k_y \rho_i$ using the multiM (16,7) preconditioner	89
2.21	Num of GK solves vs. Δt in the electrostatic limit comparing iteration initializers	92
2.22	Num of GK solves vs. Δt with electromagnetic dynamics comparing iteration initializers	93
2.23	Num of GK solves vs. Δt in the electrostatic limit comparing iteration schemes	115
2.24	Num of GK solves vs. Δt with electromagnetic dynamics comparing iteration schemes	116
2.25	Num of GK solves vs. Δt in the electrostatic limit comparing GMRES(m) for various m	119
2.26	Num of GK solves vs. Δt with electromagnetic dynamics comparing GMRES(m) for various m	120
3.1	Mode frequency vs. Δt for a kinetic Alfvén wave at low β using an ADI algorithm	134
3.2	Amplification factor vs. Δt for a kinetic Alfvén wave at low β using an ADI algorithm	135
3.3	Mode frequency vs. Δt for a kinetic Alfvén wave at high β using an ADI algorithm	137
3.4	Amplification factor vs. Δt for a kinetic Alfvén wave at high β using an ADI algorithm	138

3.5	Mode frequency vs. Δt for a kinetic Alfvén wave using a partially implicit AB2 algorithm	143
3.6	Amplification factor vs. Δt for a kinetic Alfvén wave using a partially implicit AB2 algorithm	144
3.7	Amplification factor vs. Δt for the computational mode using a partially implicit AB2 algorithm	145
3.8	Mode frequency vs. Δt for a kinetic Alfvén wave and the computational mode using a fully explicit AB2 algorithm	146
4.1	Equilibrium radial profiles of JET data from TRANSP analysis . . .	155
4.2	Flux surface shapes for JET-like plasmas	157
4.3	Real frequency and growth rate vs. κ for JET-based plasmas of varying δ and $\partial_{r/a}\beta$ in the electrostatic limit	160
4.4	Flux surface shapes for generic-based plasmas	162
4.5	Real frequency and growth rate vs. κ for generic-based plasmas of varying δ , $\partial_{r/a}\kappa$, and $\partial_{r/a}\delta$ in the electrostatic limit	163
4.6	$\omega_{d,\parallel}$ and k_{\perp}^2 vs. θ for JET-based plasmas	165
4.7	Real frequency and growth rate vs. R/L_T for JET-based plasmas in the electrostatic limit	166
4.8	Contours of electrostatic potential for a nonlinear JET-based plasma simulation	168
4.9	Variation of the geometrical quantity $\langle \nabla r \rangle / \langle \nabla r ^2 \rangle$ with κ for JET-based plasmas	171
4.10	Heat flux vs. κ for JET-based plasmas of varying δ and $\partial_{r/a}\beta$ in the electrostatic limit	172
4.11	Inverse heat flux vs. κ for various empirical scaling laws	174

4.12	Heat flux vs. R/L_T for JET-based plasmas in the electrostatic limit	175
4.13	Time evolution of the amplitude of the zonal flows for a JET-based circular plasma	177
4.14	Amplitude of the Rosenbluth-Hinton residual zonal flows vs. κ for JET-based plasmas of varying δ in the electrostatic limit	179
4.15	Real frequency and growth rate vs. κ for JET-based plasmas of varying δ comparing $\beta = 0$ and $\beta(\kappa)$	181
4.16	Real frequency and growth rate vs. R/L_T for JET-based plasmas with electromagnetic dynamics	182
4.17	Real frequency and growth rate vs. β for JET-based plasmas	184
4.18	Real frequency and growth rate vs. $k_y\rho_i$ for JET-based plasmas comparing $\beta = 0$ and $\beta(\kappa)$	186
4.19	Real frequency and growth rate vs. α for generic-based plasmas at high \hat{s}	188
4.20	Real frequency and growth rate vs. α for generic-based plasmas at low \hat{s}	189
4.21	Heat flux vs. κ for JET-based plasmas with electromagnetic dynamics at various β	192
5.1	$\omega_{d,\parallel}$ and k_{\perp}^2 vs. θ for generic plasmas	201
5.2	Trial function-averaged $\omega_{d,\parallel}$, k_{\perp}^2 , and k_{\parallel}^2 vs. σ for generic plasmas	202
5.3	Real frequency and growth rate vs. R/L_{Ti} at high q comparing GS2 and the TF code at varying C_{\parallel}	205
5.4	Real frequency and growth rate vs. R/L_{Ti} at moderate q comparing GS2 and the TF code at varying C_{\parallel}	206

5.5	Real frequency and growth rate vs. R/L_{Ti} at low q comparing GS2 and the TF code at varying C_{\parallel}	207
5.6	Local electrostatic response function M^1 and num of GK solves vs. Δt comparing fully implicit and iterative implicit schemes in the TF code	215
5.7	Growth rate vs. R/L_{Ti} for an ITG mode using the TF code in the local limit	217
5.8	Growth rate vs. $k_y \rho_i$ at various η_i for an ITG mode using the TF code in the local limit	218
5.9	Mode frequency and damping rate vs. β_e for a kinetic shear Alfvén wave using the TF code in the local limit	221
5.10	Real frequency and growth rate vs. $k_y \rho_i$ for shaped plasmas with adiabatic electrons comparing GS2 and the TF code	225
5.11	Real frequency and growth rate vs. κ with adiabatic electrons comparing GS2 and the TF code	226
5.12	Real frequency and growth rate vs. δ with adiabatic electrons comparing GS2 and the TF code	227
5.13	Real frequency and growth rate vs. $k_y \rho_i$ for shaped plasmas with gyrokinetic electrons comparing GS2 and the TF code	229
5.14	Real frequency and growth rate vs. κ with gyrokinetic electrons comparing GS2 and the TF code	230
5.15	Real frequency and growth rate vs. $k_y \rho_i$ for shaped plasmas with gyrokinetic electrons and no particle trapping comparing GS2 and the TF code	231

5.16	Real frequency and growth rate vs. κ with gyrokinetic electrons and no particle trapping comparing GS2 and the TF code	232
5.17	Real frequency and growth rate vs. R/L_T for shaped plasmas with adiabatic electrons comparing GS2 and the TF code	237
5.18	Real frequency and growth rate vs. R/L_T for shaped plasmas with gyrokinetic electrons comparing GS2 and the TF code	238
5.19	Real frequency and growth rate vs. $k_y\rho_i$ at various low R/L_T for a shaped plasma with gyrokinetic electrons comparing GS2 and the TF code	239
5.20	Real frequency and growth rate vs. $k_y\rho_i$ at various high R/L_T for a shaped plasma with gyrokinetic electrons comparing GS2 and the TF code	240
5.21	Real frequency and growth rate vs. $k_y\rho_i$ with electromagnetic dynamics comparing GS2 and the TF code	242
5.22	Real frequency and growth rate vs. β comparing GS2 and the TF code	243
5.23	Closure coefficients for the Hermite-based TF model vs. expansion order	246
5.24	Real frequency and growth rate vs. $k_y\rho_i$ with electromagnetic dynamics comparing GS2 and the TF model based on Hermite expansion of $k_{\parallel}v_{\parallel}$	248
5.25	Real frequency and growth rate vs. $k_y\rho_i$ with electromagnetic dynamics comparing GS2 and the TF models based on Hermite expansion of $k_{\parallel}v_{\parallel}$ and based on Hermite expansion of $k_{\parallel}v_{\parallel}$ and ω_{dv}	249

5.26	Real frequency and growth rate vs. β comparing GS2 and the TF model based on Hermite expansion of $k_{\parallel}v_{\parallel}$ and ω_{dv}	252
6.1	Ion heat flux vs. R/L_{Ti} comparing various grid resolutions and the use of a subgrid model	267
C.1	Time evolution of the heat flux for a JET-based circular plasma with electromagnetic dynamics showing unsaturated transport	281

List of Tables

2.1	Main gyrokinetic codes supported by the U.S. fusion program . . .	32
2.2	Growth rates of the numerically unstable mode for single-step semi implicit-explicit schemes	48
2.3	Growth rates of the numerically unstable mode for predictor-corrector semi implicit-explicit schemes	56
2.4	Computational requirements for various iterative methods	110

Chapter 1

Introduction

Drift waves are commonly believed to be responsible for anomalous cross-field transport and the resulting anomalously high heat and particle loss in tokamaks. Anomalous transport refers to that which is larger than neoclassical transport, generally by several orders of magnitude. While neoclassical transport is due to the Coulomb collisions of particles undergoing drift-orbit motion in toroidal magnetic field geometry, anomalous transport ultimately results from microturbulent fluctuations in the electric and magnetic fields, driven by drift waves, which cause fluctuations in the particles' velocities and positions. Although drift wave-induced plasma microturbulence is not catastrophic in the sense of macroscopic magnetohydrodynamic turbulence, which can disrupt the plasma, plasma microturbulence can significantly degrade the confinement properties of a tokamak by enhancing the diffusion of heat, particles, and momentum across magnetic surfaces. Thus, understanding the underlying driving mechanisms of plasma microturbulence and the means to suppress it is critical in developing more efficient fusion reactors.

The gyrokinetic equation provides a theoretical, first-principles based foundation for studying drift-like microinstability driven turbulence in magnetized plasmas. In a typical low β tokamak plasma, i.e. one which is characterized by an average plasma pressure which is much smaller than the average magnetic pressure, drift waves are essentially ion acoustic waves that are destabilized by density and temperature inhomogeneities in the plasma. They are characterized by low frequencies (compared to the cyclotron frequency) and small spatial scales (relative to the size of the tokamak). These basic properties of drift waves define the physical model used in gyrokinetic theory.

Gyrokinetic simulations of plasma microturbulence and transport could be used in the near future to design the next generation of experimental tokamaks with optimal confinement properties. However, solving the full nonlinear, 5D integro-differential gyrokinetic equation in realistic geometry with full physics, including non-adiabatic electron dynamics with trapped and passing electron physics, impurity species, collisionality, and electromagnetic fluctuations, can be computationally intensive, requiring hundreds of hours of computing time on massively parallel machines. Thus, this work focuses on the design of advanced numerical schemes and order-reduction methods for Eulerian gyrokinetic solvers that significantly improve their accuracy and time efficiency for more effective studies of plasma microturbulence. Algorithms such as these can improve our fundamental physics understanding of the driving mechanisms behind anomalous transport in tokamaks, enhance the study of transport in existing experiments, and ultimately provide predictive capabilities, which in turn will enable the design of future fusion reactors that would follow ITER (a proposed next generation international experimental burning plasma tokamak) with optimal confinement properties. Furthermore, these

algorithms may aid in advances beyond core turbulence studies, such as the development of a multiscale transport model based on nonlinear gyrokinetic simulations and the coupling of core kinetic simulations to edge kinetic formulations.

In addition to studies of algorithms for gyrokinetics, as an application of using gyrokinetic simulations to develop a further understanding of the mechanisms leading to improved confinement in tokamak plasmas, this work also explores the effects of flux surface shape on the gyrokinetic stability and turbulent transport of tokamak plasmas. These studies are performed using the GS2 code (a 5D, nonlinear, flux tube-based gyrokinetic code) as well as a new local linear trial function-based gyrokinetic code.

1.1 Background

1.1.1 The Gyrokinetic Equation

The gyrokinetic equation is derived from a fundamental kinetic description of the plasma consisting of the Boltzmann-Maxwell equations and is generally applicable for a wide range of low frequency plasma phenomena. The nonlinear gyrokinetic equation was first derived by Frieman and Chen [FRIEMAN and CHEN, 1982], followed by a number of interesting papers with alternate derivations and extensions (such as [DUBIN *et al.*, 1983; LEE, 1983; LEE, 1987; HAHM *et al.*, 1988; BRIZARD, 1992; QIN *et al.*, 2000]; see also the recent review of nonlinear gyrokinetic theory in [BRIZARD and HAHM, 2006] and a derivation in a simple local limit in [HOWES *et al.*, 2006]).

Here we briefly summarize the derivation of the gyrokinetic equation, basically following the Frieman and Chen approach. The starting point for the derivation is

the Boltzmann equation, given as follows, which, in the absence of the RHS collision term, is simply an expression of 6D phase space conservation:

$$\left(\frac{\partial}{\partial t} + \vec{v} \cdot \nabla + \frac{Z_s e}{m_s} (\vec{E} + \vec{v} \times \vec{B}) \cdot \frac{\partial}{\partial \vec{v}} \right) F = \left(\frac{\partial F}{\partial t} \right)_{coll} \quad (1.1)$$

The key steps in the derivation are as follows:

1. A coordinate transformation from phase space coordinates to guiding center coordinates is performed, i.e. $(\vec{x}, \vec{v}) \rightarrow (\vec{R}, E, \mu, \zeta)$, where \vec{R} is the guiding center position such that $\vec{x} = \vec{R} + \vec{\rho}$, $E = v^2/2$ is the particle energy, $\mu = v_{\perp}^2/2B$ is the gyrocenter magnetic moment, and ζ is the gyrophase angle. Here, the Larmor radius vector is given by $\vec{\rho} = (\hat{b} \times \vec{v})/\Omega$, and the velocity vector is given by $\vec{v} = v_{\parallel} \hat{b} + \vec{v}_{\perp}$, such that $v_{\parallel}^2 = 2(E - \mu B)$ and $\vec{v}_{\perp} = v_{\perp}(\cos(\zeta)\hat{e}_1 + \sin(\zeta)\hat{e}_2)$, where \hat{e}_1 and \hat{e}_2 are orthogonal unit vectors such that $\hat{e}_1 \times \hat{e}_2 = \hat{b}$.
2. A hierarchical set of equations is derived by expanding the distribution function as $F = F_0 + F_1 + \dots$ (where F_0 is the equilibrium distribution function and F_1 is the fluctuating distribution function) and applying the gyrokinetic ordering assumptions:

$$\frac{F_1}{F_0} \sim \frac{e\Phi}{T} \sim \frac{A_{\parallel}}{B\rho} \sim \frac{\delta B_{\parallel}}{B} \sim \frac{\omega}{\Omega} \sim \frac{\rho}{L} \equiv \epsilon \ll 1 \quad (1.2)$$

$$k_{\parallel} L \sim k_{\perp} \rho \sim O(1) \quad (1.3)$$

where ω is the characteristic fluctuation frequency, Ω is the cyclotron frequency ($\Omega_s = Z_s e B / m_s c$), ρ is the gyroradius ($\rho_s = v_{ts} / \Omega_s$, where the thermal speed is given by $v_{ts}^2 = T_s / m_s$), L is the macroscopic equilibrium

length scale, B is the equilibrium magnetic field, and k_{\parallel} and k_{\perp} are characteristic wavenumbers parallel and perpendicular to the equilibrium magnetic field. Φ , A_{\parallel} , and δB_{\parallel} represent the fluctuating fields; specifically Φ is the perturbed electrostatic potential, A_{\parallel} is the component of the perturbed magnetic vector potential parallel to the equilibrium magnetic field (such that $\delta \vec{B}_{\perp} = \hat{b} \times \nabla_{\perp} A_{\parallel}$, where \hat{b} is the unit vector in the direction of the equilibrium magnetic field), and δB_{\parallel} is the magnetic perturbation along the equilibrium magnetic field. The gyrokinetic ordering captures the essential properties of drift waves, namely small amplitude perturbations, slow time scales compared to the gyromotion, large equilibrium scales compared to the gyroradius, and strong anisotropy (i.e. large perpendicular gradients relative to the parallel gradients).

3. The gyrokinetic equation, which describes the evolution of the gyrophase independent component of F_1 (which we will denote as a non-adiabatic part h plus an adiabatic part), results from solving the hierarchical equations in the expansion up to $O(\epsilon^2)$, imposing the gyrophase average as the solubility condition. This averaging essentially reduces the dimensionality of the equations from 6D to 5D by eliminating the gyrophase angle ζ . Since ζ defines the instantaneous position of the particle on a gyro-ring, the gyrokinetic equation basically describes the evolution of an ensemble of rings of charge.

The gyrokinetic equation can be written in the following form:

$$\left(\frac{d}{dt} + v_{\parallel} \hat{b} \cdot \nabla + i\omega_{dv} \right) h_s + C(h_s) = \left(i\omega_{*T} + \frac{\partial}{\partial t} \right) \frac{Z_s e F_{Ms}}{T_{0s}} \chi \quad (1.4)$$

Over the next few pages, we will define the various terms in this equation in the

thin flux tube (or thin annulus) limit [HAMMETT *et al.*, 1993; BEER *et al.*, 1995], followed by a description of the flux tube simulation domain and spatial coordinates.

In Eq. (1.4), $h(k_x, k_y, \theta, E, \mu, t)$ is the 5D perturbed non-adiabatic part of the species' distribution function. For the equilibrium distribution function F_0 , note that the gyrokinetic ordering expansion yields that $F_0 = F_0(\vec{R}_\perp, E, \mu) = F_0(x, E, \mu)$, so F_0 is gyrophase independent and $\hat{b} \cdot \nabla F_0 = 0$. It is commonly further assumed, as we do here, that F_0 is Maxwellian with isotropic pressure, i.e. $F_{0s} = F_{Ms} \equiv n_{0s}/(\sqrt{2\pi}v_{ts})^3 e^{-\mu B/v_{ts}^2 + v_\parallel^2/2v_{ts}^2}$. The 3D generalized gyroaveraged electromagnetic potential is represented in Eq. (1.4) as $\chi(k_x, k_y, \theta, t)$ [ANTONSEN and LANE, 1980], defined as:

$$\chi \equiv J_0(\gamma_s) \left(\Phi - \frac{v_\parallel}{c} A_\parallel \right) + \frac{J_1(\gamma_s)}{\gamma_s} \frac{m_s v_\perp^2}{Z_s e} \frac{\delta B_\parallel}{B} \quad (1.5)$$

where $\Phi(k_x, k_y, \theta, t)$ is the perturbed electrostatic potential, $A_\parallel(k_x, k_y, \theta, t)$ is the parallel component of the perturbed magnetic vector potential, $\delta B_\parallel(k_x, k_y, \theta, t)$ is the parallel magnetic perturbation, and the argument of the Bessel functions is given by $\gamma_s = k_\perp v_\perp / \Omega_s$. These field perturbations are computed self-consistently from the gyrokinetic Poisson-Ampere equations as follows:

$$-k_\perp^2 \Phi = 4\pi \sum_s Z_s e \int d^3v \left(\frac{-Z_s e F_{Ms}}{T_{0s}} \Phi + J_0(\gamma_s) h_s \right) \quad (1.6)$$

$$-k_\perp^2 A_\parallel = -\frac{4\pi}{c} \sum_s Z_s e \int d^3v (v_\parallel J_0(\gamma_s) h_s) \quad (1.7)$$

$$\frac{\delta B_\parallel}{B} = -\frac{4\pi}{B^2} \sum_s \int d^3v \left(m_s v_\perp^2 \frac{J_1(\gamma_s)}{\gamma_s} h_s \right) \quad (1.8)$$

Overall, the gyrokinetic system of equations describes the evolution of the perturbed part of a species' distribution function along the trajectories of the species' guiding center. The main driving terms as represented in Eq. (1.4) are the $v_{\parallel} \hat{b} \cdot \nabla$ term, which represents the fast convective-like motion along the field line, the ω_{dv} term ($\omega_{dv} = ((v_{\parallel}^2/v_{ts}^2)\omega_{d,\parallel} + (\mu B/v_{ts}^2)\omega_{d,\perp})$), which contains the combined curvature and ∇B drift frequencies:

$$\omega_{d,\parallel} = \frac{\rho_s v_{ts}}{B^2} \vec{k}_{\perp} \cdot \vec{B} \times \hat{b} \cdot \nabla \hat{b} \quad (1.9)$$

$$\omega_{d,\perp} = \frac{\rho_s v_{ts}}{B^2} \vec{k}_{\perp} \cdot \vec{B} \times \nabla B \quad (1.10)$$

and the RHS ω_{*T} term, which is related to the temperature and density gradients:

$$\omega_{*T} = \omega_* \left[1 + \eta_s \left(\frac{v_{\parallel}^2}{2v_{ts}^2} + \frac{\mu B}{v_{ts}^2} - \frac{3}{2} \right) \right] \quad (1.11)$$

where $\eta_s = L_{ns}/L_{Ts}$ is the ratio of equilibrium density to temperature scale lengths ($L_{ns}^{-1} = -(\rho_s/n_{0s}) \vec{k}_{\perp} \cdot \hat{b} \times \nabla n_{0s}$ and $L_{Ts}^{-1} = -(\rho_s/T_{0s}) \vec{k}_{\perp} \cdot \hat{b} \times \nabla T_{0s}$) and the diamagnetic frequency is given by $\omega_* = -\frac{\rho_s v_{ts}}{L_{ns}}$. $C(h_s)$ represents a general linearized collision operator (e.g. for pitch angle scattering and energy diffusion). The nonlinear term, which couples the perpendicular spectral modes, is contained within the convective part of the total time derivative in Eq. (1.4), i.e. $\frac{dh_s}{dt} = \frac{\partial h_s}{\partial t} + \frac{c}{B} [\chi, h_s]$, where $[\ , \]$ is the perpendicular Poisson bracket, defined as $[P, Q] \equiv \frac{\partial P}{\partial x} \frac{\partial Q}{\partial y} - \frac{\partial P}{\partial y} \frac{\partial Q}{\partial x}$. The nonlinearity comes from

$$\frac{c}{B} [\chi, h_s] = \frac{c}{B} \hat{b} \times \nabla \chi \cdot \nabla h_s \equiv \delta \vec{v}_E \cdot \nabla h_s \quad (1.12)$$

where

$$\delta\vec{v}_E = \frac{c}{B}\hat{b} \times \nabla J_0(\gamma_s)\Phi - \frac{v_{\parallel}}{B}\hat{b} \times \nabla J_0(\gamma_s)A_{\parallel} + \frac{c}{B} \frac{m_s}{Z_s e} v_{\perp}^2 \hat{b} \times \nabla \frac{J_1(\gamma_s)}{\gamma_s} \frac{\delta B_{\parallel}}{B} \quad (1.13)$$

in which the first term describes the ExB drift advection, the second term describes particle motion along the perturbed field lines $\delta B_{\perp} = \hat{b} \times \nabla_{\perp} A_{\parallel} = \nabla_{\perp} \times (\hat{b} A_{\parallel})$ (i.e. magnetic flutter transport), and the third term describes the ∇B drift due to the perturbed magnetic field.

In the gyrokinetic equation in Eq. (1.4), we have adopted flux tube geometry using the field-line following spatial coordinate system developed by [BEER *et al.*, 1995], denoted as (x, y, θ) , rather than the physical toroidal coordinates (r, θ, ϕ) . Field-aligned or ballooning geometry is derived from the Clebsh representation of the magnetic field [KRUSKAL and KULSRUD, 1958], i.e. $B = \nabla\alpha \times \nabla\psi$, where $\psi = (1/2\pi)^2 \int d\tau \vec{B} \cdot \nabla\theta$ is the poloidal flux, $\alpha = \phi - q(\psi)\theta - \nu(\psi, \theta, \phi)$ (where the function ν is 2π periodic in θ and ϕ), and θ is the physical poloidal angle. Thus, in the non-orthogonal curvilinear coordinate system described by (ψ, α, θ) , ψ (the radial-like coordinate) and α (the field line label) remain constant along a field line, while θ represents the distance along the field line. The advantage of field-aligned coordinates is that, since turbulent structures are highly elongated along the field lines (i.e. $k_{\perp}/k_{\parallel} \gg 1$), a much coarser grid can be used in the coordinate that varies only along field lines. That is, a relatively coarse grid can be used in the θ direction in the field-aligned coordinates (ψ, α, θ) .

In the thin flux tube limit, perturbed quantities are expanded using a Fourier

series in the perpendicular directions as follows:

$$A(\psi, \alpha, \theta, t) = \sum_{j=-\infty}^{\infty} \sum_{k=-\infty}^{\infty} \hat{A}_{j,k}(\theta, t) e^{ij\pi(\psi-\psi_0)/\Delta\Psi + ik\pi(\alpha-\alpha_0)/\Delta\alpha} \quad (1.14)$$

and thus periodicity is assumed in ψ and α with periodicity lengths $2\Delta\psi$ and $2\Delta\alpha$. The choice of $\Delta\alpha = \pi/N$, where N is a positive integer, corresponds to simulating a flux tube/annulus that covers $1/N$ of the full torus in the toroidal direction. For small scale turbulence in the small $\rho_* = \rho/L_*$ limit, where ρ is the gyroradius (the radial correlation length of the turbulence typically scales with ρ) and L_* is the length scale over which plasma gradients are changing), it should be sufficient to choose the toroidal width of the simulation domain to be much smaller than the full toroidal extent, as long as it is a few times the decorrelation length of the turbulence. The assumption of periodicity at the boundaries in ψ and α is a natural way of modeling the interaction of turbulence in the simulation domain with turbulence in adjacent regions of the full torus. One can always check convergence by varying $\Delta\psi$ and $\Delta\alpha$. If the results are not converging as the simulation domain gets larger, then the assumption that small scale turbulence dominates is breaking down, or effects such as scale-free avalanches are becoming important. (Global gyrokinetic codes such as GYRO relax the radial periodicity assumption and use a radial grid for ψ , while still using a spectral representation in α .)

A physical function $A(r, \theta, \phi)$ is 2π periodic in the poloidal and toroidal angles θ and ϕ , so the function $A(\psi, \alpha, \theta, t)$ in the coordinate-transformed space is $2\pi/N$ periodic in α (and thus satisfies the physical periodicity in ϕ) but is not periodic in θ at fixed ψ and fixed α . Ensuring physical periodicity in θ at fixed r and fixed ϕ leads to the following boundary condition in θ in field-line following coordinates:

$A(\psi, \alpha - q(\psi)2\pi, \theta + 2\pi, t) = A(\psi, \alpha, \theta, t)$. This leads to a more complicated θ boundary condition on $\hat{A}_{j,k}(\theta)$ in Eq. (1.14) which couples together modes with different radial mode numbers. This boundary condition is explained in detail in [BEER *et al.*, 1995]. (An explanation in a simpler slab limit can be found in [HAMMETT *et al.*, 1993].)

The notation is simplified using the new variables x and y , defined as:

$$x = \frac{q_0}{B_0 r_0}(\psi - \psi_0) \quad , \quad y = -\frac{r_0}{q_0}(\alpha - \alpha_0) \quad (1.15)$$

where $\psi_T = (1/2\pi)^2 \int d\tau \vec{B} \cdot \nabla \phi$ is the toroidal flux, $q(\psi) = d\psi_T/d\psi$, such that $q_0 = q(\psi_0)$, B_0 is the magnetic field at the magnetic axis, and r_0 is the distance from the magnetic axis to the center of the box at the midplane. Thus, Eq. (1.14) becomes:

$$A(x, y, \theta, t) = \sum_{k_x=-\infty}^{\infty} \sum_{k_y=-\infty}^{\infty} \hat{A}_{k_x, k_y}(\theta, t) e^{ik_x x + ik_y y} \quad (1.16)$$

where $k_x = j2\pi/L_x$ and $k_y = -k2\pi/L_y$ for $L_x = 2q_0\Delta\psi/B_0r_0$ and $L_y = 2r_0\Delta\alpha/q_0$. The magnitude of the perpendicular wave number ($k_{\perp}^2 = k_r^2 + k_{\theta}^2$) is given in field-aligned coordinates by $k_{\perp}^2(\theta) = k_x^2 \nabla x \cdot \nabla x + 2k_x k_y \nabla x \cdot \nabla y + k_y^2 \nabla y \cdot \nabla y$. Relating k_x and k_y to the physical k-space coordinates k_r and k_{θ} , in the \hat{s} - α limit (i.e. the high aspect ratio limit in circular geometry) we find that $k_{\theta} = k_y$ and $k_r = k_x + \theta \hat{s} k_y$, so that $k_{\perp}^2(\theta) = k_y^2 + (k_x + \theta \hat{s} k_y)^2$.

The spatial simulation domain in flux tube geometry is a rectangular box of size L_x and L_y in the perpendicular dimensions which is extended along the field lines (typically for $-\pi < \theta < \pi$, such that $L_z = 2\pi q_0 R_0$) and which twists due to the magnetic shear as it wraps around the torus. As mentioned earlier, the parallel boundary conditions at $\theta = \pm\pi$ are more complicated than the simple periodic

conditions for x and y , and involve coupling different k_x modes. The flux tube formulation usually assumes that the perpendicular dimensions of the flux tube L_x and L_y are much smaller than the minor radius of the tokamak, so that gradients and background equilibrium quantities are assumed to be constant (at their local values at r_0) across the radial width of the flux tube. Flux tube geometry is appropriate for large tokamaks in the gyro-Bohm limit of small ρ_* . (The GYRO code generalizes these thin flux tube/annulus assumptions by retaining the radial variations of the background quantities, and thus can handle arbitrary ρ_* . Convergence studies have shown that GYRO agrees with the flux tube code GS2 in the small ρ_* limit [CANDY *et al.*, 2004].) For the linear terms in the gyrokinetic equation, there is no explicit dependence on x or y , so the linear gyrokinetic equation reduces to a 1D equation in θ (each (k_x, k_y) mode is independent) for a chosen magnetic surface, just like the 1D equation for MHD ballooning modes. (Note: The most unstable linear modes often occur at $k_x = 0$ (i.e. centered in the “bad-curvature” region of the tokamak, discussed in section 1.1.2, so most linear gyrokinetic simulations, including those in this thesis, focus only on these modes.)

1.1.2 Drift Wave Microinstabilities

The sources of free energy for driving drift wave microinstabilities are the equilibrium temperature and density gradients. For a general overview of drift waves, see the review article by [TANG, 1978] or more recent articles by [CONNOR and WILSON, 1994] and [HORTON, 1999]. The most significant classes of drift waves described by the gyrokinetic model for core tokamak plasmas are:

- ion/electron temperature gradient-driven modes (ITG/ETG): driven by temperature gradients.

- trapped electron modes (TEM): driven by trapped electron toroidal precession resonances and can be driven more unstable by increased density gradients.
- kinetic ballooning mode (KBM): driven by temperature or density gradients in the presence of finite β .

ITG-driven modes and TEMs are electrostatic instabilities which are unstable in the limit of large wavelengths ($k_{\perp}\rho_i \sim 1$) and have frequencies which scale as v_{ti}/L . Within this regime, the presence of perturbed electromagnetic dynamics can lead to finite β corrections to ITG turbulence (which can be stabilizing) and coupling to the KBM at $\beta > \beta_c$, where β_c is the threshold for the ideal MHD ballooning limit. ETG-driven modes are analogous to ITG-driven modes, with the role of ions and electrons reversed, and thus have much smaller length scales ($k_{\perp}\rho_e \sim 1$) and faster frequencies ($\omega \sim v_{te}/L$).

Many useful references are available on the linear stability regimes for these tokamak drift waves. Notable for background include analytic derivations of linear threshold conditions for the ITG mode (with adiabatic electrons) by [ROMANELLI, 1989], [HAHM and TANG, 1989], and [BIGLARI *et al.*, 1989]. An analogous formula for the linear threshold of toroidal ETG modes based on comprehensive linear gyrokinetic simulations is given in [JENKO *et al.*, 2001]. Analytic dispersion relations coupling the ITG mode and TEM are given in [TANG *et al.*, 1986] (in the weak density limit) and more generally in [ROMANELLI and BRIGUGLIO, 1990]. Extensive corresponding numerical results from early linear gyrokinetic simulations can be found in [REWOLDT and TANG, 1990]. A more recent article by [ERNST *et al.*, 2004] presents an interesting comprehensive numerical stability analysis of TEM turbulence, including a map of the R/L_n vs. R/L_T stability boundaries in

the ITG/TEM regime using hundreds of linear gyrokinetic simulations as well as analysis of the nonlinear critical density gradient for TEM turbulence. Finite β effects on the ITG mode and the coupling to the KBM are analyzed analytically in a local fluid limit and numerically with a linear gyrokinetic code in [KIM *et al.*, 1993]. Finally, an interesting article by [REWOLDT *et al.*, 1987] presents an analytical and numerical analysis of the effects of collisionality on all of these modes. A review of advances in studies of the stability of tokamak drift-wave turbulence using nonlinear gyrokinetic simulations are presented in the next section of this thesis.

Overall, while ITG turbulence is believed to be the primary drive for turbulent ion thermal transport in the core region of a tokamak and the trapped electron response to ITG modes often explains much of the observed electron thermal transport, the study of additional driving mechanisms for electron thermal transport is presently an active area of research. Based on mixing length estimates (i.e. $\chi \sim (\Delta x)^2/\Delta t \sim \gamma/k_{\perp}^2$, where γ is the linear growth rate), the thermal diffusivity resulting from ETG turbulence is much smaller than that resulting from TEM turbulence, specifically $\chi_{e,ETG}/\chi_{e,TEM} \sim \sqrt{m_e/m_i} \sim 1/60$. However, gyrokinetic simulations have recently shown that, because of the difference between ITG and ETG zonal flows (unlike for ITG turbulence, the zonal flow mode for ETG turbulence is also adiabatic, effectively slowing the zonal flow growth), ETG turbulence can lead to the formation of radially elongated convective cells called streamers, which essentially increase the radial correlation length scale and thus can enhance the transport above the mixing length estimate [JENKO *et al.*, 2000; DORLAND *et al.*, 2000; JENKO and DORLAND, 2002]. (Note: The KBM can also lead to significant electron thermal transport. However, 2nd stability effects

can occur at high β , depending on the value of the equilibrium β radial gradient ($\partial_{r/a}\beta = \sum_s \partial_{r/a}\beta_s = -\sum_s \beta_s (R/L_{ns} + R/L_{Ts})(a/R)$, where the total β_{total} is given by the sum over the β for each species, i.e. $\beta_{total} = \sum_s \beta_s$ for $\beta_s = 8\pi n_{0s} T_{0s}/B^2$.)

ETG turbulence is actively being explored in particular as a candidate for explaining anomalous electron thermal transport in internal transport barriers (ITBs). An ITB is a region inside a tokamak plasma marked by steep temperature and/or density gradients. It has been experimentally observed that within an ITB, ion thermal transport is reduced to neoclassical levels, while electron thermal transport remains anomalous [STALLARD *et al.*, 1999]. The reduction of ion thermal transport within an ITB is believed to be due to large-scale equilibrium ExB shear flows, which suppress ITG modes and TEMs generally when the shearing rate γ_{ExB} exceeds the maximum ITG linear growth rate in the absence of flow shear $\gamma_{ITG,max}$. This “quenching rule” has been shown previously with gyro-Landau-fluid simulations in [WALTZ *et al.*, 1995] and more recently with nonlinear gyrokinetic simulations in [KINSEY *et al.*, 2005]. In contrast, equilibrium-scale ExB shear flows most likely do not affect ETG modes due to their large growth rates. Further supporting ETG turbulence as a driving mechanism for ITB anomalous electron transport is the fact that ETG modes drive negligible ion thermal transport, since the ion response is essentially adiabatic in the small spatial scales of ETG turbulence.

While understanding the driving mechanisms in internal transport barriers may be critical in obtaining good confinement in tokamaks, ETG turbulence is difficult to resolve computationally due to its small spatial scales and fast time scales, and thus ETG turbulence has presently only been studied in the context of adiabatic ions. Specifically, ETG physics coupled with ITG/TEM physics is presently computationally intractable with realistic ion-to-electron mass ratios. While this partially

motivates the need for advanced algorithms for gyrokinetics as explored in this thesis research, ETG physics is not a focus here. Rather, this thesis research explores the regime of ITG/TEM/KBM turbulence, focusing specifically on the effects of non-adiabatic electron dynamics and electromagnetic perturbations. This regime is described in more detail below in the context of electrostatic gyrokinetic theory.

Here we investigate the stability of ITG modes via simplifications of the gyrokinetic equation for the case of a single ion species and electrons. We consider the linear, collisionless, electrostatic limit. With these assumptions, the kinetic and field equations become:

$$\left(\frac{\partial}{\partial t} + v_{\parallel} \hat{b} \cdot \nabla + i\omega_{dv} \right) h_s = \left(i\omega_{*T} + \frac{\partial}{\partial t} \right) \frac{Z_s e F_{Ms}}{T_{0s}} J_0(\gamma_s) \Phi \quad (1.17)$$

$$\Phi \sum_s \frac{Z_s^2 e^2 n_{0s}}{T_{0s}} = \sum_s Z_s e \int d^3 v J_0(\gamma_s) h_s \quad (1.18)$$

where we have also used the assumption of small Debye length (i.e. $k_{\perp} \lambda_{Di} \ll 1$, where $\lambda_{Di}^2 = \frac{T_{0i}}{4\pi n_{0i} Z_i e^2}$) to simplify the Poisson equation. For convenience, we eliminate the time derivative on the RHS of the kinetic equation by rewriting it in terms of the gyroaveraged fluctuating particle distribution function $f_s(k_x, k_y, \theta, E, \mu, t)$, i.e. $f_s = h_s - \frac{Z_s e F_{Ms}}{T_{0s}} J_0(\gamma_s) \Phi$ (recall that h_s is the non-adiabatic part). Thus, our equations now become:

$$\left(\frac{\partial}{\partial t} + v_{\parallel} \hat{b} \cdot \nabla + i\omega_{dv} \right) f_s = \left(i\omega_{*T} - v_{\parallel} \hat{b} \cdot \nabla - i\omega_{dv} \right) \frac{Z_s e F_{Ms}}{T_{0s}} J_0(\gamma_s) \Phi \quad (1.19)$$

$$\Phi \sum_s \frac{Z_s^2 e^2 n_{0s}}{T_{0s}} (1 - \Gamma_0(b_s)) = \sum_s Z_s e \int d^3 v J_0(\gamma_s) f_s \quad (1.20)$$

where $\Gamma_0(b_s) = e^{-b_s} I_0(b_s)$ and $b_s = (k_\perp v_{th}/\Omega_s)^2$. Assuming a time and θ space dependency of $e^{-i\omega t + ik_\parallel q R \theta}$ for the perturbed quantities, we find that

$$f_s = - \left(\frac{\omega_{*T} - k_\parallel v_\parallel - \omega_{dv}}{\omega - k_\parallel v_\parallel - \omega_{dv}} \right) \frac{Z_s e F_M}{T_{0s}} J_0(\gamma_s) \Phi \quad (1.21)$$

We adopt this distribution function as a kinetic treatment of the ion species. For the electrons, however, we assume an adiabatic response, i.e. $f_e = \frac{e F_M e}{T_{0e}} J_0(\gamma_e) \Phi$. To find the ion charge density, we need to integrate Eq. (1.21) over velocity-space. Here we simplify to the local limit, where we treat $\omega_{d,\parallel}$, $\omega_{d,\perp}$, k_\parallel , k_\perp , and B as constants. Specifically, we use $\omega_{d,\parallel} = \omega_{d,\perp} = -k_y \rho_i v_{ts}/R$ (where R is the major radius). We further simplify using the following ordering assumptions:

$$\frac{\omega_d}{\omega} \sim \frac{k_\parallel v_{ti}}{\omega} \sim k_\perp \rho_i = \epsilon \ll 1 \quad (1.22)$$

This allows us to expand the denominator of Eq. (1.21). We would like to retain finite k_\parallel effects in this order, so we also assume that $\frac{\omega_{*T}}{\omega_d}$, which scales as $\sim \left(\frac{R}{L_n} + \frac{R}{L_T} \right)$, is $O(1)$. With these assumptions, the perturbed ion charge density becomes:

$$\begin{aligned} \delta n_i &\equiv Z_i e \int d^3 v J_0(\gamma_i) f_i \\ &\approx \Phi \frac{Z_i^2 e^2 n_{0i}}{T_{0i}} \left[\frac{1}{\omega} (2\omega_d - \omega_*) + \frac{1}{\omega^2} \left(k_\parallel^2 v_{ti}^2 - 2\omega_d \omega_* (1 + \eta_i) + 7\omega_d^2 \right) \right] \end{aligned} \quad (1.23)$$

Substituting this and the adiabatic electron response in the RHS of the Poisson equation in Eq. (1.20) yields the following dispersion relation:

$$\omega = \frac{(2\omega_d - \omega_*)}{2 \left(\frac{1}{Z_i} \frac{T_{0i}}{T_{0e}} + k_\perp^2 \rho_i^2 \right)}$$

$$\pm \frac{\sqrt{(2\omega_d - \omega_*)^2 + 4\frac{1}{Z_i}\frac{T_{0i}}{T_{0e}}\left(k_{\parallel}^2 v_{ti}^2 - 2\omega_d \omega_* (1 + \eta_i) + 7\omega_d^2\right)}}{2\left(\frac{1}{Z_i}\frac{T_{0i}}{T_{0e}} + k_{\perp}^2 \rho_i^2\right)} \quad (1.24)$$

This expression is accurate to $O(\epsilon^2)$ for $\eta_i \leq O(1)$. In the high η_i limit ($\eta_i, R/L_{Ti} \gg 1$), it reduces to the standard purely unstable “ η_i mode”:

$$\omega = \pm i \frac{\sqrt{2\omega_d \omega_* \eta_i}}{\sqrt{\frac{1}{Z_i}\frac{T_{0i}}{T_{0e}} + k_{\perp}^2 \rho_i^2}} = \pm i k_y \rho_i \frac{\sqrt{2\frac{R}{L_{Ti}}}}{\sqrt{\frac{1}{Z_i}\frac{T_{0i}}{T_{0e}} + k_{\perp}^2 \rho_i^2}} \frac{v_{ti}}{R} \quad (1.25)$$

Eq. (1.25) shows that the linear ITG growth rate scales as $\gamma \sim v_{ti}/R$. Thus, since $R/L \sim O(1)$, the standard gyro-Bohm mixing length estimate for the thermal diffusivity is apparent from this equation, i.e. $\chi_{ITG} \sim \gamma/k_{\perp}^2 \sim \rho_i^2 v_{ti}/L$. (Note: There are subtleties about the k_{\perp}^2 scaling assumptions; here we have used the standard gyrokinetic ordering assumption that $k_{\perp} \rho_i \sim O(1)$ for simplicity.)

Note that Eq. (1.25) has the same form as the classic magnetic curvature-driven MHD interchange instability ($\gamma_{interchange} = v_{ti}/\sqrt{RL_p}$, where $L_p^{-1} = -\nabla p/p$ is related to the gradient length scale of the pressure), but with $k_{\perp} \rho_i$ terms since Eq. (1.25) represents an electrostatic drift-type mode that depends on FLR effects. While the driving effect of the temperature gradient on the ITG mode is clearly evident in Eq. (1.25), from Eq. (1.24) we can also see that there is a competing stabilizing effect of driving a parallel sound wave. Thus, we can solve for the critical temperature gradient at which the ITG mode is stabilized:

$$\left(\frac{R}{L_{Ti}}\right)_c = \frac{1}{8} \left(\frac{1}{\frac{1}{Z_i}\frac{T_{0i}}{T_{0e}} + k_{\perp}^2 \rho_i^2}\right) \left(2 - \frac{R}{L_{ni}}\right)^2 + \frac{7}{2} - \frac{R}{L_{ni}} + \frac{k_{\parallel}^2 v_{ti}^2}{2\omega_d^2} \quad (1.26)$$

The presence of non-adiabatic electrons both modifies the ITG instability and introduces a new class of drift waves, the TEM. The effect of non-adiabatic electron

dynamics on the ITG instability can most simply be seen by dividing the perturbed electron density response as:

$$\delta n_e = f_t \delta n_{e,trapped} + (1 - f_t) \delta n_{e,circulating} \quad (1.27)$$

where $\delta n_{e,trapped}$ is the density response of the trapped electrons, $\delta n_{e,circulating}$ is the density response of the free electrons, and f_t is the fraction of trapped particles. For the circulating electrons, we assume an adiabatic response, since there is nothing to prevent the free electrons from thermalizing. For the trapped electrons, we consider the bounce-average of the gyrokinetic equation in Eq. (1.19). Most significantly, the parallel convective term is eliminated, since trapped particles have zero bounce-averaged parallel velocity. For the bounce-averaged Φ and ω_d , we assume the $\theta = 0$ local limit values. Thus, using the ansatz $e^{-i\omega t + ik_{\parallel} q R \theta}$ for the perturbed quantities, we obtain:

$$f_{e,trapped} = - \left(\frac{\omega_{*T,e} - \omega_{dv,e}}{\omega - \omega_{dv,e}} \right) \quad (1.28)$$

Integrating over velocity-space using the simplification of the ordering assumptions of Eq. (1.22) to expand the denominator, we find that

$$\begin{aligned} \delta n_e \approx \Phi \frac{e^2 n_{0e}}{T_{0e}} & \left[f_t \frac{1}{\omega} (2 - \omega_{de} - \omega_{*e}) \right. \\ & + f_t \frac{1}{\omega^2} \left(-2\omega_{de}\omega_{*e}(1 + \eta_e) + 7\omega_{de}^2 \right) \\ & \left. + (1 - f_t) \right] \end{aligned} \quad (1.29)$$

Using Eq. (1.23) and Eq. (1.29) for the RHS density response in the Poisson equation in Eq. (1.20) (note that ion trapping is ignored and is often negligible due to the

long bounce time for ions), we find that:

$$\omega = \pm i \frac{2(\omega_{*i}\omega_{di}\eta_i + f_t\omega_{*e}\omega_{de}\eta_e)}{(1 - f_t)\frac{1}{Z_i}\frac{T_{0i}}{T_{0e}} + k_{\perp}^2\rho_i^2} \quad (1.30)$$

where we have assumed the large η limit for simplicity.

The dispersion relation in Eq. (1.30) basically represents the coupled ITG/TEM regime in a simple limit. Overall, instability requires that ω_{ds} and ω_{*s} have the same sign. (Note that $\omega_{de} = -Z_i\frac{T_{0e}}{T_{0i}}\omega_{di}$ and $\omega_{*e} = -Z_i\frac{T_{0e}}{T_{0i}}\frac{R/L_{ne}}{R/L_{ni}}\omega_{*i}$, i.e. the signs are reversed for electrons.) Physically, this requires that the equilibrium pressure gradient $\nabla p_0 = \nabla(n_0T_0)$ point in the same direction as ∇B , which occurs on the outer midplane of the tokamak and hence is referred to as the “bad curvature” region.

Comparing Eq. (1.30) with the pure “ η_i mode” growth rate in Eq. (1.25), we see that the effect of the nonadiabatic electrons is to increase the ITG growth rate. Physically, trapped electrons are destabilizing since they are unable to respond adiabatically to local variations in Φ and thus cannot participate in charge canceling. Note then that collisional effects are significant for TEMs, since pitch angle collisions can result in the trapping/detrapping of electrons. While non-adiabatic electron dynamics are required for simulations with magnetic perturbations, inclusion of non-adiabatic electron dynamics and collisionality is generally essential for an accurate model of combined ion and electron anomalous transport driven by drift wave turbulence in the ITG/TEM/KBM regime.

1.1.3 Advances of Nonlinear Gyrokinetic Simulations

The first nonlinear simulations of drift wave-induced plasma microturbulence in toroidal geometry were done with gyrofluid codes. The gyrofluid equations are derived from velocity moments of the gyrokinetic equation, using carefully chosen closure models to capture key kinetic effects. (There were also pioneering nonlinear toroidal simulations by C. Z. Cheng and H. Okuda in the 1970's, but these were full particle simulations before the development of the nonlinear gyrokinetic equation or the δf algorithm and the resulting resolution on those early computers was fairly coarse [CHENG and OKUDA, 1977].) The key nonlinear gyrofluid simulations were performed in the early to mid 1990's. The most significant result of these gyrofluid simulations was to show that turbulence-generated ExB shear flows play an important role in the nonlinear saturation of ITG turbulence, first shown in slab geometry [DORLAND, 1992] and later in toroidal geometry [HAMMETT *et al.*, 1993; WALTZ *et al.*, 1994; WALTZ *et al.*, 1995; BEER, 1995]. Gyrofluid simulations were also the first microturbulence codes to nonlinearly incorporate trapped electron dynamics [BEER, 1995] and electromagnetic dynamics [SNYDER, 1999], as well as to show the stabilizing effects of large-scale equilibrium ExB shear flows on ITG turbulence [WALTZ *et al.*, 1995; WALTZ *et al.*, 1998]. Significant advances in theory-based turbulent transport modeling (discussed in more detail in the next section), such as the development of the IFS-PPPL model [KOTSCHENREUTHER *et al.*, 1995b] and the GLF23 model [WALTZ *et al.*, 1997], were also made based on these nonlinear gyrofluid simulations.

Fully gyrokinetic nonlinear simulations of ITG/TEM turbulence soon followed the gyrofluid codes, using δf particle-in-cell (PIC) algorithms. Specifically, in the mid 1990's, the independently-developed PIC codes ORB [PARKER *et al.*, 1993]

and PG3EQ [DIMITS *et al.*, 1994; DIMITS *et al.*, 1996] were performing electrostatic gyrokinetic simulations of ITG turbulence (in the adiabatic electron limit). ORB used full cross-section global geometry, while PG3EQ used flux tube geometry. PG3EQ was the first code to show numerically the importance of a linearly undamped residual component of the purely poloidal ($k_y = 0$) zonal flows [ROSENBLUTH and HINTON, 1998] in saturating the level of the turbulence near marginal stability, leading to an upshift in the nonlinear critical temperature gradient [DIMITS *et al.*, 2000]. (The gyrofluid codes had been the first to emphasize the importance of zonal flows in regulating the turbulence, but the initial gyrofluid closures had too much damping of this component of the zonal flows.) For more recent work on the PIC approach, see [PARKER *et al.*, 2004] or [WANG *et al.*, 2006].

While one approach to solving the gyrokinetic equations is the Lagrangian PIC method used in the references in the above paragraph, another approach uses Eulerian or “continuum” methods. Eulerian solvers are actually a class of algorithms which can employ a variety of modern methods that have been developed for computational fluid dynamics, such as pseudo-spectral techniques, high-order upwind or WENO (weighted essentially non-oscillatory) differencing, higher-order Gaussian integration, or implicit methods. Such Eulerian methods are the focus of this thesis research. The main present-day continuum-based gyrokinetic codes are GS2 [KOTSCHENREUTHER *et al.*, 1995a; DORLAND *et al.*, 2000], GENE [JENKO, 2000], and GYRO [CANDY and WALTZ, 2003a].

The nonlinear flux tube GS2 code was the first implementation of the fully electromagnetic nonlinear gyrokinetic-Poisson-Ampere system of equations, including trapped and passing particle dynamics. (GS2 is still the only major nonlinear

gyrokinetic code which includes finite δB_{\parallel} effects, which are believed to be particularly important in high β spherical torus plasmas [BOURDELLE *et al.*, 2003].) Prior to this, the GENE code had been the first code developed to solve the drift-kinetic equation for electrons with fluid ions for edge drift-Alfvén turbulence studies. GENE has since been upgraded, first to include gyrokinetic ions (ignoring trapping) and later to include trapping [JENKO *et al.*, 2000]. Presently, GENE and GS2 contain similar gyrokinetic physics models. GS2 and GENE were recently the first codes to simulate ETG-driven turbulence (with adiabatic ions, such that ion-scale turbulence is neglected), which identified the existence of radially extended eddies called streamers which can significantly enhance anomalous electron thermal transport above mixing length estimates [JENKO *et al.*, 2000; DORLAND *et al.*, 2000; JENKO and DORLAND, 2002].

To date, the most comprehensive gyrokinetic code for tokamak microturbulence simulations is the GYRO code. This code was originally modeled after GS2 but has since been extended to include global effects, specifically profile variation in the density gradients, including equilibrium-scale ExB shear rotation. Most significantly, GYRO has been used to show the importance of including equilibrium ExB shear in modeling low confinement L-mode discharges [CANDY and WALTZ, 2003b], which are experimentally observed to have a Bohm-like scaling (i.e. $\chi_B \sim \rho_s c_s$) [MCKEE *et al.*, 2001], rather than a gyro-Bohm scaling (i.e. $\chi_{GB} \sim \chi_B \rho_s / a$), as observed for high confinement H-mode discharges [PETTY *et al.*, 1995]. This may explain why previous GS2 simulations of H-mode discharges in Alcator C-Mod, which had helped to identify the importance of including non-adiabatic electron dynamics and finite collisionality in accurately recovering the nonlinear upshift of the critical temperature gradient, were successful [MIKKELSEN *et al.*, 2002], while GS2 studies

of L-mode discharges in DIII-D yielded energy losses which were 2-3 times larger than the experimental values [ROSS and DORLAND, 2002].

Overall, GYRO simulations have identified “full physics” necessary for accurate core tokamak plasma simulations, including, in addition to equilibrium ExB shear, non-adiabatic electron dynamics with trapped and passing electron physics, collisionality, and electromagnetic fluctuations. However, presently “routine” nonlinear gyrokinetic simulations are mostly performed in the electrostatic limit, sometimes with adiabatic electrons, to reduce the computational intensity. Thus, faster algorithms for gyrokinetic solvers, such as those explored in this thesis, would be useful for more efficient studies of plasma microturbulence.

The next generation of gyrokinetic simulations will incorporate multiscale dynamics, such as bridging the ITG/TEM regime with the ETG regime, connecting the slow time scales of macroscopic transport with the fast dynamics of gyrokinetics (described further in the next section), studying the slow evolution of neoclassical tearing modes (which depend sensitively on the effects of gyrokinetic turbulence in flattening the pressure profile around the island), and coupling core tokamak simulations with the plasma edge region. The edge region is particularly complicated due to existence of low and high collisionality regimes and steep gradients, such that particle drift orbit widths can be comparable to the equilibrium radial gradient scale lengths. Presently, most edge plasma simulations are done with fluid simulation models, such as the BOUT code [XU *et al.*, 2000], so kinetic extensions are needed. A large initiative in this direction is being undertaken by the Center for Edge Plasmas [NEVINS *et al.*, 2004], and this has partially motivated the exploration of advanced implicit algorithms for Eulerian gyrokinetic solvers in this thesis.

1.1.4 Turbulent Transport Models

While gyrokinetics allows us to study the nature of low-frequency microscopic drift instabilities and to compute key properties of the turbulence which result from these instabilities (such as thermal, momentum, and particle transport coefficients), the ultimate goal of gyrokinetic simulations is to aid in the building of a turbulent transport model. Previous theoretical models of anomalous thermal and particle transport have been based on linear gyrokinetic and nonlinear gyrofluid turbulence simulations, generally in a circular flux surface limit. The most widely used of these drift wave theory-based transport models include the IFS-PPPL model [KOTSCHENREUTHER *et al.*, 1995b], the GLF23 model [WALTZ *et al.*, 1997], and the Multi-mode model [BATEMAN *et al.*, 1998].

The IFS-PPPL thermal transport model consists of an analytic formula for the ion heat coefficient based on interpolations of scans over nine parameters (R/L_T , R/L_n , q , \hat{s} , T_{0i}/T_{0e} , r/R , ν_{ei} , n_b/n_e , and Z_{eff}) using a nonlinear, toroidal, flux tube-based gyrofluid code with adiabatic electrons. Calculations of χ using this code were supplemented with linear gyrokinetic ballooning calculations with non-adiabatic electron physics to account for gyrokinetic electron dynamics and to improve the accuracy of critical temperature gradient predictions. Radial temperature profiles obtained from coupling the IFS-PPPL model with the 1D steady-state power balance code HYPED exhibited good quantitative agreement with data from TFTR L-mode discharges in the core confinement region. Good agreement was also found with data from the enhanced-confinement, high temperature, supershot regime [ERNST *et al.*, 1998] as well as with L-mode and H-mode discharges from shaped tokamaks [MIKKELSEN *et al.*, 1998] using an updated version of the IFS-PPPL model which includes ExB shear suppression effects and a relatively weak

elongation scaling factor of $\chi \sim 1/(1 + ((\kappa - 1)q/3.6)^2)$, based on linear gyrokinetic and nonlinear gyrofluid simulations of moderately shaped ($\kappa < 1.6$) plasmas [DORLAND *et al.*, 1996].

Inspired by the success of the IFS-PPPL model, the subsequent GLF23 model consists of a linear, trial function-based gyrofluid code with quasi-linear transport coefficients in an s - α circular flux surface limit [WALTZ *et al.*, 1997]. To normalize the saturation level of the fluctuating quantities in the quasi-linear flows, this model uses a mixing rate rule tuned to fit full nonlinear, single ion species, gyrofluid simulations of ITG-driven transport. Overall, the GLF23 model is comparable to the IFS-PPPL model for L-modes and H-modes in the core confinement regime. It does, however, attempt to better predict enhanced core transport barriers by including the stabilizing effects of negative magnetic shear and high Shafranov shift gradients (i.e. the MHD α parameter). ExB shear stabilization effects (which are often dominant) are also more accurately modeled in the GLF23 model than in the IFS-PPPL model, in which flow shear corrections generally appear to be too strong. However, problems with the GLF23 model's original treatment of high α and negative shear have recently been found and some interim improvements have been made, while trying to find a way to include more realistic geometry effects [STAEBLER *et al.*, 2005]. It is notable that both the IFS-PPPL model and the GLF23 model tend to be very stiff (more than fluid models like the Multi-mode model described below) in that the transport rises very rapidly once the critical gradient is exceeded. A general overview of the development of the GLF23 model, its application in predicting transport in DIII-D plasmas, and outstanding physics issues can be found in [KINSEY *et al.*, 2005]. A significant upgrade of the GLF23 model based on an extensive database of nonlinear simulations from the global

gyrokinetic code GYRO over a wide range of operating parameters is presently under development [WALTZ, 2005].

Similar to the GLF23 model, the Multi-mode model is based on quasi-linearized fluid equations describing ITG modes and TEMs [BATEMAN *et al.*, 1998]. A further approximation includes the use of only one typical value of k_y in the quasi-linear model, rather than a more accurate spectrum of modes. Although the Multi-mode model is based on circular plasmas, it does include an empirically-based κ^{-4} factor in all transport calculations as an attempt to account for the effects of elongation on transport. Additional tuning coefficients (also based on fits to experimental data) are used to account for fast ion and Shafranov shift effects. While a coupling of the Multi-mode model with the BALDUR transport code has yielded results which are in good agreement with both L-mode and H-mode discharges, the main limitation of this model is that it lacks the effects of ExB velocity shear.

Turbulent transport models based directly on nonlinear simulations of gyrokinetic simulations of plasma turbulence are not yet fully tractable, but are an active area of research. One possibility would be to iteratively couple a transport code with a gyrokinetic code. The basic idea is that thermal and particle transport coefficients from a number of independent flux tube/annulus GS2 or GYRO microturbulence simulations, each of which is simulating a different radial region of the plasma (i.e. one turbulence simulation for the region $0.1 < r/a < 0.2$, another for the region $0.2 < r/a < 0.3$, etc.) can be patched together to approximate the full radial dependence. These can then subsequently be used in a transport code to compute the evolution of plasma temperature and density profiles given time-dependent boundary conditions, which can iteratively be fed back into a gyrokinetic

code. At least for steady state problems, and assuming a fixed boundary condition inside the top of the edge pedestal, this is a challenging but seemingly feasible goal by using the latest in massively parallel computers. Such an approach would benefit from projective integration [GEAR and KEVREKIDIS, 2003a; GEAR and KEVREKIDIS, 2003b] and advanced implicit methods to stabilize the iteration between the long time scale transport code and the short time scale microturbulence code. (Alternatively, with advances in computing within the next few years, it might become feasible to run GYRO for a full tokamak cross-section.)

For a complete predictive model of tokamak behavior, one would also want to couple to a comprehensive edge turbulence simulation. Because of various special features of edge turbulence (e.g. both weak and strong collisional regimes, open and closed field lines, wall interactions, strong atomic physics effects, etc.), for which present core gyrokinetic microturbulence codes are not well suited and would require significant upgrades, there are initiatives to build new gyrokinetic codes to specifically simulate edge turbulence.

In any case, the types of fast iterative implicit solvers that we explore in this thesis research could be useful to enhance the time efficiency of both the present core microturbulence gyrokinetic codes and future edge microturbulence gyrokinetic codes. However, even with these computational savings, such direct coupling between a transport code and gyrokinetic codes would still be computationally very expensive, and one would want to have faster alternatives for scoping studies. One alternative would be a transport model based on the reduced-order trial function code which we develop in this thesis, which could then be fit to nonlinear gyrokinetic simulations. This would be a kind of kinetic extension of the GLF23 model.

1.2 Motivation

To summarize, the contribution of this thesis is the development of advanced algorithms for gyrokinetics which aid in more effective studies of plasma microturbulence and the driving mechanisms of anomalous transport in tokamaks. Accurate simulations of core tokamak plasmas which captures the physics of ITG, TEM, KBM, and ETG physics require gyrokinetic ions, non-adiabatic electron dynamics, trapped electron physics, finite β physics, collisions, impurity species, shaped plasma geometry, and equilibrium-scale ExB shear. The algorithms studied in this work focus on the regime of ITG/TEM/KBM physics and are particularly designed for faster simulations with the inclusion of non-adiabatic electron dynamics (which increase the time step restrictions of standard explicit algorithms by a factor of $\sqrt{m_i/m_e}$ in order to resolve fast parallel electron dynamics) and with electromagnetic perturbations (which increase the time step restrictions of standard algorithms by a factor of $\beta^{-1/2}$ in order to resolve the fast Alfvén waves). The latter is particularly important for extending core kinetic simulations to edge kinetic formulations, where an Alfvén wave which is even faster than the thermal electron motion exists in the low β edge/scrape-off region. Overall, this research may aid in the future building of an integrated gyrokinetic-based turbulent transport model incorporating slow macroscopic transport time scales with the driving microscopic gyrokinetic fast dynamics, as well as more generally in developing gyrokinetic simulations as a predictive tool for designing future tokamaks based on extensive optimizational design wrappers. Furthermore, in this direction, studies of the effects of shaping on gyrokinetic stability and transport in this thesis research contribute in the near-term to an extensive database of stability properties over a range of operating parameters, recently begun by the GYRO users group, which may be essential in

understanding existing experiments and in ultimately achieving a burning plasma in ITER.

1.3 Overview of this Thesis

This thesis focuses on two main themes: advanced algorithms for gyrokinetics (Chapters 2-3) and applications of gyrokinetics to study the effects of flux surface shape on the stability and transport of tokamak plasmas (Chapters 4-5).

Chapter 2 explores various possible improved numerical algorithms for initial value Eulerian gyrokinetic solvers. The algorithms explored include semi implicit-explicit schemes (which treat the distribution function terms in the gyrokinetic equation implicitly, while the field terms are treated explicitly) and iterative implicit schemes (which are based on numerical approximations of the plasma response as a model preconditioner combined with standard iterative schemes, such as Krylov solvers). For this work, we focus on the time-advancement algorithm combined with GS2's 2nd order compact finite differencing of spatial derivatives, though the difficulties with this spatial differencing are discussed.

In Chapter 3, the implementation of an Alternating Direction Implicit (ADI) algorithm for a gyrokinetic problem is explored and a stability analysis for a test problem of a shear kinetic Alfvén wave is performed. While ADI algorithms are robustly stable for many types of problems, we show that for gyrokinetic problems the ADI algorithm has a very severe time step limitation that would lead to a surprising numerical instability if violated. Comparisons with some fully explicit and semi implicit-explicit schemes are also made. This chapter is based closely on a recent paper as published in [BELLI and HAMMETT, 2005].

In Chapter 4, the effects of flux surface shape and other plasma parameters on the gyrokinetic stability and transport of tokamak plasmas is investigated using GS2. Studies of the scaling of nonlinear ITG turbulence with shaping parameters are performed starting with a representative JET-like flux surface and artificially varying elongation, triangularity and their radial gradients together using the Miller analytic equilibrium formalism [MILLER *et al.*, 1998] to approach the circular limit via linear interpolation. Comparisons are made with empirical experimentally-based elongation scalings. The effects of shaping on the Dimits upshift of the nonlinear critical temperature gradient as well as the effects of electromagnetic dynamics in the presence of shaping are also explored.

Chapter 5 formulates a reduced-order local model for linear gyrokinetics to aid in fast scoping studies of shaping effects. This model includes the effects of plasma shaping, magnetic shear, and toroidal geometry by using representative values of the equilibrium parameters averaged over a Gaussian trial eigenfunction, using the same geometrical information available in the full GS2 gyrokinetic code. Benchmarks with GS2 in the linear, collisionless, electrostatic limit for a range of shaped flux surface equilibria are presented. Extensions to include magnetic fluctuations via coupling to higher-order Hermite basis functions are also described.

Finally, Chapter 6 summarizes the main results from this thesis and presents possible new continuing areas of research based on this work.

Chapter 2

Semi-Implicit and Iterative Implicit Algorithms for Eulerian Gyrokinetic Solvers

The main numerical approaches to gyrokinetic simulations are particle-in-cell (PIC) solvers and Eulerian solvers. PIC (or Lagrangian) solvers integrate the gyrokinetic equations of motion for millions of particles, while Eulerian (or continuum) solvers use finite difference and/or spectral methods on a discrete grid. The first nonlinear toroidal gyrokinetic codes were only of the PIC type [DIMITS *et al.*, 1996; SYDORA *et al.*, 1996; PARKER *et al.*, 1999] primarily because the gyrokinetic equation is presented in characteristic form when derived with Hamiltonian formalism and the algorithms are easier to code relative to Eulerian solvers. For many years, nonlinear gyrokinetic PIC simulations were generally limited to electrostatic fluctuations or to very low β , though recent work has demonstrated a successful way to implement electromagnetic extensions at higher β [CHEN and PARKER,

	PIC	Eulerian
Local Geometry	PG3EQ (Dimits et al.) GEM (Chen & Parker)	GS2 (Kotschenreuther, Liu, & Dorland)
Global Geometry	GTC (Lin)	GYRO (Candy & Waltz)

Table 2.1: The main gyrokinetic codes currently supported by the U.S. fusion program and their primary authors. Presently, all of these codes except GTC contain electromagnetic dynamics.

2003]. Eulerian gyrokinetic simulations are relatively recent, with the first nonlinear simulations done in the local flux tube/annulus limit [JENKO, 2000; DORLAND *et al.*, 2000] and, more recently, with nonlocal effects [CANDY and WALTZ, 2003a]. (There is also a pre-gyrokinetic history of Eulerian Vlasov simulations, including early work by Cheng and Knorr [CHENG and KNORR, 1976], though the Eulerian algorithms in use today have evolved since then.) The main gyrokinetic codes presently supported by the U.S. fusion program are given in table 2.1.

There are two approaches to linear Eulerian simulations: an initial value approach and an eigenvalue approach. An initial value code solves for the distribution function using a finite difference in time. In contrast, an eigenvalue code Laplace transforms in time, which leads to an integro-differential system of equations where the frequency is an eigenvalue. This system of equations can be converted into a matrix equation by expanding the unknown perturbed electrostatic and electromagnetic potentials in terms of chosen basis functions. The eigenvalue approach allows one to find multiple linear modes with different frequencies, while the initial value approach is usually restricted to finding the fastest growing (or least damped) eigenmode. The main benefit of the initial value approach compared with

the eigenvalue approach is that initial value codes can be more easily generalized for nonlinear simulations. In this work, we focus on initial value Eulerian simulations.

There are two general schemes for time differencing a partial differential equation for use in an initial value code: implicit schemes and explicit schemes. An implicit scheme is one in which the evaluation of the unknown function f^{n+1} at the new time level t^{n+1} depends on some function of f^{n+1} . In contrast, in a fully explicit scheme, the evaluation of f^{n+1} depends only on functions of f^m which are known from previous time steps, i.e. $m < n + 1$. In general, implicit schemes are more computationally intensive per time step than explicit schemes since implicit finite differencing converts the differential equation into an algebraic equation for the vector of discrete unknowns f_i^{n+1} , where the subscript i denotes the grid indexing with respect to the non-temporal independent variables (e.g. spatial dimensions and velocity dimensions). In the case of the gyrokinetic equation, this algebraic equation is a matrix equation of the form $A\vec{x} = \vec{b}$, which must be solved for \vec{x} at each time step. However, the advantage of implicit schemes is that they are generally unconditionally stable, thus allowing for larger time steps than an explicit scheme.

For example, consider a general implicit finite difference time advancement scheme for the PDE $\frac{\partial f}{\partial t} = Lf$, where L is some arbitrary linear operator. The finite difference form of this equation (ignoring the non-temporal grid indexing) with 1st order accuracy in time is:

$$\frac{1}{\Delta t} (f^{n+1} - f^n) = L (r f^{n+1} + (1 - r) f^n) \quad (2.1)$$

where r is the time-centering parameter, such that $0 \leq r \leq 1$, where $r = 0$ represents a fully explicit scheme, $r = 1$ represents a fully implicit scheme, and $r = 1/2$ represents a time-centered 2nd order accurate implicit scheme. Defining an amplification factor A such that $f^{n+1} = Af^n$ and substituting this into Eq. (2.1), we find that

$$A = \frac{1 + \lambda_L \Delta t (1 - r)}{1 - \lambda_L \Delta t r} \quad (2.2)$$

where we have assumed that L is diagonalizable, with eigenvalues given by λ_L . For a fully explicit scheme ($r = 0$), $A = 1 + \lambda_L \Delta t$ and, thus, even if $\lambda_L = i\omega$ with real ω for stable oscillations, $|A| > 1$ for $\Delta t > 0$, i.e. the finite difference scheme is numerically unstable for undamped waves with purely imaginary λ_L for all Δt . For a fully implicit scheme ($r = 1$), however, $A = (1 - \lambda_L \Delta t)^{-1}$, and thus numerical stability is guaranteed if all of the eigenvalues of L have zero or negative real part. For the special case where the eigenvalues of L are purely imaginary, while the fully implicit scheme is numerically stable, the centered implicit scheme ($r = 1/2$) has the additional advantage of unitary $|A|$, just like the exact solution $f^{n+1} = e^{-i\omega \Delta t} f^n$, and thus has perfect stability with no artificial dissipation.

Many Eulerian codes use explicit or semi-implicit time stepping algorithms. For example, the GENE code [JENKO, 2000], which has been useful for studying various regimes of drift-Alfvén and ETG turbulence [JENKO *et al.*, 2000], originally used an explicit Lax-Wendroff finite difference technique for the linear terms with a multi-dimensional, 2nd order upwind method due to Colella [COLELLA, 1990] for the nonlinear terms. (Some of the algorithms in GENE have recently been upgraded to employ 4th and 6th order compact finite differencing with 3rd order explicit Runge-Kutta time stepping [JENKO *et al.*, 2005].) The initial algorithm of the global GYRO code [CANDY and WALTZ, 2003a] used a fully explicit, 5

stage, 4th order Runge-Kutta scheme with higher-order upwind differencing. However, this algorithm was found to be numerically unstable at small $k_{\perp}\rho_i$ even at time steps well below the electron advective Courant limit ($v_{\parallel}\Delta t/\Delta_L \ll 1$) since it was mathematically connected with the electrostatic Alfvén branch. Recent implementation of a 2nd order Implicit-Explicit Runge-Kutta splitting scheme in GYRO [CANDY and WALTZ, 2003b] using precomputed plasma response matrices for the parallel dynamics (a variant of GS2’s approach studied here) has yielded improved stability by naturally cutting off high frequency oscillations, while still asymptotically preserving accuracy in the stiff limit, unlike some higher-order splitting schemes. The Eulerian flux tube-based GS2 code [KOTSCHENREUTHER *et al.*, 1995a; DORLAND *et al.*, 2000] was the first implementation of the fully electromagnetic, nonlinear 5D gyrokinetic equations including trapped and passing particle dynamics. (The GENE code preceded GS2 in some aspects, as it was the first code developed to solve the drift-kinetic equation for electrons with fluid ions for edge drift-Alfvén turbulence studies. In [JENKO *et al.*, 2000] it was upgraded to include gyrokinetic ions (ignoring trapping) and has recently been further upgraded to include trapping.) GS2 employs a fully implicit treatment of all of the linear terms (parallel dynamics, ω_* diamagnetic terms, and magnetic drifts), and thus has no time restrictions on stability in the linear limit. Of course there is a stability limit from the explicit treatment of the nonlinear terms, but the implicit treatment of the linear terms is still a significant advantage because they contain high frequency waves that do not interact much with the turbulence of interest but still need to be treated in a numerically stable way.

While these various Eulerian gyrokinetic codes have been quite successful, there is some overhead in the precomputation of the plasma response implicit matrices,

so there is interest in exploring faster semi-implicit algorithms. Thus, here we present studies of various improved numerical algorithms for continuum/Vlasov gyrokinetic codes. While at times we focus on implementation of these algorithms in the GS2 code, the methods that we discuss are more generally applicable and may be useful in more global codes, such as GYRO. Faster implicit algorithms may be particularly useful for edge gyrokinetic simulations, which must cope with a wide range of collisional and wave time scales.

2.1 Implicit Schemes

The starting equations that we would like to solve are the coupled gyrokinetic-Poisson-Ampere equations (Eqs. (1.4) and (1.6) - (1.8)), given as follows in the linear, collisionless, $\delta B_{\parallel} = 0$ limit for simplicity:

$$\begin{aligned} \frac{\partial f_s}{\partial t} + \frac{v_{\parallel}}{qR} \frac{\partial f_s}{\partial \theta} + i\omega_{dv} f_s &= \left(i\omega_{*T} - i\omega_{dv} - \frac{v_{\parallel}}{qR} \frac{\partial}{\partial \theta} \right) \frac{eZ_s F_{Ms}}{T_{0s}} J_0(\gamma_s) \Phi \\ &- \left(i\omega_{*T} + \frac{\partial}{\partial t} \right) \frac{eZ_s F_{Ms}}{T_{0s}} J_0(\gamma_s) \frac{v_{\parallel}}{c} A_{\parallel} \end{aligned} \quad (2.3)$$

$$\sum_s \frac{n_{0s} e^2 Z_s^2}{T_{0s}} (1 - \Gamma_0(b_s)) \Phi = \rho_{dens}[\Phi, A_{\parallel}] \quad (2.4)$$

$$\frac{c}{4\pi} k_{\perp}^2 A_{\parallel} = \rho_{curr}[\Phi, A_{\parallel}] \quad (2.5)$$

where $f_s(k_x, k_y, \theta, v_{\parallel}, v_{\perp}, t)$ is the 5D perturbed part of the species' distribution function ($f_s = h_s - \frac{Z_s e F_{Ms}}{T_{0s}} J_0(\gamma_s) \Phi$, where h_s is the perturbed non-adiabatic component), $\Phi(k_x, k_y, \theta, t)$ is the perturbed electrostatic potential, $A_{\parallel}(k_x, k_y, \theta, t)$ is the parallel component of the perturbed magnetic vector potential, $\gamma_s = k_{\perp} v_{\perp} / \Omega_s$, $\Gamma_0(b_s) = e^{-b_s} I_0(b_s)$, and $b_s = (k_{\perp} v_{th} / \Omega_s)^2$. The plasma charge and current densities

are given by

$$\rho_{dens}[\Phi, A_{\parallel}] = \sum_s eZ_s \int d^3v J_0(\gamma_s) f_s \quad (2.6)$$

$$\rho_{curr}[\Phi, A_{\parallel}] = \sum_s eZ_s \int d^3v v_{\parallel} J_0(\gamma_s) f_s \quad (2.7)$$

Note that, in the linear limit, each (k_x, k_y) mode is independent.

As noted before, the GS2 algorithm [KOTSCHENREUTHER *et al.*, 1995a] is unique among gyrokinetic codes in that it is fully implicit linearly. (The nonlinear term is treated pseudo-spectrally in space (perpendicular to the field lines) with an explicit 2nd order Adams-Bashforth time stepping scheme.) To do this efficiently, GS2 uses a variation of the Beam-Warming algorithm [BEAM and WARMING, 1976]. (Note: A version of the Beam-Warming algorithm also appears earlier in the work of Wendroff [WENDROFF, 1960].) The Beam-Warming algorithm is equivalent to 2nd order compact finite differencing. Compact finite differencing is usually used to achieve higher-order accuracy. (Refer to [DURRAN, 1998] for more details on compact finite differencing.) However, in GS2 the 2nd order variant is used because it leads to an implicit algorithm that needs only a relatively simple bi-diagonal matrix inversion to advance the distribution function (though the implicit solver for the fields is more complicated). (As an aside, we should note that the implicit 2nd order compact finite differencing algorithm that we refer to as the Beam-Warming algorithm is different than another advection algorithm also attributed to Beam-Warming. This other Beam-Warming advection algorithm is an explicit 2nd order upwind-biased algorithm with conventional non-compact finite differencing [LEVEQUE, 2002].)

The essence of the Beam-Warming 2nd order compact differencing algorithm is

illustrated with the following example. Consider the simple 1D advection problem

$$\frac{\partial f}{\partial t} + v \frac{\partial f}{\partial x} = 0 \quad (2.8)$$

Denoting f_i^n as the discretized value of f at position x_i and time t^n , the Beam-Warming algorithm differences this equation as:

$$\frac{f_{i+1/2}^{n+1} - f_{i+1/2}^n}{\Delta t} + v \frac{f_{i+1}^{n+1/2} - f_i^{n+1/2}}{\Delta x} = 0 \quad (2.9)$$

Evaluating f halfway between grid points by simple averaging gives:

$$\frac{f_{i+1}^{n+1} + f_i^{n+1} - (f_{i+1}^n + f_i^n)}{2\Delta t} + v \frac{f_{i+1}^{n+1} + f_{i+1}^n - (f_i^{n+1} + f_i^n)}{2\Delta x} = 0 \quad (2.10)$$

A graphical template illustrating the grid differencing for this scheme is given in figure 2.1. Note that this algorithm is centered in both space and time and thus is 2nd order accurate. (A more general form of the Beam-Warming algorithm which allows for upwind biasing is given by:

$$\frac{f_{i+s}^{n+1} - f_{i+s}^n}{\Delta t} + v \frac{f_{i+1}^{n+r} - f_i^{n+r}}{\Delta x} = 0 \quad (2.11)$$

where $r \in [0, 1]$ is the time-centering parameter, such that $r = 1/2$ represents a time-centered 2nd order accurate implicit scheme and $r = 1$ is equivalent to implicit backward Euler, and $s \in [1/2, 1]$ is the spatial-centering parameter, such that $s = 1/2$ is the standard space-centered 2nd order accurate scheme and $s = 1$ is fully upwinded.)

The Beam-Warming algorithm's treatment of the space and time discretization

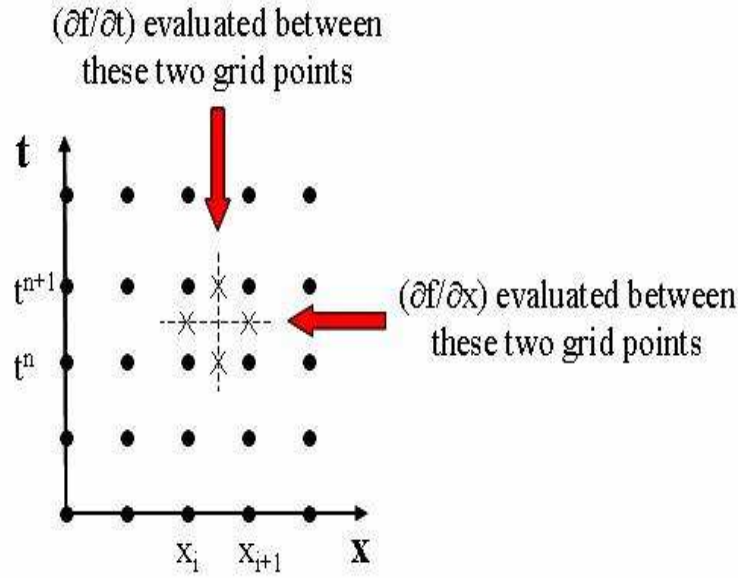


Figure 2.1: Graphical illustration of the grid differencing for the Beam-Warming 2nd order compact finite differencing algorithm.

on an equal footing, as shown in Eq. (2.10), is somewhat unique compared to many other algorithms. It is fully implicit and absolutely stable for arbitrarily large time step. Although the algorithm requires the solution of a matrix equation of the form $A_{ij}f_j^{n+1} = b_i$ due to its implicit nature, the matrix A is bi-diagonal and thus can be inverted trivially. Specifically, solving Eq. (2.10), we have:

$$f_{i+1}^{n+1} = f_i^n + \frac{1 - v\Delta t/\Delta x}{1 + v\Delta t/\Delta x} (f_{i+1}^n - f_i^{n+1}) \quad (2.12)$$

This can be solved by sweeping from $i = 2..N_x$, starting with the boundary condition that specifies f_1^{n+1} at the left boundary for $v > 0$. For $v < 0$, the boundary condition for f is on the right boundary (i.e. at $i=N_x$), and the equation is solved by sweeping from right to left (i.e. from $i = N_x - 1$ down to $i = 1$).

Considering application of the Beam-Warming 2nd order compact finite differencing algorithm to the gyrokinetic-Poisson-Ampere problem given by Eqs. (2.3) - (2.5), the finite difference form using space-centering can be represented generically for a given (k_x, k_y) mode as

$$\begin{aligned} & C_1 f_i^n + C_2 f_{i+1}^n + D_1 f_i^{n+1} + D_2 f_{i+1}^{n+1} \\ & = F_1 \Phi_i^n + F_2 \Phi_{i+1}^n + G_1 \Phi_i^{n+1} + G_2 \Phi_{i+1}^{n+1} \\ & + H_1 A_{\parallel,i}^n + H_2 A_{\parallel,i+1}^n + K_1 A_{\parallel,i}^{n+1} + K_2 A_{\parallel,i+1}^{n+1} \end{aligned} \quad (2.13)$$

$$\sum_s \frac{n_{0s} e^2 Z_s^2}{T_{0s}} (1 - \Gamma_{0s,i}) \Phi_i^{n+1} = \rho_{dens,i}[\Phi^{n+1}, A_{\parallel}^{n+1}] \quad (2.14)$$

$$\frac{c}{4\pi} k_{\perp,i}^2 A_{\parallel,i}^{n+1} = \rho_{curr,i}[\Phi^{n+1}, A_{\parallel}^{n+1}] \quad (2.15)$$

where the superscript n denotes the temporal index and the subscript i denotes the θ grid index. C , D , F , G , H , and K are generic matrix operators.

From these equations, we can see that, for an implicit scheme, implicitness arise in two parts: the finite difference scheme for computing the distribution function and the field solution algorithm. Generically, Eqs. (2.13) - (2.15) can be written as $A_{ij} f_j^{n+1} = b_i$, but, unlike the 1D advection problem, A is no longer a sparse bi-diagonal matrix since Φ_i^{n+1} and $A_{\parallel,i}^{n+1}$ involve integrals of f^{n+1} over all velocities. Thus, a brute-force implicit solve of the gyrokinetic-Poisson-Ampere equations for a given (k_x, k_y) linear mode as given by Eqs. (2.13) - (2.15) would require solving an $N_{total} \times N_{total}$ matrix problem, where $N_{total} = N_{species} N_{\lambda} N_E N_{\theta}$ (where $N_{species}$ is the number of species, N_{λ} is the number of pitch angle grid points, N_E is the number of energy grid points, and N_{θ} is the number of θ grid points). That is, because of the integro-differential nature of the system of equations, causing the implicit

matrix to be dense, a direct solve is very inefficient. Specifically, the number of operations involved in solving this system scales as $\frac{1}{3}N_{total}^3$ for initial inversion of the implicit matrix and $\frac{1}{2}N_{tot}^2$ for subsequent solutions (assuming LU decomposition). For typical simulation parameters ($N_{species} \sim 3$, $N_\lambda \sim 30$, $N_E \sim 16$, $N_\theta \sim 97$ for 32 θ grid points per 2π and a simulation domain covering $[-3\pi, 3\pi]$), $N_{total} \sim 10^5$ per (k_x, k_y) linear mode, so the computational cost per time step is on the order of 10^{10} . Thus, a direct implicit solve of the gyrokinetic-Poisson-Ampere equations is not practical.

2.1.1 Kotschenreuther's Implicit Solution

Kotschenreuther developed a trick that greatly speeds up the solution of the large matrix equation that results from applying the Beam-Warming algorithm to the gyrokinetic equation [KOTSCHENREUTHER *et al.*, 1995a]. This algorithm is based on breaking-up the distribution function into two pieces: an inhomogeneous piece (which depends only on the fields at the previous time step) and a homogeneous piece (which depends only on the fields at the new time step), i.e. $f_i^{n+1} = f_{inhomo,i}^{n+1} + f_{homo,i}^{n+1}$. This allows the charge and current densities to be written as:

$$\rho_{dens,i}[\Phi^{n+1}, A_{\parallel}^{n+1}] = \rho_{dens,i}[\Phi^{n+1} = 0, A_{\parallel}^{n+1} = 0] + M_{ij}^1 \Phi_j^{n+1} + M_{ij}^2 A_{\parallel,j}^{n+1} \quad (2.16)$$

$$\rho_{curr,i}[\Phi^{n+1}, A_{\parallel}^{n+1}] = \rho_{curr,i}[\Phi^{n+1} = 0, A_{\parallel}^{n+1} = 0] + M_{ij}^3 \Phi_j^{n+1} + M_{ij}^4 A_{\parallel,j}^{n+1} \quad (2.17)$$

where the first term on the RHS is the contribution from the inhomogeneous part of the distribution function, while the second and third terms make up the contribution from the homogeneous part of the distribution function. This latter contribution is written in terms of plasma response matrices, defined as:

$$M_{ij}^1 \equiv \sum_s eZ_s \int d^3v J_{0s,i} \frac{\delta f_i^{n+1}}{\delta \Phi_j^{n+1}} \quad (2.18)$$

$$M_{ij}^2 \equiv \sum_s eZ_s \int d^3v J_{0s,i} \frac{\delta f_i^{n+1}}{\delta A_{\parallel,j}^{n+1}} \quad (2.19)$$

$$M_{ij}^3 \equiv \sum_s eZ_s \int d^3v v_{\parallel} J_{0s,i} \frac{\delta f_i^{n+1}}{\delta \Phi_j^{n+1}} \quad (2.20)$$

$$M_{ij}^4 \equiv \sum_s eZ_s \int d^3v v_{\parallel} J_{0s,i} \frac{\delta f_i^{n+1}}{\delta A_{\parallel,j}^{n+1}} \quad (2.21)$$

where $\frac{\delta f_i^{n+1}}{\delta \Phi_j^{n+1}}$ is obtained by solving the gyrokinetic equation for f_i^{n+1} for all i using $\Phi_i^{n+1} = \delta_{ij}$ (where δ_{ij} is the standard Kronecker delta) and all other perturbed quantities equal to 0. Likewise, $\frac{\delta f_i^{n+1}}{\delta A_{\parallel,j}^{n+1}}$ is obtained by solving the gyrokinetic equation for f_i^{n+1} for all i using $A_{\parallel,i}^{n+1} = \delta_{ij}$ and all other perturbed quantities equal to 0. Note that this is fundamentally a Green's function formalism.

As an aside, note that a similar approach is used in Friedman et al.'s Vlasov equation analog of the direct implicit algorithm for particle codes [FRIEDMAN *et al.*, 1981], which is a semi-implicit algorithm that treats the parallel electron advection and parallel electrostatic potential force implicitly in the $\Delta t v_{\parallel} / \Delta z \ll 1$ limit. This leads to a kind of local approximation of the plasma response function, while in Kotschenreuther's algorithm the full linear plasma response (including all species and including ω_{dv} as well as parallel dynamics) is kept in calculation of the fields and is done for arbitrary time step Δt .

As an example of Kotschenreuther's implicit solution, ignoring the θ grid index

in Eq. (2.13) for simplicity, the gyrokinetic equation becomes:

$$Cf^n + Df_{inhomo}^{n+1} = F\Phi^n + HA_{\parallel}^n \quad (2.22)$$

$$Df_{homo}^{n+1} = G\Phi^{n+1} + KA_{\parallel}^{n+1} \quad (2.23)$$

The plasma response functions can be obtained from the latter equation, i.e.

$$\frac{\delta f^{n+1}}{\delta \Phi^{n+1}} = D^{-1}G(1) \quad (2.24)$$

$$\frac{\delta f^{n+1}}{\delta A_{\parallel}^{n+1}} = D^{-1}K(1) \quad (2.25)$$

Note that the response matrices can be pre-computed for a single constant value of Δt . Though, unlike the brute-force implicit matrix which is of size N_{total} , Kotschenreuther's matrix M is of the reduced size $N_{fields}N_{\theta}$ (where N_{fields} is the number of perturbed fields, i.e. 1 for electrostatic, 3 for fully electromagnetic). Furthermore, subsequent solutions of the gyrokinetic equation are also simplified. This can be done as follows:

1. Compute f_{inhomo}^{n+1} from the gyrokinetic equation using f^n , Φ^n , A_{\parallel}^n , and $\Phi^{n+1} = A_{\parallel}^{n+1} = 0$.
2. Solve the Poisson-Ampere equations for Φ^{n+1} and A_{\parallel}^{n+1} by solving the matrix equations that result from inserting Eqs. (2.16) and (2.17) into Eqs. (2.14) and (2.15). Note that this uses f_{inhomo}^{n+1} from step 1.
3. Compute f_{homo}^{n+1} from the gyrokinetic equation using f^n , Φ^{n+1} , A_{\parallel}^{n+1} , and $\Phi^n = A_{\parallel}^n = 0$.
4. Sum to get the new distribution function: $f^{n+1} = f_{inhomo}^{n+1} + f_{homo}^{n+1}$.

(Note: The actual implementation of this algorithm in GS2 differs slightly from that as described in [KOTSCHENREUTHER *et al.*, 1995a] and outlined here. Details of the GS2 algorithm and its equivalence to Kotschenreuther's original published algorithm are given in Appendix A.)

Considering the computational work involved using this algorithm, solving for the fields Φ^{n+1} and A_{\parallel}^{n+1} requires $(N_{fields}N_{\theta})^2$ operations, while each solution of the gyrokinetic equation for f_{inhomo}^{n+1} or f_{homo}^{n+1} requires $N_{species}N_{\lambda}N_EN_{\theta}$ operations (since the space-centered gyrokinetic equation has become a simple bi-diagonal $N_{\theta} \times N_{\theta}$ matrix equation). Thus, the total computational cost per time step for a given (k_x, k_y) linear mode is $(N_{fields}N_{\theta})^2 + 2N_{species}N_{\lambda}N_EN_{\theta}$. For typical parameters ($N_{species} \sim 3$, $N_{\lambda} \sim 30$, $N_E \sim 16$, $N_{\theta} \sim 97$ for 32 θ grid points per 2π and a simulation domain covering $[-3\pi, 3\pi]$), the computational cost per time step is then reduced from order 10^{10} (for the direct implicit solve) to order $10^{5.5}$.

While this is a very significant speed-up and is feasible in practice, the overhead in computing the response matrices M given by Eqs. (2.18) - (2.21) is large, particularly for high resolution nonlinear runs. Calculating a response row M_{ij} vs. θ_i requires solving one time step of the gyrokinetic equation to calculate the response of the plasma at position θ_i due to perturbations of each field at position θ_j . But the effective range of θ_j that we have to cover is not simply $[-\pi, \pi]$. In linear calculations, an extended ballooning angle is used. In nonlinear simulations, the primary domain is $\theta \in [-\pi, \pi]$, but the boundary conditions at $\theta = \pm\pi$ in field-line following coordinates gives rise to a coupling between different k_x modes [BEER *et al.*, 1995], separated by $k_{x1} - k_{x2} = k_y 2\pi \hat{s} p$ (where $p = \pm 1, \pm 2, \dots$). So a perturbation in a field at one position θ_j and radial mode k_{x1} can induce plasma charges and currents not only at other θ_i but also at other k_{x2} . Thus, the number of columns

of M that have to be calculated in a nonlinear simulation is $N_{fields}N_{\theta per 2\pi}N_{connect}$, where $N_{connect} = 2k_{x,max}/(k_{y,min}2\pi\hat{s})$ is the maximum number of k_x modes that are coupled together. For typical parameters, $N_{\theta per 2\pi} \sim 32$ while $N_{connect} \sim 10 - 20$ (or larger at higher resolution). So the computational cost of the initializing the response matrices for a nonlinear simulation is on the order of 10^3 times more expensive than a single step of the gyrokinetic equation. (Note that this essentially limits how often one would want to recalculate M due to changing the time step Δt , or due to time-dependent twisting of the coordinates by large-scale equilibrium ExB shear.) Overall, this large overhead for initializing M has motivated the exploration of improved algorithms, which we present here, for more efficiently treating the field solve while retaining the large time step advantages of Kotschenreuther's fully implicit algorithm.

2.2 Semi Implicit-Explicit Schemes

The use of a semi implicit-explicit algorithm for gyrokinetics is explored here within the context of GS2's space-centered finite differencing. We are interested in schemes which treat the distribution function terms in the gyrokinetic equation implicitly, while the field terms are treated explicitly since these terms are difficult to invert. Here we analyze the stability of such semi implicit-explicit routines using forward Euler differencing, Adams-Bashforth schemes, and a two-step predictor-corrector scheme. We demonstrate that, while these algorithms worked well for our local trial function code with a fixed k_{\parallel} (as described in section 5.2 in Chapter 5 of this thesis), they are all numerically unstable when combined with GS2's 2nd order compact finite differencing of spatial derivatives. This has motivated the search in section

2.3 for better iterative implicit algorithms.

Consider the following simplified gyrokinetic equation in the collisionless, electrostatic limit at small $k_{\perp}\rho_i$:

$$\frac{\partial f_s}{\partial t} + \frac{v_{\parallel}}{qR} \frac{\partial f_s}{\partial \theta} = -\frac{eZ_s}{T_{0s}} F_{Ms} \frac{v_{\parallel}}{qR} \frac{\partial \Phi}{\partial \theta} \quad (2.26)$$

Applying a space-centered, time-centered finite difference scheme and using a spectral numerical analysis in the spatial dimension, i.e. $f_j^n = \hat{f}^n e^{ik_{\parallel}qR\theta_j}$ (where n denotes the time index and j denotes the theta grid index), the time derivative becomes:

$$\begin{aligned} \frac{\partial f}{\partial t} &= \frac{1}{\Delta t} (f_{j+1/2}^{n+1} - f_{j+1/2}^n) \\ &= \frac{1}{\Delta t} (\hat{f}^{n+1} - \hat{f}^n) e^{ik_{\parallel}qR\Delta\theta(j+1/2)} \cos(k_{\parallel}qR\Delta\theta/2) \end{aligned} \quad (2.27)$$

while the spatial derivative becomes:

$$\begin{aligned} \frac{\partial f}{\partial \theta} &= \frac{1}{\Delta\theta} (f_{j+1}^{n+1/2} - f_j^{n+1/2}) \\ &= \frac{2i}{\Delta\theta} \hat{f}^{n+1/2} e^{ik_{\parallel}qR\Delta\theta(j+1/2)} \sin(k_{\parallel}qR\Delta\theta/2) \end{aligned} \quad (2.28)$$

Often the fastest growing numerical instabilities occur at the highest k_{\parallel} . Using the maximum k_{\parallel} in the system, which occurs at the Nyquist limit (i.e. $k_{\parallel}qR\Delta\theta = \pi$), we find that the time derivative given by Eq. (2.27) vanishes, so f at the new time step is determined only by the spatial derivative terms. Specifically, we find that

$$\hat{f}^{n+1} = -\hat{f}^n - \frac{eZ_s}{T_{0s}} F_{Ms} (\hat{\Phi}_*^{n+1} + \hat{\Phi}^n) \quad (2.29)$$

where $\hat{\Phi}_*^{n+1}$ represents the prediction for $\hat{\Phi}^{n+1}$, e.g.

- forward Euler: $\hat{\Phi}_*^{n+1} = \hat{\Phi}^n$
- 2nd order Adams-Bashforth: $\hat{\Phi}_*^{n+1} = 2\hat{\Phi}^n - \hat{\Phi}^{n-1}$
- 3rd order Adams-Bashforth: $\hat{\Phi}_*^{n+1} = \frac{17}{6}\hat{\Phi}^n - \frac{8}{3}\hat{\Phi}^{n-1} + \frac{5}{6}\hat{\Phi}^{n-2}$

We consider a single gyrokinetic ion species with the cases of adiabatic electrons and gyrokinetic electrons. For the case of adiabatic electrons, the Poisson equation to lowest order in $k_{\perp}\rho_i$ is given as:

$$n_{0e} \frac{e\Phi}{T_{0e}} = Z_i \int d^3v f_i \quad (2.30)$$

Discretizing this equation and substituting Eq. (2.29), we find that

$$\hat{\Phi}^{n+1} + 2\hat{\Phi}^n + \hat{\Phi}_*^{n+1} = 0 \quad (2.31)$$

where the assumptions that $Z_i = 1$ and $T_{0i} = T_{0e}$ have been applied for simplicity. We define an amplification factor as $A \equiv \frac{\hat{\Phi}^{n+1}}{\hat{\Phi}^n}$, such that modes with $|A| > 1$ denote numerical instability with a growth rate given by $\gamma\Delta t = \ln|A|_{max}$. Substituting the $\hat{\Phi}_*^{n+1}$ explicit predictions into Eq. (2.31) yields a polynomial equation for A of order 1 for the forward Euler scheme, 2 for the 2nd order Adams-Bashforth scheme, and 3 for the 3rd order Adams-Bashforth scheme. Solution of these equations surprisingly yields an unstable branch for all three explicit schemes, the growth rates for which are given in table 2.2.

Similarly, for the case of gyrokinetic electrons, the Poisson equation to lowest

	$\gamma\Delta t$, adiabatic electrons	$\gamma\Delta t$, gyrokinetic electrons
Forward Euler	$\ln(3) = 1.099$	$\ln \left \frac{4}{k_{\perp}^2 \rho_i^2} + 1 \right $ = 5.994 at $k_{\perp} \rho_i = 0.1$ = 3.258 at $k_{\perp} \rho_i = 0.4$
2nd order Adams-Bashforth	$\ln(2 + \sqrt{5}) = 1.444$	$\ln \left \frac{6}{k_{\perp}^2 \rho_i^2} + \frac{4}{3} \right $ = 6.399 at $k_{\perp} \rho_i = 0.1$ = 3.659 at $k_{\perp} \rho_i = 0.4$
3rd order Adams-Bashforth	1.679	6.644 at $k_{\perp} \rho_i = 0.1$ 3.904 at $k_{\perp} \rho_i = 0.4$

Table 2.2: The growth rates of the numerically unstable mode ($\gamma\Delta t = \ln|A|_{max}$) for various semi implicit-explicit time stepping schemes. Solution of the 3rd order Adams-Bashforth polynomial equation was found numerically.

order in $k_{\perp} \rho_i$ is given as:

$$n_{0i} e Z_i^2 k_{\perp}^2 \rho_i^2 \frac{e\Phi}{T_{0i}} = \sum_s e Z_s \int d^3 v f_s \quad (2.32)$$

from which we obtain the following discretized equation using Eq. (2.29):

$$2\hat{\Phi}_*^{n+1} + k_{\perp}^2 \rho_i^2 \hat{\Phi}^{n+1} + (2 + k_{\perp}^2 \rho_i^2) \hat{\Phi}^n = 0 \quad (2.33)$$

where the assumptions that $Z_i = 1$ and $T_{0i} = T_{0e}$ have likewise been applied. Solutions of the polynomial equations for A using the Φ_*^{n+1} explicit fields predictions in Eq. (2.33) also yield unstable branches for all three schemes, as shown in table 2.2.

Historically, we had tried these algorithms in GS2 first before performing the analysis of their numerical stability, discovered that the code was numerically unstable, and then later developed the analytic estimates of the numerical instabilities

given above. Here we show these results from implementation of the semi implicit-explicit schemes in the full GS2 code and compare them with the analytic results from the reduced gyrokinetic equation. The local parameters for the numerical test problem are based on the generic equilibrium of [WALTZ and MILLER, 1999] in concentric circular geometry in the collisionless, electrostatic limit: $r/a = 0.5$, $R/a = 3.0$, $q = 2$, $\hat{s} = 1$, $\partial_{r/a}\beta = 0$, $R/L_T = 6$, $R/L_n = 3$, $T_{0i}/T_{0e} = 1$. Runs were performed in the linear limit at small and moderate $k_y\rho_i$ values of 0.1 and 0.4, corresponding to physical ITG modes with $(\omega, \gamma) = (0.059, 0.054)v_{ti}/a$ and $(\omega, \gamma) = (0.314, 0.188)v_{ti}/a$ respectively for the case of adiabatic electrons and $(\omega, \gamma) = (0.034, 0.102)v_{ti}/a$ and $(\omega, \gamma) = (0.345, 0.342)v_{ti}/a$ respectively with the inclusion of gyrokinetic electrons.

Figure 2.2 shows the variation of the mode frequency and growth rate with time step size for the case of adiabatic electrons using the semi implicit-explicit GS2 scheme. In agreement with the analytical analysis, the results show a numerical instability with real frequency $|\omega\Delta t| = \pi$. Note that the growth rate of the numerical instability approaches the analytical predictions of table 2.2 as Δt increases and $k_y\rho_i$ decreases.

In figure 2.3, the runs were performed with a small amount of upwind biasing in the direction along the field line (spatial-centering parameter $s = 0.55$), which introduces a small amount of diffusion. For this case, while the schemes are still unstable for large Δt , all 3 schemes stabilize (matching the ITG growth rate computed by the fully implicit scheme) as Δt is decreased. Note that the forward Euler scheme exhibits a larger stability threshold ($\Delta tv_{ti}/a \leq 0.05$ for the $k_y\rho_i = 0.1$ case and $\Delta tv_{ti}/a \leq 0.1$ for the $k_y\rho_i = 0.4$ case) than 2nd order Adams-Bashforth scheme, which in turn has a larger stability threshold than the 3rd order Adams-Bashforth

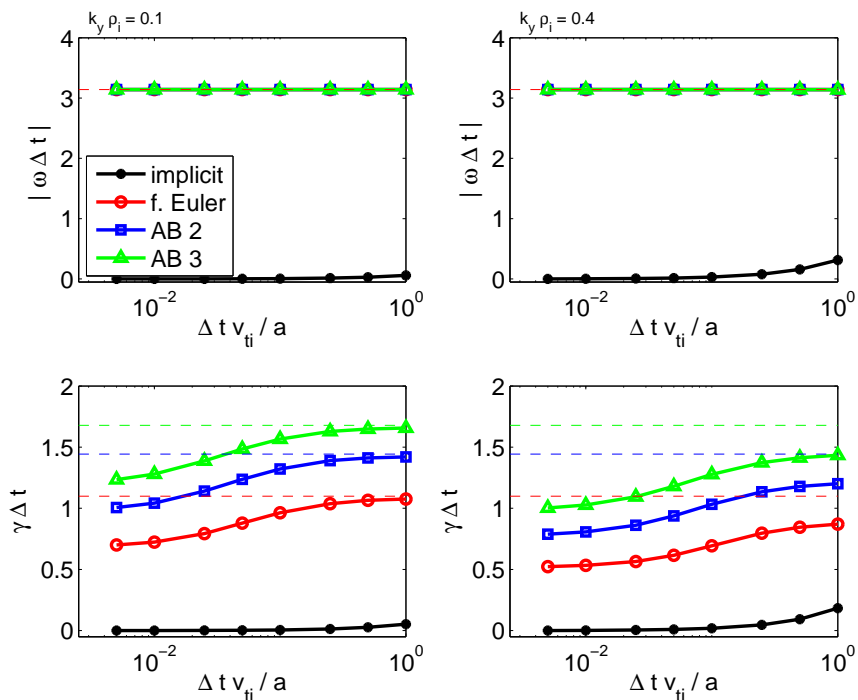


Figure 2.2: Mode frequency and linear growth rate for test case parameters with adiabatic electrons using various semi implicit-explicit schemes. The dashed lines show the predicted growth rate of the numerically unstable mode as given in table 2.2.

scheme.

Aside from upwinding, it was also found that some time step regimes for a case with no trapped particles were also numerically stable. This is shown in figure 2.4 where, for the $k_y \rho_i = 0.4$ case, the forward Euler scheme is stable in the regime $0.01 \leq \Delta t v_{ti} / a \leq 0.05$. This stabilizing effect is not seen, however, for the $k_y \rho_i = 0.1$ case nor for the Adams-Bashforth schemes. This is interesting since the finite difference form for the gyrokinetic equation is the same for trapped and passing particles. The primary difference is in the treatment of the boundary conditions. For passing ions, the boundary condition is $f=0$ at the incoming boundary. This means that the highest k_{\parallel} mode, which was most unstable analytically, is forced

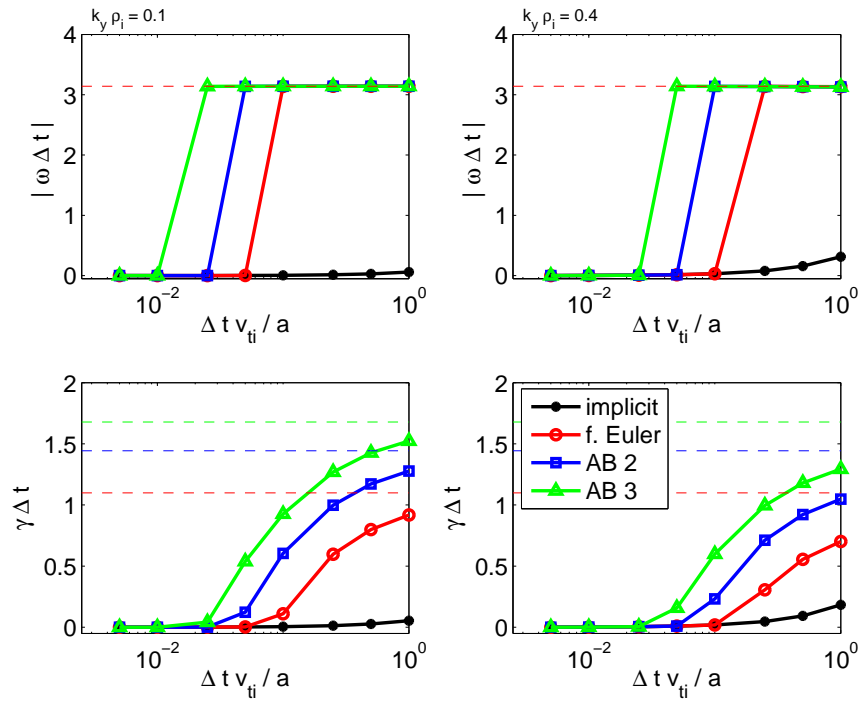


Figure 2.3: Mode frequency and linear growth rate for test case parameters with adiabatic electrons and with slight upwind diffusion using various semi implicit-explicit schemes. The dashed lines show the predicted growth rate of the numerically unstable mode as given in table 2.2. Note the stable regime for the semi implicit-explicit schemes, matching the ITG mode of the fully implicit scheme, at small Δt .

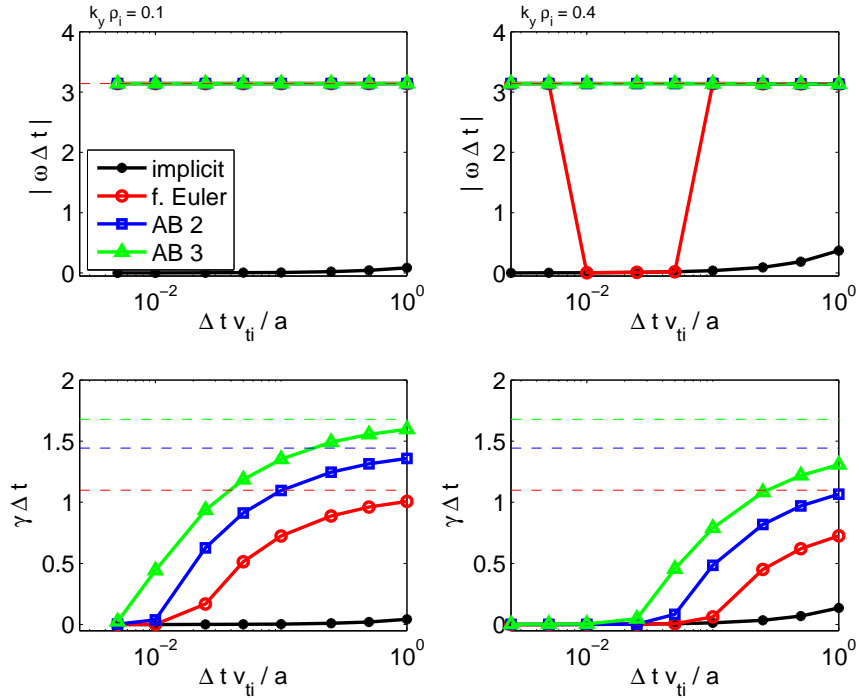


Figure 2.4: Mode frequency and linear growth rate for test case parameters with adiabatic electrons and no particle trapping ($r/a = 0.001$) using various semi implicit-explicit schemes. The dashed lines show the predicted growth rate of the numerically unstable mode as given in table 2.2. Note the stable regime for the forward Euler scheme, matching the ITG mode of the fully implicit scheme, for the case of $k_y \rho_i = 0.4$ in the range $0.01 \leq \Delta t v_{ti} / a \leq 0.05$.

to be 0 since this mode oscillates sign between adjacent grid points. For trapped ions, however, there is a periodicity condition which allows the highest k_{\parallel} mode to survive. This can be tested by performing GS2 simulations with no trapped particles and $\hat{s} = 0$ and forcing self-periodic boundary conditions so that every mode is periodic with itself. As shown in figure 2.5, these results clearly show the existence of the numerical instability with $\gamma \Delta t$ constant vs. Δt , in agreement with the analytical predictions.

The results with inclusion of gyrokinetic electrons are shown in figure 2.6. As expected, the plots show a numerical instability for all 3 schemes, with growth rates

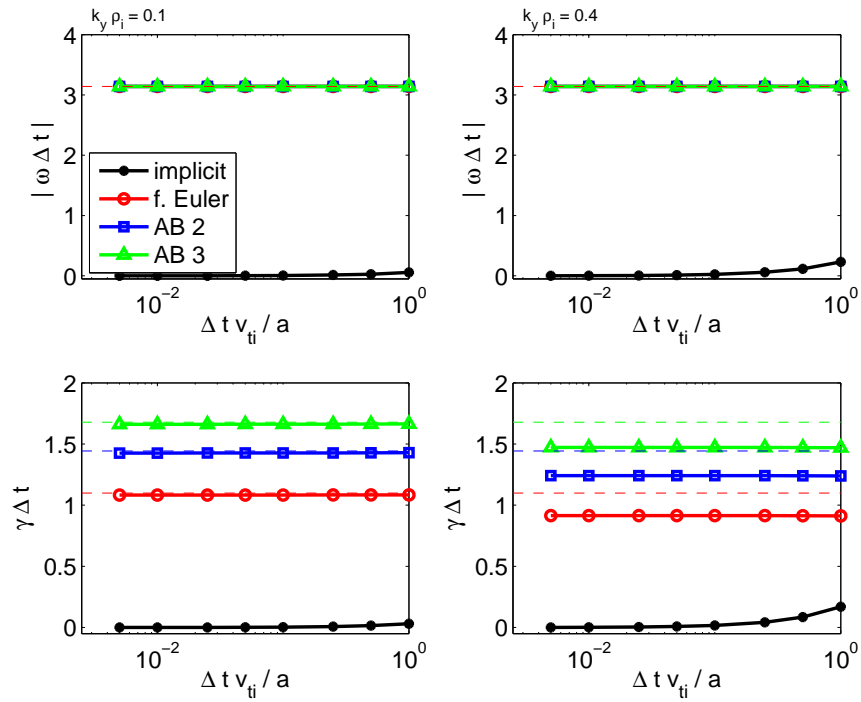


Figure 2.5: Mode frequency and linear growth rate for test case parameters with adiabatic electrons, no particle trapping ($r/a = 0.001$), and self-periodic boundary conditions with $\hat{s} = 0$ using various semi implicit-explicit schemes. The dashed lines show the predicted growth rate of the numerically unstable mode as given in table 2.2.

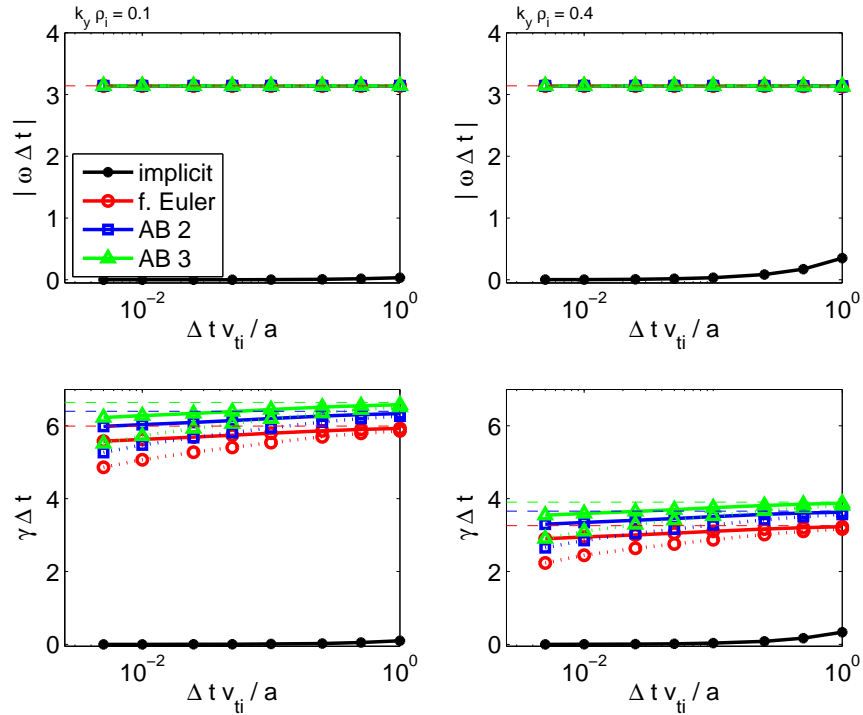


Figure 2.6: Mode frequency and linear growth rate for test case parameters with gyrokinetic electrons included using various semi implicit-explicit schemes. The dotted lines denote results from the inclusion of slight upwind diffusion. The dashed lines show the predicted growth rate of the numerically unstable mode as given in table 2.2.

which approach the analytical predictions of table 2.2 as Δt increases. However, unlike with the case of adiabatic electrons, a small amount of upwinding was not found to be stabilizing with inclusion of gyrokinetic electrons within the range of Δt which was tested.

A two-step predictor-corrector algorithm has also been explored to improve the

stability of the semi implicit-explicit scheme. This algorithm is basically a two-iteration scheme in which the solution of Φ^{n+1} from the single-step semi implicit-explicit algorithm is used as the prediction for a second solution of the gyrokinetic-Poisson equations. Thus, Eq. (2.29) becomes:

$$\hat{f}^{n+1,p+1} = -\hat{f}^n - \frac{eZ_s}{T_{0s}} F_{Ms} (\hat{\Phi}^{n+1,p} + \hat{\Phi}^n) \quad (2.34)$$

where p is the iteration index ($p = 0, 1$) such that $\hat{\Phi}^{n+1,0}$ is the prediction $\hat{\Phi}_*^{n+1}$ as for the single-step scheme, $\hat{\Phi}^{n+1,1}$ results from the Poisson integration of $\hat{f}^{n+1,1}$, and the final solution $\hat{\Phi}^{n+1,2}$ results from the Poisson integration of $\hat{f}^{n+1,2}$. Using Eq. (2.34), the discretized Poisson equation for adiabatic electrons becomes:

$$\hat{\Phi}^{n+1,p+1} + 2\hat{\Phi}^n + \hat{\Phi}^{n+1,p} = 0 \quad (2.35)$$

and the discretized Poisson equation for gyrokinetic electrons becomes:

$$2\hat{\Phi}^{n+1,p} + k_\perp^2 \rho_i^2 \hat{\Phi}^{n+1,p+1} + (2 + k_\perp^2 \rho_i^2) \hat{\Phi}^n = 0 \quad (2.36)$$

We again compute the amplification factors using the predictions for $\hat{\Phi}_*^{n+1}$ from the forward Euler and 2nd order Adams-Bashforth schemes in Eqs. (2.35) and (2.36). The results are shown in table 2.3. For the adiabatic electron case, we find that, unlike the single-step algorithm, the predictor-corrector algorithm is numerically stable for both schemes. In fact, $A = 1$, indicating that the algorithm is perfectly stable with no artificial dissipation, at least for the $k_\parallel q R \Delta\theta = \pi$ mode analyzed here. However, for the case of gyrokinetic electrons, we again find that the schemes are numerically unstable. Note that further iterations of Eq. (2.36)

	$\gamma\Delta t$, adiabatic electrons	$\gamma\Delta t$, gyrokinetic electrons
Forward Euler	(stable)	$\ln \left \frac{8}{k_{\perp}^4 \rho_i^4} \right $ = 11.290 at $k_{\perp} \rho_i = 0.1$ = 5.744 at $k_{\perp} \rho_i = 0.4$
2nd order Adams-Bashforth	(stable)	$\ln \left \frac{12}{k_{\perp}^4 \rho_i^4} \right $ = 11.695 at $k_{\perp} \rho_i = 0.1$ = 6.150 at $k_{\perp} \rho_i = 0.4$

Table 2.3: The growth rates of the numerically unstable mode ($\gamma\Delta t = \ln|A|_{max}$) for various predictor-corrector semi implicit-explicit time stepping schemes.

will not help, as each iteration will amplify errors by a factor of $\frac{2}{k_{\perp}^2 \rho_i^2}$.

Results from the implementation of the predictor-corrector algorithm in GS2 are shown in figures 2.7 and 2.8. In agreement with the analytic predictions, the predictor-corrector algorithm is numerically stable for the case of adiabatic electrons, yielding the physical ITG instability growth rate in agreement with the fully implicit GS2 scheme over the range of Δt tested, even in the absence of upwind diffusion. However, for the case of gyrokinetic electrons, the results show numerical instability over the entire range of Δt as predicted, with instability growth rates asymptotically approaching those from the analytical analysis in table 2.3. Thus, even with a predictor-corrector algorithm, a semi implicit-explicit scheme which uses an explicit treatment of the linear field dynamics combined with GS2's 2nd order compact differencing is infeasible for practical gyrokinetic simulations. This has motivated the search for a more implicit treatment of the field dynamics, which we turn to next.

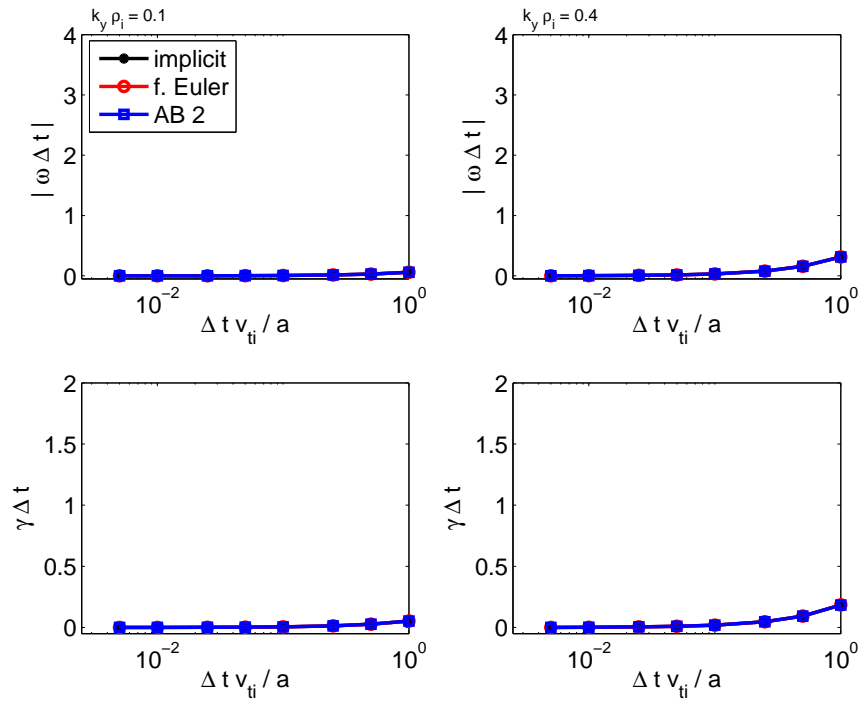


Figure 2.7: Mode frequency and linear growth rate for test case parameters with adiabatic electrons using various predictor-corrector semi implicit-explicit schemes. Note that the semi implicit-explicit schemes are numerically stable, matching the ITG mode of the fully implicit scheme, for both the case of $k_y \rho_i = 0.1$ and $k_y \rho_i = 0.4$.

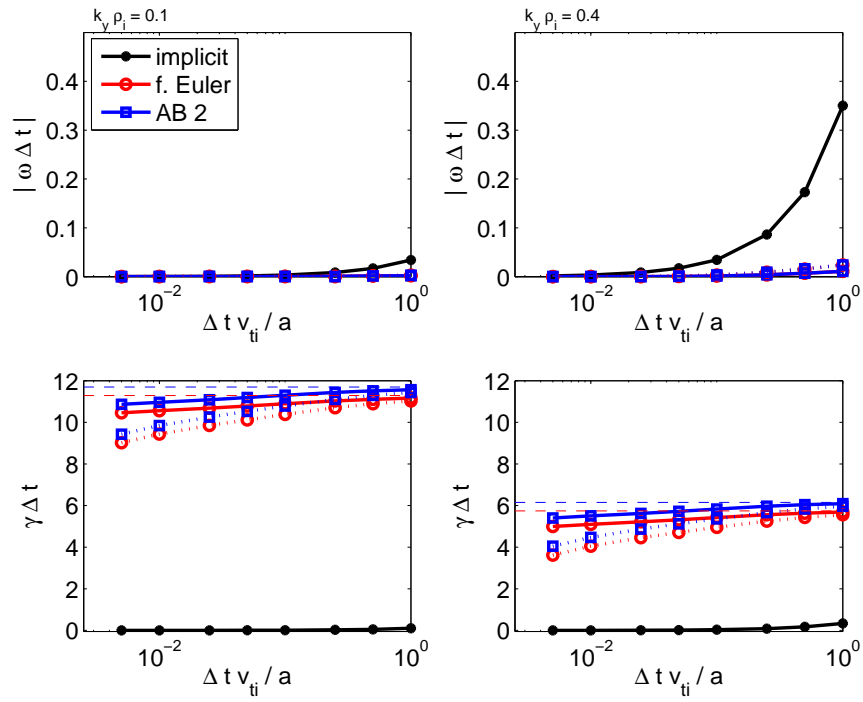


Figure 2.8: Mode frequency and linear growth rate for test case parameters with gyrokinetic electrons included using various predictor-corrector semi implicit-explicit schemes. The dotted lines denote results from the inclusion of slight upwind diffusion. The dashed lines show the predicted growth rate of the numerically unstable mode as given in table 2.3

2.3 Iterative Implicit Schemes

We have developed a fast iterative implicit algorithm for continuum/Vlasov gyrokinetic codes based on numerical or analytic approximations of the plasma response. This method reduces the long time needed to set-up implicit arrays, yet still has larger time step advantages similar to a fully implicit method compared with traditional explicit methods. Comparisons between various model preconditioners, initializers, and iteration schemes are presented.

Our starting field equations are the gyrokinetic Poisson-Ampere equations (in the $\delta B_{\parallel} = 0$ limit for simplicity), given by Eqs. (2.14) and (2.15) and using Kotschenreuther’s response matrix representation as defined by Eqs. (2.16) and (2.17). The largest expense of Kotschenreuther’s algorithm is in calculating all of the elements of the response matrix M , since each row of M requires independently solving the gyrokinetic equation (and subsequently integrating the solution over velocity-space) and there are $N_{fields}N_{\theta}$ rows for each (k_x, k_y) mode. Although it is computationally expensive to calculate all of the elements of M , it is relatively fast to calculate the matrix-vector product of M with a generic field vector \vec{x} , since this is equivalent to one solution of the gyrokinetic equation for a specific value of the fields \vec{x} and its velocity-space integrations, as is shown in section 2.3.4. This suggests that a “matrix-free” iterative algorithm, which avoids explicitly calculating the elements of M , may be ideal. However, we can further benefit from developing a fast approximation to M . (Note that once we have M or an approximation to it, computing its inverse is relatively fast. For example, for a given linear (k_x, k_y) mode, the total computational time to compute the inverse (via LU decomposition) scales as $T_{invertM} \sim \frac{1}{3}(N_{fields}N_{\theta})^3$, while the total computational time to compute all of the elements of M scales

as $T_{initializeM} \sim C(N_{fields}N_\theta)(N_{species}N_\lambda N_E N_\theta)$, where C is a large constant factor. This yields $T_{invertM}/T_{initializeM} \sim (N_{fields}^2 N_\theta)/(3CN_{species}N_\lambda N_E)$ which scales as $1/(5C)$ for typical simulation parameters ($N_{species} \sim 3$, $N_\lambda \sim 30$, $N_E \sim 16$, $N_\theta \sim 97$ for 32 θ grid points per 2π and a simulation domain covering $[-3\pi, 3\pi]$). Thus, our algorithmic approach is to develop a fast “matrix-free” iterative implicit scheme based on approximations to the plasma response matrices which are accurate enough to ensure good convergence properties yet computationally inexpensive relative to computing the exact plasma response.

Numerical results presented here are based on implementation of the iterative implicit algorithm within the framework of the GS2 code. The test case parameters are based on a circular geometry version of a JET-like plasma (shaping effects on this case are studied in Chapter 4) in the linear, collisionless limit: $r/a = 0.80$, $R/a = 3.42$, $\partial_r R_0 = -0.14$, $q = 2.03$, $\hat{s} = 1.62$, $\partial_{r/a}\beta = -0.0084$, $R/L_T = 10.81$, $R/L_n = 3.50$, $T_{0i} = T_{0e}$. Runs were performed as typical with time-centering parameter $r = 0.55$ and slight upwind diffusion (spatial-centering parameter $s = 0.55$). Figure 2.9 shows the variation of the linear ITG growth rate with $k_y \rho_i$ using the test parameters with GS2’s fully implicit scheme. Use of the iterative scheme is considered with inclusion of gyrokinetic electrons and electromagnetic dynamics.

2.3.1 Simple Iteration

The simplest iterative algorithm is based on a perturbation expansion in the error of the homogeneous charge and current densities. Our field equations, given by Eqs. (2.14) and (2.15) using Eqs. (2.16) and (2.17) for the RHS charge and current

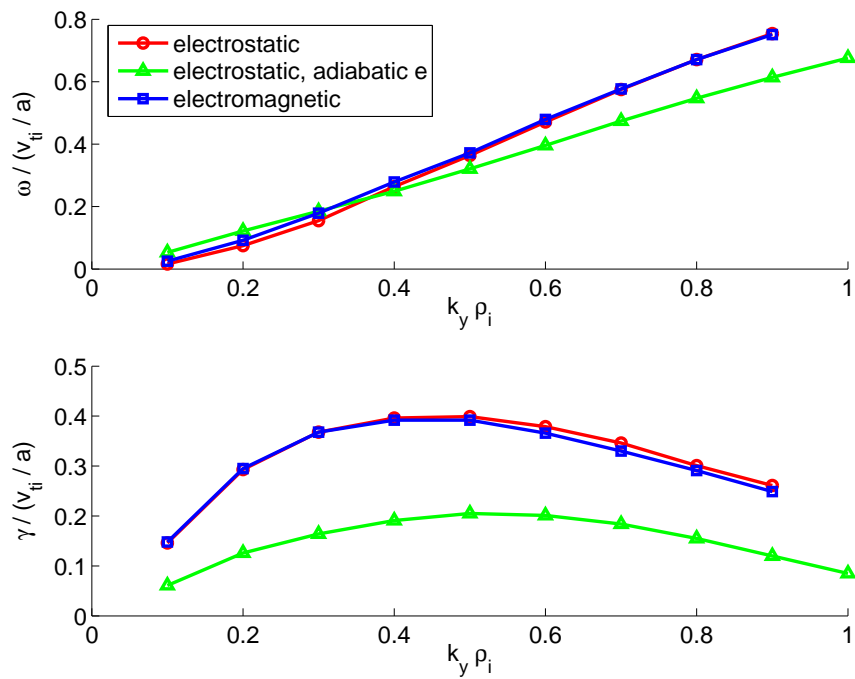


Figure 2.9: Real frequency and linear growth rate vs. $k_y \rho_i$ for test case parameters for the iterative implicit scheme. The results were obtained using GS2's fully implicit linear scheme. For the electromagnetic case, $\beta = 1.0 \times 10^{-3}$.

densities, can be written generically as

$$M\vec{x}^{n+1} = -\vec{\rho}[\vec{x}^{n+1} = 0] \quad (2.37)$$

where $\vec{x}^{n+1} = (\Phi^{n+1}, A_{\parallel}^{n+1})$ represents the field vector, $M = \begin{bmatrix} M_{GS2}^1 & M_{GS2}^2 \\ M_{GS2}^3 & M_{GS2}^4 \end{bmatrix}$ is the response matrix (where M_{GS2} is defined in Appendix A as the response matrix as implemented in GS2), and $\vec{\rho}[\vec{x}^{n+1} = 0]$ represents the inhomogeneous source term such that the total (homogeneous + inhomogeneous) charge and current source vector is given by $\vec{\rho}[\vec{x}^{n+1}] = \vec{\rho}[\vec{x}^{n+1} = 0] + (M + C)\vec{x}^{n+1}$, where C is a constant matrix independent of \vec{x} and time:

$$C \equiv \begin{bmatrix} \sum_s \frac{n_{0s} e^2 Z_s^2}{T_{0s}} (1 - \Gamma_0(b_s)) & 0 \\ 0 & \frac{c}{4\pi} k_{\perp}^2 \end{bmatrix} \quad (2.38)$$

Since computation of the exact M is to be avoided in our algorithm, an approximation is introduced as follows:

$$M_{approx}\vec{x}^{n+1} + (M - M_{approx})\vec{x}^{n+1} = -\vec{\rho}[\vec{x}^{n+1} = 0] \quad (2.39)$$

Assuming that $(M - M_{approx})$ is small, the second term on the LHS can be treated perturbatively using \vec{x} from a previous iteration, i.e.

$$M_{approx}\vec{x}^{n+1,p+1} = -\vec{\rho}[\vec{x}^{n+1} = 0] - (M - M_{approx})\vec{x}^{n+1,p} \quad (2.40)$$

where the superscript p denotes the iteration index. Noting that $\vec{\rho}[\vec{x}^{n+1} = 0] +$

$M\bar{x}^{n+1,p} = \bar{\rho}[\bar{x}^{n+1,p}] - C\bar{x}^{n+1,p}$, we find that

$$M_{approx}(\bar{x}^{n+1,p+1} - \bar{x}^{n+1,p}) = -\bar{\rho}[\bar{x}^{n+1,p}] + C\bar{x}^{n+1,p} \quad (2.41)$$

from which we can directly solve for $\bar{x}^{n+1,p+1}$. Thus, starting with an initial guess \bar{x}^0 , Eq. (2.41) can be iterated until the solution converges within a specified tolerance. However, the convergence rate depends on the accuracy of M_{approx} and convergence is not always guaranteed. Writing that $\bar{x}^{n+1,p} = \bar{x}^{n+1} + \bar{e}^p$, where \bar{e}^p is the error vector at the p-th iteration, we find that

$$\bar{e}^{p+1} = (I - M_{approx}^{-1}M) \bar{e}^p \quad (2.42)$$

Thus, if the modulus of all of the eigenvalues of $(I - M_{approx}^{-1}M)$ is < 1 , then our iterative scheme is guaranteed to converge.

A template for the generic simple iteration algorithm is given in Appendix B. Below we outline this algorithm as applied to the gyrokinetic problem for comparison with the fully implicit algorithm given in section 2.1.1. In iterative form, our field equations become:

$$\begin{aligned} & M_{approx}^1(\Phi^{n+1,p+1} - \Phi^{n+1,p}) + M_{approx}^2(A_{\parallel}^{n+1,p+1} - A_{\parallel}^{n+1,p}) \\ &= -\rho_{dens}[\Phi^{n+1,p}, A_{\parallel}^{n+1,p}] + \sum_s \frac{n_{0s} e^2 Z_s^2}{T_{0s}} (1 - \Gamma_0(b_s)) \Phi^{n+1,p} \end{aligned} \quad (2.43)$$

$$\begin{aligned} & M_{approx}^3(\Phi^{n+1,p+1} - \Phi^{n+1,p}) + M_{approx}^4(A_{\parallel}^{n+1,p+1} - A_{\parallel}^{n+1,p}) \\ &= -\rho_{curr}[\Phi^{n+1,p}, A_{\parallel}^{n+1,p}] + \frac{c}{4\pi} k_{\perp}^2 A_{\parallel}^{n+1,p} \end{aligned} \quad (2.44)$$

Thus, the simple iteration gyrokinetic algorithm is given as follows:

1. Precompute the approximate inverse plasma response matrices M_{approx}^{-1} .
2. For each time step:
 - (a) Make an initial guess for $\Phi^{n+1,0}$ and $A_{\parallel}^{n+1,0}$.
 - i. Solve the gyrokinetic equation for $f^{n+1,0}$ using f^n , Φ^n , A_{\parallel}^n , $\Phi^{n+1} = \Phi^{n+1,0}$, and $A_{\parallel}^{n+1} = A_{\parallel}^{n+1,0}$.
 - (b) For $p = 0, 1, 2, \dots$
 - i. Solve the iterative field equations (2.43) and (2.44) for $\Phi^{n+1,p+1}$ and $A_{\parallel}^{n+1,p+1}$.
 - ii. Solve the gyrokinetic equation for $f^{n+1,p+1}$ using f^n , Φ^n , A_{\parallel}^n , $\Phi^{n+1} = \Phi^{n+1,p+1}$, $A_{\parallel}^{n+1} = A_{\parallel}^{n+1,p+1}$.
 - iii. Check if the solutions for Φ^{n+1} and A_{\parallel}^{n+1} are converged; continue if necessary.

Note that if this algorithm is run using the exact response matrix, then the number of iterations should be exactly two since it is equivalent to Kotschenreuther's fully implicit algorithm. This provides a test for the implementation of the simple iteration algorithm in GS2 as well as a test of the properties of the response matrix, specifically by indicating that the matrix is not poorly conditioned and can be inverted accurately. Overall, this algorithm serves as a base template for our iterative implicit scheme upon which an optimal preconditioner and initializer can be determined and against which more robust and complex iterative schemes can be compared.

2.3.2 Preconditioners

As noted above, the success of an iterative scheme often depends on developing a good preconditioner M_{approx} . We ultimately need a preconditioner which is accurate enough to enhance convergence yet simple compared with the computational intensity of computing the exact implicit response matrix. Below we describe the development of various analytic and numerical gyrokinetic-based preconditioners and compare them in practice using the simple iteration algorithm.

For insight for our preconditioner model, we first consider simple analytical approximations for the plasma response. We consider as our simplified starting equations the gyrokinetic equation in the linear, collisionless limit in slab geometry with a uniform magnetic field and uniform background Maxwellian particles at small $k_{\perp}\rho_i$:

$$\frac{\partial f_s}{\partial t} + \frac{v_{\parallel}}{qR} \frac{\partial f_s}{\partial \theta} = -\frac{eZ_s}{T_{0s}} F_{Ms} \left(\frac{v_{\parallel}}{qR} \frac{\partial \Phi}{\partial \theta} + \frac{v_{\parallel}}{c} \frac{\partial A_{\parallel}}{\partial t} \right) \quad (2.45)$$

Using a space-centered, variable time-centered finite difference scheme, such as that which is used in GS2, we obtain:

$$\begin{aligned} & \frac{1}{2\Delta t} [f_i^{n+1} - f_i^n + f_{i+1}^{n+1} - f_{i+1}^n] \\ & + \frac{v_{\parallel}}{qR\Delta\theta} [r(f_{i+1}^{n+1} - f_i^{n+1}) + (1-r)(f_{i+1}^n - f_i^n)] \\ & = -\frac{eZ_s}{T_{0s}} F_{Ms} \frac{v_{\parallel}}{qR\Delta\theta} [r(\Phi_{i+1}^{n+1} - \Phi_i^{n+1}) + (1-r)(\Phi_{i+1}^n - \Phi_i^n)] \\ & - \frac{eZ_s}{T_{0s}} F_{Ms} \frac{v_{\parallel}}{2c\Delta t} [A_{\parallel,i}^{n+1} - A_{\parallel,i}^n + A_{\parallel,i+1}^{n+1} - A_{\parallel,i+1}^n] \end{aligned} \quad (2.46)$$

where i is the θ index, n is the time index, and r is the time-centering parameter. This equation will be used as the starting equation for developing an approximation for the plasma response functions $\frac{\delta f}{\delta \Phi}$ and $\frac{\delta f}{\delta A_{\parallel}}$ to gain insight about the form of the

response matrices as defined by Eqs. (2.18)-(2.21).

We begin by Fourier transforming Eq. (2.46) with respect to the parallel spatial dimension, i.e. applying a spectral analysis ($f_j^n = \hat{f}^n e^{ik_{\parallel} q R \Delta \theta j}$) we find that

$$\begin{aligned}
& \left[g(k_{\parallel}) + ir \hat{k}_{\parallel} v_{\parallel} \Delta t \right] \hat{f}^{n+1} \\
&= \left[g(k_{\parallel}) - i(1-r) \hat{k}_{\parallel} v_{\parallel} \Delta t \right] \hat{f}^n \\
&\quad - \frac{eZ_s}{T_{0s}} F_{Ms} i \hat{k}_{\parallel} v_{\parallel} \Delta t \left[r \hat{\Phi}^{n+1} + (1-r) \hat{\Phi}^n \right] \\
&\quad - \frac{eZ_s}{T_{0s}} F_{Ms} g(k_{\parallel}) \frac{v_{\parallel}}{c} \left[\hat{A}_{\parallel}^{n+1} - \hat{A}_{\parallel}^n \right]
\end{aligned} \tag{2.47}$$

where $\hat{k}_{\parallel} \equiv \frac{\sin(k_{\parallel} q R \Delta \theta / 2)}{q R \Delta \theta / 2}$ and $g(k_{\parallel}) \equiv \cos(k_{\parallel} q R \Delta \theta / 2)$. From this, we can determine the plasma response due to a change in Φ ($\frac{\delta f}{\delta \Phi}$) and the plasma response due to a change in A_{\parallel} ($\frac{\delta f}{\delta A_{\parallel}}$) in k_{\parallel} space:

$$\frac{\delta f}{\delta \Phi}(k_{\parallel}) = -\frac{eZ_s}{T_{0s}} F_{Ms} \frac{i \hat{k}_{\parallel} v_{\parallel} \Delta t r}{g(k_{\parallel}) + ir \hat{k}_{\parallel} v_{\parallel} \Delta t} \tag{2.48}$$

$$\frac{\delta f}{\delta A_{\parallel}}(k_{\parallel}) = -\frac{eZ_s}{T_{0s}} F_{Ms} \frac{g(k_{\parallel}) v_{\parallel} / c}{g(k_{\parallel}) + ir \hat{k}_{\parallel} v_{\parallel} \Delta t} \tag{2.49}$$

For simplicity we assume the high resolution limit (i.e. $k_{\parallel} q R \Delta \theta \rightarrow 0$), upon which the discrete Fourier sums are replaced by continuous Fourier integrals. We then use Padé approximations to match transformed solutions of the velocity integrals in the limits of low and high $k_{\parallel} v_{ts} \Delta t$, obtaining:

$$M_{ij}^1 \approx \sum_s \frac{n_{0s} Z_s^2 e^2}{T_{0s}} (G_{ij} - \delta_{ij}) \tag{2.50}$$

$$M_{ij}^2 \approx \sum_s \frac{n_{0s} Z_s^2 e^2}{T_{0s}} \left(-\frac{v_{ts}}{c} \text{sgn}(z_i - z_j) G_{ij} \right) \tag{2.51}$$

$$M_{ij}^3 \approx \sum_s \frac{n_{0s} Z_s^2 e^2}{T_{0s}} (v_{ts} G_{ij} \text{sgn}(z_i - z_j)) \tag{2.52}$$

$$M_{ij}^A \approx \sum_s \frac{n_{0s} Z_s^2 e^2}{T_{0s}} (-v_{ts}^2 G_{ij}) \quad (2.53)$$

where $z \equiv qR\theta$ and $G_{ij} \equiv \frac{\Delta z}{2v_{ts}\Delta tr} e^{-|z_i - z_j|/(v_{ts}\Delta tr)}$. Consider these results for a response row M_{ij} vs. θ_i , i.e. the current and density responses for a perturbation applied in the fields at a particular grid point θ_j . The above equations show that the response falls off very rapidly, or specifically exponentially, the farther away we are from where the perturbation is applied. While it is intuitive that the grid points most affected by the perturbation are the ones that are closest to where it is applied, these results suggest that, when we are computing the response rows exactly, we may be spending a lot of time computing the less significant tail end of the responses.

In practice, we have implemented this analytic preconditioner in our iterative code only in the electrostatic limit for testing. (We found that it wasn't sufficiently accurate and so did not implement the electromagnetic version.) However, in this implementation, we would like to preserve the property of density conservation, i.e. $\sum_i M_{ij}^1 = 0$. The analytic approximation for M_{ij}^1 preserves this property in the limit of $\Delta z \ll 2v_{ts}\Delta tr$ for which

$$\sum_i G_{ij} \approx \frac{1}{2v_{ts}\Delta tr} \int_{-\infty}^{\infty} dz e^{-|z - z_j|/(v_{ts}\Delta tr)} = 1 \quad (2.54)$$

We can reformulate G_{ij} to ensure density conservation on a finite discrete grid. We first define

$$\begin{aligned} G_{ij, i \neq j} &= \frac{1}{2v_{ts}\Delta tr} \int_{z_i - \Delta z/2}^{z_i + \Delta z/2} e^{-|z - z_j|/(v_{ts}\Delta tr)} \\ &= \frac{1}{2} \left[e^{-(|z_i - z_j| - \Delta z/2)/(v_{ts}\Delta tr)} - e^{-(|z_i - z_j| + \Delta z/2)/(v_{ts}\Delta tr)} \right] \end{aligned} \quad (2.55)$$

Then we define

$$G_{ii} \equiv 1 - \sum_{i \neq j} G_{ij} \quad (2.56)$$

Note that this also fixes the singularity in M_{ii} as $\Delta t \rightarrow 0$. Eqs. (2.55) and (2.56) in Eq. (2.50) thus define our electrostatic analytic preconditioner using physics-based Padé approximations of species-dependent response functions as implemented and tested in GS2.

We can compare this model representing the continuous or transformed limit with consideration of Eq. (2.45) in its numerically discrete form. Specifically, approximations for the plasma response due to a change in Φ ($\frac{\delta f_i}{\delta \Phi_j}$) and for the plasma response due to a change in A_{\parallel} ($\frac{\delta f_i}{\delta A_{\parallel,j}}$) can be obtained based directly on Eq. (2.46):

$$\frac{\delta f_{i+1}}{\delta \Phi_j} = -\frac{\delta f_i}{\delta \Phi_j} \left(\frac{1 - bv_{\parallel}}{1 + bv_{\parallel}} \right) + \frac{eZ_s}{T_{0s}} F_{Ms} (\delta_{ij} - \delta_{i+1,j}) \left(\frac{bv_{\parallel}}{1 + bv_{\parallel}} \right) \quad (2.57)$$

$$\frac{\delta f_{i+1}}{\delta A_{\parallel,j}} = -\frac{\delta f_i}{\delta \Phi_j} \left(\frac{1 - bv_{\parallel}}{1 + bv_{\parallel}} \right) - \frac{eZ_s}{T_{0s}} F_{Ms} (\delta_{ij} + \delta_{i+1,j}) \left(\frac{v_{\parallel}/c}{1 + bv_{\parallel}} \right) \quad (2.58)$$

where $b \equiv \frac{2\Delta t r}{qR\Delta\theta}$ and δ_{ij} is the standard Kronecker delta.

The boundary conditions for ballooning coordinates require that the distribution function must vanish as $\theta \rightarrow \pm\infty$ [KOTSCHENREUTHER *et al.*, 1995a]. This can be applied by dividing the distribution function into two parts, i.e. $f_i = g_i + h_i$, where g_i is the part of f_i corresponding to $v_{\parallel} > 0$ and h_i is the part of f_i corresponding to $v_{\parallel} < 0$. For a computational grid extending from $-n\theta$ to $n\theta$, the boundary conditions become: $\{h_{-n\theta} = 0, g_{n\theta} = 0\}$. The distribution function can then be found by solving for h_i starting at $i = -n\theta$, using the first boundary condition, and moving to the right across the θ grid; while g is determined by starting at $i = n\theta$, using the second boundary condition, and moving to the left across the θ grid.

Using this scheme for our plasma response function equations, we find that electrostatic response matrix is given by:

$$i = j : \quad M_{ij}^1 = \sum_s \frac{-2Z_s^2 e^2}{T_{0s}} \int_{v_{\parallel} > 0} d^3 v F_{Ms} \frac{bv_{\parallel}}{1 + bv_{\parallel}} \quad (2.59)$$

$$i = -n\theta \dots j - 1, j + 1 \dots n\theta : \quad M_{ij}^1 = \sum_s \frac{2Z_s^2 e^2}{T_{0s}} \int_{v_{\parallel} > 0} d^3 v F_{Ms} \frac{bv_{\parallel}}{(1 + bv_{\parallel})^2} \left((-1) \frac{1 - bv_{\parallel}}{1 + bv_{\parallel}} \right)^{|i-j|-1} \quad (2.60)$$

We simplify to the limit of $\sqrt{2}bv_{ts} \ll 1$ (or $\Delta z \gg 2\sqrt{2}\Delta trv_{ts}$), where our continuous non-conserving model begins to break down for M_{ii} . (In principle, we could also find approximations in the limit of $\Delta z \ll 2\sqrt{2}\Delta trv_{ts}$ and form a complete discrete-based analytical model using Padé approximations as we did for the continuous equations. However, a good simple analytical approximation in the large $\Delta tv_{ts}/\Delta z$ limit is difficult to find due to an interchange of limits in the velocity integral function between large $\Delta tv_{ts}/\Delta z$ and large $|i - j - 1|$. Furthermore, the resolution of a typical simulation uses $\Delta\theta = \pi/16$, giving $\Delta z/a = 1.4$ for our test case parameters. This is larger than a typical normalized time step in a nonlinear GS2 simulation: $\Delta tv_{ti}/a \sim 0.01 - 0.1$.) In the small $\Delta tv_{ts}/\Delta z$ limit, we find that

$$M_{ij}^1 \approx \sum_s \frac{-n_{0s} Z_s^2 e^2}{T_{0s}} (-1)^{|i-j|} \left(\sqrt{\frac{2}{\pi}} \frac{2v_{ts}\Delta tr}{\Delta z} - 2|i-j| \left(\frac{2v_{ts}\Delta tr}{\Delta z} \right)^2 \right) \quad (2.61)$$

to first order for M_{ii}^1 and to 2nd order for $M_{ij}^1, i \neq j$. Preserving this accuracy yet ensuring that $|M_{ij}^1|$ uniformly decays as $|i - j|$ increases, we modify this as

$$M_{ij}^1 \approx \sum_s \frac{-n_{0s} Z_s^2 e^2}{T_{0s}} (-1)^{|i-j|} \left(\frac{\sqrt{\frac{2}{\pi}} (2v_{ts}\Delta tr)/\Delta z}{1 + |i-j|\sqrt{2\pi}(2v_{ts}\Delta tr)/\Delta z} \right) \quad (2.62)$$

Note that since the dependence of M_{ij}^1 on $|i - j|$ enters in only with higher-order terms, this approximation becomes less accurate as $|i - j|$ increases relative to $\Delta z / (2v_{ts}\Delta t r)$.

Figure 2.10 compares the continuous, density conserving response rows as given by Eqs. (2.55) and (2.56) in Eq. (2.50) with the discrete-based response rows as given by Eq. (2.62). In the small time step limit, for which the discrete approximation is derived, we see that, while the continuous-based response rows approach the correct value of zero as $\Delta t \rightarrow 0$, the model overestimates the rate of decay. A further problem with the continuous preconditioner model is in capturing the Nyquist modes, which have $k_{\parallel} q R \Delta \theta = \pi$ and thus $g(k_{\parallel}) = 0$, since the high resolution assumption of $k_{\parallel} \Delta \theta \ll 1$ yields $g(k_{\parallel}) = 1$. The problem of $g(k_{\parallel}) \rightarrow 0$ (which can cause the response matrix to decay very slowly as $(i - j) \rightarrow \pm\infty$) is a result of the 2nd order compact finite differencing of the Beam-Warming algorithm and would not be an issue for other algorithms, including higher-order compact finite differencing algorithms. The discrete preconditioner model also has a major disadvantage, namely its limited time step size range. Thus, ultimately, development of a numerical preconditioner may be more practical, as we would like to accurately capture a large range of spatial and temporal resolutions as well as to account for physical effects neglected in the analytic approximations, such as the finite Larmor radius effects represented by the Bessel functions.

One simple numerical approximation involves computing a single exact response row, i.e. the exact M_{ij} vs. i for a single value of $j = j_0$, and assuming that other rows can be calculated by translation as follows:

$$M_{ij} = M_{i-j+j_0, j_0} \quad (2.63)$$

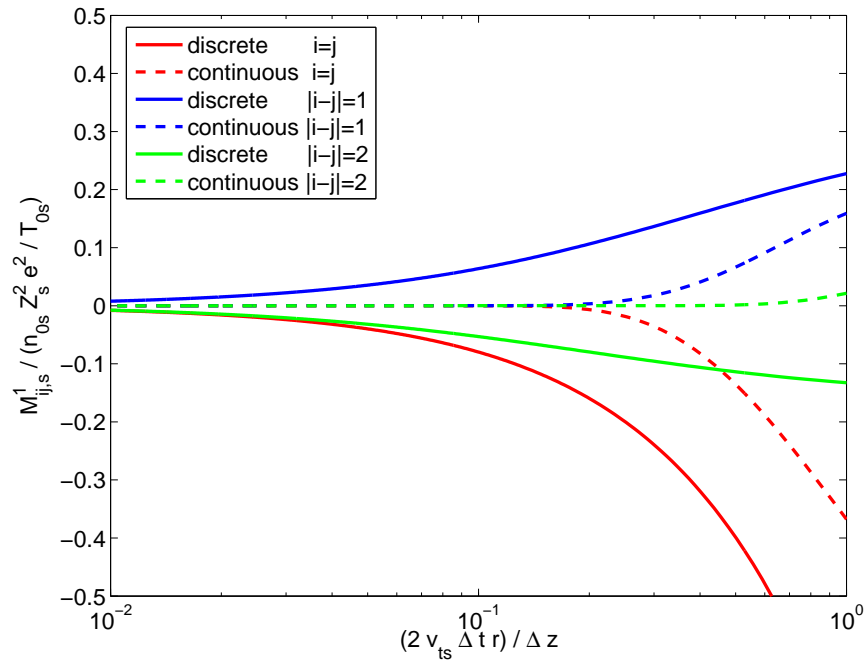


Figure 2.10: Electrostatic response row values as a function of the time step size Δt relative to the parallel spatial step size Δz comparing analytic approximations of the plasma response based on a numerically discrete form of the gyrokinetic equation and the continuous or spatially transformed limit.

Computationally, this approach reduces the number of gyrokinetic equation solves needed to pre-compute the response matrix by a factor of N_θ . The physical basis for this idea is that it is exact for an infinite uniform plasma, though in a real tokamak there are some spatial variations, which this model would not capture.

Thus, we would like to develop a model which incorporates both the idea of translation and the insight from the analytic models. Here we describe such a model, which we will refer to as multiM. Recall that to compute a row of M_{ij} exactly, we set $\Phi_i^{n+1} = 1$ at $i = j$ and 0 otherwise and then one gyrokinetic equation-Poisson-Ampere solve is done to compute the response. The multiM model is based on computing approximate values for M_{ij} vs. i at various j simultaneously (since we know from the continuous analytic approximation that the responses decay quickly as we move away from where the perturbation is applied). The response around a perturbation point j can then be retained for its corresponding response row, while the tail end of the response row can be computed using extrapolation between the retained responses and a translated response from a single exact response row M_{i,j_0} vs. i . The pseudo-code for this is given as follows:

For $n_{start} = 1 \dots n_{stride}$

- Set $\Phi_j^{n+1} = (\pm)1$ at every $j = n_{stride}$ -th grid point starting at n_{start} ; $\Phi_i^{n+1} = 0$ otherwise.
- Solve the gyrokinetic and field equations for the response row R_i .

For $i = (j - n_{ipts}) \dots (j + n_{ipts})$

- Set $M_{ij} = (\pm)R_i$

For $i = i_{min} \dots j - (n_{ipts} + 1)$

- Set $M_{ij} = (M_{i-j+j_0,j_0}/M_{j_0-n_{ipts},j_0})M_{j-n_{ipts},j}$

For $i = j + (n_{ipts} + 1) \dots i_{max}$

- Set $M_{ij} = (M_{i-j+j_0,j_0}/M_{j_0+n_{ipts},j_0})M_{j+n_{ipts},j}$

Thus, we apply perturbations at multiple grid points equally spaced apart (by n_{stride}), yet alternate the sign of the perturbations to minimize the effect of one perturbation on another. The response of the distribution function to this perturbation is then computed via solution of the gyrokinetic equation. The grid points around where a perturbation was applied are then used for that grid point's response row. For the tail end of the response row, we extrapolate based on the retained values and a single computed exact response row. Note that this method requires $N_{fields}(n_{stride} + 1)$ gyrokinetic equation solves to compute the approximation for M . Thus, one advantage of this preconditioner is that the resolution can easily be adapted to minimize the computational efficiency of the preconditioner relative to the enhancement in iteration convergence that the preconditioner provides. Furthermore, it can be extrapolated to the exact response (if $n_{stride} = N_\theta$ and $n_{ipts} = N_\theta - 1$). A graphical illustration of multiM preconditioning is given in figure 2.11. For notation, we will denote the method as “multiM (x,y)”, where $x = n_{stride}$ is the number of grid spacings between the points where the perturbations are applied simultaneously and $y = n_{ipts}$ is the one-sided number of retained points around the perturbation points.

(Aside: After developing and testing our multiM algorithm, we learned that it can be thought of as a variation of an algorithm known in the numerical methods literature as “probing” a matrix or graph “coloring”. “Probing” refers to the process of determining a Jacobian (which in our case is the Green's function or plasma

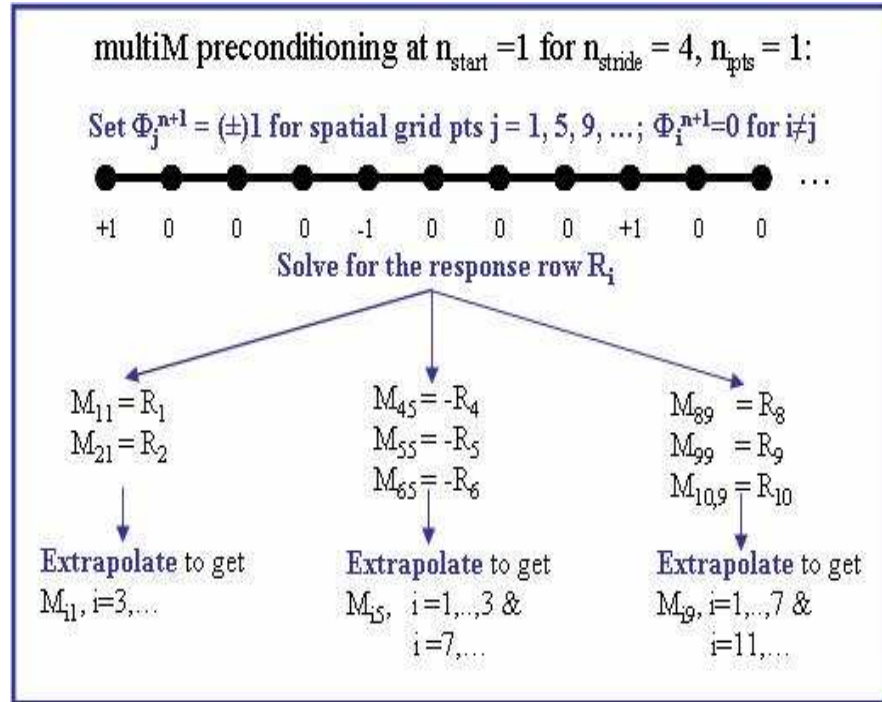


Figure 2.11: Graphical illustration of the multiM (4,1) preconditioner.

response matrix) by numerical differentiation. “Coloring” refers to the trick of calculating many elements of the Jacobian simultaneously by partitioning space into subdomains that do not interact (or, in our case, weakly interact) in a single application of the function. This is analogous to using colors to distinguish different territories in a geographical map, which is how the well-known Four-Color Map Theorem arose.)

Now that we have developed several preconditioner models, we can compare them in practice. First, figure 2.12 compares the response rows for the analytically-based continuous approximation, the numerically-based translated approximation, and the numerically-based multiM approximation with the exact plasma response matrix. Qualitatively, the approximations agree well with the exact matrix, even for perturbations applied near the boundaries of the θ grid at $\theta = \pm 3\pi$. Note that

the analytic approximation is purely real. The exact plasma response shows that the imaginary component is nonzero but negligible compared to the real part.

Although the errors $|M_{GS2,approx} - M_{GS2,exact}|$ look small in figure 2.12, what really matters for the convergence rate of an iterative algorithm is the maximum eigenvalue of $|I - M_{GS2,approx}^{-1}M_{GS2,exact}|$ (related to the error vector in Eq. (2.42)), which is plotted in figure 2.13. The errors expressed by the results in figure 2.13 appear quite large compared to what one might have expected at first from looking at figure 2.12. (Recall that the simple iteration algorithm is not guaranteed to converge if $\max |\lambda| \geq 1$.) But if $M_{GS2,approx}$ has a nearly null eigenvalue for an eigenvector that is in a slightly different direction than a nearly null eigenvector of $M_{GS2,exact}$, then $|I - M_{GS2,approx}^{-1}M_{GS2,exact}|$ could get large even though $|M_{GS2,approx} - M_{GS2,exact}|$ looks small.

Figure 2.13 also compares the convergence of the methods using simulations with the test case parameters in the electrostatic limit and the simple iteration algorithm. Overall, the results show that the numerical preconditioners are generally more accurate and likewise show better convergence than the analytic preconditioner. Note, in particular, the inaccuracy of the analytic preconditioner for $\Delta tv_{ti}/a \ll (\Delta z/a)(1/2r) = 1.2$, shown by the increased maximum eigenvalue for the smallest time step sizes and, likewise, by the increasing iteration count for the smallest time step sizes in the $k_y \rho_i = 0.5$ and 0.1 cases. (As an aside, it was also necessary to lower the iteration tolerance for the analytic preconditioner by a factor of 100 compared with that for the numerical preconditioners to ensure that ω converges in the same number of total time steps as the fully implicit scheme. More details about the iteration convergence criterion and the choice of the iteration tolerance are discussed in section 2.3.3 on initializers.) Comparing the numerical models,

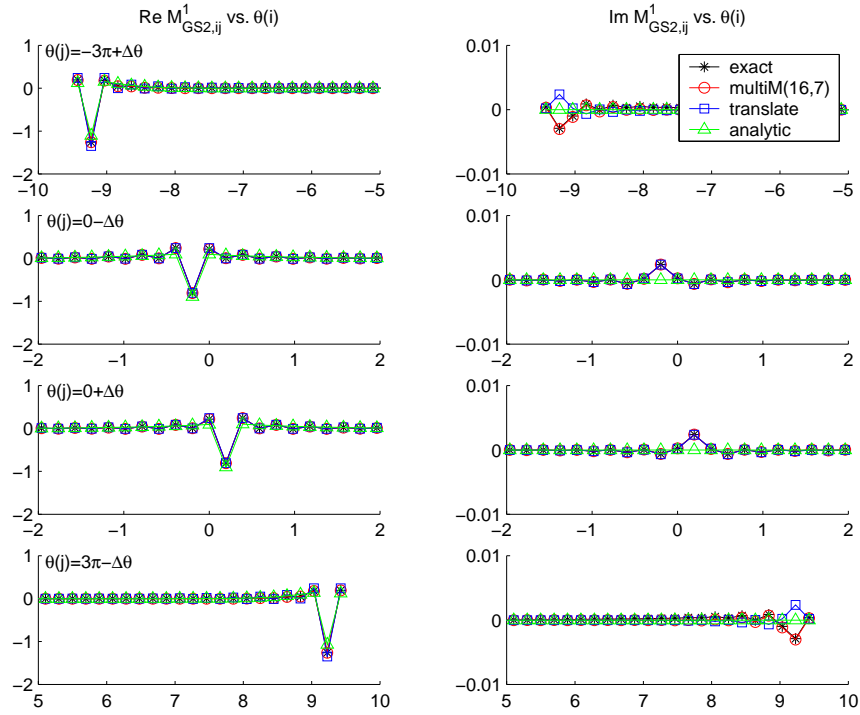


Figure 2.12: Electrostatic response rows for test case parameters at $k_y \rho_i = 0.1$ and $\Delta t v_{ti} / a = 0.1$ comparing the exact response matrix with various preconditioners: numerically-based multiM, numerically-based translate, and an analytically-based continuous approximation for the plasma response.

while the eigenvalue plots consistently show the multiM preconditioner to be more accurate than the translated preconditioner, this is not significantly shown in the convergence test runs until the largest time step sizes for the $k_y \rho_i = 0.1$ case, when the number of iterations for the translated preconditioner case rapidly increases. In general, the number of iterations for an iterative algorithm depends not only on the maximum eigenvalue λ , but also on the amplitude of the projection of the initial error in the direction of the corresponding eigenvector. Presumably, the initial error is small for small Δt and so requires fewer iterations. (Note that, even for a perfect preconditioner $M_{GS2,approx} = M_{GS2,exact}$ so $\lambda = 0$, there will still be 2 iterations.)

For future tests, we will use the multiM preconditioner. The optimum choice

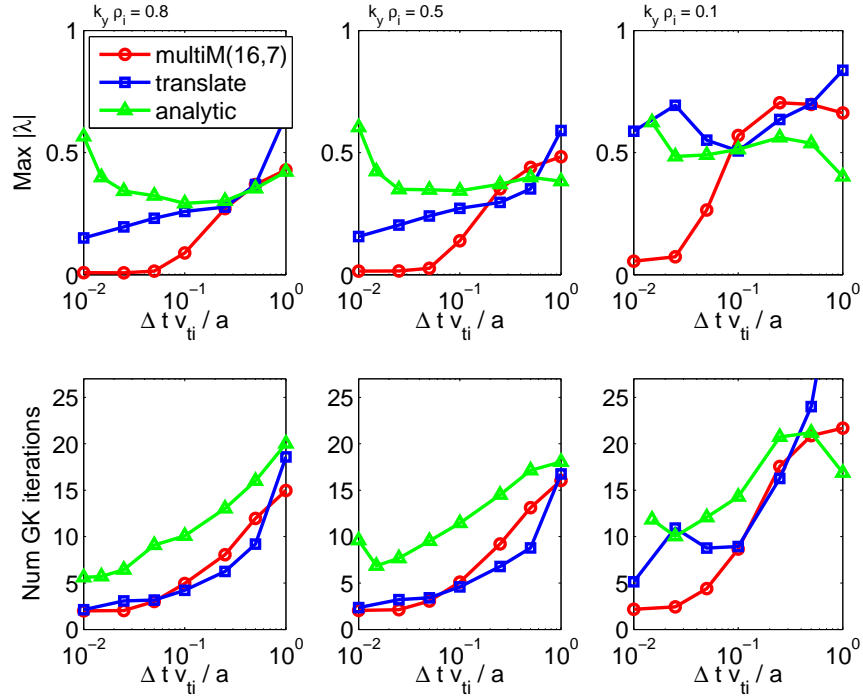


Figure 2.13: Maximum eigenvalue $|\lambda|$ of $|I - M_{GS2,approx}^{-1} M_{GS2,exact}|$ vs. normalized time step size and average number of gyrokinetic solves per time step vs. normalized time step size for test case parameters in the electrostatic limit using an iterative implicit scheme with simple iteration and a two-point iteration initializer comparing various preconditioners: numerically-based multiM, numerically-based translate, and a analytically-based continuous approximation for the plasma response. (Note that the analytic preconditioner uses an iteration tolerance which is 100 times smaller than the standard iteration tolerance).

of $n_{stride} = 16$ and $n_{ipts} = 7$ used in the tests above was chosen empirically. Note that for the test case parameters, the number of θ grid points is 32 per 2π in θ , or a total of 97 grid points for a grid extending from -3π to 3π . Thus multiM (97,96) is equivalent to computing the exact fully implicit response matrix, so multiM (16,7) does approximately 6 times fewer gyrokinetic-Poisson-Ampere solves in the initialization. Figures 2.14 and 2.15 compare the electromagnetic response rows for multiM (20,9), (16,7), (12,5), and (8,3) at a moderate $k_y \rho_i$ of 0.5 and a moderate time step $\Delta t(v_{ti}/a)$ of 0.1 for a perturbation applied near the center of the θ grid at $\theta = 0 + \Delta\theta$ and for a perturbation applied near the right boundary at $\theta = 3\pi - \Delta\theta$. On the scale shown, the agreement between the multiM preconditioner response rows and the exact response rows is good for all 4 matrices $M_{GS2}^1 - M_{GS2}^4$. The close agreement in the curves in the non-extrapolated points around the applied perturbations suggests that the effects of nearby simultaneously applied perturbations is minimal, though a slight deviation of the curves, particularly for the multiM (8,3) preconditioner, can be seen at $\theta(i) = \theta(j \pm (n_{ipts} + 1))$ where the extrapolation begins. Perhaps, in future work, an extrapolation based on a higher-order polynomial could smooth this transition for lower resolution preconditioners.

Figures 2.16 and 2.17 compare the multiM preconditioners quantitatively, showing the maximum eigenvalue of $|I - M_{GS2approx}^{-1} M_{GS2exact}|$ and the average number of iteration per time step with the test case parameters in the electrostatic limit using simple iteration for the cases of adiabatic electrons and gyrokinetic electrons respectively. Overall, for both cases, while general enhanced convergence is seen as n_{stride} increases as expected, there is not much improvement from (16,7) to (20,9), perhaps even less than the enhancement compared with increasing the resolution from (12,5) to (16,7). For the case of adiabatic electrons, the performance of the

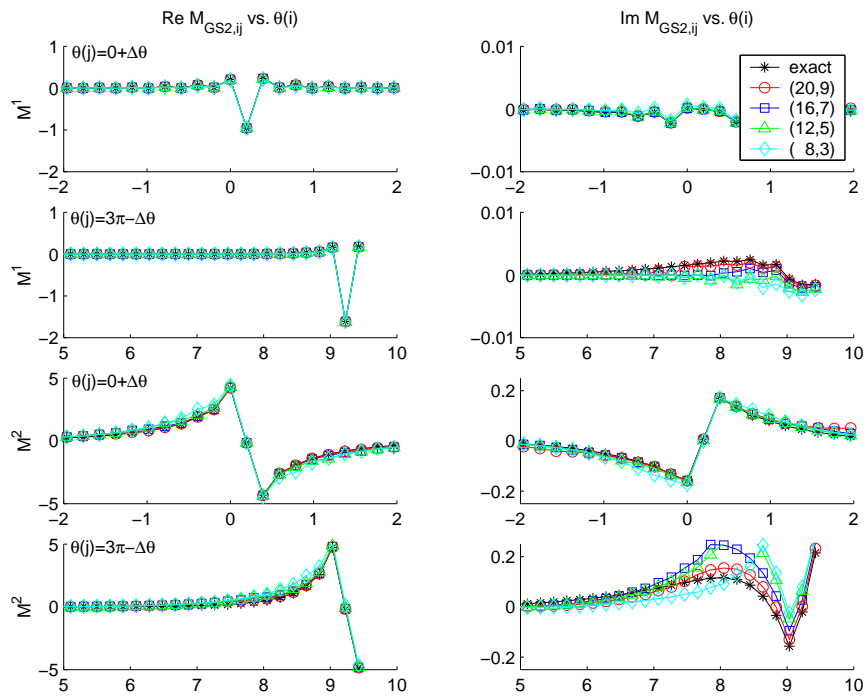


Figure 2.14: Response rows $M^1_{GS2,ij}$ and $M^2_{GS2,ij}$ vs. $\theta(i)$ for test case parameters at $k_y \rho_i = 0.5$ and $\Delta t v_{ti}/a = 0.1$ comparing the exact response matrix with the numerically-based multIM of varying resolution (n_{stride}, n_{ipts}).

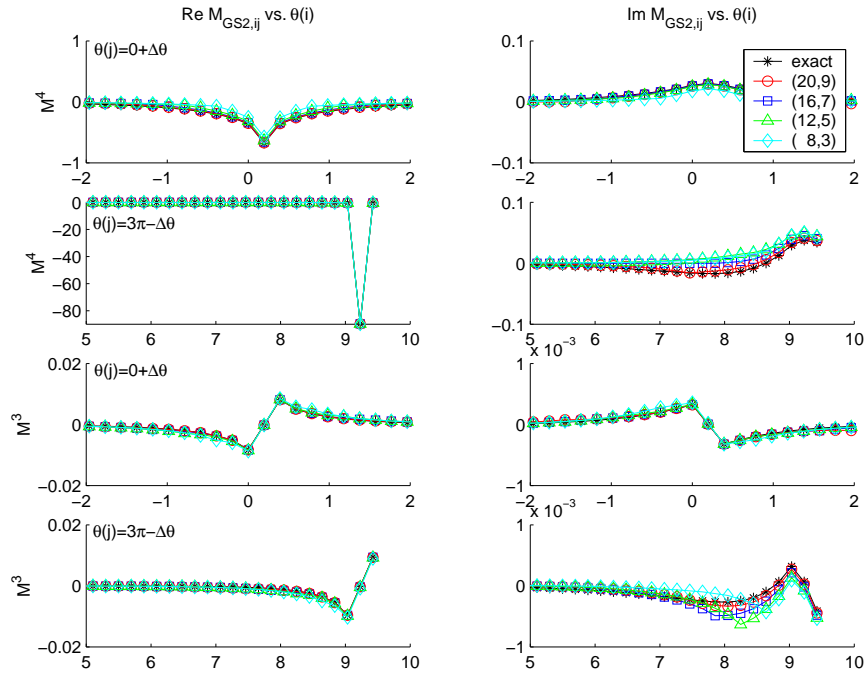


Figure 2.15: Response rows $M^4_{GS2,ij}$ and $M^3_{GS2,ij}$ vs. $\theta(i)$ for test case parameters at $k_y \rho_i = 0.5$ and $\Delta t v_{ti}/a = 0.1$ comparing the exact response matrix with the numerically-based multiM of varying resolution (n_{stride}, n_{ipts}) .

iterative scheme is particularly good across the entire range of time step widths. Specifically, multiM (20,9) - multiM (8,3) perform less than ~ 3 iterations per time step even at the largest time step width of $\Delta t v_{thi}/a = 1$ for all $k_y \rho_i$ test cases. Even multiM (4,1) performs less than 5 iterations per time step.

Considering a given time step width in the results with adiabatic electrons shown in figure 2.16, note that as $k_y \rho_i$ decreases, the maximum eigenvalue increases but not much change is seen in the number of iterations. This is interesting compared with the results with gyrokinetic electrons in figure 2.17, which shows both an increase in the maximum eigenvalue and a consistent increase in the number of iterations as $k_y \rho_i$ decreases for a given time step width. Note that the number of iterations begins to increase above 2 iterations near the limit where the time step width normalized with respect to v_{te} is comparable to the parallel spatial width Δz , i.e. for $\Delta t v_{te}/a \sim (\Delta z/a)(1/2r)$, which corresponds to $\Delta t v_{ti}/a \sim 0.021$ for the test case parameters. For the adiabatic electron case, the analogous relevant time step limit is where the time step width normalized with respect to v_{ti} is comparable to the parallel spatial width Δz , i.e. $\Delta t v_{ti}/a \sim (\Delta z/a)(1/2r)$, which corresponds to 1.2 for the test case parameters. So this limit is slightly beyond the time step range in figure 2.16. But, looking at the multiM (20,9) and (16,7) cases, the figure does show that the iteration curves are beginning to increase above 2 iterations just below the end of the range at $\Delta t v_{ti}/a = 1$.

Figure 2.18 shows analogous results to figure 2.17 with the inclusion of electromagnetic dynamics. Here we see a more significant increase in the number of iterations as Δt increases (particularly as $k_y \rho_i$ decreases) and, unlike the electrostatic case, a limitation of the time step width (above which the maximum eigenvalue approaches 1 and the algorithm fails to converge) In fact, the $k_y \rho_i = 0.1$ results

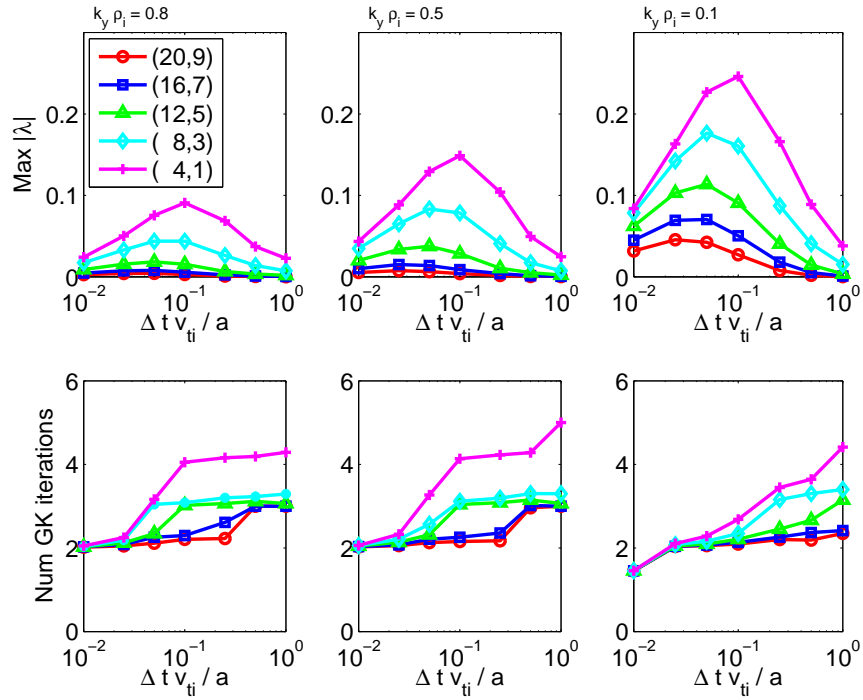


Figure 2.16: Maximum eigenvalue $|\lambda|$ of $|I - M_{GS2,approx}^{-1} M_{GS2,exact}|$ vs. normalized time step size and average number of gyrokinetic solves per time step vs. normalized time step size for test case parameters in the electrostatic limit with adiabatic electrons using an iterative implicit scheme with simple iteration and a two-point iteration initializer comparing numerically-based multiM preconditioners of varying resolution (n_{stride}, n_{ipts}) .

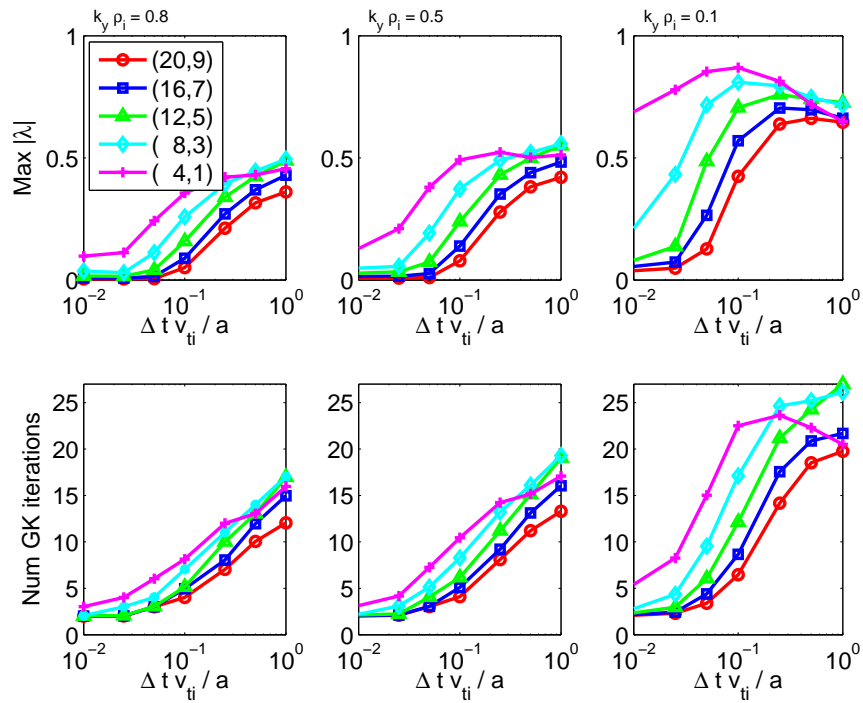


Figure 2.17: Maximum eigenvalue $|\lambda|$ of $|I - M_{GS2,approx}^{-1} M_{GS2,exact}|$ vs. normalized time step size and average number of gyrokinetic solves per time step vs. normalized time step size for test case parameters in the electrostatic limit using an iterative implicit scheme with simple iteration and a two-point iteration initializer comparing numerically-based multiM preconditioners of varying resolution (n_{stride}, n_{ipts}) .

indicate that a resolution of at least (12,5) is needed in practice, since the lower resolution preconditioners do not converge at even the smallest Δt for this case.

Overall, the result that there is a fairly sharp time step limitation for the electromagnetic cases is somewhat surprising and not fully understood. Considering the electromagnetic response row plots shown in figures 2.14 and 2.15, the response rows for the preconditioner models do not qualitatively appear more inaccurate for M_{GS2}^2 , M_{GS2}^3 , and M_{GS2}^4 than for the full electrostatic response of M_{GS2}^1 . Recall again that these plots correspond to the case of $k_y\rho_i = 0.5$ and $\Delta tv_{ti}/a = 0.1$. Although the number of iterations for multiM (20,9) and (16,7) is approximately the same electrostatically and electromagnetically at this time step width, multiM (12,5) averages 6 and 9 iterations respectively while multiM (8,3) does larger than max iterations (> 300) electromagnetically compared with 8 electrostatically.

Figure 2.19 thus addresses the issue of whether simply any nonzero β significantly affects convergence. In this figure, for multiM (20,9), (16,7), and (12,5) at $k_y\rho_i = 0.5$, we compare the maximum eigenvalue and number of iterations as a function of Δt as β is varied from the electrostatic limit of $\beta = 0$ to $\beta = 2 \times$ the test case value of 1.0×10^{-3} . In these curves, the multiM (20,9) case does not show a significant decrease in performance until $\beta = 5.0 \times 10^{-4}$, while both the multiM (16,7) and (12,5) cases show a significant deviation from the electrostatic case even for $\beta = 2.5 \times 10^{-4}$. However, considering a given Δt , while for all 3 models the maximum eigenvalue and number of iterations increases as β increases, for β larger than that for which max iterations is exceeded, there does not appear to be a significant shift in $(\Delta tv_{ti}/a)_{max}$ as β is increased further, at least for the limited range of β tested.

Here we further consider the nature of this sharp time step limitation for the

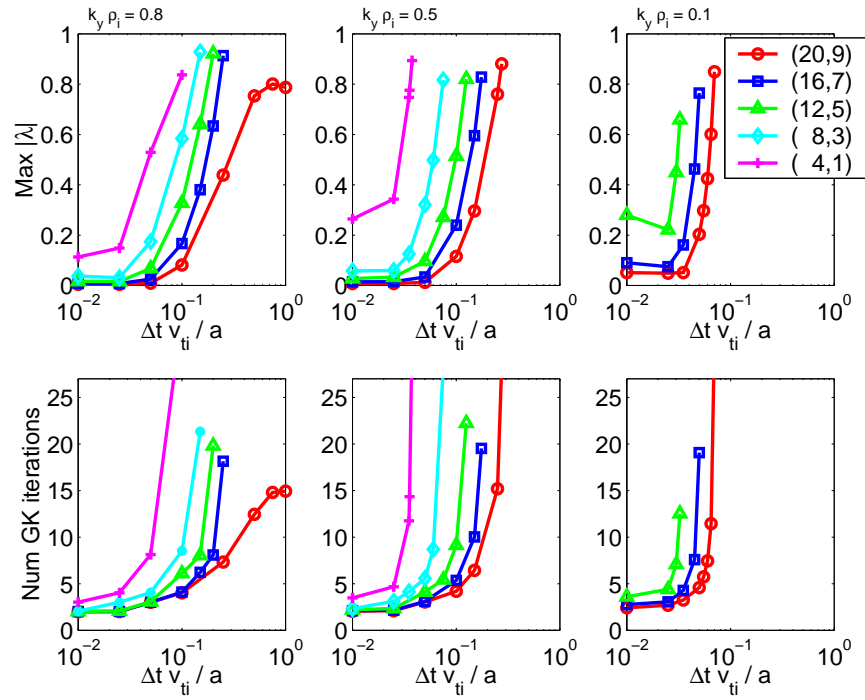


Figure 2.18: Maximum eigenvalue $|\lambda|$ of $|I - M_{GS2,approx}^{-1} M_{GS2,exact}|$ vs. normalized time step size and average number of gyrokinetic solves per time step vs. normalized time step size for test case parameters with electromagnetic dynamics ($\beta = 1.0 \times 10^{-3}$) using an iterative implicit scheme with simple iteration and a two-point iteration initializer comparing numerically-based multiM preconditioners of varying resolution (n_{stride}, n_{ipts}).

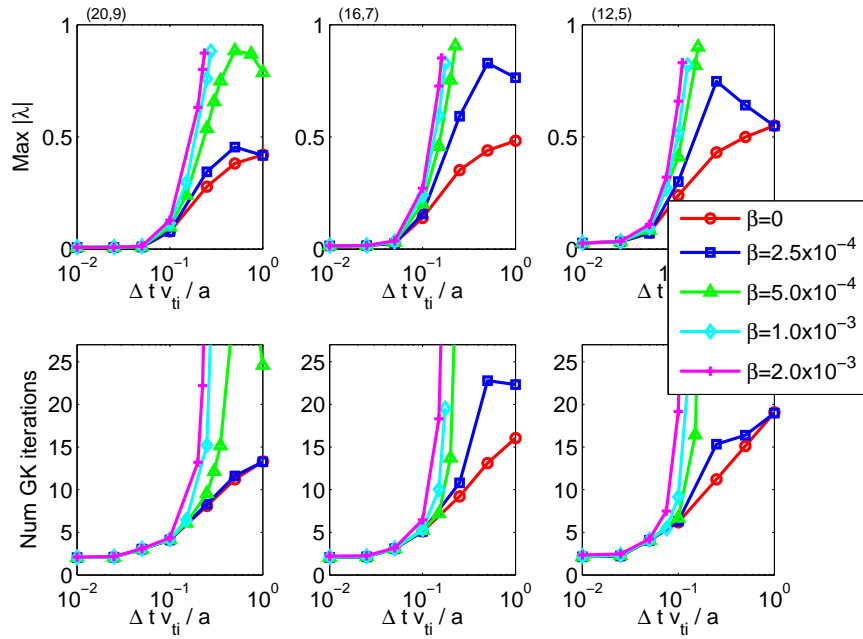


Figure 2.19: Maximum eigenvalue $|\lambda|$ of $|I - M_{GS2,approx}^{-1} M_{GS2,exact}|$ vs. normalized time step size and average number of gyrokinetic solves per time step vs. normalized time step size for test case parameters at $k_y \rho_i = 0.5$ with electromagnetic dynamics and various β using an iterative implicit scheme with simple iteration and a two-point iteration initializer comparing numerically-based multiM preconditioners of resolution $(n_{stride}, n_{ipts}) = (20,9)$, $(16,7)$, and $(12,5)$.

electromagnetic cases. It is clear from figure 2.18 that the time step at which the maximum eigenvalue approaches 1, corresponding to non-convergence, decreases as the resolution of the preconditioner model (specified by n_{stride}) decreases and as $k_y \rho_i$ decreases. (The scaling of the time step limitation with $k_y \rho_i$ is shown more clearly for the multiM (16,7) model in figure 2.20.) We have found empirically from these electromagnetic results that the maximum time step for convergence scales as

$$(\Delta t v_{te}/a)_{max} \sim (\Delta z/a)(1/2r) * (n_{stride}) * (k_y \rho_i) \quad (2.64)$$

where $n_{stride} \Delta z$ is the bandwidth of the response used for the multiM preconditioner. In the finite β electromagnetic results in figure 2.18, the number of iterations increases very rapidly if this time step is exceeded, effectively putting a stringent limit on the time step, while in the $\beta = 0$ electrostatic results in figure 2.17 the required number of iterations increases at a more modest rate if this time step is exceeded. This is surprising considering the analytic dispersion relation for the kinetic Alfvén wave, given as follows for long wavelengths:

$$\omega^2 = \frac{k_{\parallel}^2 v_A^2}{1 + \frac{2}{\beta_e} \frac{m_e}{m_i} k_{\perp}^2 \rho_s^2} = \frac{k_{\parallel}^2 v_{te}^2}{\frac{\beta_e}{2} \frac{m_i}{m_e} + k_{\perp}^2 \rho_s^2} \quad (2.65)$$

which shows that $\omega/(k_{\parallel} v_{te})$ should decrease as β increases. So one would have thought that the higher β case would be easier, not harder, than the $\beta = 0$ limit. However, an unusual feature of the Beam-Warming finite-differencing algorithm is that the $\partial A_{\parallel}/\partial t$ in the gyrokinetic equation is evaluated half-way between adjacent grid points: $\frac{\partial A_{\parallel}}{\partial t} = \frac{\partial}{\partial t} \left(\frac{A_{\parallel,j+1} + A_{\parallel,j}}{2} \right)$. Considering Fourier modes $A_{\parallel,j} \sim e^{ik_{\parallel} q R \theta_j}$, we see that the $\partial A_{\parallel}/\partial t$ operator vanishes for modes with the highest k_{\parallel} allowed on the grid, i.e. at the Nyquist limit $k_{\parallel} q R \Delta \theta = \pi$. The Nyquist mode oscillates sign

from one grid point to the next ($A_{\parallel,j} \sim (-1)^j$), so averaging it between adjacent grid points always gives 0. This means that the discrete system of equations always approaches the electrostatic $\beta = 0$ limit, but it does not explain why the finite β case actually requires more iterations. This behavior, i.e. that problems get more difficult at higher β and lower k_{\perp} , is somewhat reminiscent of the ‘‘Ampere cancellation’’ problem that affected other algorithms (but not GS2’s fully implicit algorithm) and was eventually fixed by careful treatment of two potentially large terms in the Ampere equation that should cancel each other [HAMMETT and JENKO, 2001; CANDY and WALTZ, 2003a; CHEN and PARKER, 2003]. It is possible that further investigation of this issue could lead to an improved preconditioner or modification of the treatment of some of the terms in the iteration that would provide better convergence performance for simple iteration for low $k_y \rho_i$ modes. We leave this to future work. Another option for future work would be to explore a more standard version of the compact finite differencing algorithm, which is usually implemented with 4th or 6th order accuracy, or even other non-compact finite differencing algorithms, since it is only the 2nd order version of compact finite differencing that has the problem of the $\partial/\partial t$ operators vanishing for modes at the Nyquist scale $k_{\parallel} q R \Delta \theta = \pi$.

For this work, however, we will use the simple iteration results of figures 2.17 - 2.20 and the multiM (16,7) preconditioner as a base case standard in the next two sections of this chapter in which we explore choice of an optimal iteration initializer and compare more robust and complex iterative schemes.

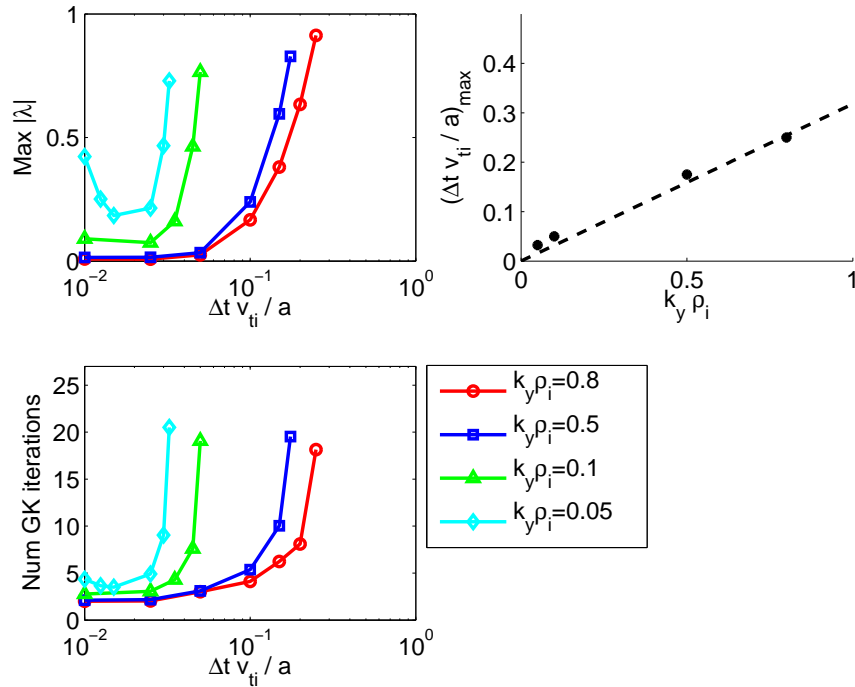


Figure 2.20: Maximum eigenvalue $|\lambda|$ of $|I - M_{GS2,approx}^{-1} M_{GS2,exact}|$ vs. normalized time step size and average number of gyrokinetic solves per time step vs. normalized time step size for test case parameters with electromagnetic dynamics ($\beta = 1.0 \times 10^{-3}$) using an iterative implicit scheme with simple iteration, a two-point iteration initializer, and multiM (16,7) preconditioner. The right plot shows the maximum time step (after which the number of iterations exceeds max iterations) vs. $k_y \rho_i$ for this data. The dashed line shows the empirical scaling given in Eq. (2.64).

2.3.3 Initializers

The choice of initialization for the fields for the 0th iteration at the beginning of each time advance was also explored. While the convergence or divergence of the iterative process does not depend on the initial guess (this depends rather on the character of the matrix), a good initializer can reduce the number of iterations. Here we compare the following initializer extrapolators:

- simple one-point: $\Phi^{n+1,0} = \Phi^n$
- linear two-point: $\Phi^{n+1,p=0} = 2\Phi^n - \Phi^{n-1}$
- polynomial three-point: $\Phi^{n+1,p=0} = 3\Phi^n - 3\Phi^{n-1} + \Phi^{n-2}$
- polynomial four-point: $\Phi^{n+1,p=0} = 4\Phi^n - 6\Phi^{n-1} + 4\Phi^{n-2} - \Phi^{n-3}$

Note that the results shown in section 2.3.2 used the linear two-point initializer. The results presented in this section use the simple iteration algorithm and the multiM (16,7) preconditioner.

Figures 2.21 and 2.22 compare the performance of the initializers for the electrostatic and electromagnetic cases respectively. Overall, the linear two-point extrapolator generally provides the fastest convergence rate. However, we note that the polynomial three-point and four-point initializers required the use of a smaller iteration tolerance (with respect to the ω tolerance) for convergence. For solution of our generic equation $\frac{d\vec{x}}{dt} = -iL\vec{x}$, where \vec{x} is the field vector (Φ, A_{\parallel}) and L is some linear operator with a spectrum of eigenvalues ω , we define the eigenfrequency of the fastest growing mode based on the L2-norm of the finite differenced equation, i.e.

$$\omega(k_x, k_y) = \frac{i}{\Delta t} \frac{\langle \vec{x}_{avg} | \vec{x}^{n+1} - \vec{x}^n \rangle}{\langle \vec{x}_{avg} | \vec{x}_{avg} \rangle} \quad (2.66)$$

where $\vec{x}_{avg} = r\vec{x}^{n+1} + (1-r)\vec{x}^n$. GS2 uses the simple convergence criterion that the ratio of the sample variance to the sample mean of ω for a specified time-averaging period be less than the specified ω tolerance. The iteration convergence criterion is likewise defined based on the L2-norm but relative to the instantaneous iteration:

$$\frac{\langle \vec{x}^{n+1,p+1} - \vec{x}^{n+1,p} \mid \vec{x}^{n+1,p+1} - \vec{x}^{n+1,p} \rangle}{\langle \vec{x}^{n+1,p} \mid \vec{x}^{n+1,p} \rangle} < (iter_tol)^2 \quad (2.67)$$

Typical results use an iteration tolerance which is set to be 1/4 of the ω tolerance ($\omega_tol = 1.0 \times 10^{-5}$). This ratio value was chosen empirically using the criterion that the iteration scheme yield the same number of total time steps to converge in ω as the fully implicit code for general test cases. With the three-point and four-point polynomial initializers, however, while the iteration converges on each time step using the standard iteration tolerance, ω does not converge in the same number of total time steps. Thus, the iteration tolerance was lowered according to this criterion, yielding $iter_tol/\omega_tol = 1/100$ for the three-point initializer and $iter_tol/\omega_tol = 1/10000$ for the four-point initializer. This lowering of the iteration tolerance of course increases the number of gyrokinetic solves per time step. To see this effect, in figures 2.21 and 2.22 the blue dashed and dotted lines show the results using the linear two-point initializer with an iteration tolerance of 1.0×10^{-7} and 1.0×10^{-9} respectively. Comparing these curves with the three-point and four-point curves, we see that, for a given iteration tolerance, the higher-order polynomial schemes perform better.

For future work, a better approach may be to measure the iteration error relative to $(\vec{x}^{n+1} - \vec{x}^n)$ rather than to \vec{x}^{n+1} . To see this, consider the uncertainty in ω .

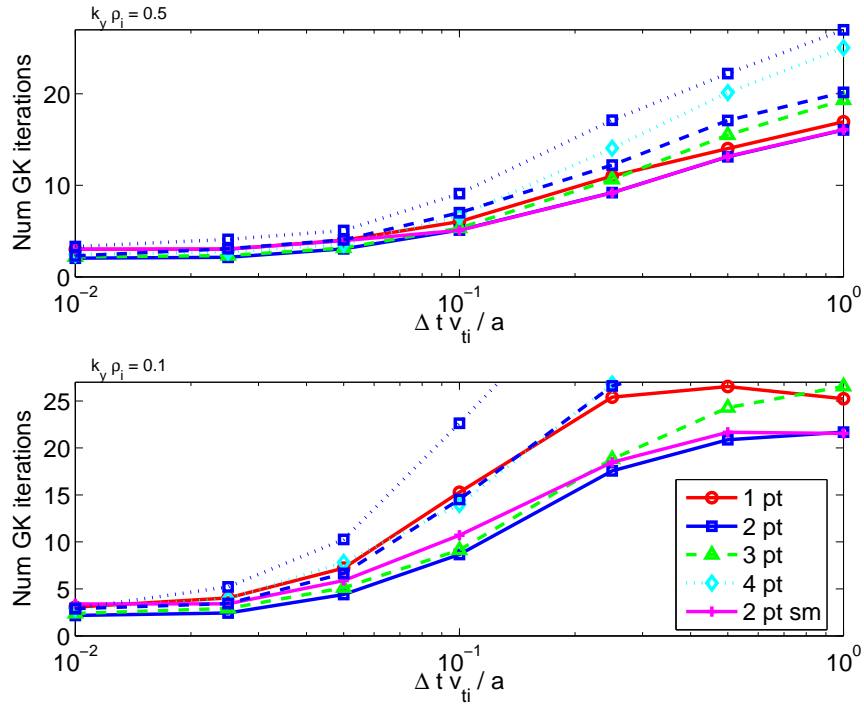


Figure 2.21: Average number of gyrokinetic solves per time step for test case parameters in the electrostatic limit using an iterative implicit scheme with simple iteration and multiM (16,7) preconditioner and comparing various iteration initializer extrapolators. The dashed lines use an iteration tolerance of 1.0×10^{-7} and the dotted lines use an iteration tolerance of 1.0×10^{-9} (The standard iteration tolerance is 2.5×10^{-6}).

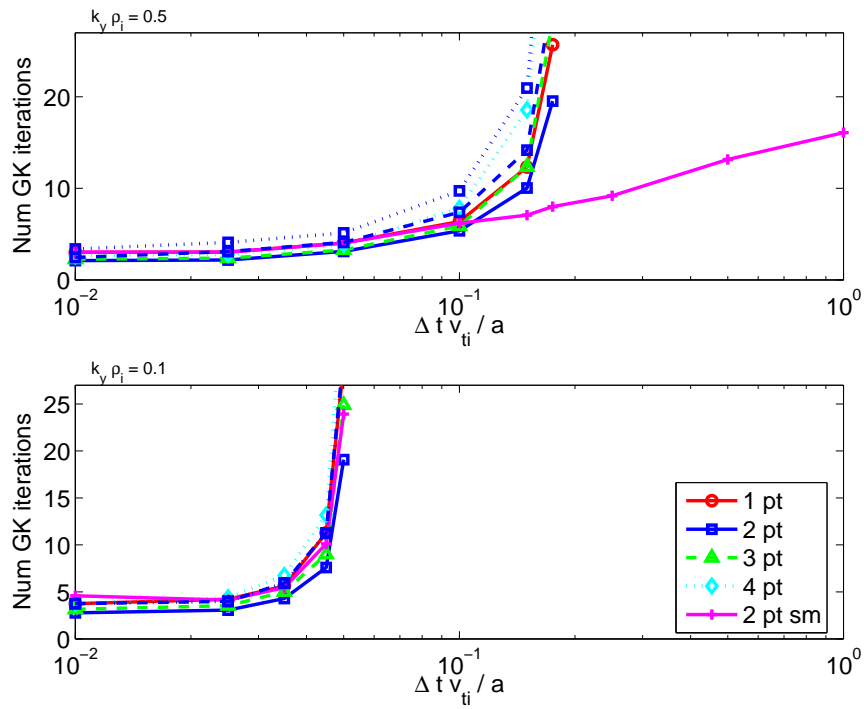


Figure 2.22: Average number of gyrokinetic solves per time step for test case parameters with electromagnetic dynamics ($\beta = 1.0 \times 10^{-3}$) using an iterative implicit scheme with simple iteration and multiM (16,7) preconditioner and comparing various iteration initializer extrapolators. The dashed lines use an iteration tolerance of 1.0×10^{-7} and the dotted lines use an iteration tolerance of 1.0×10^{-9} (The standard iteration tolerance is 2.5×10^{-6}).

Considering the electrostatic limit for simplicity, Eq. (2.66) becomes

$$\omega = \frac{i}{\Delta t} \frac{\langle \Phi_{avg} | \Phi^{n+1} - \Phi^n \rangle}{\langle \Phi_{avg} | \Phi_{avg} \rangle} \quad (2.68)$$

From this, the relative instantaneous uncertainty in ω is given by

$$\begin{aligned} \frac{\delta\omega}{\omega} &= \frac{\langle r\delta\Phi^{n+1} + (1-r)\delta\Phi^n | \Phi^{n+1} - \Phi^n \rangle + \langle \Phi_{avg} | \delta\Phi^{n+1} - \delta\Phi^n \rangle}{\langle \Phi_{avg} | \Phi^{n+1} - \Phi^n \rangle} \\ &\quad - \frac{\langle r\delta\Phi^{n+1} + (1-r)\delta\Phi^n | \Phi_{avg} \rangle}{\langle \Phi_{avg} | \Phi_{avg} \rangle} \\ &\quad - \frac{\langle \Phi_{avg} | r\delta\Phi^{n+1} + (1-r)\delta\Phi^n \rangle}{\langle \Phi_{avg} | \Phi_{avg} \rangle} \end{aligned} \quad (2.69)$$

Using Eq. (2.68) to rewrite the first term on the RHS, we can simplify Eq. (2.69)

as:

$$\frac{\delta\omega}{\omega} = \frac{1}{\langle \Phi_{avg} | \Phi_{avg} \rangle} \left[\langle r\delta\Phi^{n+1} + (1-r)\delta\Phi^n | \Phi_{avg} \rangle \right] \quad (2.70)$$

$$\begin{aligned} &+ \frac{i}{\omega\Delta t} \langle \Phi_{avg} | \delta\Phi^{n+1} - \delta\Phi^n \rangle \\ &- 2Re \left(\langle \Phi_{avg} | r\delta\Phi^{n+1} + (1-r)\delta\Phi^n \rangle \right) \end{aligned} \quad (2.71)$$

Taking the absolute value, we find that the error is bounded by

$$\begin{aligned} \frac{|\delta\omega|}{|\omega|} &\leq \frac{1}{\langle \Phi_{avg} | \Phi_{avg} \rangle} \left[|r \langle \delta\Phi^{n+1} | \Phi_{avg} \rangle| + |(1-r) \langle \delta\Phi^n | \Phi_{avg} \rangle| \right. \\ &\quad \left. + \frac{1}{|\omega\Delta t|} \left(\langle \Phi_{avg} | \delta\Phi^{n+1} \rangle + \langle \Phi_{avg} | \delta\Phi^n \rangle \right) \right. \\ &\quad \left. + 2 \langle \Phi_{avg} | r\delta\Phi^{n+1} + (1-r)\delta\Phi^n \rangle \right] \end{aligned} \quad (2.72)$$

where the relation $|A + A^*| \leq 2|A|$ has been used to further bound the last term on the RHS. Assuming that $|\delta\Phi^n| \leq |\delta\Phi^{n+1}|$, the bound in the relative error becomes:

$$\frac{|\delta\omega|}{|\omega|} \leq \frac{|\langle \Phi_{avg} | \delta\Phi^{n+1} \rangle|}{|\langle \Phi_{avg} | \Phi_{avg} \rangle|} \left(3 + \frac{2}{|\omega\Delta t|} \right) \quad (2.73)$$

Substituting from Eq. (2.68) that $\Phi_{avg} = -\frac{1}{i\omega\Delta t} (\Phi^{n+1} - \Phi^n)$ and simplifying using the Cauchy-Schwarz inequality (i.e. $|\langle A | B \rangle| \leq |A||B|$), we obtain

$$\frac{|\delta\omega|}{|\omega|} \leq \frac{|\delta\Phi^{n+1}|}{|\Phi^{n+1} - \Phi^n|} (2 + 3|\omega\Delta t|) \quad (2.74)$$

Thus, in order to achieve an instantaneous relative error tolerance in ω (i.e. $\frac{|\delta\omega|}{|\omega|} \leq \omega_{tol}$), the relative error in the change in Φ must be below a certain threshold. If we iterate until the error $\delta\Phi^{n+1}$ is sufficiently small, i.e.

$$\frac{|\delta\Phi^{n+1}|}{|\Phi^{n+1} - \Phi^n|} < iter_tol \quad (2.75)$$

then the iteration error will not affect the frequency convergence (and will thus ensure that the iterative solver converges to the same frequency in the same number of time steps as the fully implicit solver) as long as we set $iter_tol < \omega_{tol}/4$ (assuming that $|\omega\Delta t| < 2/3$).

We can relate this bound to our approach of measuring the error in Φ as in Eq. (2.67), i.e. relative to Φ^{n+1} rather than to $(\Phi^{n+1} - \Phi^n)$. We can write the relative error convergence criterion in Eq. (2.75) as

$$\frac{|\Phi^{n+1,p+1} - \Phi^{n+1,p}|}{|\Phi^{n+1,p+1} - \Phi^n|} < iter_tol_rel \quad (2.76)$$

where `iter_tol_rel` denotes the iteration tolerance measured with respect to the relative error. Equivalently, this equation can be written as:

$$\frac{|\Phi^{n+1,p+1} - \Phi^{n+1,p}|}{|\Phi^{n+1,p}|} < (\text{iter_tol_rel}) \frac{|\Phi^{n+1,p+1} - \Phi^n|}{|\Phi^{n+1,p}|} \quad (2.77)$$

In our present approach (given by Eq. (2.67)), we require that the LHS be smaller than `iter_tol`. This is equivalent to Eq. (2.77) if we choose `iter_tol` equal to the RHS, i.e.

$$\text{iter_tol} = (\text{iter_tol_rel}) \frac{|\Phi^{n+1,p+1} - \Phi^n|}{|\Phi^{n+1,p}|} \quad (2.78)$$

Using Eq. (2.68) in the limit of small Δt , we can approximate this as

$$\text{iter_tol} = (\text{iter_tol_rel}) |\omega \Delta t| \quad (2.79)$$

which requires that `iter_tol` decrease as Δt decreases. Thus, considering a given `iter_tol_rel` as required to achieve a desired relative error in ω , when using the iteration convergence as defined by Eq. (2.67) one must use a smaller iteration tolerance because of the dependence on Δt ; even though, at larger Δt , `iter_tol` could have been larger and still ensured achieving the same ω as the fully implicit code. Overall, the effect of the quantity with respect to which the convergence is measured is a topic of future research. While this may improve performance, it does not effect the overall lack of robustness of the simple iteration scheme for large Δt with electromagnetic dynamics, since the number of iterations to achieve a constant `iter_tol` rises very rapidly with Δt above a certain threshold (such as in figure 2.22).

Referring back to the general results comparing the initializers in figures 2.21 and 2.22, the fact that the linear extrapolator performs better than the one-point extrapolator reflects its higher accuracy in determining the smooth modes in the system. However, the degradation in performance with the higher-order polynomial extrapolators due to the necessary smaller iteration tolerance may represent a competing effect between more accurately representing the smoother or well-resolved modes in the system yet more inaccurately representing the high frequency Nyquist modes in the system, which oscillate sign each time step and are not well resolved. To see this, consider the initial step relative error of the iteration:

$$(rel_err)_0 = \frac{|\Phi^{n+1,0} - \Phi^{n+1}|}{|\Phi^{n+1} - \Phi^n|} \quad (2.80)$$

With the one-point extrapolator, $(rel_err)_0 = 1$ and thus it may require many iterations to reduce the relative error down to the required `iter_tol`. Compare this with the initial step relative error using the two-point extrapolator:

$$(rel_err)_0 = \frac{|2\Phi^n - \Phi^{n-1} - \Phi^{n+1}|}{|\Phi^{n+1} - \Phi^n|} \quad (2.81)$$

We define the mode amplification factor for well-resolved modes as $A \equiv \frac{\Phi^{n+1}}{\Phi^n}$, which, from Eq. (2.68), we can write as $A = \frac{1-i\omega\Delta t(1-r)}{1+i\omega\Delta tr}$. Thus, in terms of A, Eq. (2.81) becomes

$$(rel_err)_0 = \left| \frac{A-1}{A} \right| = \frac{|\omega\Delta t|}{|1-i\omega\Delta t(1-r)|} \quad (2.82)$$

In the limit of small $|\omega\Delta t|$, $(rel_err)_0 \sim |\omega\Delta t| + O(|\omega\Delta t|^2)$, which is much smaller than the $(rel_err)_0$ of 1 found for the one-point initializer. Thus, for well-resolved modes, it is expected that the two-point initializer will converge more quickly than

the one-point initializer. (However, note that in the limit of very large $|\omega\Delta t|$, which we discuss below, $A \rightarrow -1$ and $(rel_err)_0 \rightarrow 2$, requiring many iterations). Similarly, we can show that the initial relative error of the three-point initializer is given by

$$(rel_err)_0 = \left| \frac{(A-1)^2}{A^2} \right| = \frac{|\omega\Delta t|^2}{|1 - i\omega\Delta t(1-r)|^2} \quad (2.83)$$

which, in the small $|\omega\Delta t|$ limit, varies as $|\omega\Delta t|^2 + O(|\omega\Delta t|^3)$, thus yielding an even faster convergence than the two-point initializer. These results agree with our simulation results of figures 2.21 and 2.22 which show that, for a given `iter_tol`, the number of iterations per time step decreases as the order of the polynomial of the initializer increases.

However, a problem occurs for the high frequency Nyquist modes which oscillate sign each time step. To see this, consider a high frequency mode for which $|\omega\Delta t| \gg 1$, so the centered implicit Beam-Warming algorithm gives Φ^n proportional to $(-1)^n$. Then the linear two-point initializer ($\Phi^{n+1,p=0} = 2\Phi^n - \Phi^{n-1}$) predicts $\Phi^{n+1,p=0} = 3$, which is 3 times the true value of $|\Phi^{n+1}| = 1$ for a Nyquist mode. Thus, the Nyquist modes are amplified by a factor of 3 for the two-point initializer and even higher by the higher-order polynomial initializers, e.g. by a factor of 7 for the three-point initializer and by a factor of 15 for the four-point initializer. (Only the one-point initializer does not amplify the Nyquist mode.) This means that choice of the optimum order of the initializer is then a competing effect between accurately predicting both the well-resolved modes and the poorly resolved high frequency modes. That is, there will always be some small component of errors in the high frequency modes, and one needs to ensure that these modes are not amplified so much by the initial predictor step that the increased number of iterations needed to reduce the error in the high frequencies offsets the reduction of iterations

needed for low frequency modes made possible by the improved prediction for low frequencies.

In the centered Beam-Warming algorithm, modes at the Nyquist limit in spatial frequency ($k_{\parallel}qR\Delta\theta = \pi$) will also be at the Nyquist limit in temporal frequency ($\omega\Delta t = \pi$). Thus, we can consider spatial smoothing of the initializer to improve performance. Specifically, we have also implemented a two-point initializer with spatial smoothing, defined as

$$\phi_j^{n+1,p=0} = 2 \left[\frac{(\Phi_{j-1}^n + 2\Phi_j^n + \Phi_{j+1}^n)}{4} \right] - \left[\frac{(\Phi_{j-1}^{n-1} + 2\Phi_j^{n-1} + \Phi_{j+1}^{n-1})}{4} \right] \quad (2.84)$$

This initializer is designed to vanish at the spatial Nyquist mode: using a spectral numerical analysis in the spatial dimension, i.e. $\Phi_j^n = \hat{\Phi}^n e^{ik_{\parallel}qR\theta_j}$, we find that $(\Phi_{j-1}^n + 2\Phi_j^n + \Phi_{j+1}^n)$ becomes $2\hat{\Phi}^n e^{ik_{\parallel}qR\theta_j} (1 + \cos(k_{\parallel}qR\Delta\theta))$, which vanishes for $k_{\parallel}qR\Delta\theta = \pi$.

Test cases with this initializer are also shown in figures 2.21 and 2.21. While the results do not show a significant difference in convergence compared with the standard two-point initializer in the electrostatic limit (showing slightly decreased performance at small time steps, though slightly enhanced performance at the largest time steps), for the case of $k_y\rho_i = 0.5$ with electromagnetic dynamics, we see that the spatial smoothing initializer is the only method which converges in a feasible number of gyrokinetic solves at large time steps (but it still failed for the case of $k_y\rho_i = 0.1$ if Δt is too large). While the Nyquist mode is one of the important high frequency modes in our system, it is not the only one (for example, our equations also contain electrostatic Alfvén waves which can be high frequency even at k_{\parallel} less than the maximum k_{\parallel} on the grid), and spatial smoothing will not help with

these modes. Thus, for all subsequent reported results, we use the standard linear two-point extrapolator as the initializer.

2.3.4 Iteration Schemes

Various iteration schemes were considered as the basis for our algorithm. In addition to simple iteration, which we found to be not robust with electromagnetic dynamics, these include more complex schemes, such as steepest descent as well as the Krylov-based solvers of conjugate gradient, bi-conjugate gradient stabilized (Bi-CGSTAB), and generalized minimal residual (GMRES). Below we first briefly summarize the general ideas behind these methods and then provide a general performance comparison using the test case parameters with the multiM (16,7) preconditioner and linear two-point initializer. Templates (or pseudo-code) of the algorithms discussed here can be found in Appendix B.

We consider solution of a general linear system of equations $M\vec{x}^{n+1} = -\vec{\rho}$, where M is a square nonsingular complex matrix. We will also be considering a transformed left preconditioned linear system given as

$$M_{approx}^{-1}M\vec{x}^{n+1} = -M_{approx}^{-1}\vec{\rho} \quad (2.85)$$

where M_{approx}^{-1} is the preconditioner, since a good preconditioner often aids with enhanced convergence in iterative schemes. We are particularly interested in “matrix-free” schemes, i.e. those for which the matrix M itself is never directly accessed. For problems such as solution of the gyrokinetic equations, M (and its conjugate transpose) is computationally expensive to compute, particularly since M is large and sparse. So we would like to avoid computing its elements and instead use a

scheme in which only implicit operations with M , such as the matrix-vector product of M with a generic vector \vec{v} , are needed.

We start with the simple iteration method as a basis for the iterative schemes that we will consider. With this method, we found that successive approximate iterative solutions follow a path given by

$$\vec{x}^{n+1,p+1} = \vec{x}^{n+1,p} + \lambda^{p+1} \vec{s}^{p+1} \quad (2.86)$$

where $\lambda = 1$ for each iteration p and the search direction \vec{s} is found from Eq. (2.40) to be

$$\vec{s}^{p+1} = M_{approx}^{-1} \vec{r}^p = M_{approx}^{-1} [-\vec{\rho} - M \vec{x}^{n+1,p}] \quad (2.87)$$

where \vec{r} is the error residual of the original unpreconditioned matrix system. Thus, the search direction is simply the error residual of our initial preconditioned matrix equation. Note that the residual itself can also be updated with respect to the search direction analogous to Eq. (2.86) as

$$\vec{r}^{p+1} = \vec{r}^p - \lambda^{p+1} M \vec{s}^{p+1} \quad (2.88)$$

Simple iteration is known as a type of stationary iterative method since the computations involved in finding the updated iterative solution do not involve information that changes at each iteration but rather basically only involve iterative refinement. Stationary methods are generally less complex and easier to implement than non-stationary methods, though non-stationary methods can be more effective. The other methods that we consider here are non-stationary methods.

Simple iteration can be thought of as basically an unnormalized steepest descent

method. The steepest descent method is based on the idea of moving from a point P^p with position vector $\vec{x}^{n+1,p}$ to a point P^{p+1} with position vector $\vec{x}^{n+1,p+1}$ by minimizing some scalar error residual function $f(\vec{x})$ along the line extending from P^p in the direction of the local downhill gradient $-\nabla f(P^p)$. Thus, successive approximate iterative solutions follow a path which uses the same search direction as simple iteration yet now with an optimal step size λ .

We define our scalar function with respect to the M^{-1} -norm of the error residual, i.e.

$$f(\vec{x}) \equiv \langle \vec{r} | M^{-1} \vec{r} \rangle \quad (2.89)$$

Note that this definition of $f(\vec{x})$ is equivalent to minimization of the M-norm of the true error, i.e. $\langle \vec{x}^{n+1,p+1} - \vec{x}^{n+1,*} | M (\vec{x}^{n+1,p+1} - \vec{x}^{n+1,*}) \rangle$, where $\vec{x}^{n+1,*} = -M^{-1} \vec{\rho}$ is the exact solution of the original matrix equation. In the steepest descent method, the optimal step size is obtained from the single parameter local minimization of $F(\lambda^{p+1}) = f(\vec{x}^{n+1,p} + \lambda^{p+1} \vec{s}^{p+1})$, i.e. via solution of

$$0 = \frac{dF}{d\lambda^{p+1}}(\vec{x}^{n+1,p+1}) = \left\langle \nabla f \left| \frac{\partial \vec{x}^{n+1,p+1}}{\partial \lambda^{p+1}} \right. \right\rangle(\vec{x}^{n+1,p+1}) \quad (2.90)$$

The solution of this equation then yields that

$$\lambda^{p+1} = \frac{\langle \vec{r}^p | \vec{s}^{p+1} \rangle}{\langle \vec{s}^{p+1} | M \vec{s}^{p+1} \rangle} = \frac{\langle \vec{r}^p | M_{approx}^{-1} \vec{r}^p \rangle}{\langle \vec{s}^{p+1} | M \vec{s}^{p+1} \rangle} \quad (2.91)$$

where we have used the assumption that M is Hermitian (i.e. $M = M^H$, where the superscript H denotes the conjugate transpose). Note that, with the Hermitian assumption, the direction of the downhill gradient at $\vec{x}^{n+1,p}$ is indeed in the direction of the error residual \vec{r}^p . Convergence is, of course, faster if the search direction is

closer to the actual error $(\vec{x}^{n+1,*} - \vec{x}^{n+1,p}) = M^{-1}\vec{r}^p$, so the search direction for the preconditioned system is instead chosen as in Eq. (2.87), since $M_{approx}^{-1} \approx M^{-1}$. Furthermore, the steepest descent algorithm in this form is generally applicable only to Hermitian matrices which are also positive definite (i.e. $\langle \vec{v} | M \vec{v} \rangle > 0$ for all nonzero vectors $\vec{v} \in C^n$) since it is then guaranteed that there exists a unique solution \vec{x}^* to the minimization of $f(\vec{x})$. This follows from the fact that, for a Hermitian matrix M , the Hessian $D^2 f(\vec{x})$ is M and thus, if M is also positive definite, then $f(\vec{x})$ is strictly convex.

The gyrokinetic response matrix is, however, not exactly a Hermitian matrix (though inspection of figures 2.12 and 2.14-2.15 shows that it is close to Hermitian, at least for these test case parameters). Although a modified steepest descent algorithm without the Hermitian assumption can be derived analogous with the above standard formulation, it turns out that this modified algorithm is then not “matrix-free”. Thus, a common alternative to the steepest descent method for use with non-Hermitian systems involves minimizing the L2-norm of the error residual rather than the M^{-1} -norm. This method yields an optimal step size of

$$\lambda^{p+1} = \frac{\langle \vec{s}^{p+1} | M \vec{r}^p \rangle}{\langle M \vec{s}^{p+1} | M \vec{s}^{p+1} \rangle} = \frac{\langle M_{approx}^{-1} \vec{r}^p | M \vec{r}^p \rangle}{\langle M \vec{s}^{p+1} | M \vec{s}^{p+1} \rangle} \quad (2.92)$$

which is independent of the conjugate transpose of M and for which the assumption that M is Hermitian is not necessary. However, with this minimization, the true direction of the downhill gradient is $M^H \vec{r}^{n+1,p+1}$, though the method is often applied using the error residual as the search direction since M^H is often unavailable. Thus, this method is not a true “steepest descent” method.

Here we will consider only implementation of the standard steepest descent

method, though, of course, without the Hermitian and positive definite properties, convergence is not guaranteed. It is still anticipated, however, that the steepest descent method as applied to our gyrokinetic system will be an improvement over simple iteration since it uses the same search direction but of a size based on information from previous iterations. But even for Hermitian positive definite systems, it should be noted that the steepest descent method often has the general disadvantage of relatively slow convergence, particularly for functions with long narrow valleys (for which the method yields a long zig-zag path to the bottom). So more complex iteration solvers, such as Krylov solvers, will also be explored.

Krylov solvers are often more robust than simple iteration and steepest descent methods. Rather than using a simple line-search, Krylov methods are projection methods based on the idea of constructing an approximate solution by projecting onto an expanding set of Krylov subspaces $K_m(M, \vec{v}) \equiv \text{span}\{v, Mv, \dots, M^{m-1}v\}$ and then minimizing over those subspaces. For an N-dimensional matrix problem, the exact solution can be obtained after N steps since the Krylov subspaces have then expanded to fill the entire domain.

The simplest Krylov solver is the conjugate gradient method [HESTENES and STIEFEL, 1952]. This method is based on the idea of minimizing along a set of conjugate directions (from the Krylov subspace), rather than along the local gradient. It thus has better convergence properties than the steepest gradient algorithm, particularly for functions with long narrow valleys. However, like the steepest descent method, the standard “matrix-free” conjugate gradient method which we will describe is based on the assumption that M is a Hermitian matrix. For the conjugate gradient method, λ is still chosen as before, to minimize the scalar function $f(\vec{x})$, but now the new search direction is chosen so that the solution

remains optimal relative to all previous search directions. Specifically, the search directions are updated as

$$\vec{s}^{p+1} = M_{approx}^{-1} \vec{r}^p + \beta^p \vec{s}^p \quad (2.93)$$

where β^p is chosen such that the search directions are M-conjugate (i.e. $\langle \vec{s}^i | M \vec{s}^j \rangle = 0$, $i \neq j$). Note that this is equivalent to the residuals being M_{approx}^{-1} conjugate, or $\langle \vec{r}^i | M_{approx}^{-1} \vec{r}^j \rangle = 0$, $i \neq j$. Thus, we find that

$$\lambda^{p+1} = \frac{\langle \vec{r}^p | M_{approx}^{-1} \vec{r}^p \rangle}{\langle \vec{s}^{p+1} | M \vec{s}^{p+1} \rangle} \quad (2.94)$$

$$\beta^p = \frac{\langle \vec{r}^p | M_{approx}^{-1} \vec{r}^p \rangle}{\langle \vec{r}^{p-1} | M_{approx}^{-1} \vec{r}^{p-1} \rangle} \quad (2.95)$$

As for the steepest descent method which also minimizes $f(\vec{x})$, the conjugate gradient algorithm is generally applicable only to Hermitian matrices which are also positive definite. In this case, it can easily be shown that the search directions \vec{s}^i are linearly independent and thus $\{\vec{s}^0, \dots, \vec{s}^{N-1}\}$ spans C^N and the conjugate gradient algorithm is guaranteed to converge in at most N steps. Relating the conjugate gradient algorithm as a Krylov solver, it can be shown via induction [GOLUB and VAN LOAN, 1983] that

$$\begin{aligned} span\{\vec{s}^1, \dots, \vec{s}^{p+1}\} &= span\{M_{approx}^{-1} \vec{r}^0, \dots, M_{approx}^{-1} \vec{r}^p\} \\ &= span\{M_{approx}^{-1} \vec{r}^0, (M_{approx}^{-1} M) M_{approx}^{-1} \vec{r}^0, \\ &\quad \dots, (M_{approx}^{-1} M)^p M_{approx}^{-1} \vec{r}^0\} \\ &\equiv K_{p+1} \left(M_{approx}^{-1} M, M_{approx}^{-1} \vec{r}^0 \right) \end{aligned} \quad (2.96)$$

Thus, the conjugate gradient algorithm overall constructs the solution at the $(p+1)$ -th iterate as the vector from the Krylov subspace K_{p+1} which minimizes the M-norm of the true error. An important property of the conjugate gradient algorithm (compared, in particular, with the GMRES algorithm discussed below) is that it does not require storage of the Krylov basis vectors and thus has overall minimal storage requirements. Implementation of the steepest descent and conjugate gradient algorithms in GS2 follows the template in [BARRETT *et al.*, 1994].

The methods of bi-conjugate gradient stabilized (Bi-CGSTAB) [VAN DER VORST, 1992] and generalized minimal residual (GMRES) [SAAD and SCHULTZ, 1986] are designed to work better for non-Hermitian matrices. Instead of requiring minimization along conjugate directions, GMRES minimizes the residual in a Krylov subspace, i.e. by requiring $\bar{x}^{n+1,p+1}$ to minimize the L2-norm of the error residual $\bar{r}^{p+1} = -\bar{\rho} - M\bar{x}^{n+1,p+1}$ for every $\bar{x}^{n+1,p+1}$ in $\bar{x}^{n+1,0} + K_{p+1}$. This is done by first constructing an orthonormal basis $\{\vec{v}_1, \vec{v}_2, \dots, \vec{v}_{p+1}\}$ for the Krylov subspace K_{p+1} using the Arnoldi process [ARNOLDI, 1951]. Then any $\vec{z} \in K_{p+1}$ can be written as $\vec{z} = \sum_{i=1}^{p+1} y_i \vec{v}_i$. Thus the iterative solution can be constructed as $\bar{x}^{n+1,p+1} = \bar{x}^{n+1,0} + \vec{z}$ where the coefficient vector \vec{y} minimizes $\|\bar{r}^{p+1}\|_2$ and is thus the solution of the least squares problem

$$\min_{\vec{y} \in C^{p+1}} \left\| \bar{r}^0 - MV^{p+1}\vec{y} \right\|_2 \quad (2.97)$$

where the matrix $V^{p+1} = [\vec{v}_1 \vec{v}_2 \dots \vec{v}_{p+1}]$. (The advantage of the Arnoldi process is that, by using a Gram-Schmidt procedure for formation of the orthonormal basis, the least squares problem of Eq. (2.97) can be represented more efficiently such that no additional matrix-vector products are required.) Though GMRES converges in

at most N steps even for non-Hermitian matrices, the primary disadvantage is the large storage requirements, since the basis for the Krylov space must be stored at each iteration and thus storage costs (and the computational work) increase linearly as N increases. In practice, GMRES is then restarted: if the solution has not converged after m iterations, then the algorithm is restarted using the initial guess $\bar{x}^{n+1,0} = \bar{x}^{n+1,m}$. However, GMRES(m) is not guaranteed to converge. For general m , the restarted method can stagnate, though if $(M + M^H)/2$ is positive definite, it can be proved that GMRES(m) converges for any $m \geq 1$ [SAAD, 2003]. We will explore the effects of restart for our test case gyrokinetic problem. Implementation of the GMRES method in GS2 uses a modification of the package of [FRAYSSE *et al.*, 2003].

The Bi-CGSTAB algorithm is based on Lanczos bi-orthogonalization as an extension of the Bi-CG algorithm [FLETCHER, 1975]. Bi-CG is basically a generalization of the conjugate gradient algorithm for non-Hermitian systems which creates two sequences of residuals: one for the residual of M (as does the conjugate gradient algorithm) and also one for the residual of M^H . Rather than enforcing a minimization requirement, bi-orthogonality is enforced between the residuals and bi-conjugacy is enforced between the search directions. Thus, for the iterative solution $\bar{x}^{n+1,p+1} = \bar{x}^{n+1,p} + \lambda^{p+1} \bar{s}^{p+1}$, the residuals are updated as

$$\begin{aligned} \bar{r}^{p+1} &= \bar{r}^p - \lambda^{p+1} M \bar{s}^{p+1} \\ \bar{v}^{p+1} &= \bar{v}^p - \lambda^{p+1} M^H \bar{t}^{p+1} \end{aligned} \tag{2.98}$$

where the search directions are updated as

$$\begin{aligned}\bar{s}^{p+1} &= M_{approx}^{-1} \bar{r}^p + \beta^p \bar{s}^p \\ \bar{t}^{p+1} &= M_{approx}^{-H} \bar{v}^p + \beta^p \bar{t}^p\end{aligned}\tag{2.99}$$

By enforcing the bi-orthogonality condition ($\langle M_{approx}^{-1} \bar{r}^i | \bar{v}^j \rangle = 0, i \neq j$) and the bi-conjugacy condition ($\langle \bar{t}^i | M \bar{s}^j \rangle = 0, i \neq j$), we find that

$$\lambda^{p+1} = \frac{\langle M_{approx}^{-1} \bar{r}^p | \bar{v}^p \rangle}{\langle \bar{t}^{p+1} | M \bar{s}^{p+1} \rangle}\tag{2.100}$$

$$\beta^p = \frac{\langle M_{approx}^{-1} \bar{r}^p | \bar{v}^p \rangle}{\langle M_{approx}^{-1} \bar{r}^{p-1} | \bar{v}^{p-1} \rangle}\tag{2.101}$$

This algorithm is not used in practice, however, because, not only does it require knowing the Hermitian conjugate, but it also exhibits erratic behavior. Bi-CGSTAB is thus an improvement of the Bi-CG algorithm. Representing the residuals as generic polynomial sequences, note that Bi-CG generates the sequences

$$\begin{aligned}\bar{r}^p &= \mathcal{P}^p(M) \bar{r}^0 \\ \bar{v}^p &= \mathcal{P}^p(M^H) \bar{v}^0\end{aligned}\tag{2.102}$$

where choice of \bar{v}^0 is arbitrary and generally $\bar{v}^0 = \bar{r}^0$ is chosen. Bi-CGSTAB instead generates the second residual sequence as

$$\bar{v}^p = \mathcal{Q}^p(M) \mathcal{P}^p(M) \bar{r}^0\tag{2.103}$$

where

$$\mathcal{Q}^{p+1}(M) = \prod_{i=1}^p (1 - \omega_i M) \quad (2.104)$$

and ω_i is chosen to minimize \bar{v}^p . (Bi-CGSTAB actually builds on the conjugate gradient squared algorithm [SONNEVELD, 1989] which is based on the idea of constructing $\bar{v}^p = \mathcal{P}^2(M)\bar{r}^0$, yet which can be even more irregular than Bi-CG.) Overall, Bi-CGSTAB can be thought of as a blend of Bi-CG and repeatedly applied GMRES(1) [BARRETT *et al.*, 1994]. Implementation of Bi-CGSTAB in GS2 follows the template in [BARRETT *et al.*, 1994].

Use of these solvers as applied to our general left-preconditioned matrix problem requires implementation of four basic operations:

- matrix-vector multiplication: $\vec{z} \leftarrow M\vec{v}$
- inner product operations: $\alpha \leftarrow \langle \vec{v} | \vec{w} \rangle$
- left preconditioning operations: $\vec{z} \leftarrow M_{approx}^{-1}\vec{v}$
- vector updates: $\vec{z} \leftarrow \alpha\vec{v} + \vec{w}$

Table 2.4 gives a comparison of the computational work per iteration and storage requirements for the various iteration schemes as corresponding to the standard implementations outlined in the templates in Appendix B. Note that for GMRES, the computational operations and storage increase as more iterations are done. Matrix-vector products are generally the most expensive operations, though each algorithm is required to do one per iteration (plus an additional one to compute the initial residual $\bar{r}^0 = -\bar{\rho} - M\bar{x}^{n+1,0}$ given an initial guess $\bar{x}^{n+1,0}$). Though the table shows that Bi-CGSTAB requires 2 matrix-vector multiplications per iteration, note that the Bi-CGSTAB algorithm has two stopping conditions such that, upon

Iterative Scheme	$\vec{z} \leftarrow M\vec{v}$	$\alpha \leftarrow \langle \vec{v} \vec{w} \rangle$	$\vec{z} \leftarrow M_{approx}^{-1}\vec{v}$	$\vec{z} \leftarrow \alpha\vec{v} + \vec{w}$	storage
Simple Iteration	1	0	1	2	M+4V
Steepest Descent	1	2	1	2	M+5V
Conjugate Gradient	1	2	1	3	M+6V
Bi-CG STAB	2	4	2	6	M+10V
GMRES	1	p+1	1	p+1	M+(p+5)V

Table 2.4: Computational requirements per iteration for various iterative schemes. The last column gives the storage requirements in terms of the number of $N \times N$ matrices (M) (which may be sparse and thus require much less than N^2 storage) and the number of $N \times 1$ vectors (V).

convergence, some final operations (including 1 matrix-vector multiplication) may be eliminated on the final iteration. But, of course, the effect of this on the total computational work is trivial unless the total number of iterations for convergence is very small. It is also notable from the table that simple iteration does significantly less total operations than Bi-CGSTAB and GMRES. This suggests that, with a good enough preconditioner to ensure convergence in a moderate number of total iterations, the low overhead of simple iteration could make it a more feasible and efficient choice than the more complex Krylov solvers.

As noted previously, the matrix-vector multiplication must be defined implicitly since the elements of M are not computed in our iterative scheme. Here we show how this is defined for our gyrokinetic equations. Recall that our field equations are given by Eqs. (2.14) and (2.15) using Eqs. (2.16) and (2.17) for the RHS charge and current densities. Introducing an intermediate vector $(\hat{\Phi}^{n+1}, \hat{A}_{\parallel}^{n+1})$ into the

latter two equations, we can write that:

$$\begin{aligned} \begin{bmatrix} \rho_{dens} [\Phi^{n+1}, A_{\parallel}^{n+1}] \\ \rho_{curr} [\Phi^{n+1}, A_{\parallel}^{n+1}] \end{bmatrix} &= \begin{bmatrix} \rho_{dens} [\hat{\Phi}^{n+1}, \hat{A}_{\parallel}^{n+1}] \\ \rho_{curr} [\hat{\Phi}^{n+1}, \hat{A}_{\parallel}^{n+1}] \end{bmatrix} \\ &+ \begin{bmatrix} M^1 & M^2 \\ M^3 & M^4 \end{bmatrix} \begin{bmatrix} \Phi^{n+1} - \hat{\Phi}^{n+1} \\ A_{\parallel}^{n+1} - \hat{A}_{\parallel}^{n+1} \end{bmatrix} \end{aligned} \quad (2.105)$$

Substituting this into the Poisson-Ampere equations of Eqs. (2.14) and (2.15), we find that

$$\begin{aligned} \begin{bmatrix} M_{GS2}^1 & M_{GS2}^2 \\ M_{GS2}^3 & M_{GS2}^4 \end{bmatrix} \begin{bmatrix} \Phi^{n+1} - \hat{\Phi}^{n+1} \\ A_{\parallel}^{n+1} - \hat{A}_{\parallel}^{n+1} \end{bmatrix} &= - \begin{bmatrix} \rho_{dens} [\hat{\Phi}^{n+1}, \hat{A}_{\parallel}^{n+1}] \\ \rho_{curr} [\hat{\Phi}^{n+1}, \hat{A}_{\parallel}^{n+1}] \end{bmatrix} \\ &+ C \begin{bmatrix} \hat{\Phi}^{n+1} \\ \hat{A}_{\parallel}^{n+1} \end{bmatrix} \end{aligned} \quad (2.106)$$

where

$$C \equiv \begin{bmatrix} \sum_s \frac{n_{0s} e^2 Z_s^2}{T_{0s}} (1 - \Gamma_0(b_s)) & 0 \\ 0 & \frac{c}{4\pi} k_{\perp}^2 \end{bmatrix} \quad (2.107)$$

and M_{GS2} is defined in Appendix A as the response matrix as implemented in GS2. Eq. (2.106) is thus the equivalent of the desired form $M\vec{x}^{n+1} = -\vec{\rho}$ with $M \rightarrow M_{GS2}$, $\vec{x} \rightarrow (\Phi - \hat{\Phi}, A_{\parallel} - \hat{A}_{\parallel})$ and $-\vec{\rho}$ equal to the RHS. To determine the matrix-vector product of M_{GS2} with a generic vector \vec{v} , we manipulate the second term on the RHS as follows:

$$C \begin{bmatrix} \hat{\Phi}^{n+1} \\ \hat{A}_{\parallel}^{n+1} \end{bmatrix} = C \begin{bmatrix} \Phi^{n+1} \\ A_{\parallel}^{n+1} \end{bmatrix} - C \begin{bmatrix} \Phi^{n+1} - \hat{\Phi}^{n+1} \\ A_{\parallel}^{n+1} - \hat{A}_{\parallel}^{n+1} \end{bmatrix}$$

$$\begin{aligned}
&= \begin{bmatrix} \rho_{dens} [\Phi^{n+1}, A_{\parallel}^{n+1}] \\ \rho_{curr} [\Phi^{n+1}, A_{\parallel}^{n+1}] \end{bmatrix} - C \begin{bmatrix} \Phi^{n+1} - \hat{\Phi}^{n+1} \\ A_{\parallel}^{n+1} - \hat{A}_{\parallel}^{n+1} \end{bmatrix} \\
&= \begin{bmatrix} \rho_{dens} [(\Phi^{n+1} - \hat{\Phi}^{n+1}) + \hat{\Phi}^{n+1}, (A_{\parallel}^{n+1} - \hat{A}_{\parallel}^{n+1})\hat{A}_{\parallel}^{n+1}] \\ \rho_{curr} [(\Phi^{n+1} - \hat{\Phi}^{n+1}) + \hat{\Phi}^{n+1}, (A_{\parallel}^{n+1} - \hat{A}_{\parallel}^{n+1})\hat{A}_{\parallel}^{n+1}] \end{bmatrix} \\
&\quad - C \begin{bmatrix} \Phi^{n+1} - \hat{\Phi}^{n+1} \\ A_{\parallel}^{n+1} - \hat{A}_{\parallel}^{n+1} \end{bmatrix} \tag{2.108}
\end{aligned}$$

Combining this with Eq. (2.106), we find that the matrix-vector product is defined as

$$\begin{aligned}
M_{GS2}\vec{v} &= - \begin{bmatrix} \rho_{dens} [\hat{\Phi}^{n+1}, \hat{A}_{\parallel}^{n+1}] \\ \rho_{curr} [\hat{\Phi}^{n+1}, \hat{A}_{\parallel}^{n+1}] \end{bmatrix} \\
&\quad + \begin{bmatrix} \rho_{dens} [v_{\Phi} + \hat{\Phi}^{n+1}, v_{A_{\parallel}} + \hat{A}_{\parallel}^{n+1}] \\ \rho_{curr} [v_{\Phi} + \hat{\Phi}^{n+1}, v_{A_{\parallel}} + \hat{A}_{\parallel}^{n+1}] \end{bmatrix} - C \begin{bmatrix} v_{\Phi} \\ v_{A_{\parallel}} \end{bmatrix} \tag{2.109}
\end{aligned}$$

In our implementation, we arbitrarily choose $(\hat{\Phi}^{n+1}, \hat{A}_{\parallel}^{n+1}) = (\Phi^{n+1,0}, A_{\parallel}^{n+1,0})$ as the intermediate vector. (Thus, our initial guess is $\vec{x}^{n+1,0} = \vec{0}$.) Note that the introduction of this intermediate vector eliminates the need for the computation of the inhomogeneous solution by basically replacing it with the initial guess computation. Recall from Eqs. (2.6) and (2.7) that computation of $\rho_{dens} [\Phi^*, A_{\parallel}^*]$ and $\rho_{curr} [\Phi^*, A_{\parallel}^*]$ involves velocity-space integrations of the distribution function $f^{n+1,*}$ obtained from solution of the gyrokinetic equation using f^n , Φ^n , A_{\parallel}^n , $\Phi^{n+1} = \Phi^*$, and $A_{\parallel}^{n+1} = A_{\parallel}^*$. Thus, assuming that the charge and current densities of the initial guess are stored, each matrix-vector multiplication in the iterative algorithm involves one solution of the gyrokinetic equation (and its velocity-space integrations). Matrix-vector products are thus computationally expensive since the efficiency of

the iterative schemes is ultimately measured with respect to the total number of gyrokinetic solves per time step.

Note that, for the test case results, the reported average number of gyrokinetic solves per time step includes those from matrix-vector multiplications performed within the iteration loop as well as gyrokinetic solves involved in the initialization and finalization of the iteration. Specifically, as noted previously, each of the iterative schemes which we consider also requires a matrix-vector product to compute the initial residual from the initial guess. In addition, a gyrokinetic solve is also required upon completion of the iteration for each time step to compute the distribution function f^{n+1} corresponding to the converged solution $(\Phi^{n+1}, A_{\parallel}^{n+1})$.

The exception, however, is with the implementation of the simple iteration only, for which we do not perform a final gyrokinetic solve since we measure convergence with respect to $\bar{x}^{n+1,p+1}$ rather than \bar{r}^{p+1} . Referring to the template in Appendix B, the matrix-vector product involved in the update of the residual is needed only for the next iteration. Thus, in our actual implementation, the $(p+1)$ -th residual is not computed until after the convergence of $\bar{x}^{n+1,p+1}$ is determined. Unlike the other iterative schemes in which the final matrix-vector product performed before the convergence check is done with an intermediate quantity, that with simple iteration is performed with $\bar{x}^{n+1,p}$ and thus the last-computed distribution function at convergence of $\bar{x}^{p_{final}+1}$ is directly $f^{n+1,p_{final}}$, which we thus use as the approximate solution for f^{n+1} . Note then that, with this implementation, the residual can be considered as computed at the beginning of the iteration loop, so the simple iteration does not have an “additional” pre-iteration matrix-vector multiplication either. Thus, simple iteration only performs as many gyrokinetic solves as iterations.

Figures 2.23 and 2.24 show the results for simulations with the test case parameters comparing implementation of the various iterative schemes in GS2. These simulations use the linear two-point extrapolation initializer and multiM (16,7) preconditioner. The GMRES results shown in these figures do not use restart. Also, note that all of the schemes except GMRES are implemented using the convergence criterion with respect to the field vector as given in Eq. (2.67). The GMRES package of [FRAYSSE *et al.*, 2003] has its own built-in criterion that is rather based on the L2-norm of the residual, given with the default parameters as $\|M_{approx}^{-1} \vec{r}^{p+1}\|_2 / \|M_{approx}^{-1} \vec{\rho}\|_2 < (iter_tol)$. It is first required that this criterion is satisfied with respect to the computed residual and then, afterwards, with respect to the true residual (i.e. $M_{approx}^{-1} (-\vec{\rho} - M\vec{x}^{n+1,p+1})$) to account for finite precision arithmetic errors in the computed residual from the Arnoldi process. This is shown in the template in Appendix B. For the GMRES simulations, $iter_tol/\omega_tol = 10$ is used, as empirically found to be sufficient to ensure that the iteration convergence does not affect the ω convergence. Recall that this latter criterion was also used to choose $iter_tol/\omega_tol = 1/4$ for the other iterative schemes, which use Eq. (2.67) as the stopping criterion.

Overall, figures 2.23 and 2.24 show that simple iteration performs quite well (i.e. even better than the more complex Krylov solvers) for small to moderate time steps in the electrostatic limit and for sufficiently small time steps with electromagnetic dynamics. This is primarily due to the low overhead of simple iteration: specifically, the two additional initialization and finalization gyrokinetic solves required for the more complex algorithms are relatively significant when the number of iterations is small. At larger time steps, the figures show that the conjugate gradient algorithm diverges more quickly than the other algorithms. In fact, the

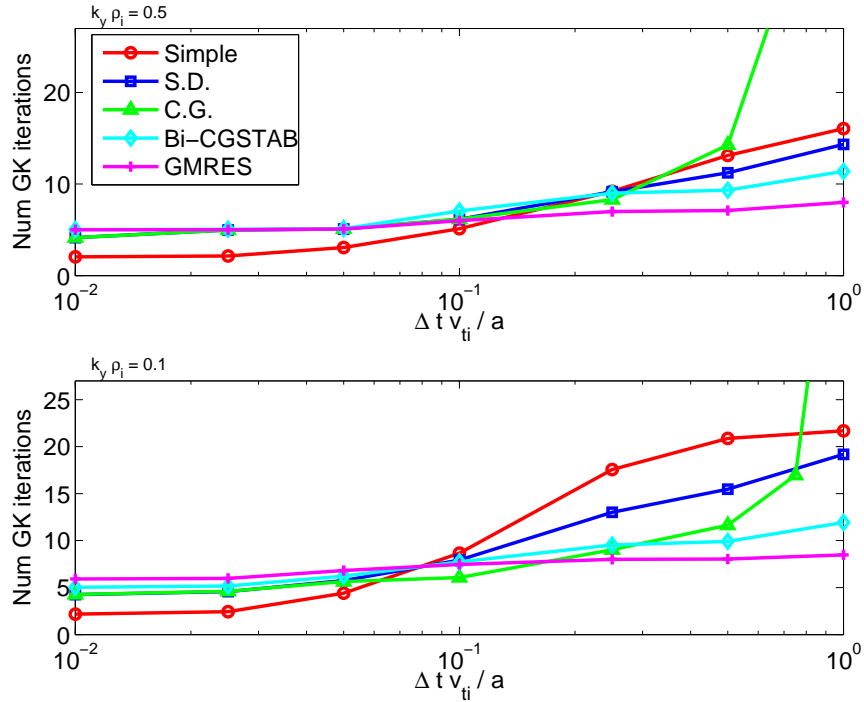


Figure 2.23: Average number of gyrokinetic solves per time step for test case parameters in the electrostatic limit using an iterative implicit scheme with a linear two-point extrapolator initializer and multiM (16,7) preconditioner and comparing iteration schemes.

conjugate gradient algorithm fails to converge within the maximum allowable iterations for even the smallest time steps in the electromagnetic cases. This is not entirely surprising since the theoretical basis behind the derivation of this algorithm was not applicable for non-Hermitian systems. Although this is also true for the steepest descent algorithm, its performance was better than the conjugate gradient algorithm. The steepest descent algorithm, which basically attempts a correction of the simple iteration algorithm search directions, performs similar to the simple iteration algorithm for these test cases, yielding slightly better convergence at larger time steps for the electrostatic cases and a slightly larger time step limit for the electromagnetic cases.

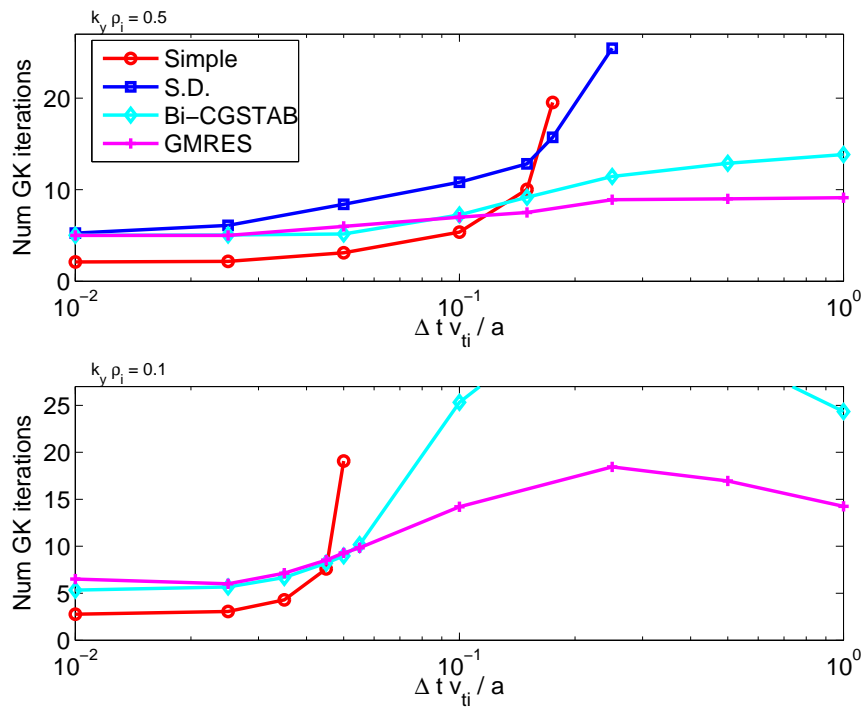


Figure 2.24: Average number of gyrokinetic solves per time step for test case parameters with electromagnetic dynamics ($\beta = 1.0 \times 10^{-3}$) using an iterative implicit scheme with a linear two-point extrapolator initializer and multiM (16,7) preconditioner and comparing iteration schemes.

While simple iteration or steepest descent may be useful for electrostatic simulations (since the typical time step for a nonlinear GS2 simulation is $\Delta tv_{ti}/a \sim 0.01 - 0.1$), figure 2.24 ultimately shows that the more robust Krylov solvers are necessary for larger time steps with electromagnetic dynamics. This may be particularly true for nonlinear electromagnetic runs, in which there is a wide range of $k_{\perp}\rho_i$ modes, with the smallest resolved $k_{\perp}\rho_i$ usually less than 0.1. (Recall from figure 2.20 and the corresponding empirical scaling in Eq. (2.64) that the time step limitation for electromagnetic cases for the simple iteration algorithm becomes more severe as $k_y\rho_i$ decreases). Comparing Bi-CGSTAB and GMRES, differences in performance are trivial in the electrostatic limit and with electromagnetic dynamics, except for the $k_y\rho_i = 0.1$ electromagnetic case at large time steps. For this case, the largest difference in iterations for the range of time step widths tested occurs at $\Delta tv_{ti}/a = 0.25$, for which Bi-CGSTAB does ~ 38 GK solves per time step while GMRES which does ~ 18 . However, recall from table 2.4 that, at these large iteration numbers, GMRES requires about twice as much vector storage. (GMRES is also doing a larger amount of work in the other computational operations (for example, ~ 189 total inner products per time step compared with ~ 152 for Bi-CGSTAB), but this work is negligible compared to the gyrokinetic solves.) For a moderate number of iterations, storage requirements are not a significant concern for our gyrokinetic problem since it applies to the 3D field vectors rather than the 5D distribution function. However, for large nonlinear simulations with many (k_x , k_y) modes, the extra storage required for GMRES may not be practical.

Thus, we also consider GMRES(m), the results of which are shown in figures 2.25 and 2.26. In the electrostatic limit at $k_y\rho_i = 0.5$, GMRES(1) performs as well as GMRES(N) even at the largest time steps. A slight decrease in performance is seen

for $k_y \rho_i = 0.1$ at large time steps for $m=1$; though, the performance of GMRES(4) is nearly identical to that of GMRES(N). However, for these electrostatic results, the number of iterations is very small overall and does not increase much with Δt . In contrast, with electromagnetic dynamics, GMRES(1) diverges even at $k_y \rho_i = 0.5$. Furthermore, for the more difficult case of $k_y \rho_i = 0.1$, even GMRES(4) diverges. (Note that only GMRES(N) is guaranteed to converge.) These results amplify the significance of the Bi-CGSTAB convergence since, as can be seen in the template for the algorithm in Appendix B, Bi-CGSTAB is not generally guaranteed to converge. Also, the results for Bi-CGSTAB are surprising in this context since, as we noted previously, the Bi-CGSTAB algorithm is related to GMRES(1).

Overall, the choice of an optimal algorithm for Eulerian gyrokinetic simulations will of course depend on the circumstances, such as the time step and simulation size requirements set by the nonlinear turbulence, and on how often the time step might be changed or how often the response matrices have to be recalculated to handle time-dependent shearing of the grid if a large-scale equilibrium ExB flow is included. For moderate size nonlinear simulations that do not go to very low $k_\perp \rho_i$, and/or for simulations where the time step does not need to change very often, the original fully implicit algorithm of GS2 might be best. Otherwise, in some cases simple iteration with a somewhat small time step will work, while the GMRES iterative solver (or Bi-CGSTAB iterative solver if there is limited memory storage) might provide the most robust alternative to the fully implicit algorithm.

Future work might explore how to modify the GMRES algorithm so that it can converge in a minimum of two gyrokinetic solves and thus be competitive with simple iteration for a sufficiently small time step (and/or a sufficiently good preconditioner) while also being more robust than simple iteration for large time steps.

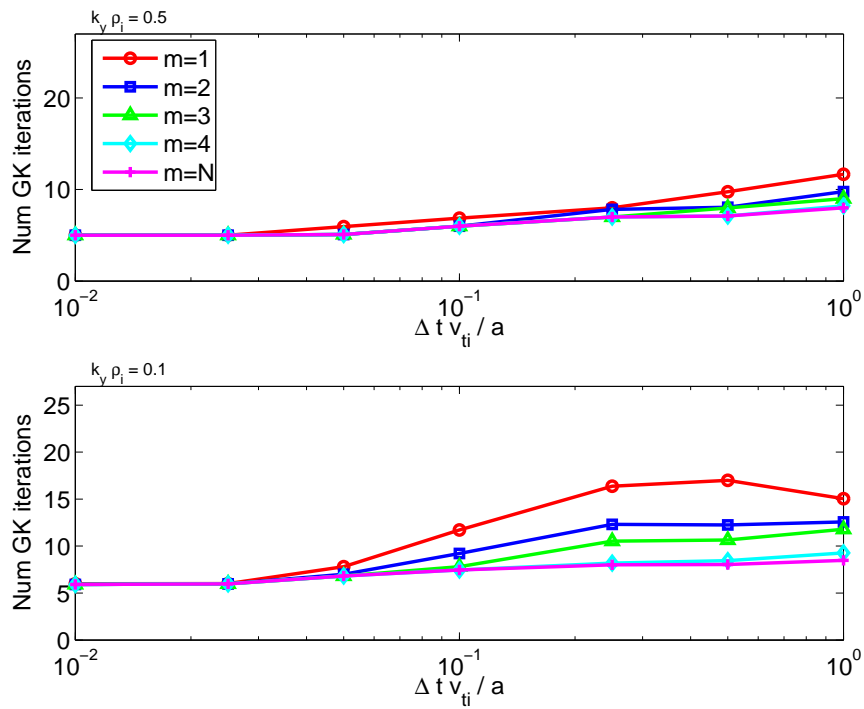


Figure 2.25: Average number of gyrokinetic solves per time step for test case parameters in the electrostatic limit using an iterative implicit scheme with a linear two-point extrapolator initializer, multiM (16,7) preconditioner, and GMRES iterative scheme comparing the restart parameter m . Note the $m=N$, where N is the total size of the field vector, corresponds to no restart.

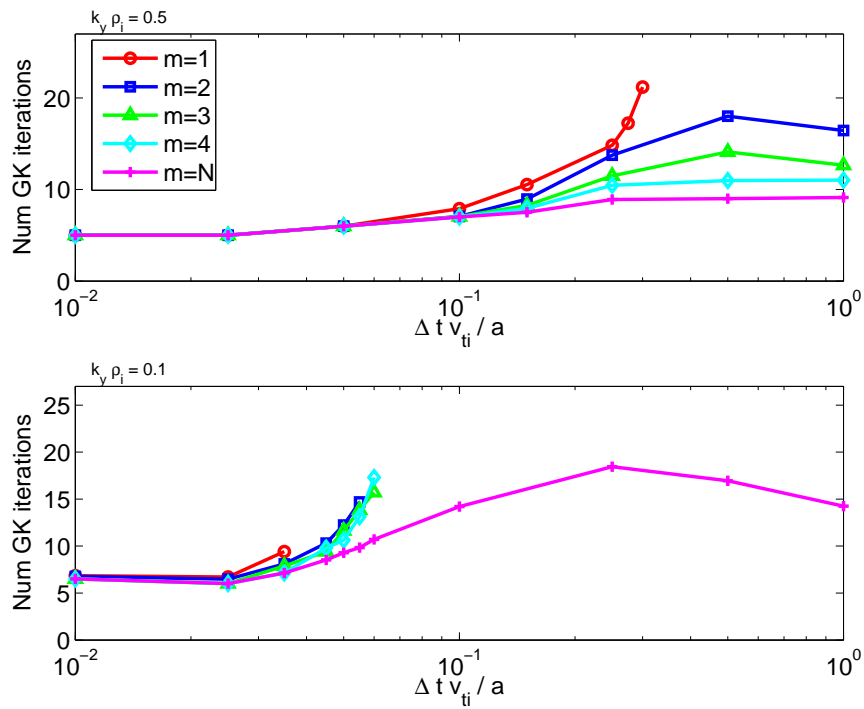


Figure 2.26: Average number of gyrokinetic solves per time step for test case parameters with electromagnetic dynamics ($\beta = 1.0 \times 10^{-3}$) using an iterative implicit scheme with a linear two-point extrapolator initializer, multiM (16,7) preconditioner, and GMRES iterative scheme comparing the restart parameter m . Note that $m=N$, where N is the total size of the field vector, corresponds to no restart.

Specifically, this would require modification of the iteration tolerance stopping criterion of the GMRES algorithm (as implemented in the package of [FRAYSSE *et al.*, 2003]; see Appendix B) to skip the extra calculation of the true residual and instead rely on just the Arnoldi-computed residual, which should be sufficient if it converges in just a few iterations. Another necessary modification would be to store the distribution function f corresponding to the evaluation of $\omega_1 = M^{-1}Av_1$ for the first evaluation of the “For j” loop in line 6 of Appendix B in constructing the basis using the Arnoldi process. At present, an extra evaluation of the gyrokinetic equation is required once the optimal step size y is determined on line 16 of the algorithm, while this could be avoided at the expense of some additional storage.

2.4 Summary

Several numerical algorithms for Eulerian gyrokinetic codes were explored. For this study, we have focused on the framework of the flux tube-based GS2 code, which employs a fully implicit treatment of the linear dynamics. A semi implicit-explicit scheme which uses an explicit treatment of the linear field dynamics combined with GS2’s 2nd order compact differencing (which leads to between-grid spatial averaging of the $\frac{\partial f}{\partial t}$ term) was found to be numerically unstable at the Nyquist limit. However, with upwinding, a stable regime was found for the case of adiabatic electrons using a forward Euler scheme. While a two-step predictor-corrector scheme is stable for the case of adiabatic electrons even in the absence of upwinding, both the single-step and two-step schemes are numerically unstable upon inclusion of gyrokinetic electrons.

Thus, we have focused on developing an iterative implicit scheme based on numerical approximations of the plasma response. This method reduces the long time needed to set-up implicit arrays, yet still has larger time step advantages similar to a fully implicit method. Various model preconditioners, iteration initializers, and iteration schemes were studied via implementation within the framework of GS2. A numerical preconditioner was developed based on computing the response of simultaneously applied perturbations and refining the tail end of the response using an extrapolation with the translation of a single exact response row. While this numerical preconditioner with a simple iteration algorithm works fairly well for both the electrostatic limit and the more general electromagnetic case with a sufficiently small time step due to its low overhead, more robust Krylov solvers such as Bi-CGSTAB and GMRES (without restart) are necessary with electromagnetic dynamics for large time steps. Note that although the test cases for developing these algorithms focused on linear gyrokinetic dynamics, they are easily applicable to nonlinear gyrokinetic simulations, particularly with codes like GS2 in which the nonlinear term is treated explicitly, so the implicitness applies only to the linear dynamics anyways. This as well as extension of the algorithm to more global Eulerian codes such as GYRO are topics of future research.

The original fully implicit algorithm of GS2 is absolutely stable for arbitrarily large time step, but requires $N_{fields}N_{\theta per 2\pi}N_{connect} \sim 10^3$ evaluations (see section 2.1.1 for definitions of these parameters) of the gyrokinetic equation to initialize the plasma response matrix M . In comparison, the multiM method which we develop here calculates an approximate plasma response matrix with only $N_{fields}(n_{stride} + 1) \sim 50$ evaluations of the gyrokinetic equation, and thus speeds up the initialization process by a factor of 20. This speed-up may be partially offset by the additional

iterations required for later gyrokinetic solves (for example, see figures 2.23 and 2.24), but if the time step is sufficiently small anyways (due to the nonlinear Courant limit), then simple iteration with the multiM preconditioner converges as quickly as with the exact response matrix.

It might be possible that the advantages of the iterative implicit algorithms studied here would be larger (requiring fewer iterations or allowing larger time steps) if GS2's finite differencing algorithm for the spatial derivative was upgraded from its present usage of Beam-Warming 2nd order compact finite differencing. While this choice of spatial differencing has the advantage of leading to a fully implicit algorithm that needs only a relatively simple bi-diagonal matrix inversion to advance the distribution function, it introduces a high frequency Nyquist mode in the system with $k_{\parallel}qR\Delta\theta = \pi$ and $\omega\Delta t = \pi$. This may be limiting the effectiveness of the implicit iterative solvers explored here (since $\omega\Delta t$ independent of Δt makes higher-order predictor steps ineffective). Iterative implicit methods might be more effective with a different choice for the spatial differencing, such as 4th or 6th order compact finite differencing, which would eliminate the high frequency Nyquist mode. Upgrading from 2nd order to 4th order compact finite differencing in GS2 would be computationally very tractable (it just requires using a tri-diagonal solver rather than a bi-diagonal solver), but it would require some nontrivial programming (for example, one of the difficulties will be re-formulating the boundary conditions at trapped particle turning points) and so is left for possible future work.

Chapter 3

An ADI Algorithm for Gyrokinetics

In addition to semi-implicit and iterative implicit algorithms, we have also explored the implementation of an Alternating Direction Implicit (ADI) algorithm for a gyrokinetic plasma problem and its resulting numerical stability properties. The ADI algorithm is a type of operator splitting method in which each time step is split into two successive fractional steps of size $\Delta t/2$, treating a different operator implicitly on each fractional step. ADI algorithms are often useful in solving PDEs where an operator that is difficult to invert can be split into two operators that are much simpler to invert. ADI schemes often have the property that they are absolutely stable for arbitrarily large time step, which makes them relatively robust (though of course there are accuracy limits on the time step).

Consider a general problem of the form $\partial f/\partial t = Lf$, where L is some arbitrary linear operator. Rather than applying a single-step implicit finite difference time advancement scheme as in Eq. (2.1) in Chapter 2, in the ADI scheme we split L

into two linear operators as $L = L_1 + L_2$ and apply a two-step scheme as follows:

$$\frac{1}{\Delta t/2} (f^{n+1/2} - f^n) = L_1 f^{n+1/2} + L_2 f^n \quad (3.1)$$

$$\frac{1}{\Delta t/2} (f^{n+1} - f^{n+1/2}) = L_1 f^{n+1/2} + L_2 f^{n+1} \quad (3.2)$$

In the first step, the L_1 term is treated implicitly, while the L_2 term is treated explicitly. In the second step, the L_2 term is treated implicitly, while the L_1 term is treated explicitly. Note that, in addition to being implicit, this scheme is 2nd order accurate in time, like the $r = 1/2$ time-centered scheme in Eq. (2.1). Stability of the ADI scheme is guaranteed if the split operators L_1 and L_2 are diagonalizable and if all of the eigenvalues of L_1 and L_2 satisfy $\Re(\lambda_{1,j}) \leq 0$ and $\Re(\lambda_{2,j}) \leq 0$ [HUNSDORFER, 1998].

In practice, application of ADI schemes to many physical problems has been successful. For example, an ADI scheme applied to a parabolic problem with two spatial variables (such as the 2D heat conduction equation) can easily be shown to be absolutely stable [PEACEMAN and RACHFORD, 1955; DOUGLAS and RACHFORD, 1956]. Furthermore, stabilizing correction schemes, also a class of implicit schemes of alternating direction, can be used to achieve absolute stability for purely parabolic problems of higher dimensionality [DOUGLAS and RACHFORD, 1956] as well as for some advection-diffusion and advection-reaction equations [HUNSDORFER, 1998].

In this work, we apply a standard ADI scheme to the gyrokinetic problem, using it to divide the field solve from the particle distribution function advance. This algorithm has previously been found to work well for certain plasma kinetic problems involving 1 spatial and 2 velocity dimensions, including collisions and an

electric field. However, as we will show, for the gyrokinetic problem we find a severe stability restriction on the time step. Furthermore, we find that this numerical instability limitation also affects some other algorithms, such as a partially implicit Adams-Bashforth algorithm, where the parallel motion operator $v_{\parallel}\partial/\partial z$ is treated implicitly and the field terms are treated with an Adams-Bashforth explicit scheme. Ultimately, fully explicit algorithms applied to all terms can be better at long wavelengths than these ADI or partially implicit algorithms.

3.1 Motivation

Edge plasmas are known to play a critical role in tokamak confinement. A complete model of fusion edge plasma turbulence requires a full gyrokinetic description for all ions and electrons to accurately capture the large range of spatial scales due to the high degree of variation in the collisionality across the edge region. While computations of the electrostatic gyrokinetic equation with adiabatic electrons can be performed with straightforward numerical schemes, the inclusion of kinetic electrons and electromagnetic effects has been numerically challenging due to the smaller length scales and faster time scales associated with the fast parallel electron dynamics relative to the modes of interest. Furthermore, for edge turbulence codes, the existence of an Alfvén wave in the low β edge/scrape-off region, where the wave is even faster than the thermal electron motion, causes most standard explicit algorithms to need very small time steps for numerical stability. A semi-implicit or fast implicit algorithm that could use larger time steps, without excessive computational overhead, would thus be advantageous.

Various hybrid methods have been studied for extending Lagrangian particle-in-cell (PIC) gyrokinetic codes to include kinetic electrons and fully electromagnetic dynamics (see [CHEN and PARKER, 2001; COHEN *et al.*, 2002a; COHEN *et al.*, 2002b] and references therein). Recent breakthroughs in the PIC approach to electromagnetic gyrokinetics have been achieved via careful treatment of cancellations that should occur in the magnetic potential field equation [CHEN and PARKER, 2003]. Here we focus on algorithms useful for Eulerian codes (where these cancellations are straightforward to ensure and are in fact automatic in some formulations). Eulerian codes are being intensively used for nonlinear electromagnetic gyrokinetic simulations. While there are interesting issues involved in various choices of spatial discretization of the gyrokinetic equation [DANNERT and JENKO, 2004; CANDY and WALTZ, 2003a; KOTSCHENREUTHER *et al.*, 1995a], here we will focus on the time-advancement algorithm and will just Fourier transform in the spatial directions.

An Alternating Direction Implicit (ADI) algorithm developed by Kupfer *et al.* [KUPFER *et al.*, 1996] has recently been considered for kinetic edge microturbulence simulations. This two-step scheme splits the treatment of the parallel advection terms from the treatment of the electric field acceleration terms, treating them implicitly on alternating steps. This method has the advantage of avoiding the set up of large plasma response matrices needed for an unsplit implicit treatment of the linear gyrokinetic terms. Kupfer successfully used this ADI algorithm for a kinetic equation for electrons with 1 spatial dimension (in the parallel direction) and 2 velocity dimensions, including collisions with fixed Maxwellian background ions and imposing a quasi-neutrality constraint. While this model is useful for understanding aspects of scrape-off layer plasmas, the equations used did not contain

the Alfvén wave dynamics of the full gyrokinetic equation, which would be needed for a complete 3D simulation of edge plasmas.

Here we use a simple kinetic Alfvén wave limit of the gyrokinetic equation to test an ADI algorithm. We find the somewhat surprising result that not only does the ADI algorithm for this equation have a stability limit on the time step, but also that stability limit can be quite short for long wavelength modes, even worse than some fully explicit algorithms. This problem exists even at higher β , where the Alfvén wave is slower than the electrons. Thus, one needs to look at other options for faster gyrokinetic algorithms.

3.2 Kinetic Alfvén Wave Test Problem

As a starting point, we consider the test problem of a shear kinetic Alfvén wave at small $k_{\perp}\rho_i$. Thus, for the simplified starting equations, we consider the gyrokinetic equation [FRIEMAN and CHEN, 1982; ANTONSEN and LANE, 1980; CATTO *et al.*, 1981] in the linear, collisionless limit in slab geometry with a uniform magnetic field and uniform background Maxwellian particles. For further simplicity, we also neglect the kinetic equation for ion perturbations, assuming $\omega \gg k_{\parallel}v_{ti}$. Thus, the only ion contribution to perturbations will be through the ion polarization density. With these assumptions, the kinetic and field equations in Eqs. (2.3) - (2.5) become:

$$\frac{\partial f_e}{\partial t} + v_{\parallel} \frac{\partial f_e}{\partial z} = -\frac{Z_e e}{T_{0e}} v_{\parallel} F_{Me} \left(\frac{\partial \Phi}{\partial z} + \frac{1}{c} \frac{\partial A_{\parallel}}{\partial t} \right) \quad (3.3)$$

$$\frac{(Z_i e)^2 n_{0i}}{T_{0i}} k_{\perp}^2 \rho_i^2 \Phi = Z_e e \int d^3 v f_e \quad (3.4)$$

$$k_{\perp}^2 A_{\parallel} = \frac{4\pi}{c} Z_e e \int d^3 v v_{\parallel} f_e \quad (3.5)$$

Here, $f_e(z, \vec{v}, t)$ is the electron distribution function, z and v_{\parallel} are the position and velocity along the magnetic field, Φ is the electrostatic potential, A_{\parallel} is the parallel component of the perturbed magnetic vector potential, ρ_i is the thermal ion gyro-radius, T_{0i} and T_{0e} are the ion and electron temperatures, and F_{Me} is a Maxwellian distribution for the background electrons. For simplicity in this analysis, we also assume that $Z_i = 1$ ($Z_e = -1$). These or very similar equations have been used previously to study kinetic Alfvén waves and various numerical methods [COHEN *et al.*, 2002a; DANNERT and JENKO, 2004; SNYDER, 1999; HAHM and CHEN, 1985; LEE, 1987].

Using a Fourier transform in time and space, i.e. $f_e = \hat{f}_e e^{-i\omega t + ik_{\parallel} z}$, we find that

$$\hat{f}_e = \frac{Z_e e}{T_{0e}} F_{Me} \frac{k_{\parallel} v_{\parallel} \left(\Phi - \frac{\omega}{k_{\parallel} c} A_{\parallel} \right)}{\omega - k_{\parallel} v_{\parallel}} \quad (3.6)$$

Using this result in the field equations and expanding to lowest non-trivial order in the limit of $\omega \gg k_{\parallel} v_{te}$, we obtain the dispersion relation

$$\omega^2 = \frac{k_{\parallel}^2 v_A^2}{1 + \frac{2}{\beta_e} \frac{m_e}{m_i} k_{\perp}^2 \rho_s^2} \quad (3.7)$$

where $\beta_e = 8\pi n_0 T_{0e} / B^2$, $\rho_s^2 = c_s^2 / \Omega_{ci}$ is the sound-based gyroradius, $c_s^2 = T_{0e} / m_i$ is the sound speed, and $v_A^2 = (2/\beta_e) c_s^2$ is the Alfvén speed. Note that this is just the dispersion relation for a simple shear Alfvén wave in a straight magnetic field, with some finite gyroradius corrections. (A gyrofluid version of this derivation can be found in [SNYDER, 1999].) If $\beta_e < 2m_e/m_i$, such as in regions of very low density edge and scrape-off plasmas, then the Alfvén wave is faster than the thermal electron speed. A stable treatment of this wave in this regime is important.

However, consideration of these equations in the pure electrostatic limit (i.e. $\beta_e \rightarrow 0$) yields the high frequency electrostatic shear Alfvén wave [LEE, 1987], i.e. $\omega^2 = k_{\parallel}^2 v_{te}^2 / (k_{\perp}^2 \rho_s^2)$. Thus, to avoid this excessively high frequency mode at low k_{\perp} , it is useful to include magnetic perturbations from A_{\parallel} , as we do here.

Following the approach used in most existing continuum gyrokinetic codes (such as the GENE code [JENKO *et al.*, 2000] and the GYRO code [CANDY and WALTZ, 2003a]), we eliminate the $\partial A_{\parallel} / \partial t$ term from the electron kinetic equation by defining $g_e = f_e + \frac{Z_e e}{T_{0e}} F_{Me} \frac{v_{\parallel}}{c} A_{\parallel}$. (Other codes, such as GS2 [KOTSCHENREUTHER *et al.*, 1995a], which uses a linearly fully implicit algorithm, retain the $\partial A_{\parallel} / \partial t$ term, though both formulations are equivalent.) With this substitution, the equations for our kinetic Alfvén wave test problem become:

$$\frac{\partial g_e}{\partial t} + v_{\parallel} \frac{\partial g_e}{\partial z} = -\frac{Z_e e}{T_{0e}} v_{\parallel} F_{Me} \left(\frac{\partial \Phi}{\partial z} - \frac{v_{\parallel}}{c} \frac{\partial A_{\parallel}}{\partial z} \right) \quad (3.8)$$

$$\frac{(Z_i e)^2 n_{0i}}{T_{0i}} k_{\perp}^2 \rho_i^2 \Phi = Z_e e \int d^3 v g_e \quad (3.9)$$

$$\left(k_{\perp}^2 + \frac{4\pi (Z_e e)^2 n_{0e}}{c^2 m_e} \right) A_{\parallel} = \frac{4\pi}{c} Z_e e \int d^3 v v_{\parallel} g_e \quad (3.10)$$

Eqs. (3.8)-(3.10) provide a relatively simple problem with 1 spatial and 1 velocity coordinate that could provide a very useful testbed for studying alternative gyrokinetic algorithms. With appropriate normalizations, these equations can be written as the following set of integro-differential equations:

$$\frac{\partial g_e}{\partial t} + v_{\parallel} \frac{\partial g_e}{\partial z} = v_{\parallel} F_{Me} \left(\frac{\partial \Phi}{\partial z} - v_{\parallel} \frac{\partial A_{\parallel}}{\partial z} \right) \quad (3.11)$$

$$k_{\perp}^2 \Phi = - \int dv_{\parallel} g_e \quad (3.12)$$

$$(k_{\perp}^2 + \hat{\beta}) A_{\parallel} = -\hat{\beta} \int dv_{\parallel} v_{\parallel} g_e \quad (3.13)$$

where k_{\perp}^2 is normalized to $Z_i \rho_s^2$ and $\hat{\beta} \equiv (\beta_e/2) \frac{m_i}{m_e}$. The electron thermal velocity v_{te} has been normalized to unity, so that the Maxwellian equilibrium is $F_{Me} = \exp(-v_{\parallel}^2/2)/\sqrt{2\pi}$. Because $v_A^2 = v_{te}^2/\hat{\beta}$, Eq. (3.7) becomes

$$\omega^2 = \frac{k_{\parallel}^2/\hat{\beta}}{1 + k_{\perp}^2/\hat{\beta}} \quad (3.14)$$

A more complete general comprehensive test of the numerical stability of an algorithm for this problem would include a typical range of parameters, particularly, $k_{\perp} = 0.01 - 10$ and $\hat{\beta} = 0.1 - 10$, and perhaps also the addition of collisions in Eq. (3.11) to test the collisional component of the algorithm.

3.3 Implementing and Testing an ADI Algorithm

Kupfer's ADI algorithm as applied to the kinetic equation is a two-step algorithm: the first step is implicit in the parallel advection term and explicit in the field terms, while the second step is explicit in the parallel advection and implicit in the fields. (This is equivalent to a standard view of ADI as an "alternating direction" approach, since the electric field term represents motion in the velocity direction of (z, v_{\parallel}) phase space.) Thus, the discrete equations are:

$$\begin{aligned} & \frac{1}{\Delta t/2} (g_e^{n+1/2} - g_e^n) + v_{\parallel} \frac{\partial g_e^{n+1/2}}{\partial z} \\ & = -\frac{Z_e e}{T_{0e}} v_{\parallel} F_{Me} \left(\frac{\partial \Phi^n}{\partial z} - \frac{v_{\parallel}}{c} \frac{\partial A_{\parallel}^n}{\partial z} \right) \end{aligned} \quad (3.15)$$

$$\begin{aligned}
& \frac{1}{\Delta t/2} (g_e^{n+1} - g_e^{n+1/2}) + v_{\parallel} \frac{\partial g_e^{n+1/2}}{\partial z} \\
&= -\frac{Z_e e}{T_{0e}} v_{\parallel} F_{Me} \left(\frac{\partial \Phi^{n+1}}{\partial z} - \frac{v_{\parallel}}{c} \frac{\partial A_{\parallel}^{n+1}}{\partial z} \right)
\end{aligned} \tag{3.16}$$

$$\frac{(Z_i e)^2 n_{0i}}{T_{0i}} k_{\perp}^2 \rho_i^2 \Phi^{n+1} = Z_e e \int d^3 v g_e^{n+1} \tag{3.17}$$

$$\left(k_{\perp}^2 + \frac{4\pi (Z_e e)^2 n_{0e}}{c^2 m_e} \right) A_{\parallel}^{n+1} = \frac{4\pi}{c} Z_e e \int d^3 v v_{\parallel} g_e^{n+1} \tag{3.18}$$

To analyze the stability of the combined scheme, we use the ansatz $e^{ik_{\parallel}z}$ for the perturbed quantities and combine Eqs. (3.15) and (3.16) to express the time advanced distribution function g_e^{n+1} in terms of the fields:

$$\begin{aligned}
g_e^{n+1} &= \frac{1 - ik_{\parallel} v_{\parallel} \Delta t/2}{1 + ik_{\parallel} v_{\parallel} \Delta t/2} \left[g_e^n - \frac{Z_e e}{T_{0e}} (ik_{\parallel} v_{\parallel} \Delta t/2) F_{Me} \left(\Phi^n - \frac{v_{\parallel}}{c} A_{\parallel}^n \right) \right] \\
&\quad - \frac{Z_e e}{T_{0e}} (ik_{\parallel} v_{\parallel} \Delta t/2) F_{Me} \left(\Phi^{n+1} - \frac{v_{\parallel}}{c} A_{\parallel}^{n+1} \right)
\end{aligned} \tag{3.19}$$

Defining a complex amplification factor per time step as $a \equiv e^{-i\omega\Delta t}$ and using the further ansatz for all fields that $g_e^n = a^n \hat{g}_e(v)$, we find that

$$\hat{g}_e = \frac{Z_e e}{T_{0e}} F_{Me} \left(\hat{\Phi} - \frac{v_{\parallel}}{c} \hat{A}_{\parallel} \right) \frac{k_{\parallel} v_{\parallel}}{\hat{\omega} - k_{\parallel} v_{\parallel}} (1 + k_{\parallel} v_{\parallel} \hat{\omega} (\Delta t/2)^2) \tag{3.20}$$

where $\hat{\omega}$ is an effective frequency defined such that $\frac{a-1}{a+1} \equiv -i\hat{\omega}\Delta t/2$, or

$$a = \frac{1 - i\hat{\omega}\Delta t/2}{1 + i\hat{\omega}\Delta t/2}. \tag{3.21}$$

For real $\hat{\omega}$, $|a| = 1$ and perfect stability with no artificial damping is obtained, even for arbitrarily large time step. Absolute stability $|a| \leq 1$ also occurs for all modes with $\text{Im}(\hat{\omega}) \leq 0$. However, we will find that if the time step is too large, then

the numerical dispersion relation for the ADI algorithm has roots with $\text{Im}(\hat{\omega}) > 0$, which correspond to $|a| > 1$ and thus a numerical instability.

Using the result of Eq. (3.20) in the field equations and again expanding to lowest non-trivial order in $k_{\parallel}v_{te}/\hat{\omega}$, we find that

$$\hat{\omega}^2 = \left[\frac{k_{\parallel}^2 v_A^2 (k_{\perp} \rho_s)^2 (1 + 3(k_{\parallel} v_{te} \Delta t / 2)^2)}{\left(\frac{2}{\beta_e} \frac{m_e}{m_i} k_{\perp}^2 \rho_s^2 + 1 + 3(k_{\parallel} v_{te} \Delta t / 2)^2 \right) \left((k_{\perp} \rho_s)^2 - (k_{\parallel} v_{te} \Delta t / 2)^2 \right)} \right] \quad (3.22)$$

Note that this discrete version of the dispersion relation agrees with the analytic result in Eq. (3.7) in the limit $\Delta t \rightarrow 0$. In the electrostatic limit ($\beta_e \rightarrow 0$), the dispersion relation becomes

$$\hat{\omega}^2 = (k_{\parallel} v_{te})^2 \left[\frac{1 + 3(k_{\parallel} v_{te} \Delta t / 2)^2}{(k_{\perp} \rho_s)^2 - (k_{\parallel} v_{te} \Delta t / 2)^2} \right] \quad (3.23)$$

Thus, for both the electrostatic limit and the general electromagnetic case of Eq. (3.22), the algorithm is numerically unstable if $\Delta t / 2 > \left| \frac{k_{\perp} \rho_s}{k_{\parallel} v_{te}} \right|$. Figures 3.1 and 3.2 show plots of $\hat{\omega}$ and $|a|$ as a function of the temporal resolution $k_{\parallel} v_{te} \Delta t$ for the right-moving wave for a set of standard parameters, showing the onset of the numerical instability at $|k_{\parallel} v_{te} \Delta t| \sim |2k_{\perp} \rho_s| \sim 0.06$. This result implies that, with this algorithm, the electrostatic shear Alfvén wave must be fully resolved for stability in both the electrostatic and electromagnetic cases. Overall, this can be a potentially severe limitation for numerical simulations employing this type of ADI algorithm.

While the results thus far have focused on the limit of low $(\beta_e/2)(m_i/m_e)$, where the Alfvén wave is faster than the electron thermal speed and expansions in $k_{\parallel} v_{te}/\omega \ll 1$ could be done, we have also analyzed the numerical stability of the ADI algorithm more generally, including the regime of high $(\beta_e/2)(m_i/m_e)$, where

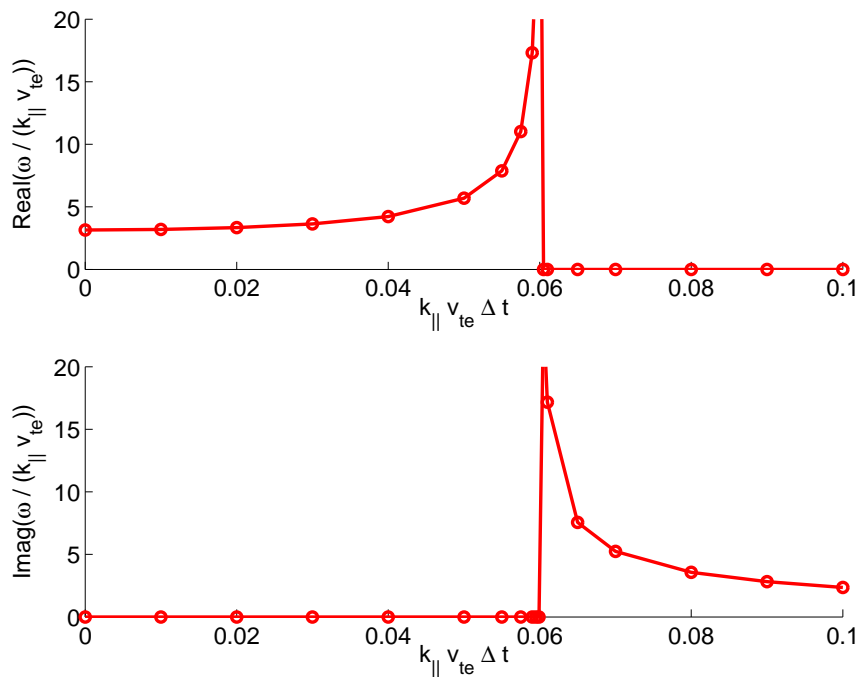


Figure 3.1: Normalized mode frequency vs. normalized time step for the kinetic Alfvén wave at $k_{\perp}\rho_s = 0.03$ and $(\beta_e/2)(m_i/m_e) = 0.1$ using an ADI algorithm.

the Alfvén wave is slower than the thermal electron speed. This analysis was performed via consideration of an n th-order generalized Lorentzian approximation (i.e. $e^{-x} \approx \left(1 + \frac{x}{n}\right)^{-n}$) for the parallel component of the Maxwellian in Eq. (3.20). It can be shown that $n \geq 3$ is necessary for convergence of the velocity integrals over the Maxwellian terms in the field equations. For consistency in the transformation of the field equations upon elimination of the $\partial A_{\parallel}/\partial t$ term, we have added normalization constants to the Lorentzian approximation to ensure that the density and pressure integrals are exact. Specifically, we assume that

$$F_{Me}(v_{\parallel}) \approx \frac{n_{0e}}{\sqrt{2\pi}v_{te}} \frac{C_0}{\left(1 + C_1 \frac{v_{\parallel}^2}{2v_{te}^2}\right)^n} \quad (3.24)$$

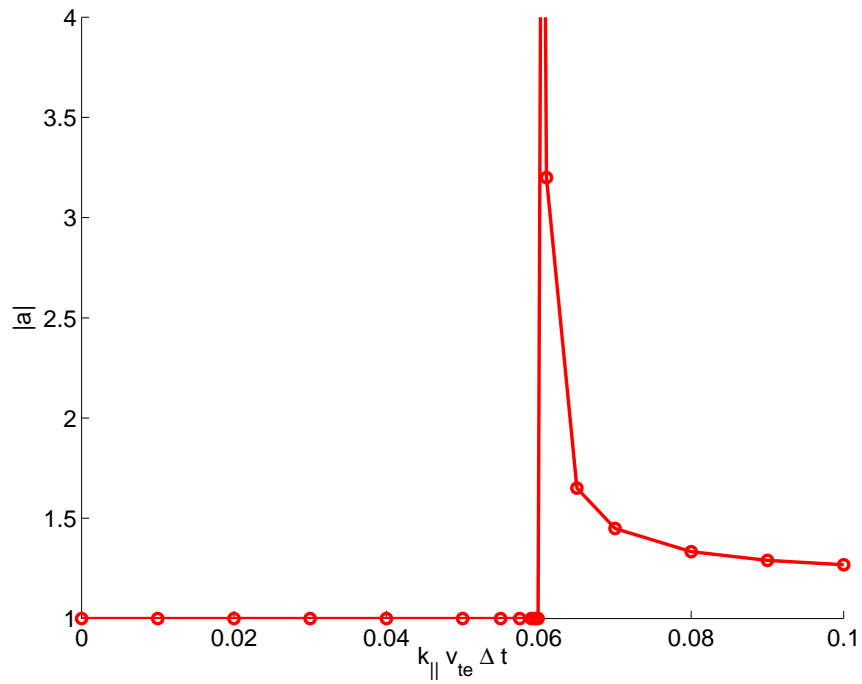


Figure 3.2: Amplification factor vs. normalized time step for the kinetic Alfvén wave at $k_{\perp} \rho_s = 0.03$ and $(\beta_e/2)(m_i/m_e) = 0.1$ using an ADI algorithm.

where

$$C_0 = \frac{\Gamma(n)\Gamma^{1/2}(n-3/2)}{\Gamma^{3/2}(n-1/2)} \quad (3.25)$$

$$C_1 = \frac{\Gamma(n-3/2)}{\Gamma(n-1/2)} \quad (3.26)$$

For this analysis, a 3rd order Lorentzian approximation was used and the field equations using Eq. (3.20) with Eq. (3.24) as an approximation for \hat{g}_e were solved numerically using the software Maple (Maple is a symbolic computational system from <http://www.maplesoft.com>) for given values of $k_\perp \rho_s$ and $(\beta_e/2)(m_i/m_e)$. (Note that if an exact Maxwellian is used, the integrals cannot be evaluated analytically but can be written in terms of the plasma dispersion Z function. With a Lorentzian $F_{Me}(v_\parallel)$, Maple is able to do the integrals analytically, resulting in essentially a multipole approximation to the Z function. Alternatively, one can interpret the resulting dispersion relation as exact for an equilibrium distribution function given by this generalized Lorentzian, and so it is a physically realizable exact dispersion relation. Since Alfvén waves should be physically stable even with this Lorentzian equilibrium according to the Penrose stability criterion, this provides a useful test of the stability of numerical algorithms.)

The result, demonstrated in figures 3.3 and 3.4, surprisingly also shows a severe stability limit on the ADI algorithm of $|k_\parallel v_{te} \Delta t| \sim |2k_\perp \rho_s| \sim 0.06$, i.e. the same stability criterion as found in the $\beta_e = 0$ limit in Eq. (3.23), even though the Alfvén wave is slower than the electron thermal velocity at high $(\beta_e/2)(m_i/m_e)$. A time step of $k_\parallel v_{te} \Delta t = 0.06$ corresponds to $\omega \Delta t = 0.02$, so both the parallel electron motion time scale and the actual mode frequency would appear to be very well resolved, yet still there is a numerical instability.

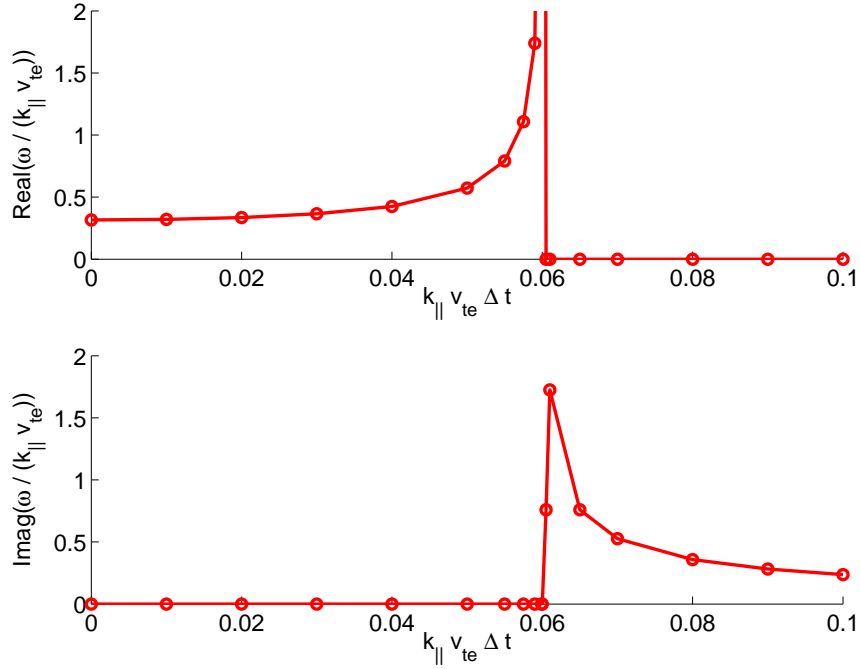


Figure 3.3: Normalized mode frequency vs. normalized time step for the kinetic Alfvén wave at $k_{\perp} \rho_s = 0.03$ and $(\beta_e/2)(m_i/m_e) = 10$ using an ADI algorithm.

3.4 Simpler Illustration of the Difficulties

Here we further illustrate the numerical difficulties of an ADI algorithm by an equivalent application of the algorithm to a Landau-fluid approximation to the kinetic equation. This reduces the operators involved to 2x2 matrices. This limit is useful for understanding why the ADI algorithm in this case has a stability limit at all, unlike other applications where an ADI algorithm is absolutely stable.

Integrating the normalized Eqs. (3.11)-(3.13) over velocity and defining the perturbed density $\rho = \int dv_{\parallel} g_e$, the perturbed fluid velocity $u = \int dv_{\parallel} g_e v_{\parallel}$, and the perturbed pressure $p = \int dv_{\parallel} g_e v_{\parallel}^2$ leads to the fluid equations:

$$\frac{\partial \rho}{\partial t} = -\frac{\partial u}{\partial z} - \frac{\partial A_{\parallel}}{\partial z} \quad (3.27)$$

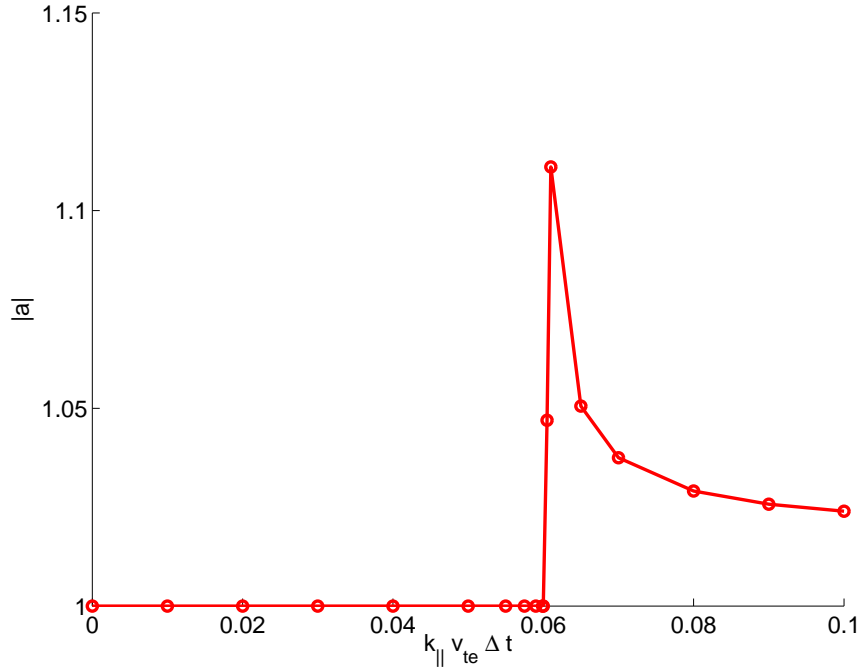


Figure 3.4: Amplification factor vs. normalized time step for the kinetic Alfvén wave at $k_{\perp} \rho_s = 0.03$ and $(\beta_e/2)(m_i/m_e) = 10$ using an ADI algorithm.

$$\frac{\partial u}{\partial t} = -\frac{\partial p}{\partial z} + \frac{\partial \Phi}{\partial z} \quad (3.28)$$

$$k_{\perp}^2 \Phi = -\rho \quad (3.29)$$

$$(k_{\perp}^2 + \hat{\beta}) A_{\parallel} = -\hat{\beta} u \quad (3.30)$$

Assuming a general closure approximation of the form $-\partial p/\partial z = -\Gamma \partial \rho/\partial z - \nu |k_{\parallel}| u$ (see [HAMMETT *et al.*, 1992] and references therein for a discussion of closure approximations that model kinetic effects such as Landau-damping) and Fourier transforming in space leads to

$$\frac{\partial \rho}{\partial t} = -ik_{\parallel} u - ik_{\parallel} A_{\parallel} \quad (3.31)$$

$$\frac{\partial u}{\partial t} = -ik_{\parallel}\Gamma\rho - \nu|k_{\parallel}|u + ik_{\parallel}\Phi \quad (3.32)$$

which can be written as

$$\frac{\partial}{\partial t} \begin{pmatrix} \rho \\ u \end{pmatrix} = \begin{pmatrix} 0 & -ik_{\parallel} \\ -i\Gamma k_{\parallel} & -\nu|k_{\parallel}| \end{pmatrix} \begin{pmatrix} \rho \\ u \end{pmatrix} + \begin{pmatrix} 0 & \frac{ik_{\parallel}\hat{\beta}}{k_{\perp}^2 + \hat{\beta}} \\ -\frac{ik_{\parallel}}{k_{\perp}^2} & 0 \end{pmatrix} \begin{pmatrix} \rho \\ u \end{pmatrix} \quad (3.33)$$

Denoting the first matrix on the RHS by \mathbf{P} , which represents the spatial propagation operator, and the second matrix on the RHS by \mathbf{E} , which represents the electric field term, and denoting the state vector $\vec{y} = (\rho, u)$, this can be written as

$$\frac{\partial \vec{y}}{\partial t} = \mathbf{P}\vec{y} + \mathbf{E}\vec{y} \quad (3.34)$$

Applying the ADI algorithm to this in an equivalent way as used in Eqs. (3.15)-(3.16), where the electric field is explicit on the first half step while all other terms are implicit and then vice versa on the next step, leads to

$$\frac{\vec{y}^{n+1/2} - \vec{y}^n}{\Delta t/2} = \mathbf{P}\vec{y}^{n+1/2} + \mathbf{E}\vec{y}^n \quad (3.35)$$

$$\frac{\vec{y}^{n+1} - \vec{y}^{n+1/2}}{\Delta t/2} = \mathbf{P}\vec{y}^{n+1/2} + \mathbf{E}\vec{y}^{n+1} \quad (3.36)$$

Combining these two steps of the ADI algorithm gives

$$\vec{y}^{n+1} = \left(1 - \frac{\Delta t}{2}\mathbf{E}\right)^{-1} \left(1 + \frac{\Delta t}{2}\mathbf{P}\right) \left(1 - \frac{\Delta t}{2}\mathbf{P}\right)^{-1} \left(1 + \frac{\Delta t}{2}\mathbf{E}\right) \vec{y}^n \quad (3.37)$$

In common ADI cases where the operators being split are diagonalizable and have eigenvalues with zero or negative real part, the ADI algorithm is absolutely stable for arbitrarily large time step (though of course there are accuracy restrictions),

because Δt appears in the numerators of the RHS of this equation. Consider our case first in the electrostatic $\hat{\beta} = 0$ limit. Then the operator corresponding to the electric field \mathbf{E} is not diagonalizable because its only non-zero entry is off-diagonal. This operator has the property that $\mathbf{E}^n = 0$ for all $n > 1$ (i.e. \mathbf{E} is a nilpotent matrix). This means that $\left(1 - \frac{\Delta t}{2}\mathbf{E}\right)^{-1} = 1 + \frac{\Delta t}{2}\mathbf{E}$ and what appeared to be an implicit step was actually equivalent to an explicit step. Thus the ADI algorithm for this case will be unstable if the time step Δt is too big. (In fact, analysis of the eigenvalues of the amplification matrix corresponding to Eq. (3.37) for this case recovers the onset of a numerical instability at $|k_{\parallel}\Delta t| \sim |2k_{\perp}|$, as found for the kinetic equations.) For the more general electromagnetic case, though \mathbf{E} is diagonalizable for nonzero $\hat{\beta}$, the eigenvalues λ of \mathbf{E} are given by $\lambda^2 = (k_{\parallel}/k_{\perp})^2\hat{\beta}/(k_{\perp}^2 + \hat{\beta})$, and the positive branch gives an instability. This is in contrast to the behavior of the unsplit operator $\mathbf{P} + \mathbf{E}$, which has negative values of λ^2 (in the $\nu = 0$ limit for simplicity), which correspond to stable oscillations.

3.5 Comparison with Adams-Bashforth Schemes

For comparison, we perform a similar analysis of the kinetic Alfvén wave test problem using an Adams-Bashforth algorithm. We first consider a partially implicit scheme, in which the parallel derivative term is treated implicitly and time-centered while the field terms are treated fully explicitly with a 2nd order Adams-Bashforth algorithm. Thus, the single-step discrete kinetic equation becomes

$$\begin{aligned} & \frac{1}{\Delta t/2} (g_e^{n+1} - g_e^n) + v_{\parallel} \frac{\partial}{\partial z} \frac{1}{2} (g_e^{n+1} + g_e^n) \\ & = -\frac{Z_e e}{T_{0e}} v_{\parallel} F_{Me} \frac{\partial}{\partial z} \left(\frac{1}{2} (3\Phi^n - \Phi^{n-1}) - \frac{v_{\parallel}}{c} \frac{1}{2} (3A_{\parallel}^n - A_{\parallel}^{n-1}) \right) \end{aligned} \quad (3.38)$$

Again using the ansatz $e^{ik_{\parallel}z}$ and defining $g_e^n = a^n \hat{g}_e(v)$, we find that

$$\hat{g}_e = \frac{Z_e e}{T_{0e}} F_{Me} \left(\hat{\Phi} - \frac{v_{\parallel}}{c} \hat{A}_{\parallel} \right) \frac{k_{\parallel} v_{\parallel}}{\hat{\omega} - k_{\parallel} v_{\parallel}} (1 - i\hat{\omega}\Delta t) \frac{(1 + i\hat{\omega}\Delta t/2)}{(1 - i\hat{\omega}\Delta t/2)} \quad (3.39)$$

where $\hat{\omega}$ is again defined in agreement with Eq. (3.21).

We again examine the stability of the algorithm in both the low and high $(\beta_e/2)(m_i/m_e)$ limits. For the low $(\beta_e/2)(m_i/m_e)$ analysis, substitution of Eq. (3.39) into the field equations and expansion to lowest order in $k_{\parallel}v_{te}/\hat{\omega}$ yields a 4th order complex equation for $\hat{\omega}$, which we solve numerically with Maple using our standard parameters. Analysis in the high $(\beta_e/2)(m_i/m_e)$ limit is likewise performed as before, using a 3rd order Lorentzian approximation for the parallel component of the Maxwellian term in (3.39) and using Maple to numerically solve the field equations with this approximation.

Figures 3.5 and 3.6 show the results of the analysis for the kinetic Alfvén wave. Though there is a slight artificial decay for both the low and high $(\beta_e/2)(m_i/m_e)$ cases, the numerical instability that we saw for the ADI scheme does not occur in either regime for these roots. However, the discrete dispersion relation contains multiple roots and these plots are for the eigenmode corresponding to the physical Alfvén wave only. Furthermore, an Adams-Bashforth algorithm introduces unphysical “computational modes” which must be also damped or there will still be a numerical instability. For both the low and high $(\beta_e/2)(m_i/m_e)$ cases, the physical modes found in the analysis are numerically stable over the range of Δt studied. These include the right and left moving kinetic Alfvén waves and a heavily damped entropy mode related to Landau damping (there are 3 physical roots of the analytic dispersion relation for a 3rd order Lorentzian equilibrium). However,

one of the computational mode becomes numerically unstable. The amplification factor as a function of normalized time step for this mode is shown in figure 3.7 for $k_{\perp}\rho_s = 0.01, 0.03$ (our standard case), and 0.05, for both $(\beta_e/2)(m_i/m_e) = 0.1$ and $(\beta_e/2)(m_i/m_e) = 10$. The onset of the numerical instability occurs at $|k_{\parallel}v_{te}\Delta t| \sim |k_{\perp}\rho_s|$, as indicated by the rapid rise in the modulus of the amplitude above 1. Thus, the partially implicit Adams-Bashforth algorithm is subject to a stability limit which is twice as strict as that found for the ADI algorithm. Though it is the physical mode which becomes numerically unstable for the ADI algorithm, while just the computational mode (which is introduced solely as a result of the numerical discretization) becomes unstable for the partially implicit Adams-Bashforth algorithm, the more severe stability limit for the partially implicit Adams-Bashforth algorithm makes it highly unpractical for edge gyrokinetic simulations. We have also tried a partially implicit algorithm using a 3rd order Adams-Bashforth for the electric field terms and found that it had an even smaller stability limit on the time step than the 2nd order Adams-Bashforth method.

For comparison, we also analyze the stability of a fully explicit Adams-Bashforth algorithm. For this case, we treat the parallel derivative operator term as well as the field terms with a 2nd order Adams-Bashforth scheme. Using our usual ansatz, we find that

$$\hat{g}_e = \frac{Z_e e}{T_{0e}} F_{Me} \left(\hat{\Phi} - \frac{v_{\parallel}}{c} \hat{A}_{\parallel} \right) \frac{k_{\parallel} v_{\parallel}}{\hat{\omega} - k_{\parallel} v_{\parallel}} \quad (3.40)$$

where here the effective frequency is defined such that $\frac{a(a-1)}{3a-1} = -i\hat{\omega}\Delta t/2$.

The result of Eq. (3.40) has the same form as the exact time continuous result (i.e. the equivalent of Eq. (3.6) for our starting equations) and is thus surprisingly not subject to the same stability restrictions $|k_{\parallel}v_{te}\Delta t| \lesssim |k_{\perp}\rho_s|$ as the ADI and

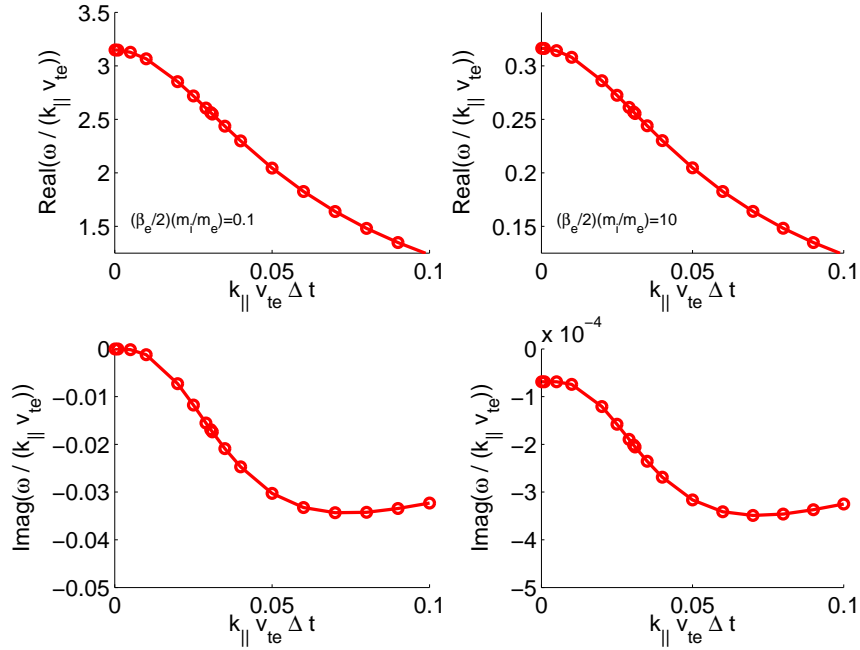


Figure 3.5: Normalized mode frequency vs. normalized time step for the kinetic Alfvén wave at $k_{\perp}\rho_s = 0.03$ using a partially implicit Adams-Bashforth algorithm.

partially-implicit Adams-Bashforth algorithms for this problem.

As is well known, a 2nd order Adams-Bashforth algorithm does induce a small amount of artificial growth. The amplification factor for this case is given by

$$a = \frac{1}{2} \left[1 - \frac{3}{2}i\hat{\omega}\Delta t \pm \sqrt{1 - i\hat{\omega}\Delta t - \frac{9}{4}(\hat{\omega}\Delta t)^2} \right] \quad (3.41)$$

as shown in figure 3.8 for the low and high $(\beta_e/2)(m_i/m_e)$ cases. We show both the physical Alfvén mode, for which $|a| \rightarrow 1$ in the limit of $\Delta t \rightarrow 0$, and the unphysical computational mode, for which $|a| \rightarrow 0$ in the limit of $\Delta t \rightarrow 0$. These levels of artificial growth would be quite adequate for many gyrokinetic turbulence simulations. One just needs to keep the time step sufficiently small so that this artificial amplification is small compared to physical dissipation mechanisms, or in turbulent

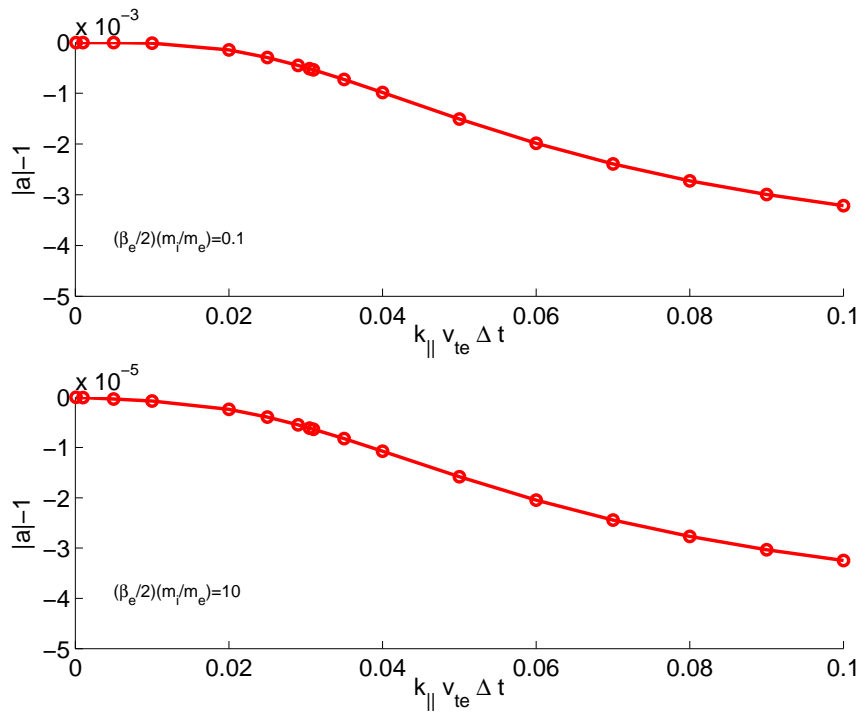


Figure 3.6: Amplification factor vs. normalized time step for the kinetic Alfvén wave at $k_{\perp} \rho_s = 0.03$ using a partially implicit Adams-Bashforth algorithm.

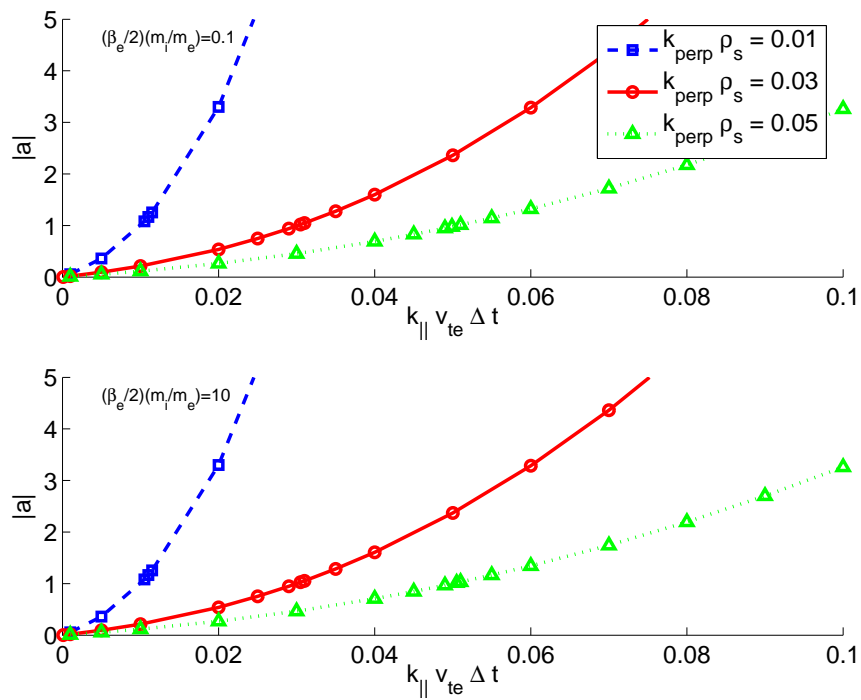


Figure 3.7: Amplification factor vs. normalized time step for the computational mode using a partially implicit Adams-Bashforth algorithm.

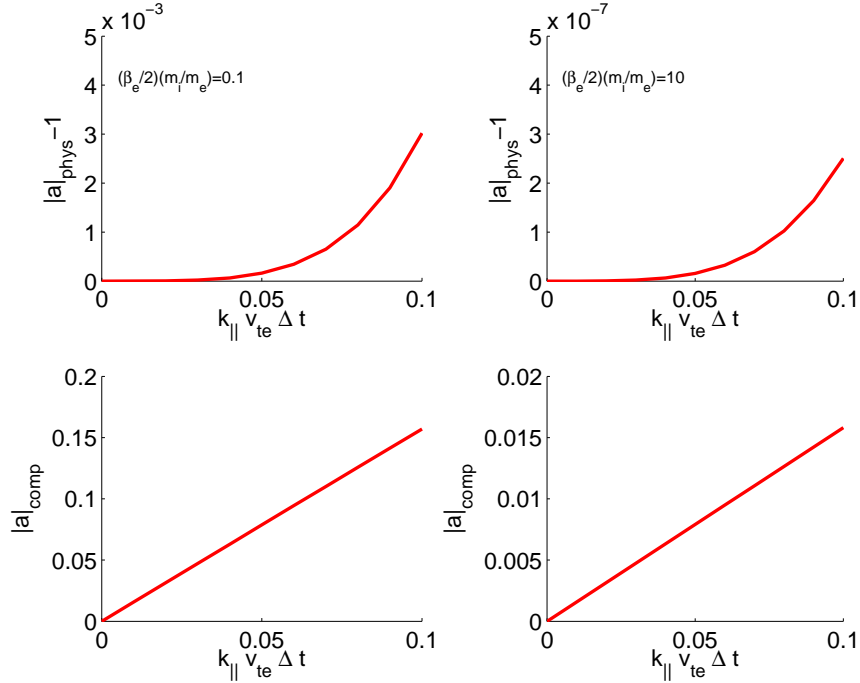


Figure 3.8: Amplification factor vs. normalized time step for the physical mode and the computational mode at $k_{\perp} \rho_s = 0.03$ using a fully explicit Adams-Bashforth algorithm.

systems, small compared to the rate at which nonlinear interactions take energy out of undamped modes and transfer energy to damped modes. Overall, this analysis suggests that even a 2nd order purely explicit Adams-Bashforth algorithm can be better at long wavelengths than the ADI or partially implicit Adams-Bashforth algorithms explored here.

By going to an even higher-order explicit algorithm, one can completely eliminate artificial growth over a range of time step, since the stability boundaries in the complex $\omega \Delta t$ plane are well known [GEAR, 1971; DURRAN, 1998]. Often a 3rd order Adams-Bashforth (AB3) or a 4th order Runge-Kutta (RK4) algorithm is chosen to provide a good balance between maximum stable time step and computational cost. On the real ω axis, the maximum stable time step for AB3 is

$|\omega|\Delta t = 0.72$, while for purely damped modes the maximum stable time step for AB3 is $|\omega|\Delta t = 0.55$. The stability limit of a 4th order Runge-Kutta algorithm is comparable (after dividing by 4 to account for the 4 intermediate steps that make up a full step of a 4th order Runge-Kutta algorithm), equivalent to $|\omega|\Delta t = 0.71$ for real ω , and $|\omega|\Delta t = 0.70$ for purely damped modes. The dispersion relation that follows from the 3rd order Lorentzian in Eq. (3.24) has 3 roots. For $(\beta_e/2)(m_i/m_e) = 0.1$ and $k_\perp \rho_s = 0.03$, these roots are $\omega = \pm 3.2k_\parallel v_{te}$ (the Alfvén waves) and $\omega = -5.2ik_\parallel v_{te}$ (a heavily damped entropy mode related to Landau damping). This heavily damped mode would set a stability limit for an RK4 algorithm of $k_\parallel v_{te} \Delta t = 0.14$, 2.2 times better than the stability limit of the ADI algorithm. For lower k_\perp modes, a fully explicit RK4 or AB3 algorithm would be even better in comparison to the ADI and partially implicit algorithms studied here.

3.6 Summary

Though ADI algorithms applied to many problems have the nice property that they are absolutely stable for arbitrarily large time step, and though Kupfer's ADI algorithm has previously worked for a related plasma kinetic problem, we have found that the implementation in a gyrokinetic problem yields a severe time step restriction. It is somewhat surprising not only that the ADI algorithm for this problem has a stability limit, but also that this stability limit is so short, even worse than some fully explicit algorithms.

Specifically, for a test problem of a shear kinetic Alfvén wave at small $k_\perp \rho_i$, the ADI algorithm is numerically unstable for $\Delta t/2 > |k_\perp \rho_s / (k_\parallel v_{te})|$ in both the

low $(\beta_e/2)(m_i/m_e)$ regime and the high $(\beta_e/2)(m_i/m_e)$ regime, where the Alfvén wave is slower than the electron thermal speed and all of the important dynamics would seem to be well resolved. Furthermore, this stability problem is not unique to the ADI algorithm, as a partially implicit Adams-Bashforth scheme yielded a restriction on the time step twice as low as the ADI algorithm for this problem. A simple set of gyrofluid model equations was constructed to illustrate the source of the problems. In the simple electrostatic limit, one of operators used in the alternating implicit steps was nilpotent and was not diagonalizable, so that what appeared to be an implicit step was actually equivalent to an explicit step.

Eventually, the best approach for kinetic edge microturbulence simulations might be a fully implicit algorithm for the linear terms, perhaps employing preconditioned Krylov solvers from an advanced package such as PETSc [BALAY *et al.*, 2005] or SUNDIALS [HINDMARSH *et al.*, 2003]. A key to successful use of such iterative methods is a good preconditioner. As part of the preconditioning, one might use precomputed plasma response matrices as used in the linearly fully implicit GS2 algorithm [KOTSCHENREUTHER *et al.*, 1995a] or a similar approach used in GYRO [CANDY and WALTZ, 2003b]. As a starting point short of these more complicated implicit methods, one might use a fully explicit 4th order Runge-Kutta algorithm.

Chapter 4

Effects of Shaping on Gyrokinetic Plasma Turbulence

In this chapter, the effects of flux surface shape and other plasma parameters on the gyrokinetic stability and transport of tokamak plasmas are studied using high resolution, fully electromagnetic, 5D simulations of plasma microturbulence. Here we are interested primarily on the effects of elongation ($\kappa \equiv Z_{max}/a$, where Z_{max} is the highest point on the plasma boundary and a is the midplane half-width) and triangularity ($\delta \equiv (R(Z_{max}) - R_0)/a$ where R_0 is the major radius at the center of the flux surface).

Previous experimental studies indicate that shaping effects are important in improving the performance of tokamaks. Recall that an efficient tokamak must simultaneously achieve both high β (to increase the fusion gain) and a large self-driven bootstrap current (to reduce the amount of external auxiliary current drive needed for steady state operation). However, tokamaks are generally subject to pressure, current, and density limits, above which MHD instabilities are driven

(such as kink/ballooning modes, edge-localized modes, resistive wall modes, and neoclassical tearing modes), which can lead to catastrophic disruptions. This includes the Troyon β limit, which was found numerically via pressure profile optimization at varying shaped equilibrium and constant current and which yields that the maximum β is limited by the MHD ballooning instability such that the Troyon-normalized β ($\beta_N = \beta/(I_p/(aB_T))$) is around 4% [TROYON *et al.*, 1984]. (Troyon’s expression captures most of the effects of plasma shaping on the β limit, specifically through the fact that an elongated plasma can carry more current at fixed q than a circular plasma: $\beta_{Troyon} = I_p/(aB_T) \propto (a/Rq_{95})(1 + \kappa^2(1 + 2\delta^2))/2$ (approximately). However, there is some dependence of the MHD β limit on plasma shape and current profile that is not captured by Troyon’s simple expression.) High shaping has been shown to be favorable in experiments; for example, providing significant increases in the β stability limit in DIII-D (with increased elongation and triangularity) [LAZARUS *et al.*, 1991; FERRON *et al.*, 2005] and also yielding simultaneous high density (relative to the Greenwald density limit) and high confinement in JET ELMy H-mode discharges (by increasing the triangularity) [ON-GENA *et al.*, 2001]. The observed enhanced performance of tokamaks with shaping is essentially attributable to the associated increase in the plasma current (at fixed q , which is generally constrained by the kink instability), providing higher β_{Troyon} . This increased plasma current also yields a higher fraction of the bootstrap current ($f_{BS} \propto \beta_P \propto q\beta_N$), which reduces the amount of recirculated power needed for current drive and thus improves the overall engineering performance of the tokamak. However, while shaping is favorable in tokamaks, the degree of shaping is somewhat limited. Specifically, the plasma elongation is limited primarily by the vertical instability (though this can be controlled with a vertical feedback control system and

passive stabilizing structures for sufficiently modest elongations $\kappa \lesssim 2.2$), while the plasma triangularity is primarily limited by divertor constraints.

While the effects of shaping have been studied theoretically in some detail with respect to MHD stability and gyrokinetic linear stability, the effects of shaping on nonlinear gyrokinetic microturbulence, are not well known. Early gyrokinetic studies by [REWOLDT *et al.*, 1982] using the FULL gyrokinetic code interfaced with a general geometry numerical MHD equilibrium and focusing on TEMs showed that elongation is strongly stabilizing on the TEM, while the effect of increasing the triangularity (at fixed $\kappa = 1.0$) is slightly destabilizing, though relatively weak compared to the effect of elongation. Similarly, later linear gyrokinetic shaping studies of the ITG mode (with adiabatic electrons) by [HUA *et al.*, 1992] varying the global equilibrium (rather than local shaping parameters) showed that the ITG growth rate decreases as elongation increases but is insignificantly affected by triangularity. More recent studies by [WALTZ and MILLER, 1999] using the Miller local analytic equilibrium model [MILLER *et al.*, 1998] to systematically vary the flux surface shape likewise found a general improvement of the ITG mode (with gyrokinetic electrons) with elongation (in the absence of triangularity) as well as an improvement with reverse triangularity (at fixed moderate $\kappa = 2.0$), in agreement with the FULL results, due to drift reversal on the trapped electron drive. Lacking in these linear gyrokinetic studies, however, is an understanding of the effects of the coupling of elongation and triangularity as well as the variation of local radial gradients of the shaping parameters. Furthermore, while some studies of the nonlinear transport in general geometry have been done, mostly with gyrofluid codes, (for example, in their 1999 paper, Waltz and Miller also coupled the Miller equilibrium model with a gyrofluid code to begin to explore a scaling of the heat flux with

elongation for ITG turbulence with adiabatic electrons), these studies have been limited and are generally sparse.

Thus, the goal of our studies is to extend these studies to develop an understanding of and predictive models for the scaling of nonlinear turbulence levels with shaping parameters through systematic gyrokinetic simulations of plasma microturbulence in varying geometric equilibria. Overall, a better theoretical understanding of the effects of shaping on plasma turbulence and transport could be used to optimize the design of tokamaks and could ultimately improve the economics of fusion energy.

In relation to gyrokinetic stability, shaping the plasma can influence the ITG turbulence by changing the local magnetic shear [KESSEL *et al.*, 1994; ANTONSEN *et al.*, 1996]. Recall that the toroidal ITG instability is driven by “bad-curvature” effects. However, because particles that produce an eddy tend to follow the field lines, ITG turbulence can be reduced by reversed magnetic shear (i.e. local shear $\hat{s} < 0$), which twists an eddy in a short distance to point in the good curvature direction. In contrast, for positive magnetic shear, convective cells tend to remain oriented in the ∇R direction and are thus more strongly driven. (A nice illustration of this can be found in figure 2 of [ANTONSEN *et al.*, 1996].) Most commonly, locally reversed magnetic shear can be produced naturally by squeezing the field lines at high pressure. To see this, recall that $\hat{s} = (r/q)(dq/dr)$, so reversed magnetic shear is q dropping with r . Since $q = (r/R)(B_T/B_p)$, this can be achieved by increasing B_p with r . This creates the so-called “2nd stability” of an advanced tokamak [JARDIN *et al.*, 2005] and spherical torus [JARDIN *et al.*, 1997]. However, reversed magnetic shear can also be produced by changing the plasma shape (such as varying the elongation and triangularity) since this changes B_p . These effects

are explored here.

4.1 The Equilibrium

In these studies, we use the gyrokinetic code GS2 [KOTSCHENREUTHER *et al.*, 1995a; DORLAND *et al.*, 2000] for studies of the effects of local flux surface shape on plasma microturbulence. GS2 is a flux tube-based Eulerian code, which includes nonlinear effects, gyrokinetic electron dynamics, trapped particles, electromagnetic perturbations, and a pitch angle scattering collision operator. GS2 can use either a full numerical equilibrium or a local parameterized equilibrium such as developed by Miller *et al.* [MILLER *et al.*, 1998] to obtain a realistic treatment of plasma shape. For these shaping studies, we use the analytic Miller local equilibrium model. According to Mercier and Luc [MERCIER and LUC, 1974], an equilibrium in the neighborhood of a chosen flux surface ψ_0 can be obtained via local expansion of the Grad-Shafranov equation, given the shape of the reference flux surface as defined by $R_s(\theta)$ and $Z_s(\theta)$, the poloidal field on the flux surface $B_{ps}(\theta)$, and the two free functions of the poloidal flux ($p'(\psi_0)$ and $I'(\psi_0)$). In the Miller model, nine parameters are required to fully describe the local equilibrium: κ (elongation), δ (triangularity), \hat{s} (global magnetic shear), α (pressure gradient), A (aspect ratio), q (safety factor), $\partial_r R_0$, $\partial_r \kappa$, and $\partial_r \delta$. The shape of a flux surface is specified using a standard formula for D-shaped plasmas, i.e.

$$R_s = R_0 + r \cos \left[\theta + \left(\sin^{-1} \delta \right) \sin \theta \right] \quad (4.1)$$

$$Z_s = \kappa r \sin(\theta) \quad (4.2)$$

The primary advantage of this model compared with a full numerical equilibrium is that the parameters can be individually varied, thus allowing for systematic studies of the effects of each upon stability and transport for shaped flux surfaces.

4.1.1 JET-based Plasmas

For these studies, we use representative shapes based on the JET tokamak. A complete scan of a 9D parameter space as described by the Miller local equilibrium model using generic equilibria would be difficult due to the computational intensity of nonlinear gyrokinetic simulations. Furthermore, in most real experiments, the various shaping parameters are not fully independent and tend to be correlated with each other. Thus, we consider a single cut through the space of shaping parameters, beginning with parameters from an existing tokamak as a base case. Specifically, our simulation studies begin with shaping parameters based on JET experimental data. We have focused on JET ELMy shot 52979, $t=22.0\text{s}$. This shot was run as a long duration, high density experiment to study density peaking. Studies of this shot have been published in [VALOVIC *et al.*, 2002]. TRANSP analysis [HAWRYLUK, 1980; ONGENA *et al.*, 1998] of this data was provided by R. V. Budny. The resulting radial profiles of the shaping parameters and the ion and electron temperatures and densities are shown in figure 4.1. (Note that the kinky behavior in the ion temperature profile is due the effects of the high density of the shot on the diagnostic. Some smoothing was done before calculating the local temperature gradient given below.) We have chosen one radial zone as a representative shaped flux surface and then artificially varied the shaping parameters using the Miller formalism to approach the circular limit via linear interpolations. This zone (which we will refer to as zone 75) corresponds to $r/a = 0.80$ and was

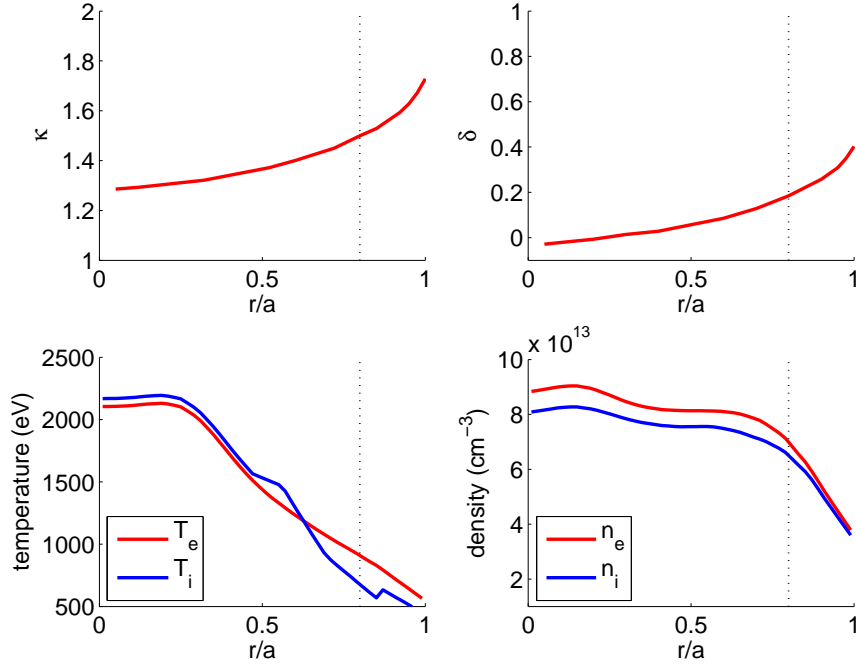


Figure 4.1: TRANSP analysis of the experimental data from JET ELMy shot 52979, $t=22.0s$: specifically, the radial variation of the elongation, triangularity, electron and hydrogenic ion temperature, and electron and deuterium density. The dotted vertical lines mark zone75, i.e. the radial zone chosen as the base case for the JET-based shaping studies.

chosen in particular because shaping effects are strongest near the plasma edge, yet experimental measurements too close to the edge are subject to large uncertainties.

The standard local parameters based on the JET zone 75 equilibrium are given as follows: $r/a = 0.80$, $R/a = 3.42$, $\partial_r R_0 = -0.14$, $q = 2.03$, $\hat{s} = 1.62$. The original shaping parameters for zone 75 are: $\kappa = 1.46$, $\partial_{r/a}\kappa = 0.57$, $\delta = 0.19$, $\partial_{r/a}\delta = 0.60$. Thus, the parameterizations of the shaping factors based on linear interpolations of this data are given by:

$$\partial_{r/a}\kappa(\kappa) = (0.57/0.46)(\kappa - 1) \quad (4.3)$$

$$\delta(\kappa) = (0.19/0.46)(\kappa - 1) \quad (4.4)$$

$$\partial_{r/a}\delta(\kappa) = (0.60/0.19)\delta(\kappa) \quad (4.5)$$

Plots of neighboring flux surfaces for the JET-based parameter scan showing the effects of κ and δ on the equilibrium can be seen in figure 4.2. We limit our scan to $\kappa \leq 2.6$ since, in real experiments, tokamaks with very high elongation are subject to the catastrophic MHD vertical instability. (The exact threshold for the vertical instability is very sensitive to experiment-specific parameters, such as how close passive stabilization plates and feedback coils are. However, modern tokamaks are typically designed with elongations less than 2.2.) In the GS2 simulations, we use a single ion species (i.e. we neglect impurity species) and include gyrokinetic electrons with the following base case parameters: $R/L_{ni} = R/L_{ne} = 3.50$, $R/L_{Ti} = R/L_{Te} = 10.81$, $T_{0i} = T_{0e}$, $\nu_{ei}/(v_{ti}/a) = 0.393$, $\nu_{ii}/(v_{ti}/a) = 9.88 \times 10^{-3}$.

For studies of electromagnetic effects, we also vary β with shaping to keep the Troyon-normalized β fixed ($\beta_N = \beta/(I_p/(aB_T))$) while also holding q_{95} fixed (where q_{95} is the plasma safety factor at the flux surface that encloses 95% of the total poloidal flux). Tokamaks are generally designed to work at fixed β_N (constrained by the stability of ballooning modes) and q_{95} (constrained by the stability of kink modes). We assume a scaling for the shaping factor based on a modification of the empirically-based formula of [UCKAN, 1990], i.e.

$$\beta_{Troyon} \propto \frac{a}{Rq_{95}} \left[\frac{1 + \kappa^2(1 + 2\delta^2)}{2} \right] \quad (4.6)$$

At fixed q_{95} , as the plasma elongates, the poloidal current I_p increases. Thus, we vary β as

$$\beta(\kappa) = \beta_{zone75} \left[\frac{1 + \kappa^2(1 + 2\delta^2)}{1 + \kappa_{zone75}^2(1 + 2\delta_{zone75}^2)} \right] \quad (4.7)$$

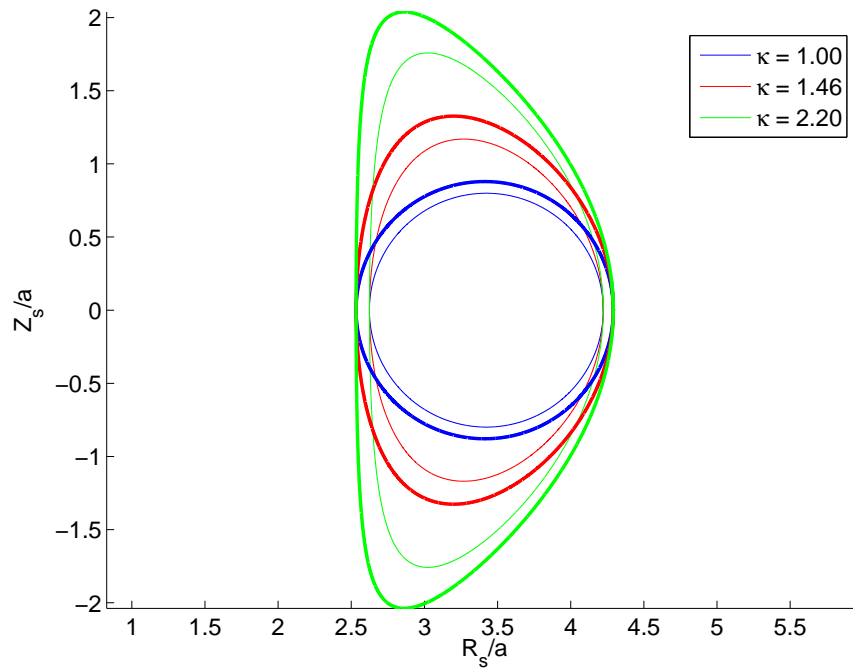


Figure 4.2: Neighboring flux surface shapes for representative JET-like plasmas. The $\kappa = 1.46$ case corresponds to the original experimental JET zone 75 equilibrium.

where $\beta_{zone75} = 7.58 \times 10^{-3}$. (Note: We use the notation $\beta = \beta_i = \beta_e$, where $\beta_s = 8\pi n_{0s} T_{0s} / B^2$ and the total β_{total} is given by $(\beta_i + \beta_e)$.)

For consistency, the equilibrium β radial gradient should also be varied as defined, i.e.

$$-\partial_{r/a}\beta(\kappa) = \sum_s \beta_s(\kappa) \left(\frac{R}{L_{ns}} + \frac{R}{L_{Ts}} \right) \frac{a}{R} \quad (4.8)$$

(In this notation, the density and temperature length scales are defined as $L_{ns} \equiv -[\partial(\ln n_{0s})/\partial r]$ and $L_{Ts} \equiv -[\partial(\ln T_{0s})/\partial r]$ such that $-\partial_{r/a}\beta(\kappa)$ is a positive quantity.) Recall, however, that in gyrokinetics $\partial_{r/a}\beta$ enters in as an equilibrium parameter (related to the second derivative of the Shafranov shift in the Miller equilibrium model), while β is a dynamical parameter (controlling the magnitude of A_{\parallel}), so each can be varied independently. In the simulation results presented in this chapter, for electromagnetic runs, β and $\partial_{r/a}\beta$ are varied as above. For electrostatic runs denoted as “ $\beta_prime(\kappa)$ ” results, $\partial_{r/a}\beta$ is varied with shaping as in Eq. (4.8) even though β itself is zero. This allows for a direct comparison between the electrostatic and electromagnetic results showing the effects of the dynamical β , since the equilibrium is unchanging from the electrostatic to the electromagnetic description. For electrostatic runs denoted as “ $\beta_prime=const$ ” results, the β gradient is kept fixed at the original zone 75 value ($-(\partial_{r/a}\beta)_{zone75} = -0.063$) across shaping parameters. In comparison with electrostatic “ $\beta_prime(\kappa)$ ” results, this allows for a study of the effects of the equilibrium generated by the β gradient on the dynamics.

4.2 Linear Gyrokinetic Stability

We first explore the effects of shaping on the linear gyrokinetic stability. For all of the linear results, we report the maximum linear growth in a scan over $k_y \rho_i$ in the

range $0.1 \leq k_y \rho_i \leq 1.0$. The results presented in this section were performed in the electrostatic limit.

We begin with studies of the variation of the linear ITG growth rate with κ , shown in figure 4.3. In general, the results show that elongation has a stabilizing influence on the linear growth rate. The $\delta = 0$ curve is used as a base case comparison with the $\delta(\kappa)$ curve, from which we observe that triangularity is slightly destabilizing at low to moderate κ and slightly stabilizing at very high κ . However, overall, the dependence of the linear stability on triangularity is very weak compared with the stabilizing effects of elongation. Comparison with the curve at constant β radial gradient shows that increasing $|\partial_{r/a}\beta|$ is also stabilizing. The stabilizing influence of the β gradient has been shown previously and has been demonstrated to be particularly important in high β spherical torus plasmas [BOURDELLE *et al.*, 2003]. This can be seen intuitively in \hat{s} - α geometry, where the curvature drift frequency can be written as:

$$\omega_{d,\parallel} = - \left(\frac{k_y \rho_s v_{ts}}{R_0} \right) [\cos \theta + (\hat{s}\theta - \alpha \sin \theta) \sin \theta] \quad (4.9)$$

where $\alpha = -q^2(R_0/a)\partial_{r/a}\beta$ (related to the second derivative of the Shafranov shift) and $\omega_{d,\parallel} < 0$ corresponds to drifts in the “bad-curvature” direction. Thus, Eq. (4.9) shows that the stabilizing effect of increased $-\partial_{r/a}\beta$ (or, equivalently increased α) is analogous to that due to reversed local magnetic shear.

Overall, the results of figure 4.3 agree with our previous GS2 shaping studies based on a generic equilibrium as an extension of the initial shaping studies of [WALTZ and MILLER, 1999]. The parameters for these studies are: $r/a = 0.5$, $R/a = 3.0$, $\partial_r R_0 = -0.0$, $q = 2.0$, $\hat{s} = 1.0$, $\partial_r \beta = -0.0$. We have artificially varied

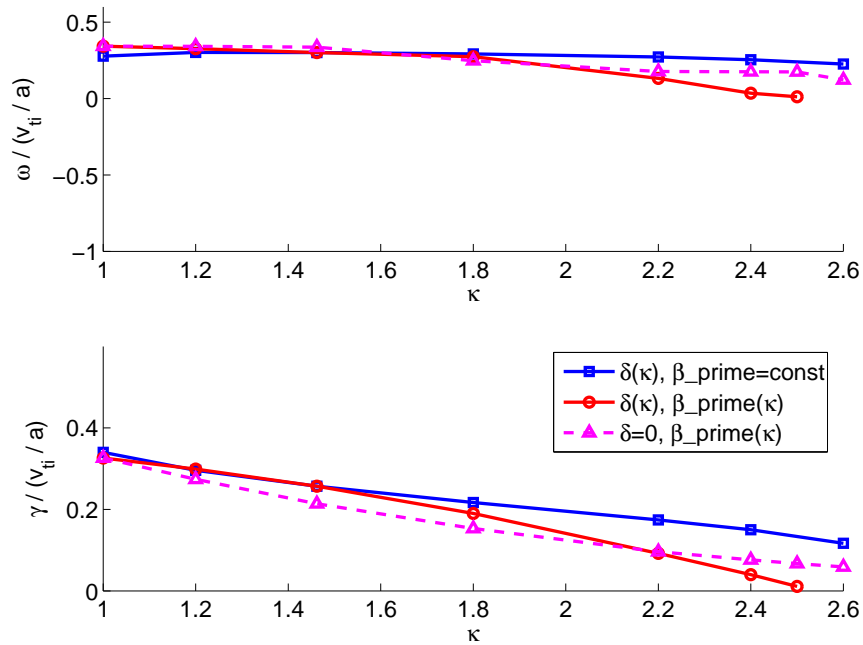


Figure 4.3: Real frequency and linear growth rate vs. elongation for JET-based plasmas in the electrostatic limit comparing zero triangularity and triangularity varied with κ , as well as comparing constant β radial gradient and β radial gradient varied with κ .

the input shaping parameters, starting with a concentric circular base case and using simple approximations for the gradients and a linear interpolation of the parameters in [WALTZ and MILLER, 1999] as an approximation of the triangularity variation with elongation, given as follows:

$$\partial_{r/a}\kappa(\kappa) = (\kappa - 1)/(r/a) \quad (4.10)$$

$$\delta(\kappa) = C_\delta(0.416/0.66)(\kappa - 1) \quad (4.11)$$

$$\partial_{r/a}\delta(\kappa) = \delta(\kappa)/(r/a) \quad (4.12)$$

where the constant $C_\delta = 0.75$ was chosen to maintain the physical restriction $0 \leq \delta \leq 1$ for the range of κ of interest. Note that this is similar to the variation of the shaping parameters in the JET-based study, but with a different equilibrium base case and a more simple variation of the shaping gradients. Plots of neighboring flux surfaces for this generic-based parameter scan can be seen in figure 4.4. This figure specifically shows the effects of δ on the equilibrium. Note the qualitative similarity with the flux surfaces of the JET-based equilibrium scan shown in figure 4.2. In particular, the triangularity at any given κ is larger for the JET-based plasmas. The increased triangularity gradient for the JET-based plasmas is also particularly noticeable by the increased relative closeness of the neighboring flux surfaces for the $\kappa = 2.2$ case compared with the corresponding generic-based case.

In the GS2 simulations for the generic-based parameterization, we use a single ion species and include gyrokinetic electrons with the following base case parameters: $R/L_{ni} = R/L_{ne} = 3.00$, $R/L_{Ti} = R/L_{Te} = 6.00$, $T_{0i} = T_{0e}$, $\nu_{ei}/(v_{ti}/a) = \nu_{ii}/(v_{ti}/a) = 0$. Results showing the variation of the real frequency and linear ITG growth rate with the shaping parameters can be seen in figure 4.5. In agreement

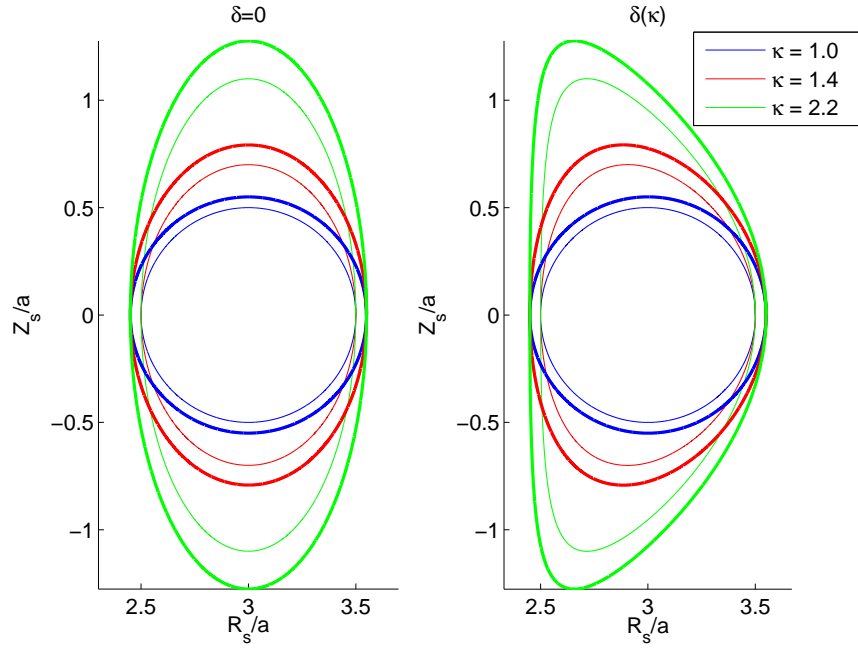


Figure 4.4: Neighboring flux surface shapes for representative generic-based plasmas.

with the JET-based results in figure 4.3, these generic-based results show a general improvement in the linear ITG stability as κ increases and a weak dependence on δ . In these studies, the effects of the shaping gradients themselves were also studied via artificially adjusting the elongation gradient and triangularity gradient by a factor of 2 and 0.5 respectively. These results are also shown in figure 4.5. It is generally observed that a high elongation gradient is more stabilizing, while the effect of increased triangularity gradient is much less significant though slightly destabilizing.

Overall, insight about the stabilizing effects of high shaping observed in figures 4.3 and 4.5 can be obtained by considering the equilibrium. Figure 4.6 shows the variation of the curvature drift and k_{\perp}^2 equilibrium parameters with the ballooning mode extended angle θ for the JET-based plasmas (δ is also varied with κ here).

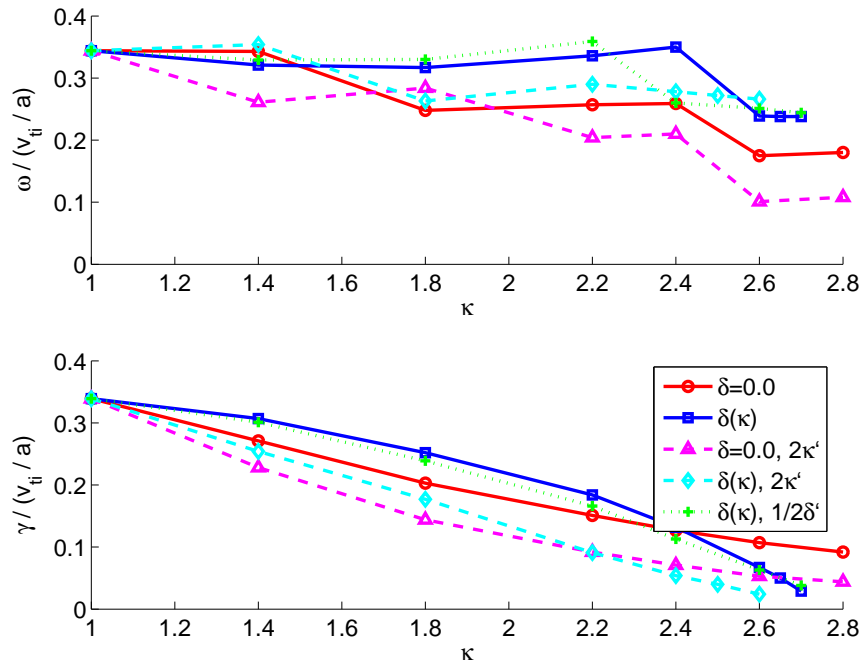


Figure 4.5: Real frequency and linear growth rate vs. elongation for generic-based plasmas in the electrostatic limit comparing variations of triangularity and the radial gradients of the elongation and triangularity.

In general, moderate levels of shaping appear to have little effect on the curvature drift. However, the case of $\kappa = 2.20$ shows a significantly more narrow region in the “bad-curvature” direction. This is also reflected in the k_{\perp}^2 plot, which narrows with increasing shaping. (Instabilities are generally suppressed at large k_{\perp}^2 by FLR averaging, so the region of interest is near $k_{\perp}^2 = 0$.) Thus, the equilibrium plots show that with high shaping, only unstable modes which are very highly localized will persist in the system. It should also be noted that the Jacobian factor associated with the $\partial/\partial l$ operator ($\partial/\partial l = (\partial\theta/\partial l)\partial\theta$) is slightly larger for higher shaping. Freedom in the definition of θ has been exploited to remove the θ dependence from $(\partial\theta/\partial l)$. For these parameters, we find that $(\partial\theta/\partial l)a = \{0.1492, 0.1522, 0.1569\}a$ for the cases of $\{\kappa = 1.00, \kappa = 1.46, \kappa = 2.20, \}$ respectively, thus indicating a higher amount of stabilizing Landau damping with increased shaping.

The effects of shaping on the linear critical temperature gradient were also studied for the JET-based plasmas. The results are shown in figure 4.7 for the electrostatic limit. Note that $\partial_{r/a}\beta$ is varied with shaping (κ and δ) as well as consistently with R/L_T . While shaping was found to be stabilizing in the regime of $R/L_T = 10.81$ in figure 4.3, we find surprisingly that shaping has no significant effect on the linear critical temperature gradient. Specifically, all three shaped plasmas yield a stabilizing gradient for the ITG mode near that observed for the circular shape, i.e. $R/L_T \sim 3.42$. The dashed lines in figure 4.7 for the $\kappa = 1.46$ and $\kappa = 2.20$ cases correspond to constant zero triangularity (rather than varying triangularity with κ as for the solid lines). Again we see that the dependence of the ITG growth rate on δ is insignificant across the entire temperature gradient length scale regime, except for the upshift in the linear critical temperature gradient with zero triangularity for the $\kappa = 2.20$ case.

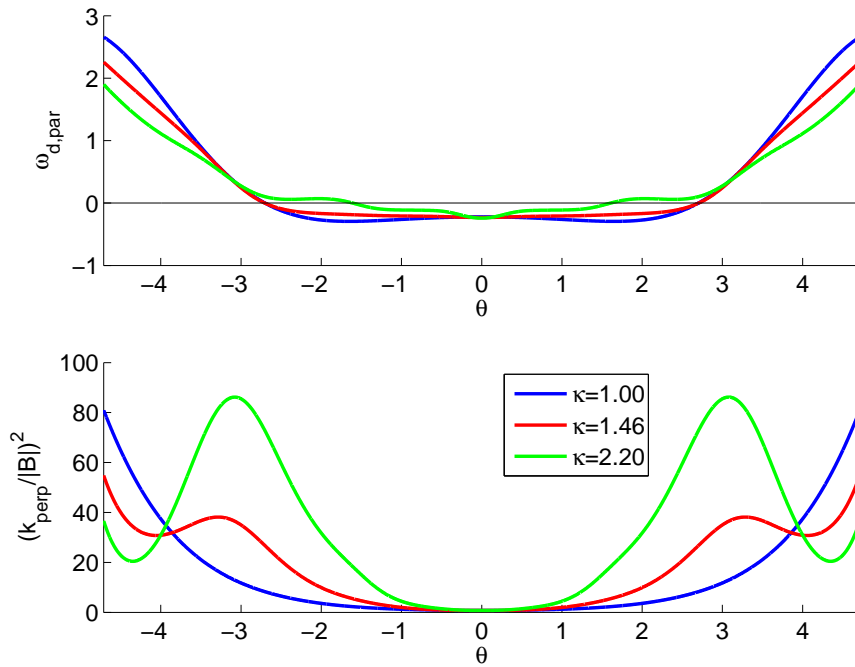


Figure 4.6: Curvature drift (normalized as $\omega_{d,\parallel}/(v_{ti}/a)/(k_y\rho_i)$) and $k_{\perp}^2/|B|^2$ (normalized as $(k_{\perp}^2/k_y)^2/(|B|/|B_0|)^2$) as a function of θ computed using the Miller formalism for JET-based plasma input parameters. $\omega_{d,\parallel} < 0$ corresponds to drifts in the “bad-curvature” direction.

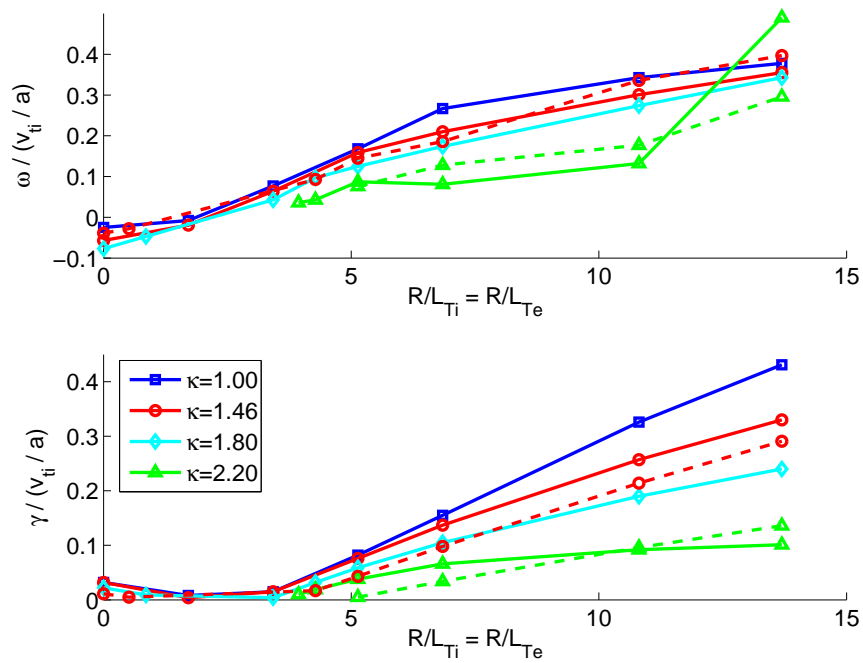


Figure 4.7: Real frequency and linear growth rate vs. temperature gradient length scale for JET-based plasmas in the electrostatic limit. The solid lines correspond to results from varying triangularity with κ , while the dashed lines correspond to zero triangularity.

4.3 Nonlinear ITG Turbulence

Extensions to study the scaling of nonlinear turbulence with shaping have also been explored. The simulation domain for these studies has $L_x = 74.28\rho_i$ and $L_y = 62.83\rho_i$ with the number of grid points in the perpendicular directions given by $N_x = 72$ and $N_y = 36$, such that $\Delta x = 1.05\rho_i$ and $\Delta y = 1.80\rho_i$. In spectral space, this corresponds to resolving nonzero modes in the range $0.085 \leq |k_x\rho_i| \leq 1.95$ and $0.10 \leq k_y\rho_i \leq 1.10$. The domain along the field line has length $L_z = 2\pi qR = 12.75R$, with $N_\theta = 32$ grid points per 2π in θ . The velocity grid has $N_E = 16$ total energy grid points and $N_\lambda = 37$ pitch angle grid points ($\lambda = \mu/E$), divided into trapped and untrapped regions. Runs were performed as typical with time-centering parameter $r = 0.55$ and slight upwind diffusion (spatial-centering parameter $s = 0.55$).

Contours of electrostatic potential for the $\kappa = 1.8$ JET-based case near the beginning and near the end of the simulation can be seen in figure 4.8. (Note that the toroidal width of the simulation domain is not to scale in this figure and is much wider than shown.) At the beginning of the nonlinear stage, when the amplitudes of the Fourier harmonics are small, the spectrum is dominated by the fastest growing linearly unstable, “bad-curvature”-driven modes. This is shown in the early-time visualization in figure 4.8 by the radially elongated eddies (which have zero radial wavenumber) at the outboard midplane, which are extended along the field lines, since parallel Landau damping quickly damps any high k_\parallel components. These eddies basically provide a mechanism for heat and particles to escape from the tokamak. However, as the simulation is evolved, the ExB nonlinearities transfer energy between different k_\perp modes until a statistically steady, yet turbulent steady state is reached. Physically, nonlinear generation of sheared ExB flows essentially

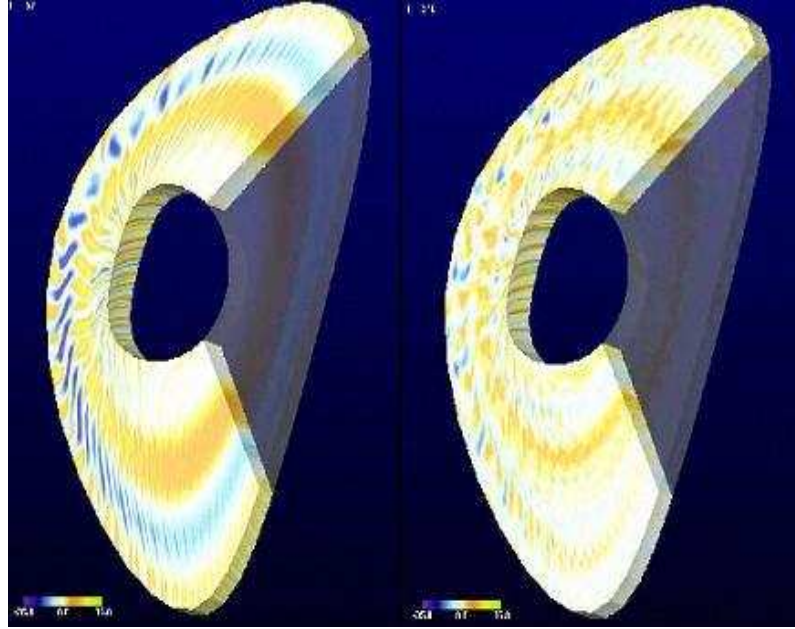


Figure 4.8: Contours of electrostatic potential for the JET-based case of ($\kappa = 1.8$, $\delta(\kappa) = 0.3343$) in the early-time linear phase (left) and in the late-time steady-state turbulent phase (right) for a nonlinear GS2 simulation in the electrostatic limit.

breaks apart the radially elongated eddies and converts them into poloidal flows. This is shown in the late-time visualization in figure 4.8. This process has previously been described by a parasitic instability model, in which the equilibrium is unstable to primary (linear) instabilities, which in turn are unstable to secondary instabilities. The balance between the primary instabilities (which grow like $e^{\gamma_{lin}t}$) and the secondary growth instabilities (which grow with the amplitude of the primary instabilities, i.e. like $e^{\gamma_{lin}t}$) determines the saturation level for the turbulence [COWLEY *et al.*, 1991; ROGERS *et al.*, 2000].

The heat diffusivities presented in this chapter are written in terms of χ_{iter} , a quantity defined by the ITER Expert Group such that the 1D radial heat transport

equation is given by:

$$\frac{3}{2} \frac{\partial(nT)}{\partial t} + \frac{1}{V'} \frac{\partial}{\partial r} \left[V' \langle |\nabla r|^2 \rangle \chi_{iter} \left(n \frac{\partial T}{\partial r} \right) \right] = S_E \quad (4.13)$$

where V is the flux surface volume and $V' = dV/dr$. The transport equation in this form has the advantage that χ_{iter} is independent of the flux surface label r . In our GS2 simulations, we choose r to be the minor radius. Based on the formulation adopted in GS2, χ_{iter} can be computed as

$$\chi_{iter} = \chi_{GS2} \frac{\langle |\nabla r| \rangle}{\langle |\nabla r|^2 \rangle} \quad (4.14)$$

While the geometric quantities $\langle |\nabla r| \rangle$ and $\langle |\nabla r|^2 \rangle$ can be computed exactly for general geometry using Eqs. (4.1) and (4.2), here we assume the limit of concentric ellipses to get a simplified expression for the translation from χ_{GS2} to χ_{iter} , yet one which essentially retains the key dependence on κ . Specifically, this corresponds to

$$R(r, \theta) = R_0 + r \cos(\theta) \quad (4.15)$$

$$Z(r, \theta) = \kappa r \sin(\theta) \quad (4.16)$$

i.e. we have assumed that $\delta = 0$, $\partial_r R_0 = 0$, and $\partial_r \kappa = 0$. This yields that

$$|\nabla r|^2 = (1/\kappa) \left(\kappa^2 \cos^2(\theta) + \sin^2(\theta) \right) \quad (4.17)$$

Taking the flux surface average (given by $\langle f \rangle \equiv (1/V') \frac{\partial}{\partial r} \int dV f$), we find that the

conversion factor for χ_{GS2} is given by:

$$\frac{\langle |\nabla r| \rangle}{\langle |\nabla r|^2 \rangle} = \left(\frac{4}{\pi}\right) \left(\frac{\kappa}{1 + \kappa^2}\right) E(\sqrt{1 - \kappa^2}) \quad (4.18)$$

where $E(x) \equiv \int_0^1 dt \left(\sqrt{1 - x^2 t^2} / \sqrt{1 - t^2}\right)$ is the incomplete elliptic integral.

Though this relation does not include triangularity, the Shafranov shift, nor the radial elongation gradient, we could use it to approximate our JET-based shaping results in terms of χ_{iter} , since we are primarily interested in the dependence of the ITG turbulence on κ . (Recall from figures 4.3 and 4.5 that the dependency of the ITG linear growth rate on both δ and $\partial_{r/a}\kappa$ is relatively weak compared to the dependence on κ .) However, instead we have modified GS2's geometry module to compute this geometric conversion factor numerically for the actual full Miller equilibrium and instead use this to convert our χ_{GS2} results into χ_{iter} . But we can use a comparison of our approximation in Eq. (4.18) to get a qualitative idea of the strength of the triangularity and radial gradients of the elongation and triangularity on the shaping scaling. This is shown in figure 4.9. Overall, over the range of our JET-based shapes, we note that the scaling of this geometrical factor is weak, i.e. it remains fairly close to unity even for the more highly shaped plasmas. Comparing the exact case for $\delta = 0$ with the approximation (which also has zero triangularity), we infer that the effects of the radial gradient of the elongation (and finite Shafranov shift) on the scaling may be relatively weak. However, comparison of the $\delta = 0$ case with the exact case for $\delta(\kappa)$, which shows a reversal in the curve at high shaping, suggests that high elongation when coupled with high triangularity may be influential on the scaling. These inferences are, of course, completely heuristic and do not account for the dynamics in the kinetic computation of the heat flux,

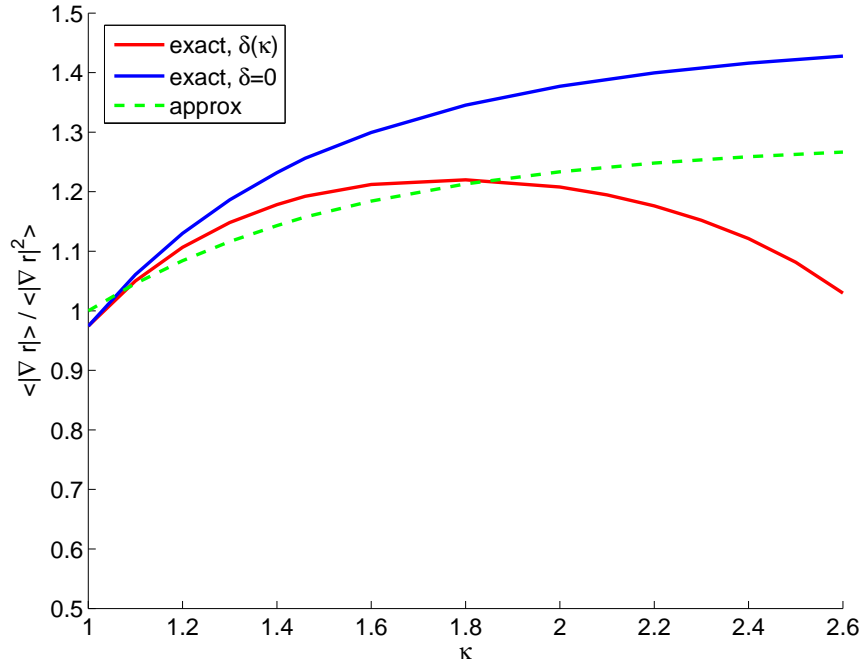


Figure 4.9: Variation of the geometrical quantity $\langle |\nabla r| \rangle / \langle |\nabla r|^2 \rangle$ (which is the conversion factor for $\chi_{GS2} \rightarrow \chi_{iter}$) with κ for JET-based plasmas comparing zero triangularity and triangularity varied with κ and comparing an exact numerical calculation based on the actual Miller equilibrium with an analytic approximation which neglects triangularity, the Shafranov shift, and the radial shaping gradients.

though this figure together with the simulation results may help to identify scaling regimes of the heat flux and give a qualitative understanding of the dependence on triangularity.

The effects of shaping on the nonlinear ITG turbulence in the electrostatic limit for the JET-based plasmas, analogous with the electrostatic linear results in figure 4.3, are shown in figure 4.10. In agreement with the linear results, the nonlinear results show that high shaping has a stabilizing influence. Also, similar to the linear stability, the dependence of the nonlinear heat flux on triangularity is weak across the entire range. It is particularly notable that the results at constant β radial gradient do not vary as strongly with κ . This suggests that most of the variation

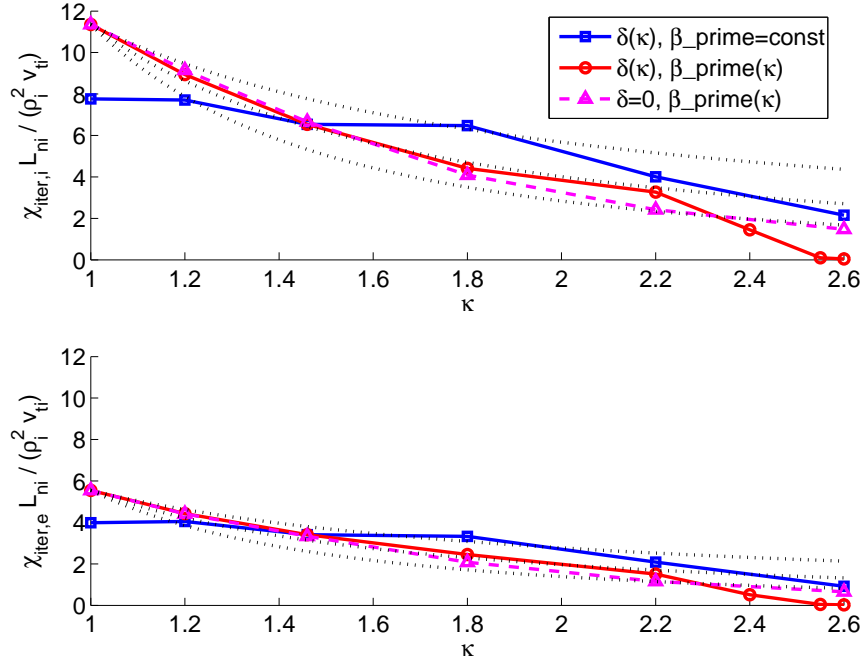


Figure 4.10: Ion and electron heat flux vs. elongation for JET-based plasmas in the electrostatic limit comparing zero triangularity and triangularity varied with κ , as well as comparing constant β radial gradient and β radial gradient varied with κ . The dotted lines show the empirical scalings κ^{-1} , $\kappa^{-1.5}$, and κ^{-2} .

of the standard case $(\delta(\kappa), \beta_{\text{prime}}(\kappa))$ is coming from the variation of $\partial_{r/a}\beta$ as given by Eqs. (4.7) and (4.8). We compare the GS2 data with empirical scalings of κ^{-1} , $\kappa^{-1.5}$, and κ^{-2} , designed to fit the data at $\kappa = 1.0$. These are plotted as the dotted lines in figure 4.10. Qualitatively, we find that both the ion and electron heat flux scale as $\chi \sim \kappa^{-1.5}$. It is further interesting that, in the regime where triangularity is slightly destabilizing, the scaling of the case with zero triangularity becomes stronger ($\chi \sim \kappa^{-2}$). Note from figure 4.9 that the transition between the $\chi \sim \kappa^{-1.5}$ scaling regime and the $\chi \sim \kappa^{-2}$ regime is near where we observed the deviations in the trend of the geometrical heat flux conversion factor $\langle |\nabla r| \rangle / \langle |\nabla r|^2 \rangle$ between the $\delta = 0$ case and the $\delta(\kappa)$ case.

Compared with previous numerical studies, the simulation results in figure

4.10 are within the range of previous gyrofluid results which found a scaling of $\chi \sim 2/(1 + \kappa^2)$ (for $\delta = 0$ and adiabatic electrons) [WALTZ and MILLER, 1999]. However, our nonlinear gyrokinetic simulations of core turbulence overall do not completely explain the much stronger effects of shaping found experimentally, particularly not the strong triangularity dependence observed in tokamaks. For example, in figure 4.11, we show the scaling of $1/\chi$ with κ of various experimentally-based empirical scaling relations in comparison with the scaling of $1/\chi \sim \kappa^{1.5}$ or $\kappa^{2.0}$ observed in our GS2 simulations. The scaling laws which we plot include the standard IPB98(y,2) scaling [ITER PHYSICS EXPERT GROUP ON CONFINEMENT and TRANSPORT *et al.*, 1999], which is based on H-mode global confinement data and was used for the ITER design, for both $\beta = \text{constant}$ (“IPB98y2($\kappa, 0$)”) and $\beta/\beta_{\text{Troyon}} = \text{constant}$ (“IPB98y2(κ, β)”) and the standard Error in Variables scaling of [CORDEY *et al.*, 2005] (“EIV05_maxerr(P)(κ)”), which is similar to the IPB98(y,2) scaling yet uses a modified H-mode database, resulting in a weaker β dependence. From figure 4.11, it is clear that our GS2 simulations yield a weaker scaling than the experiments and thus do not fully capture the strong stabilizing effects of highly shaped plasmas. While the fact that the Dimits nonlinear critical temperature gradient shift depends on shaping, which we observed with the GS2 simulations and show next, may help to explain the remainder of the scaling to match the empirical scaling relations from experiments, stronger shaping dependence in tokamaks most likely comes in through edge boundary conditions for core turbulence, so this will be a key topic of future research. In fact, very recent work by Kendl and Scott exploring the effects of shaping on plasma turbulence for edge-like parameters using gyrofluid simulations shows a scaling of $\chi \sim \kappa^{-4}$ [KENDL and SCOTT, 2006], i.e. a stronger shape dependence than we found with our core

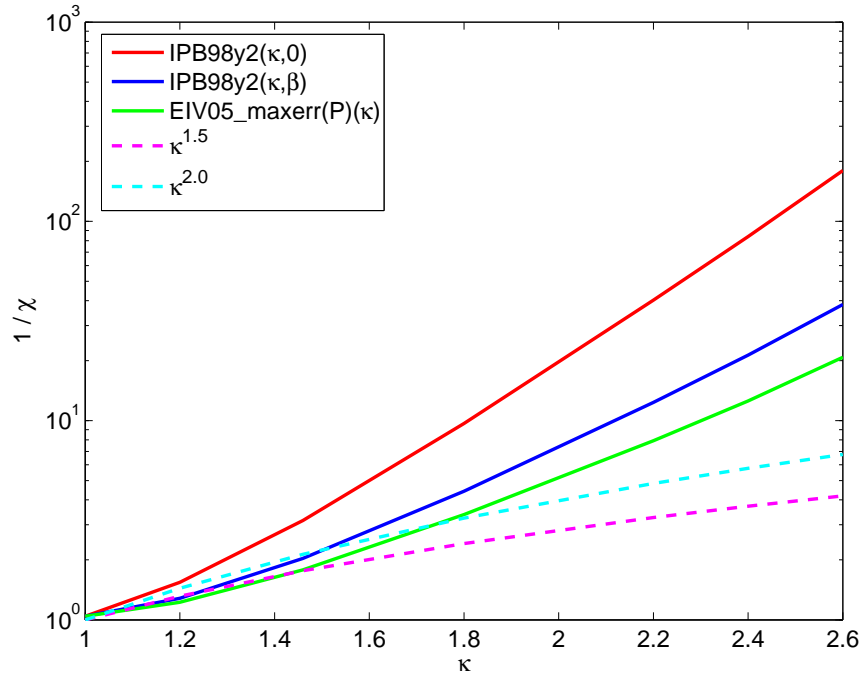


Figure 4.11: Inverse heat flux vs. κ (assuming triangularity varies with κ) for various experimentally-based empirical scaling laws, namely the standard IPB98(y,2) H-mode scaling for $\beta = \text{constant}$ (“IPB98y2($\kappa, 0$)”) and for $\beta/\beta_{Troyon} = \text{constant}$ (“IPB98y2(κ, β)”) and the standard Error in Variables scaling of Cordey et al. (“EIV05_maxerr(P)(κ)”). For comparison, the scalings of $\kappa^{1.5}$ and $\kappa^{2.0}$ (observed in our GS2 simulations) are shown.

gyrokinetic simulations. There are a number of differences between core and edge turbulence, such as the stronger role played by nonlinear non-adiabatic electron dynamics in edge turbulence, which could be interesting to explore further.

Here we present results from studies of the effects of shaping on the nonlinear critical temperature gradient. The GS2 simulation results are shown in figure 4.12 for the electrostatic limit. While shaping was found to be stabilizing on the nonlinear ITG turbulence in the regime of $R/L_T = 10.81$ in figure 4.10 in agreement with the linear results, here we see that shaping is also stabilizing near the regime of zero net heat flux. In particular, the results show that the nonlinear critical

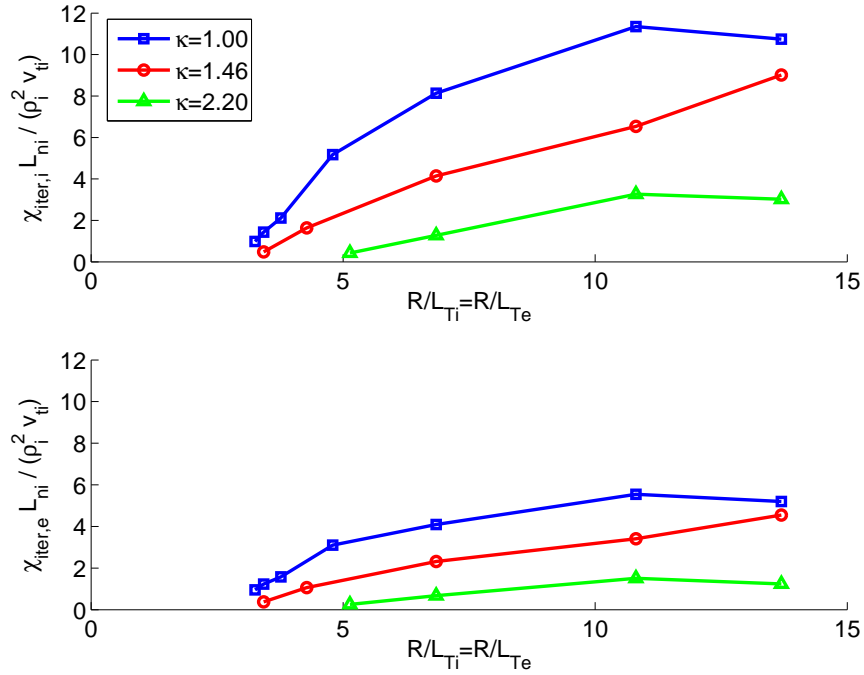


Figure 4.12: Ion and electron heat flux vs. temperature gradient length scale for JET-based plasmas in the electrostatic limit for triangularity varied with κ .

temperature gradient increases with strong shaping. For example, $R/L_{Tc} \sim 3.42$ for the $\kappa = 1.00$ and $\kappa = 1.46$ cases, while $R/L_{Tc} \sim 5.13$ for the $\kappa = 2.2$ case. This is unlike the linear results in figure 4.7 which showed that shaping has little effect on the linear critical temperature gradient.

The results of figure 4.12 are somewhat surprising and worthy of further analysis. Here we show that the larger upshift of the nonlinear critical temperature gradient with higher shaping may be due to enhanced zonal flows. Zonal flows are the purely poloidal flows (i.e. $k_y = 0$ modes) driven by ITG turbulence which are believed to play an important role in saturating the level of the turbulence [HAMMETT *et al.*, 1993; DIMITS *et al.*, 1996; DIMITS *et al.*, 2000]. Rosenbluth and Hinton found analytically that a component of the zonal flows is undamped by linear collisionless

processes and that the residual amplitude of these flows scales as

$$\frac{\Phi_{fin}}{\Phi_{init}} = \frac{1}{1 + \frac{1.6}{h}} \quad (4.19)$$

where $h = \sqrt{\epsilon}/q^2$ (where $\epsilon = r/R$ is the inverse aspect ratio) [ROSENBLUTH and HINTON, 1998]. This result was derived for concentric circular plasmas. However, h is related to the physics of banana widths, which depends on the poloidal magnetic field, and thus it is natural that h should scale with the shaping parameters.

Physically, what we are considering here is the bounce-averaged gyrokinetic response of the plasma to shield an externally imposed Φ . This has been explained qualitatively by [HAMMETT, 1997], which we summarize here. The usual classical gyroradius shielding comes from the ion polarization density term $\propto (1 - \Gamma_0(k_\perp^2 \rho_i^2))$ in the gyrokinetic Poisson equation (see the LHS of Eq. (2.4)). Thus, in the limit of small $k_\perp \rho_i$, the classical perpendicular plasma dielectric can be approximated as $D_{classical} \sim 1 + \rho_i^2/\lambda_{Di}^2 \sim \rho_i^2/\lambda_{Di}^2 \gg 1$, where λ_{Di} is the Debye length ($\lambda_{Di}^2 = \frac{T_{0i}}{4\pi n_{0i} Z_i e^2}$). This shielding effect is set-up in a short time, i.e. after a few gyroperiods. In the long time limit, i.e. after a few bounce times, neoclassical polarization shielding also arises due to the distortion of the banana orbits by the radial electric field. Thus, the neoclassical perpendicular plasma dielectric scales as $D_{neoclassical} \sim (\rho_{banana}^2/\lambda_{Di}^2) f_{trapped}$, where $\rho_{banana} \sim \rho_i q/\sqrt{\epsilon}$ is the banana orbit width and $f_{trapped} \sim \sqrt{\epsilon}$ is the fraction of trapped particles (representing the fact that trapped particles have larger radial excursions off a flux surface than passing particles). Thus, we find that $D_{neoclassical}/D_{classical} \sim q^2/\sqrt{\epsilon}^2 = 1/h$. Assuming an initial Φ due only to the classical polarization density, in the long

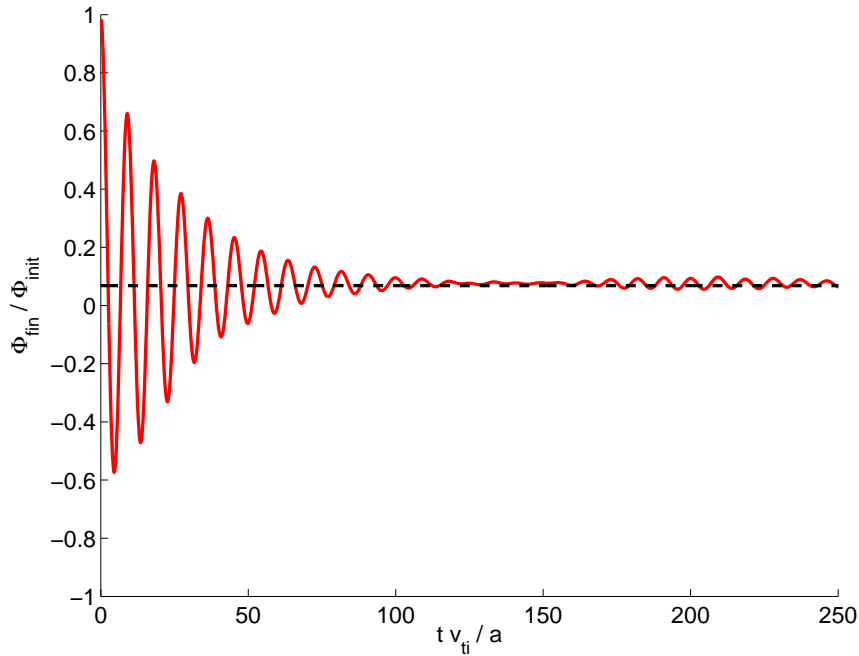


Figure 4.13: Time evolution of the amplitude of the zonal flows for the JET-based circular case computed using GS2 with an initial external potential $\Phi_{ext} \sim (1/k_r) \cos(k_r r)$. The dashed line shows the Rosenbluth-Hinton prediction for these parameters ($h = 0.1171$).

time limit considered by Rosenbluth and Hinton (i.e. $\omega \ll \omega_{bounce}$), Φ will be reduced due to the neoclassical enhancement of polarization shielding by a factor of $D_{classical}/(D_{neoclassical} + D_{classical})$, which we find scales as $\sim 1/(1 + 1/h)$, in qualitative agreement with the Rosenbluth-Hinton result given in Eq. (4.19). (The factor of 1.6 in Eq. (4.19) comes from a more accurate kinetic calculation which also includes the contribution of passing particles.) Physically, in the time evolution, the amplitude of the potential appears as the superposition of transit-time damping oscillations (known as the geodesic acoustic modes) and an undamped residual component (which we refer to as the Rosenbluth-Hinton component of the zonal flows), as shown in figure 4.13.

Here we explore the effects of shaping on the Rosenbluth-Hinton residual flows,

focusing specifically on the dependence of h on shaping. Using GS2, we find the amplitude of the Rosenbluth-Hinton residual flows by adding an external Φ to the gyrokinetic Poisson equation and then computing the response of the plasma to it. Figure 4.14 shows the results, specifically the saturated amplitude of the Rosenbluth-Hinton residual zonal flows vs. κ for the JET-based parameters. Overall, we find that shaping enhances the Rosenbluth-Hinton component of the zonal flows. This provides an explanation for the larger upshift of the nonlinear critical temperature gradient with higher shaping observed in figure 4.12, since zonal flows help to saturate the turbulence.

A model prediction for the scaling of h with shaping was found empirically based on these GS2 results, assuming

$$\frac{\Phi_{fin}}{\Phi_{init}} = \frac{1}{1 + \frac{1.6}{Ch_{shaping}}} \quad (4.20)$$

where

$$h_{shaping} = \frac{\sqrt{\epsilon}}{q^2} f(\kappa, \delta) \quad (4.21)$$

The constant $C=0.887$ was chosen to match the GS2 circular case with the original Rosenbluth-Hinton model. (Note that Rosenbluth-Hinton assumed concentric circular plasmas, while our JET-based plasmas have a non-zero Shafranov shift.) A good fit was found with the shaping function

$$f(\kappa, \delta) = \frac{1}{2} [1 + \kappa^2 (1 + \delta)^2] \quad (4.22)$$

This is shown as the lines in figure 4.14. Note the good agreement between the GS2 results and the model prediction both with zero triangularity and with triangularity

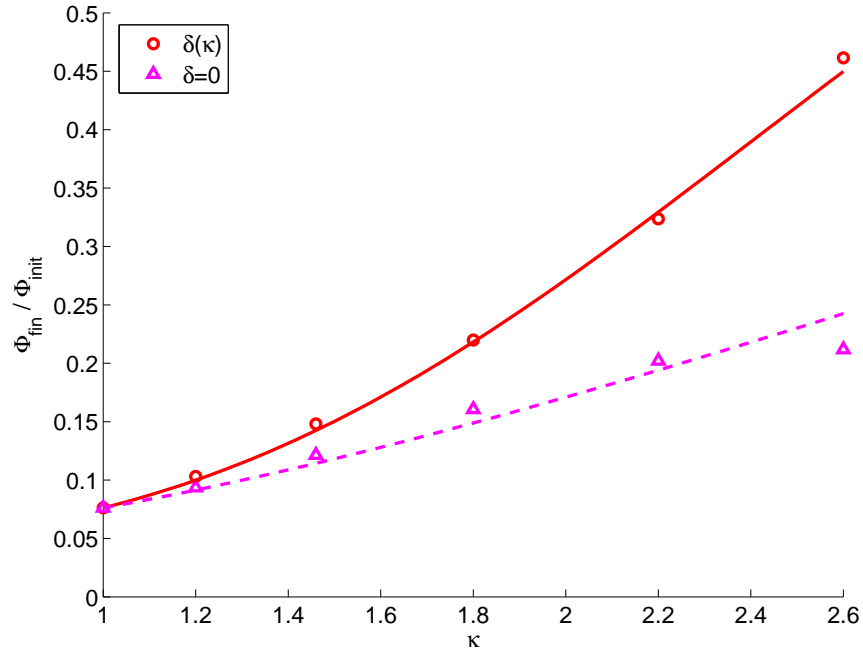


Figure 4.14: Amplitude of the Rosenbluth-Hinton residual zonal flows vs. elongation for JET-based plasmas in the electrostatic limit comparing zero triangularity with triangularity varied with κ . The data points are the GS2 results; the lines are the analytic model prediction.

varied with δ . It is interesting to compare this shaping function with that found empirically based on experiments for the pressure limit, such as the Troyon β limit given by Eq. (4.6). The shaping function of Eq. (4.22) for the residual zonal flows has a similar κ dependence as the empirical Troyon β limit, yet with a slightly weaker δ dependence. Future work could pursue a more rigorous analytic physics-based calculation of $f(\kappa, \delta)$. However, overall, this analysis shows that geometry does affect the residual zonal flows, and this may help to explain why strong shaping is favorable in experiments.

4.4 Electromagnetic Effects

The effects of electromagnetic dynamics (i.e. finite β) coupled with shaping are also explored for the JET-based plasmas. For these studies, both β and $\partial_{r/a}\beta$ are varied with shaping, as given by Eqs. (4.7) and (4.8) respectively. These results are thus analogous to those above performed in the electrostatic limit in which $\partial_{r/a}\beta$ was varied but the dynamical parameter β was zero. For these electromagnetic results, we retain the parallel Ampere equation in addition to Poisson equation, though we neglect compressional magnetic perturbations (i.e. $\delta B_{\parallel} = 0$), which are generally insignificant for low β tokamak plasmas (but can be important for high β plasmas like NSTX [BOURDELLE *et al.*, 2002]).

4.4.1 Linear Results

We first consider the linear limit to develop insights and then consider extensions to include nonlinear dynamics. Figure 4.15 shows the variation of the linear growth rate with κ comparing the electrostatic $\beta = 0$ limit and the electromagnetic $\beta(\kappa)$ description for the same equilibrium (i.e. $\partial_{r/a}\beta$ is varied with shaping for both cases). The results show a general enhanced stability of the linear ITG mode with electromagnetic effects (except at the highest κ). This is expected for $\beta < \beta_c$, where β_c is the threshold for the kinetic ballooning instability. Specifically, it has been shown previously that, considering a scan over β , the ITG mode dominates at low β ($< \beta_c$) and is stabilized with increased β . As β is further increased, the kinetic ballooning mode dominates and is further destabilized with increasing β [KIM *et al.*, 1993], though 2nd stability can occur at high β , depending on the value of $\partial_{r/a}\beta$.

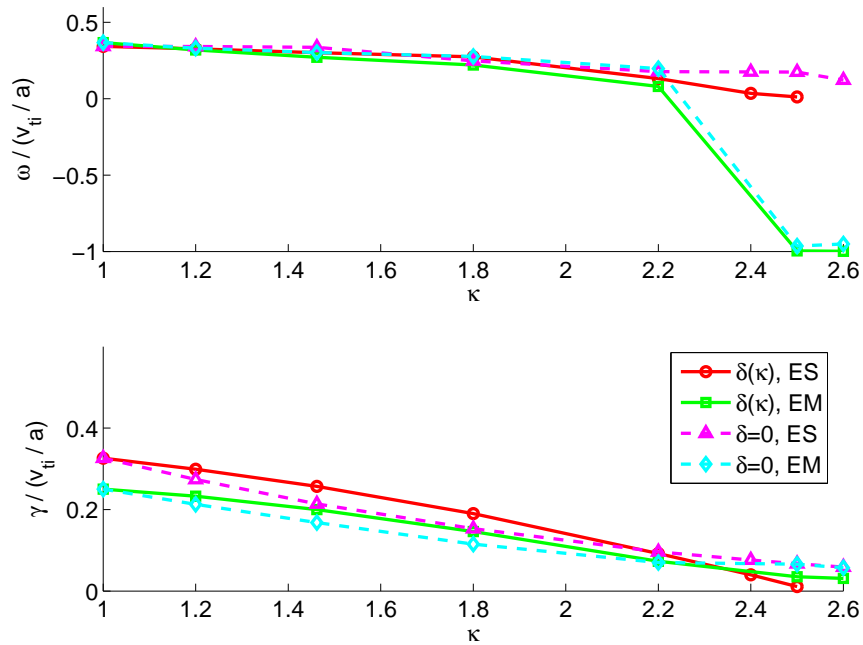


Figure 4.15: Real frequency and linear growth rate vs. elongation for JET-based plasmas comparing the electrostatic limit (i.e. $\beta = 0$) and the electromagnetic description (i.e. $\beta(\kappa)$) for both zero triangularity and triangularity varied with κ . (Note that the β radial gradient is varied with κ for both cases.)

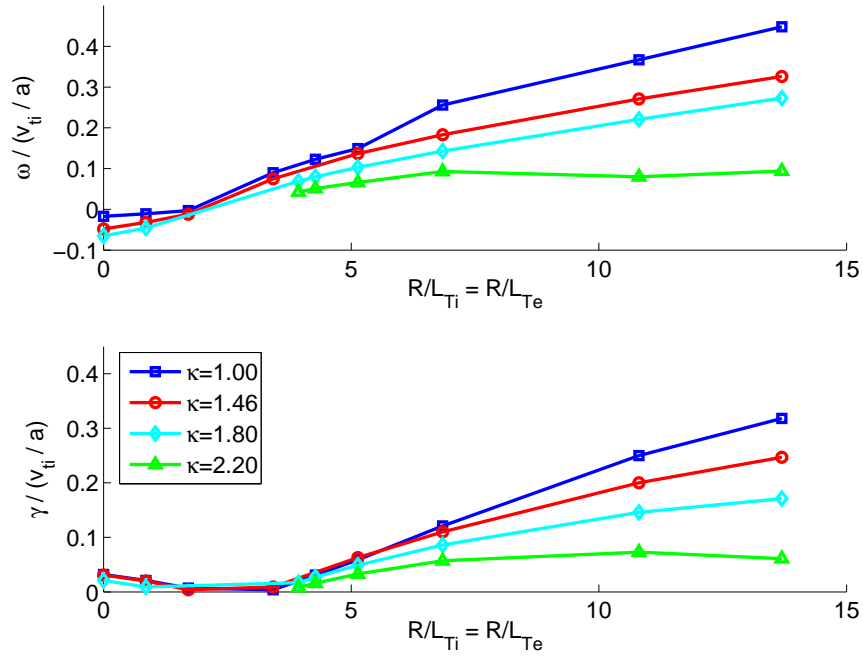


Figure 4.16: Real frequency and linear growth rate vs. temperature gradient length scale for JET-based plasmas with electromagnetic dynamics.

The electromagnetic analog of the linear scan over the temperature gradient length scale in figure 4.7 is shown in figure 4.16. As with the electrostatic results, the electromagnetic results also show surprisingly that, while higher shaping is stabilizing for steep temperature gradients, shaping has no effect on the linear critical temperature gradient. Furthermore, comparing figure 4.7 and figure 4.16, while electromagnetic dynamics are stabilizing in the regime of high R/L_T (as observed in figure 4.15), the value of the linear critical temperature gradient does not shift with electromagnetic effects.

The relationship between $\beta(\kappa)$ and β_c is explored in figure 4.17, which shows a linear scan over β for the JET-based plasmas. For the noncircular plasmas, as β increases, the linear growth rate decreases, i.e. β is stabilizing over the entire range. While a mode transition from the dominant ITG mode to a dominant mode

in the electron direction occurs (note that this latter mode was also observed in figure 4.15 at the highest shaping values with electromagnetic effects), there is no evidence of transition through a dominant kinetic ballooning instability regime, but rather directly to a 2nd stabilizing regime. This is different from the circular case ($\kappa = 1.0$, $\delta = 0.0$), where there is a regime at intermediate β where the kinetic ballooning instability dominates. Consider the circular case in more detail. At low β , the dominant ITG mode is stabilized as β is increased. However, near $\beta \sim 0.01$, transition to a strongly destabilized mode is observed. This mode peaks at small $k_y \rho_i$ (~ 0.1), as is typical of the kinetic ballooning instability. However, as β is further increased, a second transition occurs to the dominant negative real frequency mode that was also observed with the noncircular plasmas. Thus, these results suggest that shaping opens up to a type of 2nd stability regime.

A simple estimate for the ideal MHD ballooning instability limit can be obtained using a program provided by GS2, which finds the solution of the Euler-Lagrange equation for the variational energy δW using the same geometrical information used for the GS2 gyrokinetic simulation. This yields that $\beta_c \sim 0.00671$ for the $\kappa = 1.00$ case, which is in approximate agreement with the kinetic ballooning limit shown in figure 4.17. As shaping increases, the estimate for the ideal MHD ballooning threshold significantly increases. For example, $\beta_c \sim 0.0101$ for the $\kappa = 1.20$ case, $\beta_c \sim 0.0182$ for the $\kappa = 1.46$ case, and no instability was found for the higher shapes. However, no kinetic ballooning instability regime was observed for any of the shaped plasmas with the gyrokinetic simulation. From this, we note that even for the $\kappa = 1.20$ and $\kappa = 1.46$ cases, $\beta(\kappa)$ is well below even the estimated MHD β_c . This is important for the nonlinear electromagnetic simulations presented in section 4.4.2, since the growth at small $k_y \rho_i$ associated with the kinetic ballooning

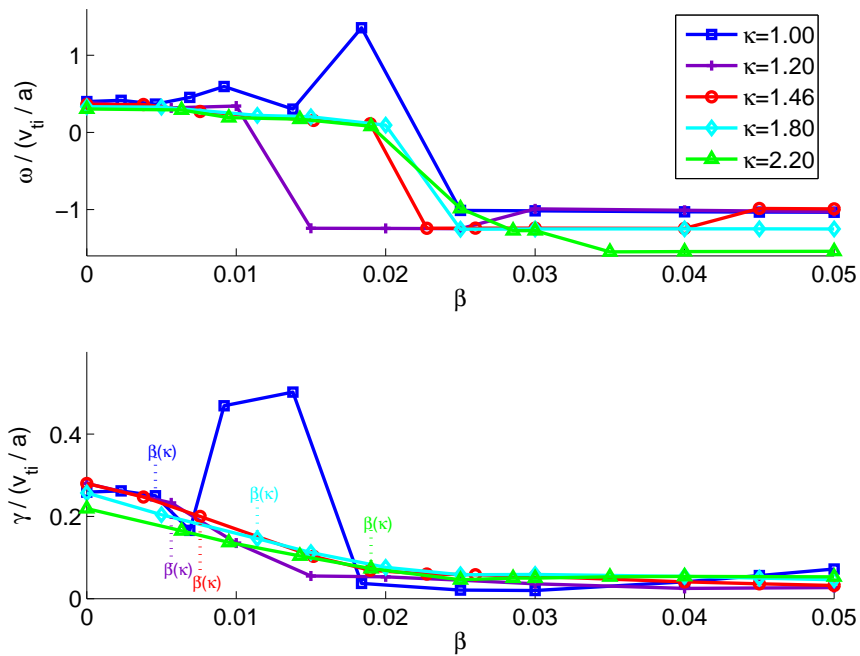


Figure 4.17: Real frequency and linear growth rate vs. β for JET-based plasmas for triangularity varied with κ . (Note that the β radial gradient is varied consistently with β .) The points marked $\beta(\kappa)$ denote the standard case β values using the assumed variation of β with shaping given by Eq. (4.7).

instability can cause unsaturated transport.

However, we should note that in figure 4.17, only the growth rates for the dominant modes in a scan of $k_y \rho_i$ over the range $[0.1, 1.0]$ are reported. This means that, for the noncircular cases, a kinetic ballooning mode may exist, but might not be dominant over the ITG mode. To check this, we examine the scans of $k_y \rho_i$ at constant β , as shown in figure 4.18 for $\beta(\kappa)$ (and for $\beta = 0$ for comparison with the electrostatic ITG mode). Recall that the ballooning mode is generally marked by significant growth at small $k_y \rho_i$ ($< \sim 0.1$), while the ITG mode tends to dominate at moderate $k_y \rho_i$ ($\sim 0.3 - 0.6$). Figure 4.18 shows no growth at small $k_y \rho_i$ for $\beta = \beta(\kappa)$ for any noncircular case, indicating that these cases are not near the ballooning limit. In contrast, note that the $\kappa = 1.00$ case shows evidence of the ballooning instability for β near its estimated β_c (the dashed curve). Surprisingly, however, the $\kappa = 1.46$ case does not show evidence of the ballooning instability, not even near its estimated β_c . In any case, these results support the conclusion that $\beta(\kappa)$ is well below β_c for all of the shaped plasmas.

Overall, the main result of figure 4.17 that shaping opens up access to a type of 2nd stability regime is supported by a previous study which we performed based on a generic equilibrium. This study focuses on the variation of the linear growth rate with α (and varying β consistently) at various values of global shear, thus paralleling an MHD \hat{s} - α stability analysis. The parameters for this study are based on a generic equilibrium used as a test case in [MILLER *et al.*, 1998]: $r/a = 0.83$, $R/a = 2.63$, $\partial_r R_0 = -0.354$, $q = 3.03$. Two sets of shaping parameters are compared: $\kappa = 1.66$ with $\partial_{r/a} \kappa = 1.4$ (original Miller parameters) and $\kappa = 2.00$ with $\partial_{r/a} \kappa = 2.12$ ($= (1.4/0.66) * (\kappa - 1)$, i.e. assumed linear interpolation); $\delta = 0.0$ with $\partial_{r/a} \delta = 0.0$ and $\delta = 0.7$ with $\partial_{r/a} \delta = 0.84$ ($= \delta/(r/a)$). In the GS2 simulations,

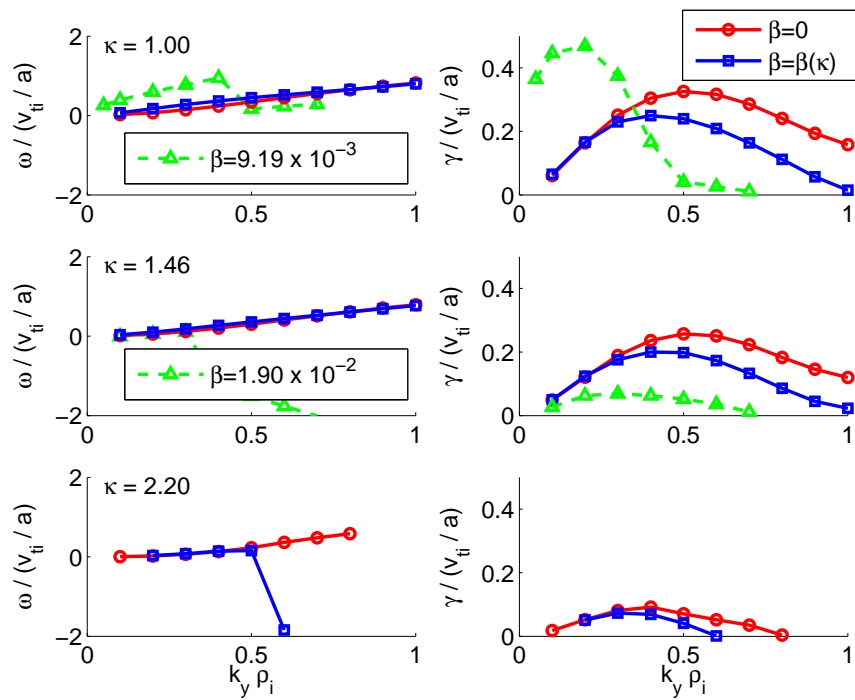


Figure 4.18: Real frequency and linear growth rate vs. $k_y \rho_i$ at constant β for JET-based plasmas for triangularity varied with κ comparing the electrostatic ($\beta = 0$) limit and the electromagnetic (finite β) description. The dashed curves correspond to β near the estimated ideal MHD ballooning limit.

we use a single ion species and include gyrokinetic electrons with the following base case parameters: $R/L_{ni} = R/L_{ne} = 2.63$, $R/L_{Ti} = R/L_{Te} = 7.89$, $T_{0i} = T_{0e}$, $\nu_{ei}/(v_{ti}/a) = \nu_{ii}/(v_{ti}/a) = 0$.

Figure 4.19 shows the results at high shear ($\hat{s} = 2.85$), while figure 4.20 shows the results at $\hat{s} = 1$ and $\hat{s} = 0$. These results show that at a fixed κ , increasing δ has a destabilizing effect at low α , yet can have a stabilizing influence at high α . In particular, for the high shear case, a kind of 2nd stability regime is observed at high α and high δ . This can be contrasted with the zero triangularity cases which show transition from a stabilizing regime at low α to a destabilizing regime at moderate to high α . Overall, this observed effect that high triangularity opens up access to a type of 2nd stability regime at high α is qualitatively similar to previous studies of the effects of triangularity on MHD ballooning stability [MILLER *et al.*, 1998]. (In our case, complete stabilization is not observed, but the growth rates of the microinstabilities are decreasing as α increases in this 2nd stability-like regime.) In contrast, the low shear results in figure 4.20 show that the effect of δ on the stability at high α is not significant. However, the destabilizing effect of δ at low α are qualitatively similar to that at high shear.

Comparing the effects of elongation alone, in figure 4.19 we also see that high elongation has a stabilizing effect at both low and high α . This is qualitatively consistent with the linear κ scan for the generic equilibrium at fixed $\alpha = 0$ in figure 4.5 and the JET-based equilibrium in figure 4.3 (electrostatic) and in figure 4.15 (electromagnetic). In the context of the JET-based results of figure 4.17, these results are in agreement in that the $\kappa = 1$ JET-based plasma showed a destabilizing region at moderate β (and β gradient, which scales with α), while the more highly shaped plasmas (with increased κ and δ) transitioned more rapidly to

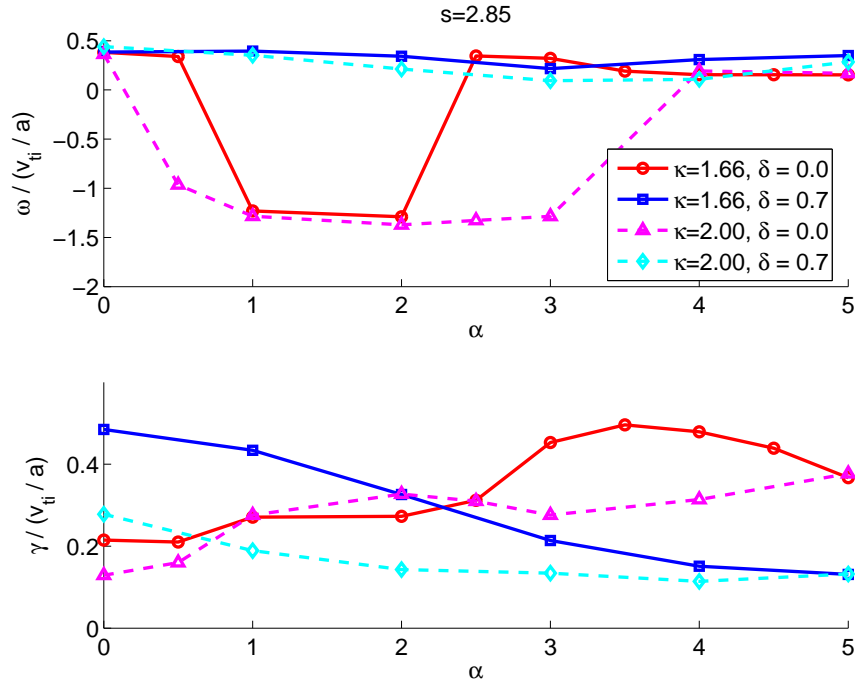


Figure 4.19: Real frequency and linear growth rate vs. α (also varying β) for generic-based plasmas with electromagnetic dynamics at a global shear $\hat{s} = 2.85$.

a 2nd stability-like regime at high β .

4.4.2 Nonlinear Results

The effects of the shaping on the nonlinear ITG turbulence with electromagnetic dynamics are presented here. The simulation domain for these studies was modified from that for the electrostatic nonlinear simulations to give finer resolution in k_x . Specifically, the simulation domain for the electromagnetic nonlinear simulations has $L_x = 151.92\rho_i$ and $L_y = 85.68\rho_i$ with the number of grid points in the perpendicular directions given by $N_x = 64$ and $N_y = 48$, such that $\Delta x = 2.41\rho_i$ and $\Delta y = 1.82\rho_i$. In spectral space, this corresponds to resolving nonzero modes in the range $0.041 \leq |k_x\rho_i| \leq 0.87$ and $0.073 \leq k_y\rho_i \leq 1.10$. The resolution along the field

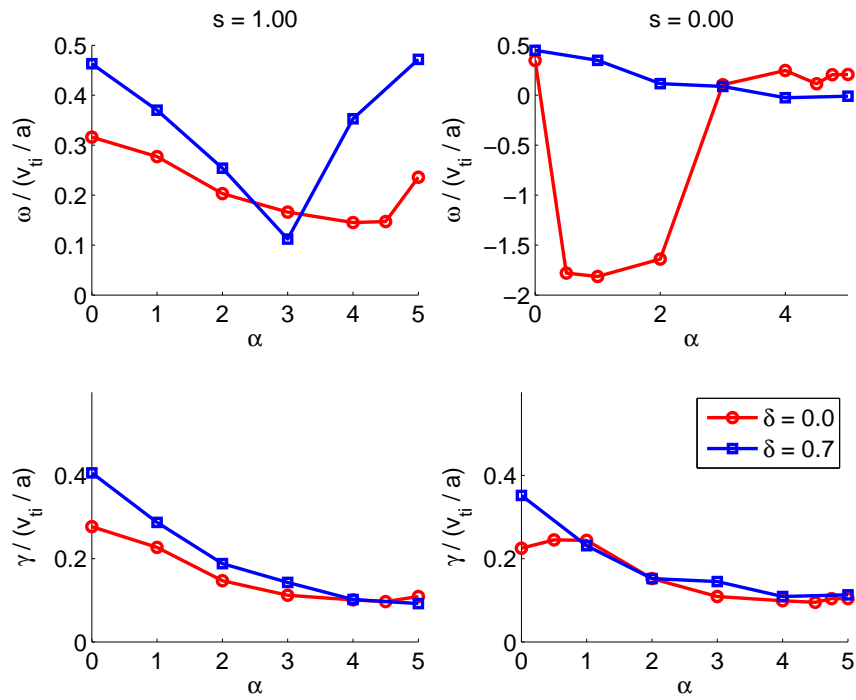


Figure 4.20: Real frequency and linear growth rate vs. α (also varying β) for generic-based plasmas with $\kappa = 1.66$ with electromagnetic dynamics at global shear $\hat{s} = 1.00$ and 0.00 .

line and in velocity space was the same as for the electrostatic nonlinear results.

The nonlinear results with electromagnetic dynamics, analogous with the linear results in figure 4.15, are shown in the LHS plots in figure 4.21 for various values of β relative to $\beta(\kappa)$. For comparison, the electrostatic case ($\beta = 0$, $\partial_{r/a}\beta(\kappa)$) is also shown. For the electromagnetic results, $\partial_{r/a}\beta$ is varied consistently with β . Surprisingly, while finite β was found to be stabilizing on the ITG linear growth rate, with nonlinear effects we find that β strongly negatively affects the electron transport. In fact, unsaturated transport was observed in some cases, particularly as $\beta/\beta(\kappa)$ increases and as shaping decreases. (For example, unsaturated transport occurred as low as $\beta = \frac{1}{3}\beta(\kappa)$ for the $\kappa = 1.00$ case.) However, we address these cases of observed unsaturated transport separately in Appendix C, as more comprehensive numerical convergence studies may be needed to exclude the possibility of numerical issues for these cases. Regardless, we can observe from the results in the figure 4.21 that the negative effects of β on the nonlinear ITG turbulence are strongest for more circular plasmas. The general result that β has little effect at high shaping (such as shown in the results for the $\kappa = 2.20$ case) is in agreement with the linear results in figure 4.15.

Overall, the observed strong effect of β on the electron transport is surprising since the linear results in figure 4.17 show that $\beta(\kappa)$ is well below the linear kinetic ballooning limit for all of these cases. (Recall that growth at small $k_y\rho_i$ associated with the kinetic ballooning instability can cause unsaturated transport.) In fact, these nonlinear gyrokinetic results are even more extreme than previous gyrofluid results which showed dramatically enhanced transport as β is increased above $\sim \beta_c/2$ [SNYDER, 1999]. Those gyrofluid results had also shown significant reduction in transport for low values of β , analogous with stabilization of the linear ITG mode

with finite β . So it is somewhat surprising that, even as β is decreased, we do not observe nonlinear finite β stabilization. However, studies over a more extended lower regime of β may be needed. Recent gyrokinetic results from the GYRO code run in the flux tube limit with \hat{s} - α geometry found that, in a scan over β , finite β has a weak effect on the ion transport, yet a strong effect on the electron transport, with roughly 50% of the total electron thermal diffusivity being driven by magnetic flutter just above $\beta_{e,c}/2$ [CANDY, 2005]. Our results at low shaping, including looking at the dashed lines in figure 4.21 which denote the component of χ_e due to magnetic flutter transport, are at least qualitatively in agreement with the GYRO results.

Studies of the effects of shaping on the nonlinear critical temperature gradient in the presence of electromagnetic dynamics are also of interest and a topic of future research. Presently, this is difficult due to the computational intensity of nonlinear electromagnetic gyrokinetic simulations. However, as a beginning, we have also performed GS2 simulations using a smaller temperature gradient length scale, specifically $R/L_T = 5.31$, i.e. near the nonlinear critical gradient for $\kappa = 2.20$ in the electrostatic limit shown in figure 4.12. These simulations were performed only for the cases of $\beta = 0$ and $\beta = \frac{1}{3}\beta(\kappa)$. The results are shown in the RHS plots in figure 4.21 for comparison with the LHS plots corresponding to the base-case steeper temperature gradient length scale of $R/L_T = 10.81$. Note that for these runs, $\partial_{r/a}\beta$ is varied consistently with both β and R/L_T . For these results, it is not surprising that finite β does not appear to significantly affect the nonlinear critical temperature gradient for $\kappa = 2.20$, since we already observed that this case is not strongly affected by β linearly nor nonlinearly at a higher temperature gradient. However, at moderate shaping, finite β appears to have a smaller effect on both

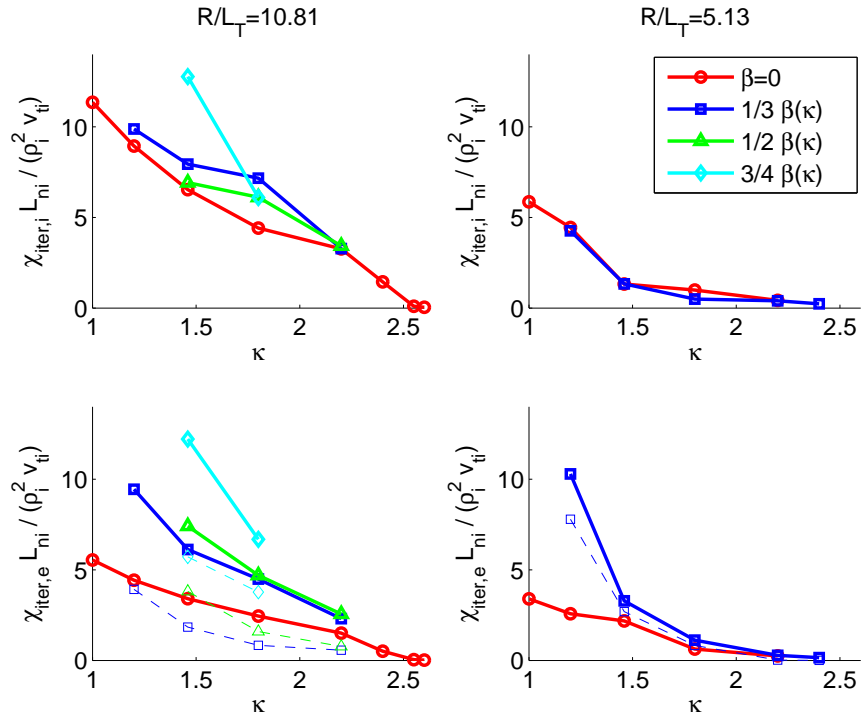


Figure 4.21: Ion and electron heat flux vs. elongation for JET-based plasmas with electromagnetic dynamics for triangularity varied with κ comparing various values of β . (Note that the β radial gradient is varied consistently as β is varied, except for the electrostatic ($\beta = 0$) case for which $\partial_{r/a}\beta = \partial_{r/a}\beta(\kappa)$). The dashed lines denote the component of χ due to magnetic flutter transport (from $A_{||}$).

the electron and ion heat flux at this lower R/L_T compared with the standard case at higher R/L_T . This may indicate that β may not have a strong effect on the nonlinear critical temperature gradient, though of course a comprehensive study analogous with the nonlinear electrostatic temperature gradient scan in figure 4.12 is necessary.

4.5 Summary

The GS2 code has been used to study the effects of flux surface shape on the gyrokinetic stability and transport of tokamak plasmas. Studies of the scaling of the linear growth rate and nonlinear turbulence with shaping parameters were performed starting with a representative JET-like flux surface and artificially varying elongation, triangularity, and their radial gradients together using the Miller analytic local equilibrium model to approach the circular limit via linear interpolation. In the electrostatic limit, high elongation was found to have a stabilizing influence on both the linear ITG instability and the nonlinear ITG turbulence. Triangularity was somewhat destabilizing at moderate κ or α , but could be stabilizing at high κ or combined high α and high \hat{s} . A general scaling of $\chi \sim \kappa^{-1.5}$ was found for the nonlinear turbulence, with a slightly stronger dependence on κ of $\chi \sim \kappa^{-2}$ with zero triangularity in the high κ regime where triangularity is destabilizing. This scaling is consistent with previous gyrofluid simulations [WALTZ and MILLER, 1999]. Investigations of the effects of shaping on the critical temperature gradient showed that, while shaping had little effect on the linear critical temperature gradient, high shaping resulted in a larger upshift of the nonlinear critical temperature gradient due to enhanced zonal flows.

The effects of electromagnetic dynamics coupled with shaping were also explored. In these studies, β was varied with shaping to keep the Troyon-normalized β fixed while also holding q_{95} fixed. Linearly, finite β was found to be stabilizing. A scan over β found that shaping opens up access to a type of 2nd stability regime, and an apparent increase in the threshold of the linear kinetic ballooning instability with higher shaping was observed. However, nonlinear results showed that β strongly negatively affects the electron transport, particularly for more circular

plasmas, even at $\beta \ll \beta_c$. Future nonlinear studies will focus on a scan over a wider range of β and R/L_T . The effects of shaping on the Dimits nonlinear critical temperature gradient in the presence of electromagnetic dynamics may be of particular interest for future work.

Overall, while our nonlinear gyrokinetic simulations of core turbulence capture some of the shaping effects found experimentally, they do not completely explain the degree of this dependence on shaping, particularly the strong triangularity dependence observed in tokamaks. While the result that the Dimits nonlinear shift is enhanced with shaping may help to further explain why shaping is favorable in experiments, the experimentally-observed strong triangularity dependence is most likely related to the edge boundary conditions for core turbulence and will be explored in future research. Furthermore, future work to develop a more complete understanding of shaping effects could include scanning shaping parameters over a range of values of q , as some previous gyrofluid work suggests that stronger κ dependence at lower q [WALTZ and MILLER, 1999], or exploring higher degree shaping moments such as “squareness” (which modifies the D-shaped plasma formula in Eqs. (4.1) and (4.2) by $Z_s \rightarrow \kappa r(\sin(\theta) + \zeta \sin(2\theta))$, where ζ is the squareness parameter), which has been found to have a significant stabilizing effect in some DIII-D experiments [FERRON *et al.*, 2000; OSBORNE *et al.*, 2000] and in MHD studies [TURNBULL *et al.*, 1999].

Chapter 5

Trial Function-Based Methods

A common approach of gyrokinetic simulations is to use reduced spatial geometry via consideration of the gyrokinetic equation in the flux tube limit. Flux tube-based simulations use a simulation geometry which resolves only a thin flux tube (or equivalently, a fraction of the toroidal direction of a thin annulus) rather than the full torus. This geometry essentially exploits the elongated nature of the turbulence, which has short perpendicular scales and long parallel scales. In the linear limit, flux tube geometry is equivalent to the ballooning representation, so the gyrokinetic equation reduces to a 1D equation in coordinate space along the equilibrium magnetic field line on a single chosen magnetic surface. The numerical advantage is that flux tube simulations allow for high resolution simulations in realistic geometries while more easily retaining more significant physical effects, such as non-adiabatic electron dynamics and nonlinear electromagnetic effects. Physically, flux tube simulations assume that the turbulence has a small radial correlation length relative to the size of the tokamak and thus usually assume that quantities

such as ω_d and ω_{*T} (proportional to the density and temperature gradients) are constant over the radial width of the flux tube. This is appropriate for large tokamaks in the gyro-Bohm limit of small $\rho_* = \rho/L_*$, where ρ is the gyroradius (the radial correlation length of the turbulence typically scales with ρ) and L_* is the length scale over which plasma gradients are changing. Global simulations (or extensions of flux tube/annulus simulations) relax this radially local assumption and include effects such as the radial variation of profiles, which can be important in some regimes at large ρ_* , particularly near the plasma edge or near transport barriers. Both flux tube and global simulations are useful for different regimes and resolution requirements. Presently, the flux tube approach is used in the Eulerian nonlinear initial value codes GS2 [KOTSCHENREUTHER *et al.*, 1995a; DORLAND *et al.*, 2000] and GENE [JENKO, 2000], the Eulerian linear eigenvalue code FULL [REWOLDT *et al.*, 1982; REWOLDT *et al.*, 1987], and the PIC nonlinear code GEM [CHEN and PARKER, 2003].

Here we explore even further approximations to reduce the geometrical computational grid. Specifically, we have developed a local linear gyrokinetic model which enhances the efficiency of flux tube-based microinstability calculations by using representative values of the equilibrium parameters averaged over a Gaussian trial function. The code based on this trial function model uses the same geometrical information available in the full GS2 gyrokinetic code. Thus it can use either a full numerical equilibrium or a local parameterized equilibrium such as developed by Miller *et al.* [MILLER *et al.*, 1998].

Previously, a trial function has been used in the quasi-linear gyro-Landau-fluid code GLF23, though only allowing for an \hat{s} - α shifted circular equilibrium [WALTZ *et al.*, 1997]. In this code, even and odd Gaussian trial functions were introduced

and the trial function width was scaled as a linearly decreasing function of q and \hat{s} . Comparisons with the linear ballooning mode gyrokinetic stability code GKS showed good agreement in scans over $k_y \rho_i$ and \hat{s} for a range of q , T_{0i}/T_{0e} , and ν_{ei} in the electrostatic limit. (Very recently, this model has been replaced with a finite series of Hermite polynomial basis functions and extended to separate the gyro-Landau-fluid model equations for passing and trapped particles [STAEBLER *et al.*, 2005]. It is presently still limited to shifted circular geometry and the electrostatic limit, though upgrades to general geometry are being planned.) Likewise, the use of a trial function in the linear, collisionless, electrostatic gyrokinetic code KINEZERO has been successful in the concentric-circular limit [BOURDELLE *et al.*, 2002]. In this case, the trial function was chosen to be the most unstable exact solution obtained in the fluid limit.

As an extension of the ideas in these models, the trial function model which we describe retains the full velocity-space dependence of the gyrokinetic equation (in contrast with the GLF23 model) and allows for the inclusion of noncircular flux surfaces and non-adiabatic electron dynamics. Modifications to include electromagnetic dynamics are also discussed. The motivation for this work is that, upon the inclusion of a quasi-linear approximation or nonlinear effects with subgrid models in future research, such a code might be more practical than a full geometry code for real-time between-shot analysis studies of existing experiments and for optimization studies for future tokamaks. For example, such a code could serve as a next step beyond the gyrofluid-based GLF23 transport model in the multiscale coupling between fast microinstability dynamics and slow macroscopic transport time scales, based directly on coupling a quasi-linear or nonlinear gyrokinetic code and a transport code, which would require a large number of iterations to accurately

describe the transport coefficients.

5.1 Formulation of the Model

In general, the equilibrium parameters required as input in a flux tube-based gyrokinetic simulation (particularly the curvature drift $\omega_{d,\parallel}$, the ∇B drift $\omega_{d,\perp}$, k_{\perp}^2/B^2 , and $(\partial\theta/\partial l)$) depend on the ballooning mode extended angle θ . To reduce the equations to a local dimensionality yet still retain the effects of the geometry, we have developed a trial function model based on computations of weighted averages of these parameters over an even Gaussian trial function as follows:

$$\langle F \rangle = \frac{\int d\theta F e^{-\theta^2/(2\sigma^2)}}{\int d\theta e^{-\theta^2/(2\sigma^2)}} \quad (5.1)$$

where σ is the arbitrarily defined trial function width. (Choice of σ will be discussed further below.) The Gaussian form for the weight function is motivated by the fact that drift wave eigenmodes tend to be localized in the “bad curvature” (i.e. $\theta = 0$) region.

As an example, in the low β , high aspect ratio limit in circular geometry at $k_x = 0$, the equilibrium parameters are given by:

$$\omega_{d,\parallel} = \omega_{d,\perp} = - \left(\frac{k_y \rho_s v_{ts}}{R_0} \right) (\cos(\theta) + \hat{s}\theta \sin(\theta)) \quad (5.2)$$

$$k_{\perp}^2 = k_y^2 |1 + \hat{s}^2 \theta^2| \quad (5.3)$$

$$|B| = B_0 (1 - \epsilon \cos(\theta)) \quad (5.4)$$

$$k_{\parallel} = - \frac{i}{q R_0} \frac{\partial}{\partial \theta} \quad (5.5)$$

where R_0 is the major radius at the center of the flux surface, $\epsilon = r/a$, where a is the minor radius, and $\omega_{d,\parallel} < 0$ corresponds to drifts in the “bad curvature” direction. The trial function averages (on an infinite θ grid) then become:

$$\langle \omega_{d,\parallel} \rangle = \langle \omega_{d,\perp} \rangle \approx - \left(\frac{k_y \rho_s v_{ts}}{R_0} \right) e^{-\sigma^2/2} (1 + \hat{s}\sigma^2) \quad (5.6)$$

$$\left\langle \frac{k_\perp^2}{|B|^2} \right\rangle \approx \frac{k_y^2}{B_0^2} \left[1 + \hat{s}^2 \sigma^2 + 2\epsilon e^{-\sigma^2/2} (1 + \hat{s}^2 \sigma^2 - \hat{s}^2 \sigma^4) \right] \quad (5.7)$$

$$\sqrt{\langle k_\parallel^2 \rangle} = \frac{1}{2qR_0\sigma} \quad (5.8)$$

Thus, as σ increases, the averaged k_\parallel decreases, indicating a lower amount of Landau damping, while the averaged k_\perp^2 generally increases, indicating increased mode suppression due to FLR averaging. The curvature and ∇B drifts, however, have the largest negative values at $\sigma^2 = (2\hat{s} - 1)/\hat{s}$ (assuming $\hat{s} > 1/2$), so the most unstable mode in a scan over σ might be expected near this moderate value of σ .

Examples of the equilibrium parameters comparing realistic geometrical parameters with the high aspect ratio circular limit can be seen in figures 5.1 and 5.2. The equilibrium parameters are computed using the analytic Miller formalism as implemented in GS2 and are based on input from variations of an equilibrium used in [WALTZ and MILLER, 1999]: $r/a = 0.5$, $R/a = 3.0$, $\partial_r R_0 = -0.0$, $q = 2.0$, $\hat{s} = 1.0$, $\partial_{r/a} \beta = -0.0$. The radial derivatives of the input shaping parameters κ (elongation) and δ (triangularity) are approximated as $\partial_{r/a} \kappa = (\kappa - 1)/(r/a)$ and $\partial_{r/a} \delta = \delta/(r/a)$. The high aspect ratio limit is obtained by using $r/a = 0.001$.

Figure 5.1 shows the variation of ω_d and k_\perp (at $k_y \rho_s = 1$) with θ . Note the agreement between the high aspect ratio Miller-computed \hat{s} - α limit and the analytic limit given by Eqs. (5.2) - (5.4). Freedom in the definition of θ has been

exploited to remove the θ dependence from the $\partial/\partial l = (\partial\theta/\partial l)\partial/\partial\theta$ operator factor and we thus obtain $k_{\parallel}a = \{0.1666, 0.1666, 0.1666\} \frac{\partial}{\partial\theta}$ for $r/a = 0.001$ and $k_{\parallel}a = \{0.1684, 0.1671, 0.1733\} \frac{\partial}{\partial\theta}$ for $r/a = 0.5$ for the cases of $\{\kappa = 1, \delta = 0; \kappa = 2, \delta = 0; \kappa = 2, \delta = 0.47\}$ respectively. Thus, the high aspect ratio Miller-computed \hat{s} - α model k_{\parallel} also agrees with Eq. (5.5). The trial function averages computed numerically on a finite θ grid using the trial function code are shown in figure 5.2. Agreement between the analytic \hat{s} - α limit (Eqs. (5.6)- (5.8)) and the high aspect ratio Miller-computed \hat{s} - α limit supports the validity of the numerical trial function averaging in the code.

Overall, for these parameters, note from figure 5.1 that the case of $\kappa = 2$ with nonzero triangularity shows a significantly more narrow region in the “bad curvature” (i.e. $\omega_{d,\parallel} < 0$) direction. This is likewise captured by the trial function averaging in figure 5.2, which generally shows a larger averaged $\omega_{d,\parallel}$ at any particular σ . The narrowing of k_{\perp} with increased κ is also notable and is reflected by the larger and more rapidly increasing trial function averaged k_{\perp} . These fundamental trends suggest then that it is expected that the local trial function model will be able to capture the key physics of shaped plasmas.

The collisionless gyrokinetic equation for the trial function model, analogous to the full ballooning equation in Eq. (1.4) in the linear limit, is given by

$$\begin{aligned} & \left(\frac{\partial}{\partial t} + i\sqrt{\langle k_{\parallel}^2 \rangle} v_{\parallel} + i\langle \omega_{dv} \rangle \right) h \\ &= \left(i\omega_{*T} + \frac{\partial}{\partial t} \right) \frac{Z_s e F_M}{T_{0s}} \langle J_{0s} \rangle \left(\Phi - \frac{v_{\parallel}}{c} A_{\parallel} \right) \\ & - C_{\parallel} \left| \sqrt{\langle k_{\parallel}^2 \rangle} v_{\parallel} \right| h \end{aligned} \quad (5.9)$$

where $h(v_{\parallel}, v_{\perp}, t)$ is the perturbed non-adiabatic part of the species' distribution

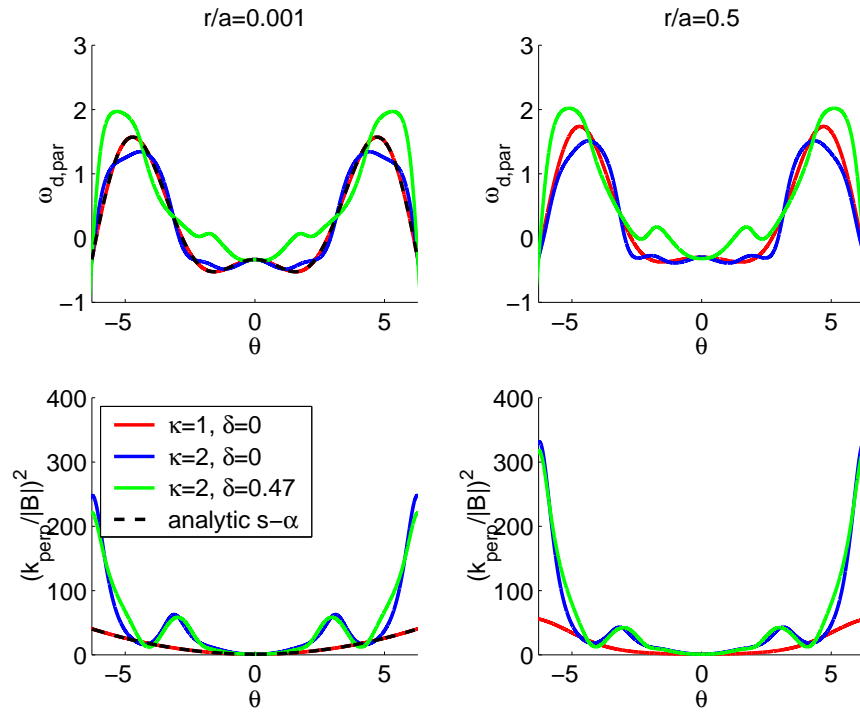


Figure 5.1: Curvature drift (normalized as $\omega_{d,\parallel}/(v_{ti}/a)/(k_y\rho_i)$) and $k_{\perp}^2/|B|^2$ (normalized as $(k_{\perp}^2/k_y)^2/(|B|/|B_0|)^2$) as a function of θ computed using the Miller formalism for generic input parameters. Note that the analytic $\hat{s}-\alpha$ curve and the Miller-computed $\hat{s}-\alpha$ curve ($\kappa = 1, \delta = 0$) overlap in the high aspect ratio limit ($r/a = 0.001$).

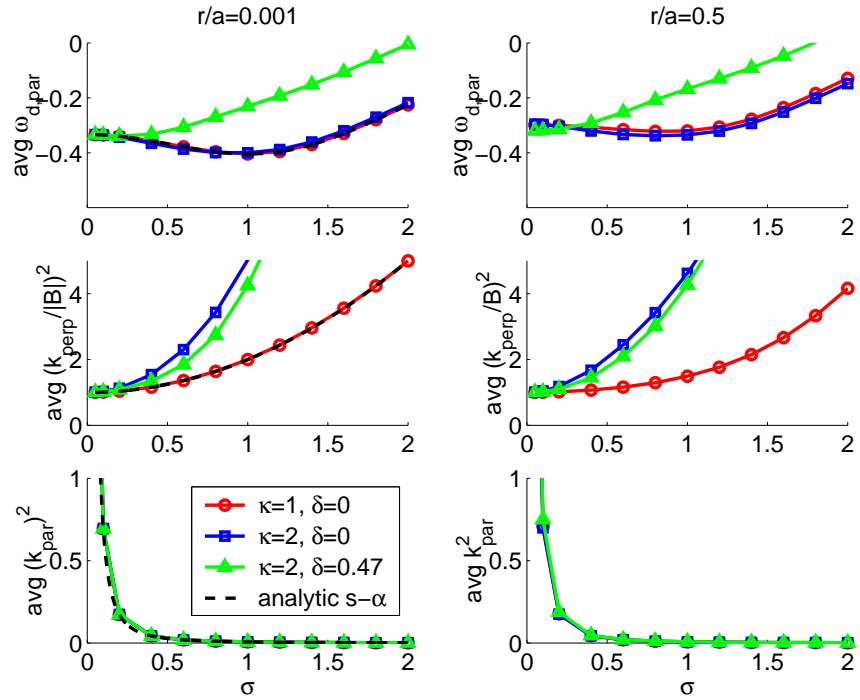


Figure 5.2: Curvature drift (normalized as $\omega_{d, \parallel} / (v_{ti} / a) / (k_y \rho_i)$), $k_{\perp}^2 / |B|^2$ (normalized as $(k_{\perp}^2 / k_y)^2 / (|B| / |B_0|)^2$), and k_{\parallel}^2 (normalized as $k_{\parallel}^2 a^2$) averaged over a Gaussian trial function as a function of the trial function width σ for generic input parameters. Note that the analytic $\hat{s}-\alpha$ curve and the Miller-computed $\hat{s}-\alpha$ curve ($\kappa = 1, \delta = 0$) overlap in the high aspect ratio limit ($r/a = 0.001$).

function, $\Phi(t)$ is the electrostatic potential, and $A_{\parallel}(t)$ is the parallel component of the perturbed magnetic vector potential, all of which are local in spatial dimensionality with respect to the trial function averaged k_{\parallel} and k_{\perp} for a specified (k_x, k_y) linear mode. Note that the argument of the Bessel function is also affected by the trial function average, i.e. $\langle J_{0s} \rangle \equiv J_{0s} \left(\sqrt{\langle \frac{k_{\perp}^2}{\Omega^2} \rangle} v_{\perp} \right)$. (Note: Averaging the Bessel function directly over the trial function, rather than averaging its argument, was also explored. This essentially averages over the oscillations in the Bessel function and thus yields a smaller value than our present approximation. However, the test case results were negligibly affected.) As mentioned previously, choice of the trial function width used to define the averages is a free parameter. Unlike the model of [WALTZ *et al.*, 1997] which chooses σ based on parameterizations, we solve the gyrokinetic equation given by Eq. (5.9) for a range of σ and report the largest linear growth rate over this scan as the worst-case result.

The additional final term on the RHS of Eq. (5.9) represents a model for the parallel free-streaming of particles out of the bad curvature region and can be thought of as an outgoing boundary condition model. Specifically, without this term, the model has a purely imaginary k_{\parallel} dependence, which is equivalent to a periodic system of length $L_{\parallel} = 2\pi/k_{\parallel}$. Physically, this means that particles can never escape the bad curvature region; i.e. they can go out one side of the parallel domain box but just come back in the other side, always seeing the same value of ω_d . In reality, particles are able to escape the bad curvature region and do so at a rate of order $|v_{\parallel}/qR| \sim |k_{\parallel}v_{\parallel}|$, thus providing the physical basis for the inclusion of the parallel loss term in our model. Note that for physical consistency, the parallel loss term as given in Eq. (5.9) has been constructed to ensure the correct adiabatic response (by applying the parallel loss term only to the non-adiabatic part of the

distribution function). For the trial function simulations, a value of 0.13 has been chosen for the parallel loss constant C_{\parallel} for both ion species and electrons for all runs based on optimizations of ITG runs (with adiabatic electrons) in the low q limit.

In practice, the parallel loss term was included in the trial function model to obtain better accuracy for ITG modes near marginal stability. Examples of this are shown in figures 5.3-5.5. The parameters for this scan are modified from [MILLER *et al.*, 1998], most significantly using the high aspect ratio limit (so that trapped particle effects are not important), smaller (more typical) \hat{s} , no triangularity, and the electrostatic limit at various q : $r/a = 0.001$, $R/a = 2.631$, $\partial_r R_0 = -0.354$, $\hat{s} = 0.5$, $\partial_{r/a}\beta = -0.0$, $\kappa = 1.66$, $\partial_{r/a}\kappa = 1162$, $\delta = 0$, $\partial_{r/a}\delta = 0$. The figures show scans of the real frequency and linear growth rate vs. the temperature gradient length scale (at constant density gradient $R/L_{ni} = 2.63$) comparing the effects of the parallel loss operator at low to high q and overall comparing the trial function model (the solid lines) with GS2. (The dotted lines in these figures represent a persistent mode at very high σ , corresponding to very small k_{\parallel} and ω_d and large $k_{\perp}\rho_i$, which, as can be seen in the figures, is sometimes dominant over the physical ITG mode in a scan over σ . In general, we will neglect this unphysical mode; though this is discussed further in section 5.4.) In all three figures, we see that the most significant effect of the parallel loss term is that, at high $k_y\rho_i$ near marginal stability, both GS2 and the trial function code with nonzero C_{\parallel} linearly transition from unstable to damped modes, while the trial function code without the parallel loss term has a persistent residual slowly growing mode even when it should have been stable. Note also that the effect of the parallel loss term becomes more evident as q decreases from 10 to 3.03 to 1.5, as expected since the parallel connection length

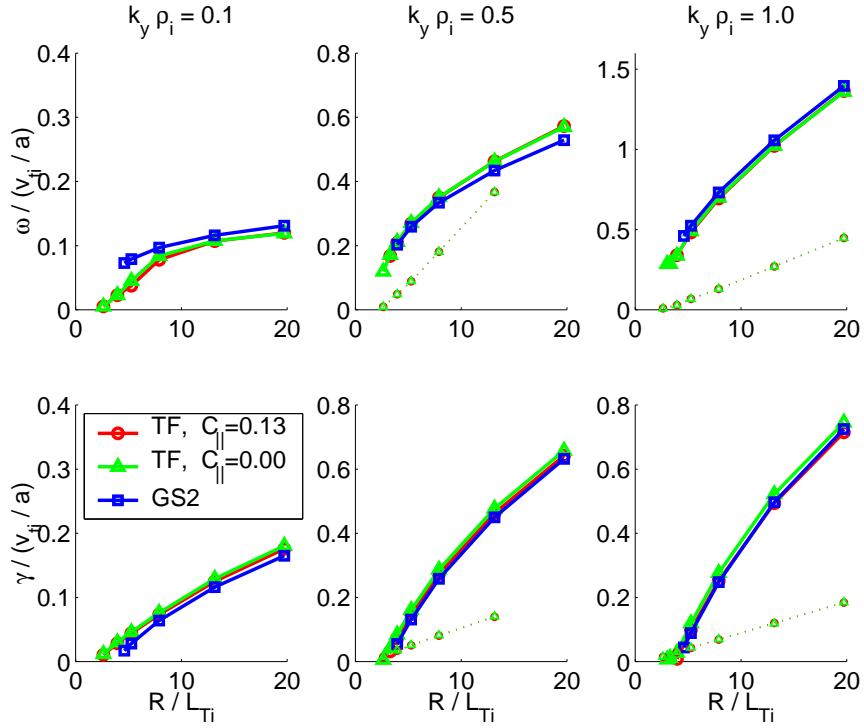


Figure 5.3: Real frequency and linear growth rate vs. normalized temperature gradient length scale at various $k_y \rho_i$ for generic parameters with $q = 10$ and adiabatic electrons comparing results from GS2 with the trial function code run both with and without a parallel loss model. (The dotted lines show a persistent secondary dominant unphysical mode at very high σ .)

$L_{\parallel} \sim qR$ is becoming smaller. Thus, the case of $q = 1.5$ was used to help set an appropriate level for C_{\parallel} . For all future runs, the parallel loss term is included for all species to improve the threshold critical gradient for instability.

In addition to the parallel loss model, a simple model for trapped particle effects is also included. In general, the parallel velocity is modulated along the magnetic field, i.e. $v_{\parallel} = \pm \sqrt{2E/m - \mu B(\theta)/m}$, where the energy $E = mv^2/2$ and magnetic moment $\mu = mv_{\perp}^2/2B$ are adiabatic invariants. The numerical trial function model uses a $(v_{\perp}, v_{\parallel})$ grid in velocity-space, though this is modified with the following trapped particle model: if $v_{\parallel}^2/v_{\perp}^2 \leq |B(\theta)|_{max}/|B(\theta)|_{min} - 1$, then $\langle v_{\parallel} \rangle = 0$. Note

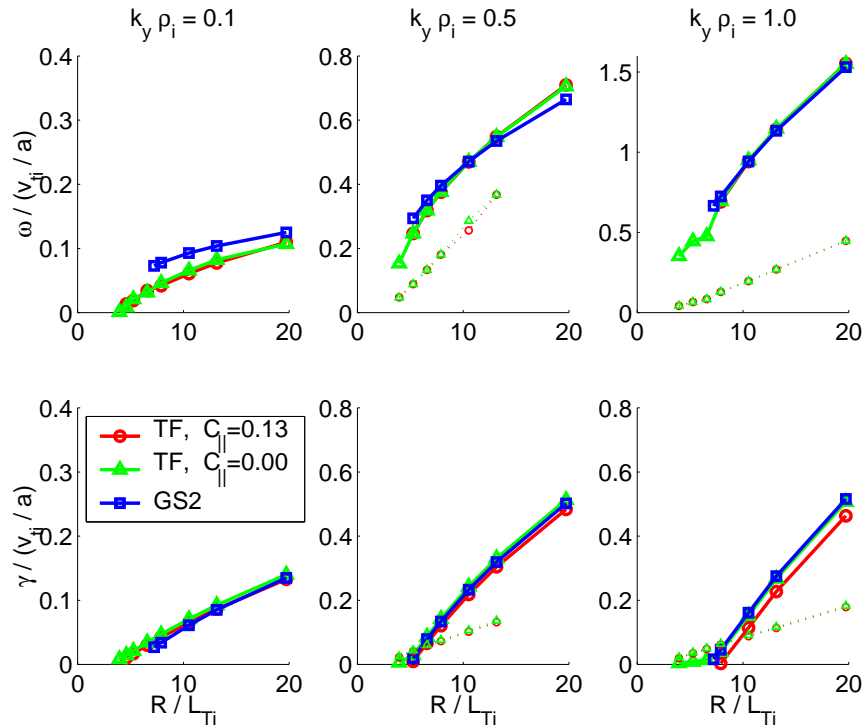


Figure 5.4: Real frequency and linear growth rate vs. normalized temperature gradient length scale at various $k_y \rho_i$ for generic parameters with $q = 3.03$ and adiabatic electrons comparing results from GS2 with the trial function code run both with and without a parallel loss model. (The dashed lines represent a persistent secondary dominant unphysical mode at very high σ .)

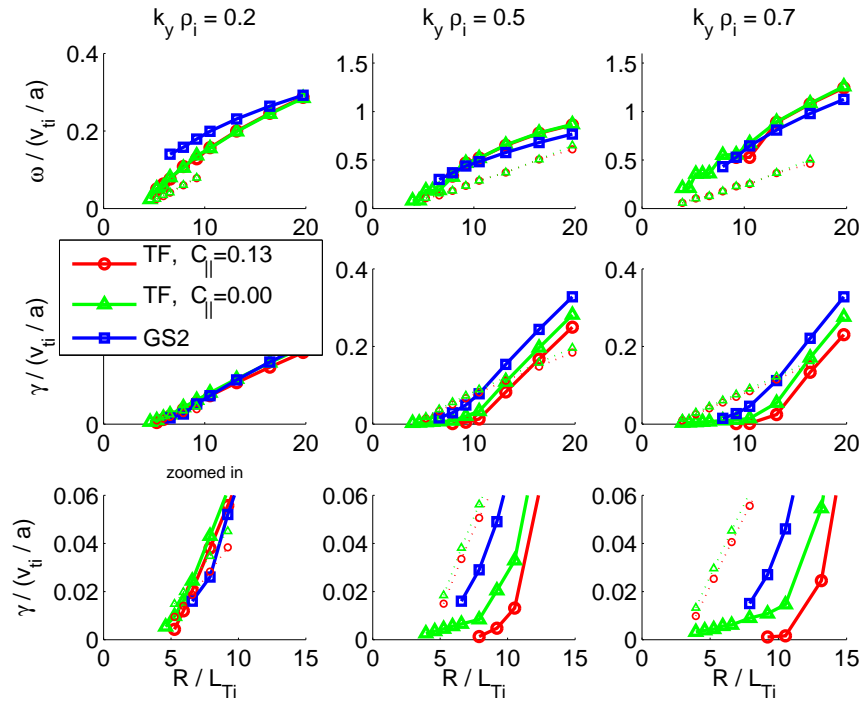


Figure 5.5: Real frequency and linear growth rate vs. normalized temperature gradient length scale at various $k_y \rho_i$ for generic parameters with $q = 1.5$ and adiabatic electrons comparing results from GS2 with the trial function code run both with and without a parallel loss model. (The dashed lines represent a persistent secondary dominant unphysical mode at very high σ .)

then that the trapped particle condition also applies to the parallel loss term ($\propto \left| \sqrt{\langle k_{\parallel}^2 \rangle} \langle v_{\parallel} \rangle \right|$), reflecting the fact that trapped particles cannot escape along the field line because of the magnetic mirror. The trapping condition is applied only to the electron species in our trial function model. The reason for this is that most drift wave ITG/TEMs of interest are in the parameter regime: $k_{\parallel} v_{ti} \ll \omega_* \ll k_{\parallel} v_{te}$, so ion trapping is negligible. Ion trapping might become important for very long wavelength modes, but these modes are most likely suppressed by ion-ion collisions. (Non-local mode effects, which our trial function model does not capture, are also important for these long wavelength modes.) In practice, ion trapping was ignored to eliminate modes which persisted at very high k_{\parallel} with growth rates larger than the drift instability.

5.2 The Algorithm

The gyrokinetic solver in the trial function code is Eulerian-based, using a finite difference scheme in time, while the spatial dimension is treated locally, specifying a (k_x, k_y) linear mode and using the trial function averaging in θ . The equations implemented in the code are rewritten in terms of $h_s \rightarrow g_s + \frac{Z_s e F_M}{T_{0s}} \langle J_{0s} \rangle \left(\Phi - \frac{v_{\parallel}}{c} A_{\parallel} \right)$ to eliminate the time derivatives of the fields. With this transformation, the gyrokinetic equation in Eq. (5.9) becomes:

$$\begin{aligned}
 & \left(\frac{\partial}{\partial t} + i \sqrt{\langle k_{\parallel}^2 \rangle} v_{\parallel} + i \langle \omega_{dv} \rangle \right) g \\
 &= \left(i \omega_{*T} - i \sqrt{\langle k_{\parallel}^2 \rangle} v_{\parallel} - i \langle \omega_{dv} \rangle \right) \frac{Z_s e F_M}{T_{0s}} \langle J_{0s} \rangle \left(\Phi - \frac{v_{\parallel}}{c} A_{\parallel} \right) \\
 & - C_{\parallel} \left| \sqrt{\langle k_{\parallel}^2 \rangle} v_{\parallel} \right| \left[g + \frac{Z_s e F_M}{T_{0s}} \langle J_{0s} \rangle \left(\Phi - \frac{v_{\parallel}}{c} A_{\parallel} \right) \right]
 \end{aligned} \tag{5.10}$$

and the field equations become:

$$\sum_s \frac{n_{0s} e^2 Z_s^2}{T_{0s}} (1 - \langle \Gamma_{0s} \rangle) \Phi = \rho_{dens}[\Phi, A_{\parallel}] \quad (5.11)$$

$$\left(\langle k_{\perp}^2 \rangle + \frac{4\pi}{c^2} \sum_s \frac{n_{0s} e^2 Z_s^2}{m_s} \langle \bar{\Gamma}_{0s} \rangle \right) A_{\parallel} = \frac{4\pi}{c} \rho_{curr}[\Phi, A] \quad (5.12)$$

where the plasma charge and current densities are given by

$$\rho_{dens}[\Phi, A_{\parallel}] = \sum_s e Z_s \int d^3 v \langle J_{0s} \rangle g_s \quad (5.13)$$

$$\rho_{curr}[\Phi, A_{\parallel}] = \sum_s e Z_s \int d^3 v v_{\parallel} \langle J_{0s} \rangle g_s \quad (5.14)$$

Note that the Γ_{0s} in the Poisson equation is computed as $\langle \Gamma_{0s} \rangle \equiv \Gamma_{0s}(\langle b_s \rangle) = e^{-(b_s)} I_0(\langle b_s \rangle)$ for $\langle b_s \rangle = \left\langle \frac{k_{\perp}^2}{\Omega^2} \right\rangle v_{ts}^2$, while the Γ_{0s} factor in the Ampere equation (denoted as $\langle \bar{\Gamma}_{0s} \rangle$), is computed numerically, i.e. as the numerical integration of $\int d^3 v \langle J_{0s} \rangle^2 F_{Ms}$ on the velocity grid, rather than from the analytic relation. This is crucial to avoid the ‘‘Ampere cancellation’’ problem pointed out by G. W. Hammett and F. Jenko [HAMMETT and JENKO, 2001] and so is commonly used in several present-day gyrokinetic codes [JENKO, 2000; CANDY and WALTZ, 2003a; CHEN and PARKER, 2003].

Given an input of the equilibrium parameters as a function of θ , the trial function-based local code computes the trial function averages and then solves for each species’ distribution function on a $(v_{\perp}, v_{\parallel})$ velocity grid. The temporal finite difference in the gyrokinetic equation is done via a partially implicit

scheme, in which the field terms are treated explicitly with a 2nd order Adams-Bashforth scheme while the g_s terms are treated implicitly with a backward time-centered scheme. Thus, the time derivative on the LHS of Eq. (5.10) is differenced as $\frac{1}{\Delta t/2} (g_s^{n+1} - g_s^n)$; the k_{\parallel} , ω_{dv} and C_{\parallel} terms on the LHS are differenced as $\frac{1}{2} (g_s^{n+1} + g_s^n)$; and the field terms on the RHS are differenced as $\frac{1}{2} (3\Phi^n - \Phi^{n-1})$ and $\frac{1}{2} (3A_{\parallel}^n - A_{\parallel}^{n-1})$ (where n is the temporal index). The final discretized equation based on this scheme can be easily inverted analytically and the resulting equation for g_s^{n+1} at a particular velocity grid point is implemented as a direct solve.

Solution of the evolution of the distribution function via the linear gyrokinetic equation yields the real frequency and linear growth rate of the fastest growing mode in the long time limit. In reality, the gyrokinetic equation has many normal modes of oscillation. However, most of these modes are highly damped and the fastest growing mode eventually dominates, with $\Phi \sim e^{-i\omega_r t + \gamma t}$. We measure the instantaneous frequency as $\omega = (i/\Delta t) \log(\Phi^{n+1}/\Phi^n)$. Convergence is then defined as: $|\omega_r^{n+1} - \omega_r^n| / |\omega_r^n| < \omega_{tol}$ and $|\gamma_r^{n+1} - \gamma_r^n| / |\gamma_r^n| < \gamma_{tol}$. (Note that this is similar to the approach in the standard version of GS2, though, since GS2 has a θ grid, ω is measured from Φ at $\theta = 0$. Convergence in GS2 is measured with respect to the ratio of the sample variance to the time averaged ω for a specified time history, rather than the instantaneous value as we do here, to reduce the chances of the change in ω being small by coincidence, particularly for small time steps. However, most often, the problem with measuring convergence comes from interference effects between two modes with almost the same growth rate, in which case the code must be run for a very long time before one mode dominates over the other. Φ can be decomposed from multiple time steps into two modes to measure the frequency of each separately to reduce this problem and this has been tested previously, though

we do not address this here.)

In general, the trial function code is susceptible to time step restrictions due to its semi implicit-explicit algorithm. Recall from section 3.5 in Chapter 3 of this thesis that the numerical analysis of a partially implicit Adams-Bashforth scheme for the test problem of a shear kinetic Alfvén wave at small $k_{\perp}\rho_i$ yielded the onset of a numerical instability at $|k_{\parallel}v_{te}\Delta t| \sim |k_{\perp}\rho_s|$ in both the low and high $(\beta_e/2)(m_i/m_e)$ regimes. This is not as severe as for the semi implicit-explicit algorithms explored in section 2.2, which were found to be numerically unstable at the Nyquist limit due to the combination with 2nd order compact finite differencing. However, both schemes motivate the search for a more implicit treatment of the field dynamics. Here we explore the development of an iterative implicit scheme for the trial function code. This has primarily served as a simple test bed for the iterative implicit algorithm discussed in section 2.3 which, for a full code like GS2, reduces the computational intensity of computing the implicit arrays. However, here we also compare the convergence rate of the method with the CFL condition for the original semi implicit-explicit algorithm as a further motivation for the use of implicit-based schemes for gyrokinetics in general.

We consider an implicit algorithm in the context of Kotschenreuther’s algorithm described in section 2.1.1. We will assume the electrostatic limit for simplicity. For the local gyrokinetic model, the electrostatic plasma response matrix as defined by Eq. (2.18) is greatly simplified, i.e. reduced from an $N_{\theta} \times N_{\theta}$ matrix to a local function of k_{\parallel} as follows:

$$M^1(k_{\parallel}) \equiv \sum_s eZ_s \int d^3v \langle J_{0s} \rangle \frac{\delta g^{n+1}}{\delta \Phi^{n+1}}(k_{\parallel}) \quad (5.15)$$

We use an analytic approximation for M^1 , similar to the analytic model in the continuous limit developed in section 2.3.2. This analytic approach is more simple here because we do not have to inverse Fourier transform the solution back to the real space θ grid. However, we do have the additional complication of retaining the physics of the parallel loss term.

We consider as our simplified starting equation the trial function averaged gyrokinetic equation (given by Eq. (5.10)) for a uniform plasma in slab geometry at small $\langle k_{\perp} \rho_i \rangle$:

$$\begin{aligned} & \left(\frac{\partial}{\partial t} + i\sqrt{\langle k_{\parallel}^2 \rangle} v_{\parallel} + C_{\parallel} \left| \sqrt{\langle k_{\parallel}^2 \rangle} v_{\parallel} \right| \right) g \\ &= - \left(i\sqrt{\langle k_{\parallel}^2 \rangle} v_{\parallel} + C_{\parallel} \left| \sqrt{\langle k_{\parallel}^2 \rangle} v_{\parallel} \right| \right) \frac{Z_s e F_M}{T_{0s}} \Phi \end{aligned} \quad (5.16)$$

From the time-centered discretization of this equation, we find that

$$\frac{\delta g_s^{n+1}}{\delta \Phi^{n+1}}(k_{\parallel}) = - \langle J_{0s} \rangle \frac{Z_s e F_M}{T_{0s}} \frac{i \hat{L}}{1 + i \hat{L}} \quad (5.17)$$

where

$$\hat{L} \equiv \frac{1}{2} \Delta t \left(\sqrt{\langle k_{\parallel}^2 \rangle} v_{\parallel} - i C_{\parallel} \left| \sqrt{\langle k_{\parallel}^2 \rangle} v_{\parallel} \right| \right) \quad (5.18)$$

Note that this response function is equivalent to that for the continuous preconditioner model given by Eq. (2.48) in the high resolution limit (i.e. such that $\hat{k}_{\parallel} = k_{\parallel}$ and $g(k_{\parallel}) = 1$) except with the addition of the C_{\parallel} term in \hat{L} . To integrate the distribution function response over velocity-space analytically, we again use Padé approximations to match solutions in the limit of low and high $x \equiv k_{\parallel} v_{ts} \Delta t$. In the

low x limit, we find that

$$M_{low}^1(k_{\parallel}) \approx \sum_s \frac{n_{0s} Z_s^2 e^2}{T_{0s}} \langle \Gamma_{0s} \rangle \left(-\frac{x^2}{4} (1 - C_{\parallel}^2) - \frac{C_{\parallel}}{\sqrt{2\pi}} x \right) \quad (5.19)$$

While in the high x limit, we find that

$$M_{high}^1(k_{\parallel}) \approx \sum_s \frac{n_{0s} Z_s^2 e^2}{T_{0s}} \langle \Gamma_{0s} \rangle \left(-1 - \frac{1}{x^2/4 (1 + C_{\parallel}^2)} + C_{\parallel} \sqrt{\frac{2}{\pi}} \frac{\ln(x^2/4)}{x} \right) \quad (5.20)$$

Using Padé approximations to match the solutions given by Eq. (5.19) and the 0th order part of Eq. (5.20), we obtain the following as our analytic-based preconditioner model:

$$M^1(k_{\parallel}) \approx - \sum_s \frac{n_{0s} Z_s^2 e^2}{T_{0s}} \langle \Gamma_{0s} \rangle \left(\frac{x^2/4 (1 - C_{\parallel}^2) + C_{\parallel} x / \sqrt{2\pi}}{1 + x^2/4 (1 - C_{\parallel}^2) + C_{\parallel} x / \sqrt{2\pi}} \right) \quad (5.21)$$

Figure 5.6 shows the results of implementation of the iterative implicit scheme using simple iteration (described in section 2.3.1) and a linear two-point initializer for the field term (i.e. $\Phi^{n+1,0} = 2\Phi^n - \Phi^{n-1}$). The test case parameters are the same as used for the optimization scans for the C_{\parallel} term at high q : $r/a = 0.001$, $R/a = 2.631$, $\partial_r R_0 = -0.354$, $\hat{s} = 0.5$, $\partial_{r/a} \beta = -0.0$, $q = 10$, $\kappa = 1.66$, $\partial_{r/a} \kappa = 1162$, $\delta = 0$, $\partial_{r/a} \delta = 0$. We use a single ion species and include gyrokinetic electrons with the following parameters: $R/L_{ni} = R/L_{ne} = 2.631$, $R/L_{Ti} = R/L_{Te} = 7.893$, $T_{0i} = T_{0e}$. The runs were done at a constant small value of $k_y \rho_i = 0.05$. A scan over σ using a fully implicit algorithm (i.e. with the exact response function) was first done to find the maximum linear growth rate. This occurred at $\sigma = 1.3$, corresponding to $\sqrt{\langle k_{\parallel}^2 \rangle} a = 0.0146$. The results shown in figure 5.6 were done for this single constant value of σ . The upper plots compare the exact and approximate

electrostatic response functions. In general, good qualitative agreement is seen even at large time steps and with the inclusion of the parallel loss term. The plot of the number of gyrokinetic iterations vs. Δt shows how well the iterative method works in practice. Even at the largest time steps, the iterative method requires less than 10 iterations per time step on average. The significance of this result is more evident when considering the plot of the linear growth rate vs. Δt for the original partially implicit 2nd order Adams-Bashforth scheme. In this plot, we see that the method becomes numerically unstable for $\Delta t v_{ti}/a > 0.1$ for $C_{\parallel} = 0.13$. This is slightly larger than the predicted onset of numerical instability from section 3.5 at $\Delta t \sim |k_{\perp} \rho_s / k_{\parallel} v_{te}|$ which occurs at $\Delta t v_{ti}/a \sim 0.0564$ for our test case parameters (though the analysis in section 3.5 did not include the parallel loss term). For comparison, the γ vs. Δt curve in figure 5.6 also shows the results for $C_{\parallel} = 0.00$, and we indeed see a numerical instability at the predicted threshold. Comparing the results of the partially implicit scheme with the plot of iterations for the iterative implicit method, the number of iteration begins to rise more quickly near the CFL threshold but is still less than a factor 4 above the 2 gyrokinetic solves required for a fully implicit scheme. Thus, here we have demonstrated that an iterative implicit scheme is beneficial compared with a semi implicit-explicit scheme since, even with a simple iterative scheme and simple analytic preconditioner, time efficient results can be obtained even when the CFL condition is strongly violated.

5.3 Benchmarks in the Local Limit

Before we look at the trial function model, we first consider the validity of the code in the local limit as proof of correctness. In the local limit, we treat the equilibrium

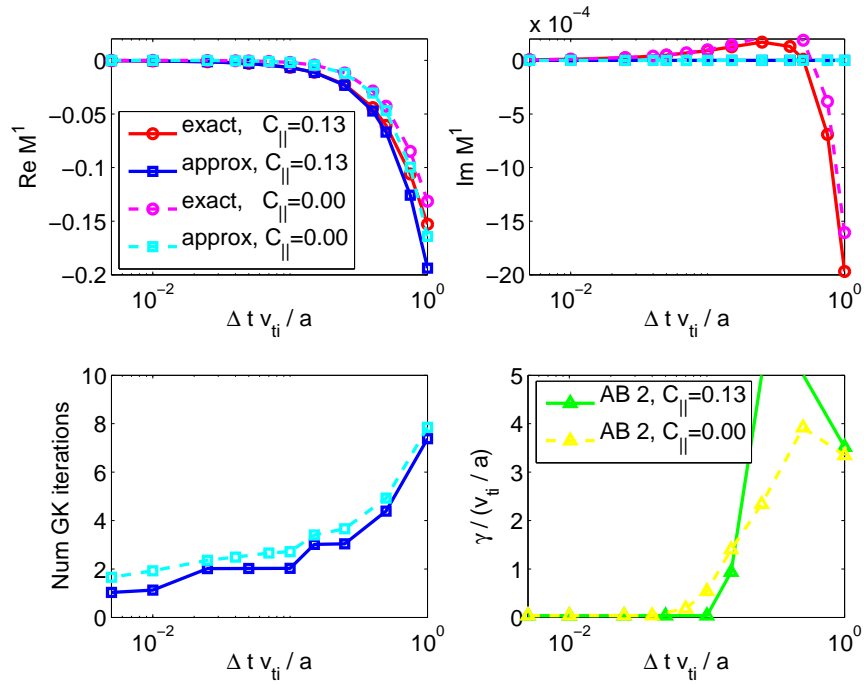


Figure 5.6: Local electrostatic response function vs. normalized time step size for test case parameters ($\sqrt{\langle k_{\parallel}^2 \rangle} a = 0.0146$) comparing the exact response function with the an analytically-based approximation for the plasma response. The lower left plot shows the average number of gyrokinetic iterations vs. normalized time step using the analytic preconditioner in an iterative implicit scheme with simple iteration. The lower right plot shows the linear growth rate vs. normalized time step for a partially-implicit 2nd order Adams-Bashforth scheme for the same test case parameters. The linear growth rate for the fully implicit scheme occurs at $\gamma/(v_{ti}/a) = 0.0353$ for $C_{\parallel} = 0.13$ and $\gamma/(v_{ti}/a) = 0.0371$ for $C_{\parallel} = 0.00$.

parameters as input constants, rather than reducing a θ -varied profile using the trial function model. Specifically, because we are interested in bad curvature-driven ITG physics, we use the \hat{s} - α values of the equilibrium parameters at the outboard midplane ($\theta = 0$): $\omega_{d,\parallel} = \omega_{d,\perp} = -k_y \rho_i v_{ti} / R$, $k_{\perp} = k_y$. The parallel wavelength is chosen using a representative normal connection length for the mode ($k_{\parallel} = L_{\parallel}^{-1} \sim 1/(qR)$); in the purely toroidal limit, $k_{\parallel} = 0$. Furthermore, particle trapping and parallel free-streaming effects are also omitted.

5.3.1 Electrostatic Results

We first consider verification of the underlying physics of the ITG instability in the electrostatic limit. Figure 5.7 shows a scan of the linear growth rate vs. the ion temperature gradient length scale R/L_{Ti} using the trial function code in the local limit for the case of adiabatic electrons and a single ion species (with $Z_i = 1$, $T_{0i} = T_{0e}$, and $R/L_{ni} = 1.0$) in the long wavelength limit ($k_{\perp} \rho_i = 0.01$) for $k_{\parallel} R = 0$ and $k_{\parallel} R = 0.05$. The solid lines show the analytic approximation of Eq. (1.24) for the ITG instability. Note the close agreement between the analytic relation and the local code data points, particularly at high η_i where the ordering assumptions given in Eq. (1.22) are more appropriate, but also for the critical temperature gradient. The $k_{\parallel} R = 0.05$ case also verifies the stabilizing effects of parallel Landau damping.

We have also performed electrostatic local benchmarks including finite, realistic FLR effects. Figure 5.8 shows the reproduction of the gyrokinetic results of figure 2.4 of [BEER, 1995] using the trial function code in the local limit. This figure shows a scan of the linear growth rate as a function of $k_y \rho_i$ for various η_i for $k_{\parallel} R = 0.5$ (corresponding to $q = 2$) using adiabatic electrons and a single ion species with $Z_i = 1$, $T_{0i} = T_{0e}$, and $R/L_{ni} = 5.0$. Note the linear variation of

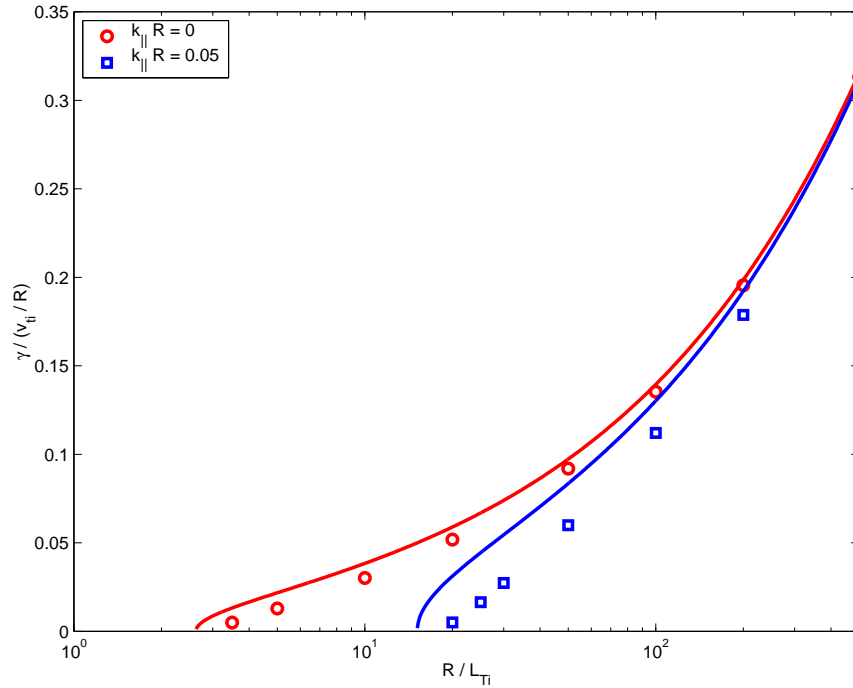


Figure 5.7: Local linear ITG growth rate vs. normalized temperature gradient length scale at $R/L_{ni} = 1.0$ and $k_{\perp}\rho_i = 0.01$ with adiabatic electrons comparing results from the trial function code run in the local limit (the data points) and the analytic result of Eq. (1.24) (the solid lines).

both the real frequency and growth rate as $k_y\rho_i$ becomes small, as expected from Eq. (1.24). The mode stabilization cutoff near $k_y\rho_i \sim (k_{\parallel}R)(R/L_{ni})^{-1} = 0.1$ as observed in figure 2.4 of [BEER, 1995] due to parallel Landau damping effects is also verified. (Ignoring the k_{\perp} terms in our analytic approximation for the ITG cutoff given by Eq. (1.26), we find that $(k_y\rho_i)_c \sim (k_{\parallel}R)(R/L_{ni})^{-1} * factor$, where $factor = (0.4\eta_i + 0.03)^{-1/2} \sim O(1)$ for these parameters.)

5.3.2 Electromagnetic Results

For benchmarks in the local limit with the inclusion of non-adiabatic electron dynamics and electromagnetic effects, we use the simple case of low frequency shear

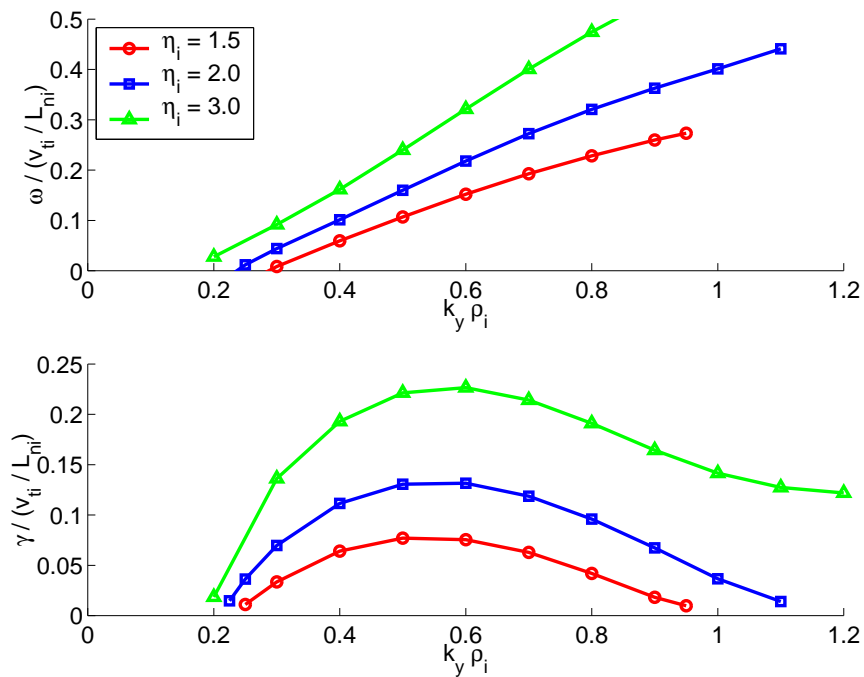


Figure 5.8: ITG mode frequency and local linear growth rate vs. $k_y \rho_i$ for various η_i at $R/L_{ni} = 5.0$ and $k_{\parallel} R = 0.5$ with adiabatic electrons using the trial function code run in the local limit for comparison with figure 2.4 of [BEER, 1995]. These results show good agreement with Beer's gyrokinetic results.

Alfvén waves [LIN and CHEN, 2001]. For a shearless slab with uniform magnetic field, the linear local gyrokinetic equation becomes:

$$\frac{\partial g_s}{\partial t} + ik_{\parallel}v_{\parallel}g_s = -i\frac{Z_s e}{T_{0s}}J_{0s}F_{Ms}k_{\parallel}v_{\parallel}\left(\Phi - \frac{v_{\parallel}}{c}A_{\parallel}\right) \quad (5.22)$$

Assuming an $e^{-i\omega t}$ time dependence for the perturbed quantities, we find that

$$g_s = \frac{Z_s e}{T_{0s}}J_{0s}F_{Ms}\frac{k_{\parallel}v_{\parallel}\left(\Phi - \frac{v_{\parallel}}{c}A_{\parallel}\right)}{\omega - k_{\parallel}v_{\parallel}} \quad (5.23)$$

Using this relation in Eqs. (5.13) and (5.14) in the local limit, we obtain the following for the plasma charge and current densities:

$$\rho_{dens} = -\sum_s \frac{n_{0s}e^s Z_s^2}{T_{0s}}\Gamma_{0s}(1 + \zeta_s Z_0(\zeta_s))\left(\Phi - \frac{\omega}{k_{\parallel}c}A_{\parallel}\right) \quad (5.24)$$

$$\rho_{curr} = -\sum_s \frac{n_{0s}e^s Z_s^2}{T_{0s}}\Gamma_{0s}\left[\frac{\omega}{k_{\parallel}c}(1 + \zeta_s Z_0(\zeta_s))\left(\Phi - \frac{\omega}{k_{\parallel}c}A_{\parallel}\right) - \frac{v_{ts}^2}{c}A_{\parallel}\right] \quad (5.25)$$

where $\zeta_s \equiv \frac{\omega}{\sqrt{2}k_{\parallel}v_{ts}}$, and $Z_0(\zeta_s) \equiv \frac{1}{\sqrt{\pi}}\int_{-\infty}^{\infty} dx \frac{e^{-x^2}}{x - \zeta_s}$ is the 0th order plasma dispersion function. Substituting these expressions for a single kinetic ion species and for kinetic electrons into the Poisson-Ampere equations given by Eqs. (5.11) and (5.12) and using the long wavelength approximation (i.e. $k_{\perp}\rho_i \ll 1$), we obtain the following linear dispersion relation:

$$\left[\left(\frac{\omega}{k_{\parallel}v_A}\right)^2 - 1\right]\left[(1 + \zeta_i Z_0(\zeta_i) + \frac{1}{Z_i}\frac{T_{0i}}{T_{0e}}(1 + \zeta_e Z_0(\zeta_e))\right] = k_{\perp}^2 \rho_i^2 \quad (5.26)$$

where $v_A^2 = (2/\beta_{0i})v_{ti}^2$ is the normalized Alfvén speed and $\beta_{0s} = 8\pi n_{0s}T_{0s}/B^2$.

We consider the limit of $\frac{v_A}{v_{te}} = \sqrt{\frac{m_e}{\beta_e m_i}} \ll 1$. Physically, this implies that the

electron thermal velocity is much larger than the wave phase velocity, i.e. the assumption of “hot” electrons. This assumption allows us to simplify the dispersion relation via the application of the following first order relations:

$$1 + \zeta_e Z_0(\zeta_e) \approx \frac{1}{1 - \zeta_e Z_0(\zeta_e)} \quad (5.27)$$

$$Z_0(\zeta_e) \approx -2\zeta_e + i\sqrt{\pi} \quad (5.28)$$

Furthermore, we omit the ion contribution for the purpose of suppressing the ion acoustic wave ($\omega = k_{\parallel} c_s$, $c_s^2 = T_{0e}/m_i$). With these assumptions, we obtain the following approximate relations for the kinetic shear Alfvén wave real frequency and damping rate:

$$\omega_r = k_{\parallel} v_A \sqrt{1 + k_{\perp}^2 \rho_i^2} \quad (5.29)$$

$$-\gamma = k_{\parallel} v_A \sqrt{\frac{\pi}{8}} \frac{v_A}{v_{te}} k_{\perp}^2 \rho_i^2 \quad (5.30)$$

We perform the simulation of this mode using the trial function code in the local limit, as for the local electrostatic benchmarks. Furthermore, the slab limit and omission of the ion contribution to the gyrokinetic Poisson and Ampere equations are strictly enforced in the coding itself. We use the parameters of [LIN and CHEN, 2001] as input: $k_{\perp} \rho_i = 0.4$, $k_{\parallel}/k_{\perp} = 0.01$, and $m_e/m_i = 5.44 \times 10^{-4}$. An initialization of the form $g_s(t=0) = F_{Ms} \left(1 + C \frac{v_{\parallel}}{v_{ts}}\right)$ is applied, where C is chosen such that the parallel Ohm’s law, given as follows, is satisfied for the initial A_{\parallel} and Φ :

$$\frac{1}{c} \frac{\partial A_{\parallel}}{\partial t} + \hat{b} \cdot \nabla \Phi = 0 \quad (5.31)$$

Specifically, using the ansatz $e^{ik_{\parallel}z - i\omega t}$ and initializing a right-moving shear Alfvén

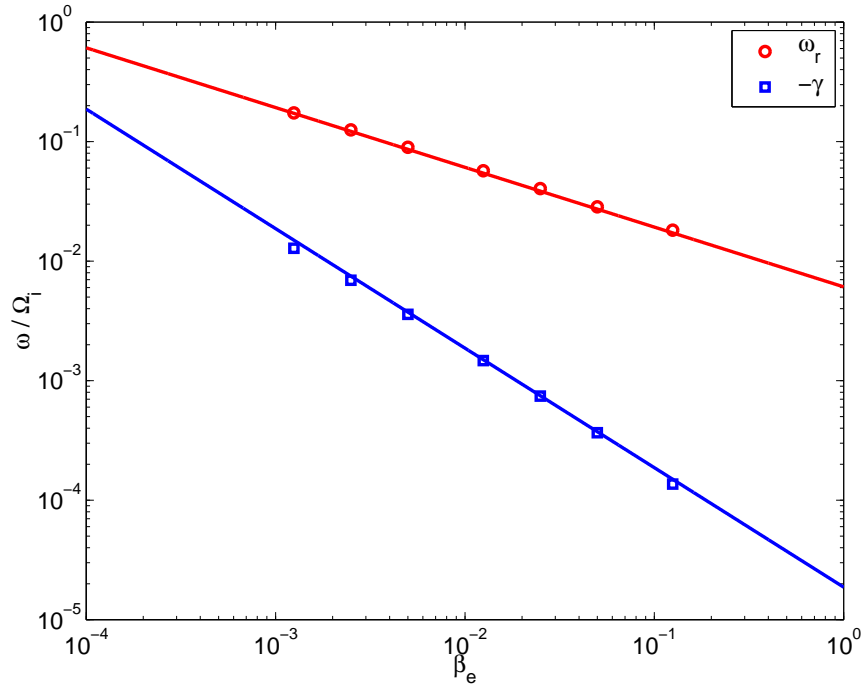


Figure 5.9: Kinetic shear Alfvén wave mode frequency and local linear damping rate vs. electron β for $k_{\perp}\rho_i = 0.4$, $k_{\parallel}/k_{\perp} = 0.01$, and $m_e/m_i = 5.44 \times 10^{-4}$ using the trial function code run in the local limit (the data points) for comparison with figure 1 of [LIN and CHEN, 2001]. These results show good agreement with Lin’s gyrokinetic results and with the analytic result of Eq. (5.30) (the solid lines).

wave, the initial condition is set such that $\hat{A}_{\parallel} = \frac{c}{v_A} \frac{1}{\sqrt{1+k_{\perp}^2\rho_i^2}}\Phi$. Figure 5.9 shows the results of the simulation. Note that this figure is a reproduction of the gyrokinetic results of figure 1 of [LIN and CHEN, 2001]. The simulation results are in good agreement with both the results of Lin and the analytic dispersion relations, thus verifying the validity of the trial function code with non-adiabatic electron dynamics and electromagnetic effects.

5.4 Test Cases for Shaped Flux Surfaces

We would ultimately like to use the trial function code to aid in fast scoping studies of shaping effects on gyrokinetic plasma turbulence. Thus, now that we have established the validity of the code in the local limit, we test the robustness of the trial function physical model by performing benchmarks with the full GS2 gyrokinetic code for a range of shaped flux surfaces.

5.4.1 Electrostatic Results

We first perform the benchmarks in the electrostatic limit. The equilibrium parameters for these studies are based on an extension of initial shaping studies performed by Waltz and Miller [WALTZ and MILLER, 1999]: $r/a = 0.5$, $R/a = 3.0$, $\partial_r R_0 = -0.0$, $q = 2.0$, $\hat{s} = 1.0$, $\partial_{r/a}\beta = -0.0$. The input shaping parameters are artificially varied starting with a concentric circular base case and using simple approximations for the gradients and a linear interpolation of the parameters in [WALTZ and MILLER, 1999] as an approximation of the triangularity variation with elongation as follows:

$$\partial_{r/a}\kappa(\kappa) = (\kappa - 1)/(r/a) \quad (5.32)$$

$$\delta(\kappa) = C_\delta(0.416/0.66)(\kappa - 1) \quad (5.33)$$

$$\partial_{r/a}\delta(\kappa) = \delta(\kappa)/(r/a) \quad (5.34)$$

where the constant $C_\delta = 0.75$ was chosen to maintain the physical restriction $-1 \leq \delta \leq 1$ for the range of κ of interest. The test cases are run in the collisionless limit with a single ion species and either adiabatic electrons or a gyrokinetic electron

species with: $R/L_{ni} = R/L_{ne} = 3.00$, $R/L_{Ti} = R/L_{Te} = 9.00$, $T_{0i}/T_{0e} = 1.00$.

Figures 5.10-5.12 first show the results using adiabatic electrons. In the plots of real frequency and linear growth rate in figures 5.11 and 5.12, the reported values are maximized over a scan of $k_y \rho_i$ ranging from 0.1 to 1.0. Figure 5.10 shows these scans for the circular geometry case and for $\kappa = 2.0$ at $\delta = 0.0$ and at $\delta(\kappa) = 0.4727$. As mentioned previously, the reported values for the trial function code are maximized over a scan of the trial function width σ . The dotted curves in figure 5.10, however, show a persistent secondary dominant mode at high σ . While both GS2 and the trial function see a dominant ITG mode (the solid curve) at low to moderate $k_y \rho_i$, the trial function model predicts that the unphysical high σ mode dominates at high $k_y \rho_i$, when the growth rate of the ITG mode becomes small. This high σ mode generally occurs at very large $\left\langle \frac{k_{\perp}^2}{|B|^2} \right\rangle (> 2k_y)$ and very low k_{\parallel} and $\omega_{d,\parallel}$. Recall that this mode was also shown in the plots of linear growth rate vs. temperature gradient length scale in section 5.1 for the optimization of the value of C_{\parallel} (figures 5.3-5.5). In these plots, the high σ mode (the dotted lines) also occurred at high $k_y \rho_i$ and dominated at small R/L_{Ti} (where the ITG growth rate was small), particularly for the low q case. Note, however, that the mode appears to be affected very little by the C_{\parallel} term in these plots; though, at high σ , k_{\parallel} is small and the parallel loss term is relatively trivial. Overall, this mode is unphysical (i.e. it appears with our local approximations but not in the full non-local GS2 eigenfunction calculation), in contrast with the ITG mode (which occurs at moderate σ where bad curvature effects are significant) and, as we will see with the inclusion of gyrokinetic electrons, the TEM mode (which occurs at low σ where trapped particle effects are significant). Thus we neglect this unphysical mode in future trial function results.

Overall, figure 5.11 shows good agreement between the trial function code and GS2 for both the $\delta = 0$ case and the more highly shaped $\delta(\kappa)$ cases. Specifically, for the $\delta = 0$ case, the trial function code shows the stabilizing effects of high κ on the linear ITG instability that are seen with GS2. As κ increases, the dominant mode transitions from a mode with $k_y\rho_i$ of 0.4 to 0.3 to 0.2 and the trial function code also sees this in the scan over $k_y\rho_i$. This is evident in the jumps in the real frequency curve and, more clearly, in the scans over $k_y\rho_i$ for the cases of $\kappa = 1.0$ and $\kappa = 2.0$ in figure 5.10. Comparing the $\delta(\kappa)$ curve with the $\delta = 0$ curve in figure 5.11, the trial function code also shows that δ is slightly destabilizing at low κ and slightly stabilizing at high κ , though the exact stabilizing transition point of the trial function code occurs at lower κ and δ than in GS2. In this case, the dominant mode transitions from a mode with $k_y\rho_i$ of 0.4 to 0.3 and, as shown in the real frequency curve, the trial function transitions to the dominant 0.3 mode earlier. The ability of the trial function code to follow shaping trends is further explored in figure 5.12, which shows the variation of the linear growth rate with δ (also varying $\partial_{r/a}\delta$) for the cases of $\kappa = 1.4$ and $\kappa = 2.0$ (The $\delta(\kappa)$ values for these cases corresponding to figure 5.11 are 0.1891 and 0.4727 respectively). This figure shows that the trial function code is able to follow the trend in GS2 that δ is destabilizing for both cases, yet becomes stabilizing at very high δ for the high $\kappa = 2.0$ case.

Results with the addition of gyrokinetic electrons are shown in figures 5.13 and 5.14. As seen in the scans over $k_y\rho_i$, there are two physical modes: an ITG mode with positive real frequency and a TEM with negative real frequency. While good agreement is seen with the trial function code for both modes for the circular geometry case, for the $(\kappa = 2.0, \delta = 0.0)$ case the trial function code predicts the

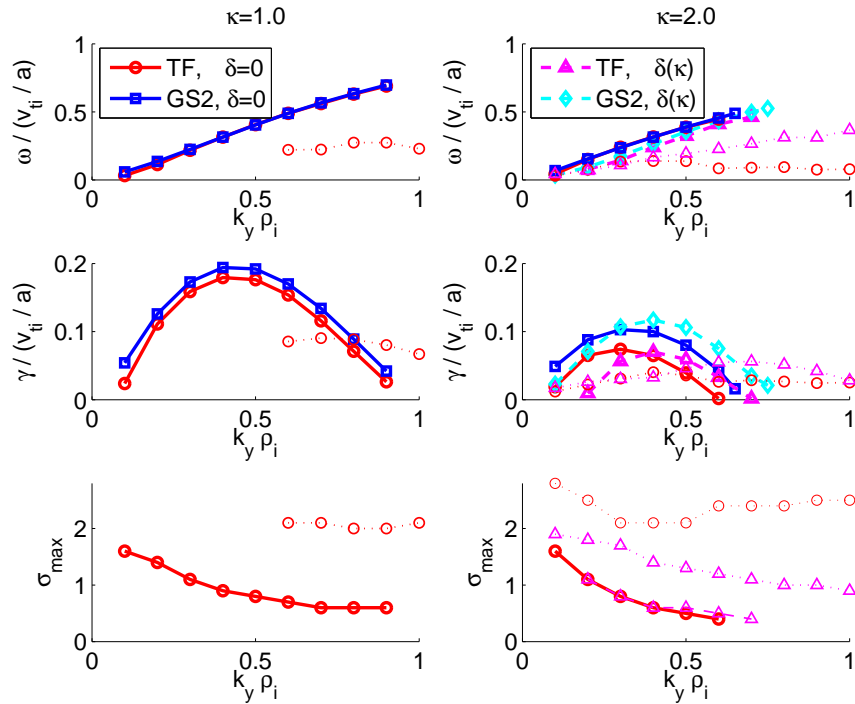


Figure 5.10: Real frequency and linear growth rate vs. $k_y \rho_i$ for generic test case parameters with adiabatic electrons at $(\kappa = 1.0, \delta = 0.0)$, $(\kappa = 2.0, \delta = 0.0)$, and $(\kappa = 2.0, \delta(\kappa) = 0.4727)$ comparing results from GS2 with the trial function code. The lower plots show the corresponding value of the trial function width σ at which the maximum growth rate occurs for a particular $k_y \rho_i$ using the trial function code. (The dotted lines show a persistent unphysical secondary dominant mode at very high σ .)

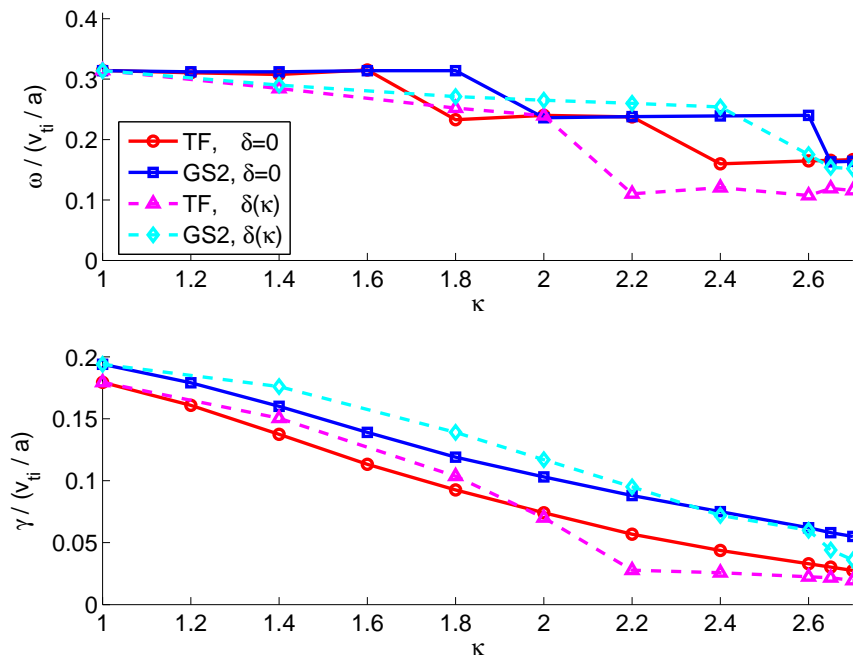


Figure 5.11: Real frequency and linear growth rate vs. κ for generic test case parameters with adiabatic electrons for both $\delta = 0.0$ and δ varied with κ comparing results from GS2 with the trial function code. The reported results are maximized over a scan of $k_y \rho_i$ ranging from 0.1 to 1.0.

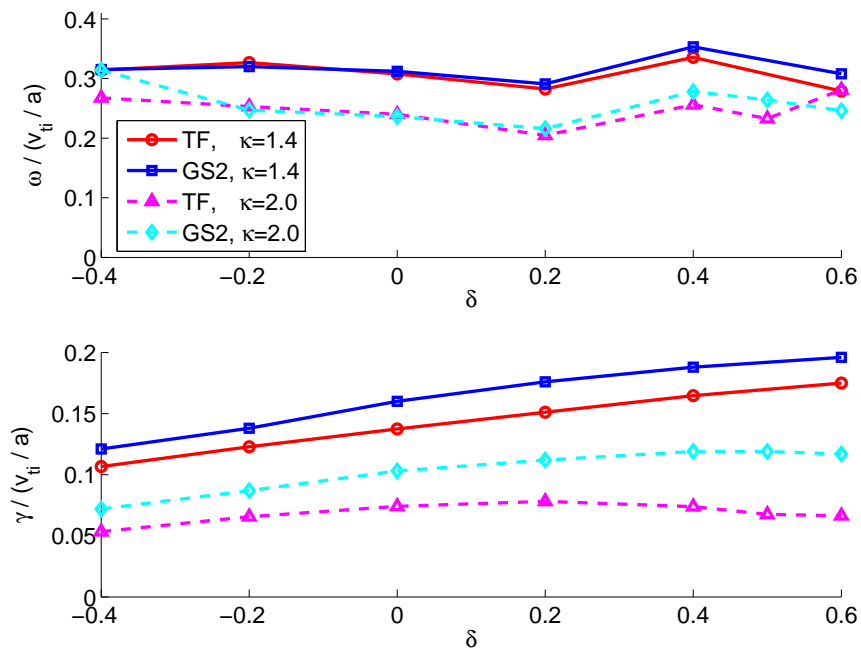


Figure 5.12: Real frequency and linear growth rate vs. δ for generic test case parameters with adiabatic electrons for both $\kappa = 1.4$ and $\kappa = 2.0$ comparing results from GS2 with the trial function code. The reported results are maximized over a scan of $k_y \rho_i$ ranging from 0.1 to 1.0.

TEM as dominant over the entire $k_y\rho_i$ range above 0.1, while GS2 predicts the transition at $k_y\rho_i = 0.7$. For the $\delta(\kappa)$ case, the TEM dominates over the entire range for the trial function model. In these figures we also show the ITG mode (the dotted lines) from the trial function code which appears as the second fastest growing mode below the TEM in a scan over σ . Note that the ITG growth rate is close to the TEM growth rate at low $k_y\rho_i$ and is in agreement with the GS2 results. However, in the trial function scan, the ITG mode disappears above $k_y\rho_i = 0.4$ for the $\delta = 0$ case and above $k_y\rho_i = 0.6$ for the $\delta(\kappa)$ case. In both cases, this is well below GS2's transition point from the dominant ITG mode to the dominant TEM. Even for the circular geometry case we can see that the trial function code overpredicts the TEM growth rate and, considering the previous adiabatic results in which the trial function code underpredicts the ITG growth rate, it is not surprising that the trial function code shows an earlier transition.

Because of this difference, in the shaping scan shown in figure 5.14 we report values at $k_y\rho_i = 0.4$ (where the growth rate is maximum in a scan over $k_y\rho_i$ for $\kappa = 1.0$), rather than maximizing over $k_y\rho_i$ for each equilibrium (yet we are still maximizing the growth rate over σ). Here we see good agreement between GS2 and the trial function code for low to moderate shaping. However, the trial function code predicts a TEM mode dominant over the ITG mode starting at $\kappa = 1.8$ for $\delta = 0.0$ and starting at $\kappa = 2.0$ for $\delta(\kappa)$, while GS2 shows the ITG mode as dominant over the entire range for both cases. However, the dotted lines showing the continuation of the secondary ITG mode in the trial function code are again in good agreement with GS2. This agreement is better for the less-shaped $\delta = 0$ curve, while for $\delta(\kappa)$ the trial function code overpredicts the stabilizing effect of higher shaping and thus shows a steeper gradient. This was also seen in the adiabatic electron results in

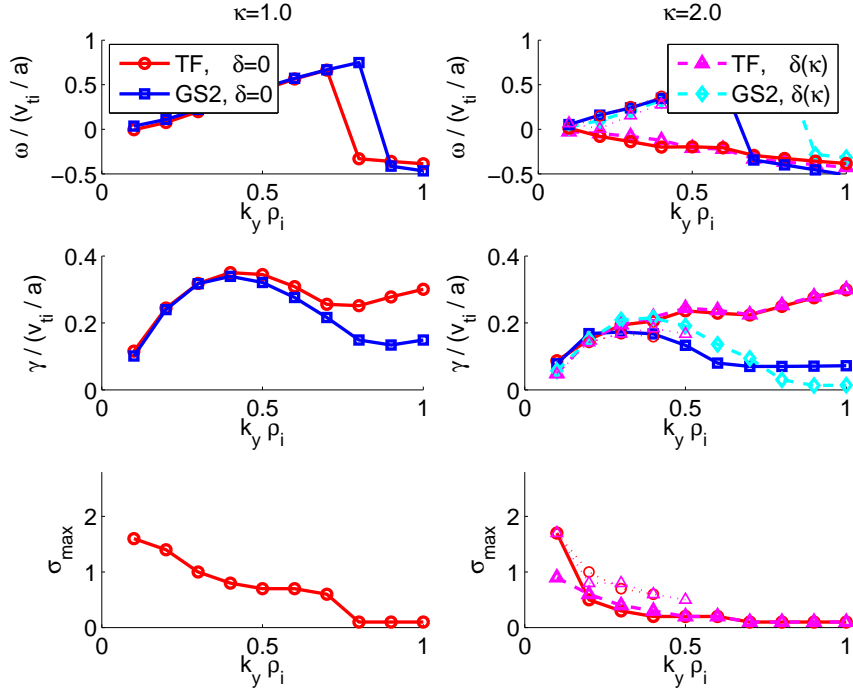


Figure 5.13: Real frequency and linear growth rate vs. $k_y \rho_i$ for generic test case parameters including gyrokinetic electrons at $(\kappa = 1.0, \delta = 0.0)$, $(\kappa = 2.0, \delta = 0.0)$, and $(\kappa = 2.0, \delta(\kappa) = 0.4727)$ comparing results from GS2 with the trial function code. The lower plots show the corresponding value of the trial function width σ at which the maximum growth rate occurs for a particular $k_y \rho_i$ using the trial function code. The dotted lines for the $\kappa = 2.0$ plots show the continuation of the ITG mode, which has become secondary to the TEM.

figure 5.11.

To emphasize the qualitative success of the trial function code even with gyrokinetic electrons, we compare the above results with those obtained without particle trapping effects (artificially obtained using $r/a = 0.001$). These results are shown in figures 5.15 and 5.16. Note that the linear growth rates are generally smaller than for the adiabatic electron case and gyrokinetic electron case with trapping effects. Overall, the agreement between the trial function code and GS2 is good and comparable to the agreement in the adiabatic electron case and for the ITG

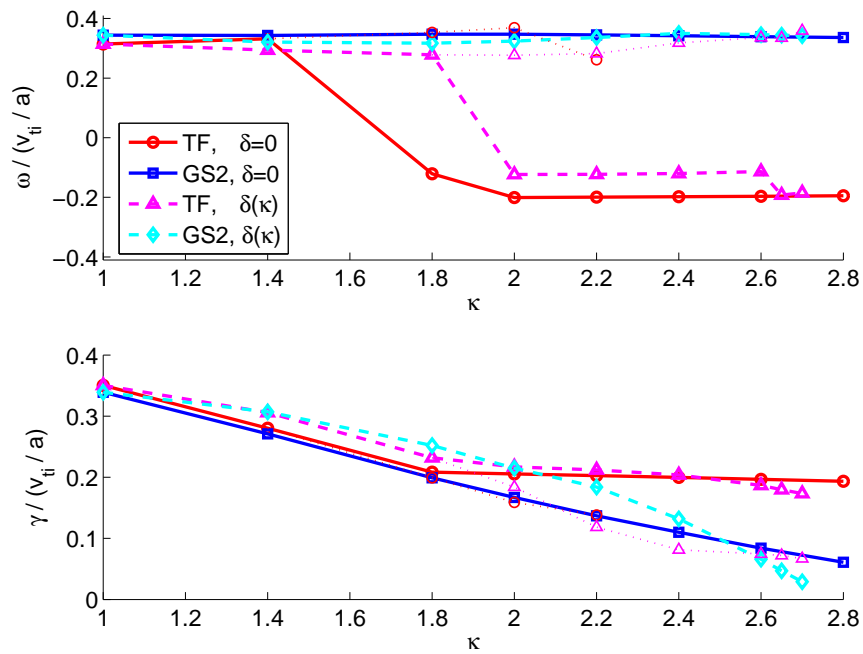


Figure 5.14: Real frequency and linear growth rate vs. κ for generic test case parameters at $k_y \rho_i = 0.4$ including gyrokinetic electrons for both $\delta = 0.0$ and δ varied with κ comparing results from GS2 with the trial function code. The dotted lines show the continuation of the ITG mode, which has become secondary to the TEM.

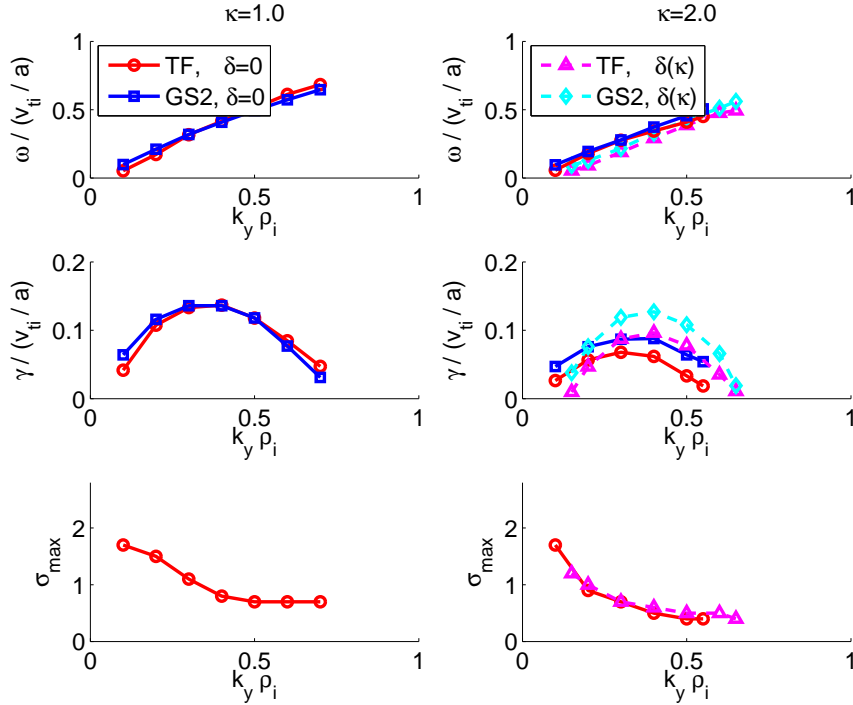


Figure 5.15: Real frequency and linear growth rate vs. $k_y \rho_i$ for generic test case parameters including gyrokinetic electrons but neglecting trapping ($r/a = 0.001$) at $(\kappa = 1.0, \delta = 0.0)$, $(\kappa = 2.0, \delta = 0.0)$, and $(\kappa = 2.0, \delta(\kappa) = 0.4727)$ comparing results from GS2 with the trial function code. The lower plots show the corresponding value of the trial function width σ at which the maximum growth rate occurs for a particular $k_y \rho_i$ using the trial function code.

mode in the gyrokinetic electron case with trapping effects. For this case, since the shaping curve is done at constant $k_y \rho_i$ rather than maximizing over $k_y \rho_i$, the $\delta(\kappa)$ curve shows the complete stabilization of the ITG mode at high shaping. (In the adiabatic curve at high shaping a transition to a still unstable mode at smaller $k_y \rho_i$ was seen.) However, again because of the trial function code's underprediction of the ITG growth rate which becomes more inaccurate at high shaping, the stabilization is seen much earlier than with GS2.

Overall, the results of figures 5.10-5.16 show that the trial function code is able to follow the same shaping trends as GS2 both in the adiabatic electron limit and

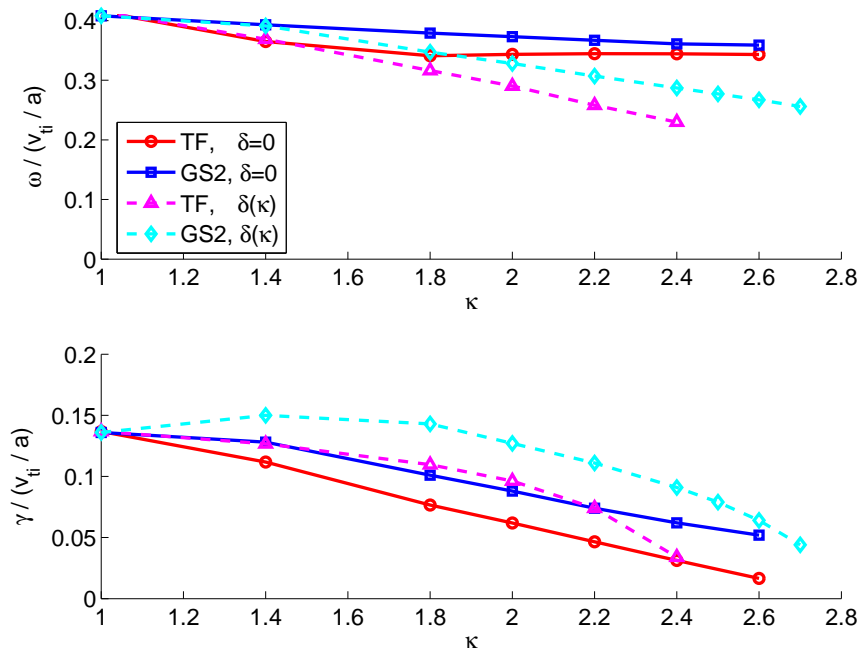


Figure 5.16: Real frequency and linear growth rate vs. κ for generic test case parameters at $k_y \rho_i = 0.4$ including gyrokinetic electrons but neglecting trapping ($r/a = 0.001$) for both $\delta = 0.0$ and δ varied with κ comparing results from GS2 with the trial function code.

with the inclusion of gyrokinetic electron dynamics. Good agreement was seen for both the ITG mode and the TEM. However, overprediction of the TEM growth rate has led to inaccuracies in the trial function model in predicting the transition from a dominant ITG mode to a dominant TEM mode, suggesting that a better model for trapped particles is needed.

The result that the trial function code usually overpredicts the growth rate of the TEM may be a consequence of its oversimplification of trapped particle dynamics. At present, it models all trapped particles as having a toroidal drift precession frequency given by $\langle \omega_{dv}(v_{\parallel}v_{\perp}) \rangle_{TF}$, where $\langle \dots \rangle_{TF}$ is an average over the trial eigenfunction. However, a better approximation would probably be to use the bounce-averaged $\langle \omega_{dv} \rangle_{B.A.}$, i.e. by averaging ω_{dv} around a trapped particle's orbit, which depends on the particle pitch angle. This would account for the difference between barely trapped particles and deeply trapped particles. Barely trapped particles spend most of their time on the good curvature side of a tokamak, and so have a positive $\langle \omega_{dv} \rangle_{B.A.}$ and have a stabilizing influence on the mode. In contrast, deeply trapped particles spend most of their time on the bad curvature side of a tokamak, and so have a negative $\langle \omega_{dv} \rangle_{B.A.}$ and can contribute to destabilizing modes. We leave exploration of an improved model using a bounce-averaged $\langle \omega_{dv} \rangle_{B.A.}$ for future work.

It is interesting to compare the optimal σ scan in our trial function model with the model of Waltz [WALTZ *et al.*, 1997], which uses even and odd Gaussian trial functions and scales the trial function width as $\sigma_{Waltz} = (\pi/3)[1 + 0.2(q/2 - 1)]^{-1}[1 + 0.1(\hat{s} - 1)^2]^{-1/2}$, based on empirical fits with test case parameters. For our parameters, this yields $\sigma_{Waltz} = 1.0472$, which is generally on the same order as our scan over σ . (We found σ to be smaller (~ 0.5) for larger $k_y\rho_i$ and for the

TEM (~ 0.1 .) Exact equivalence between our σ and Waltz's σ is not expected since, in addition to the use of an odd Gaussian trial function for k_{\parallel} , the Waltz model also uses empirically-based fitting parameters to adjust k_{\parallel} and the trapping condition (by adjusting them by factors slightly below unity), which has the effect of decreasing the effective σ with respect to $1/k_{\parallel}$. Recall also that the Waltz model was developed for use in \hat{s} - α geometry. Indeed, looking at the σ_{max} plots for our results, we do not see a large variation in σ_{max} at a particular $k_y \rho_i$ across shaping in figure 5.15 and in the ITG branch of figure 5.13, i.e. comparing $\kappa = 1.0$ with $\kappa = 2.0$, $\delta = 0.0$ and $\kappa = 2.0$, $\delta(\kappa)$. However, as we found with the unphysical high σ mode, choice of σ for the model is somewhat arbitrary, and our method of reporting the “worst case physical result” as the dominant growth rate seems to benchmark fairly well with GS2. In the end, there is of course trade-off between a σ calculation which is accurate for arbitrary equilibrium yet significantly less computationally intensive than solution of the gyrokinetic equation on a θ grid.

While the above results were done at fixed temperature gradient, the ability of the trial function code to predict the scaling of the critical temperature gradient in the presence of shaping was also explored. These results are shown in figures 5.17 and 5.18 for the cases of adiabatic electrons and inclusion of gyrokinetic electrons respectively. The parameters for this scan are modified from [MILLER *et al.*, 1998]: $r/a = 0.83$, $R/a = 2.631$, $\partial_r R_0 = -0.354$, $q = 3.03$, $\hat{s} = 2.85$, $\partial_{r/a} \beta = -0.0$. The original shaping parameters of [MILLER *et al.*, 1998] correspond to $\kappa = 1.66$, $\partial_{r/a} \kappa = 1.40$, $\delta = 0.416$, $\partial_r \delta = 1.50$. The figures show scans of the real frequency and linear growth rate vs. the temperature gradient length scale (at constant density gradient $R/L_{ni} = 2.63$ and $T_{0i} = T_{0e}$) at various δ . We vary $\partial_{r/a} \delta$ proportionately as δ is varied from the original parameters. For the case of $\kappa = 2.075$, $\partial_{r/a} \kappa$ is

likewise varied as a linear interpolation between the circular case and the value at the original shaping. The reported growth rates at each temperature gradient are maximized over $k_y \rho_i$ in the range $[0, 1]$.

Consider first the case of adiabatic electrons, shown in figure 5.17. In general, the trial function code is able to accurately follow GS2 in both the low and high temperature gradient regimes for the ITG mode. Note that because the trial function results and GS2 results were maximized over $k_y \rho_i$ independently, this figure also verifies that the trial function is able to find the correct maximum at all temperature gradient regimes. Looking at the shaping trends, it is interesting that the destabilizing effect of triangularity is seen even near the critical temperature gradient. In contrast, for the higher κ case at the original $\delta = 0.416$, both GS2 and the trial function code show a slight stabilizing upshift in the linear critical temperature gradient.

For the case of inclusion of gyrokinetic electron dynamics, shown in figure 5.18, good agreement is similarly found between the trial function code and GS2 in the high temperature gradient regime (where the ITG mode dominates) at all degrees of shaping. The general destabilizing effect of triangularity on the ITG mode is also again observed. As the temperature gradient decreases, the trial function code is able to follow the transition from the dominant ITG mode to the dominant TEM and the agreement of the TEM growth rate with that found by GS2 is fairly good, at least at higher δ . The exact value near the transition point appears to be more inaccurate for the $\delta = 0$ case, though the growth rates are generally smaller across the entire R/L_T regime for this case, so the relative error is reasonable. (The exact transition point can be difficult to predict for any initial value code in general due to the interference effects between the two modes which have similar dominant growth

rates at this point.) Near the transition point, the trial function code is predicting the maximum growth rate in the scan over $k_y\rho_i$ near $k_y\rho_i = 1.0$, rather than near $k_y\rho_i = 0.5$, as does GS2 and both codes for the higher R/L_T regime. This can be seen in figures 5.19 and 5.20 which show the scans over $k_y\rho_i$ for each temperature gradient for the $\delta = 0.416$ case. These figures show that the maximum growth rate occurs at larger $k_y\rho_i$ for smaller the R/L_T regime than for the larger R/L_T regime. However, near the transition point ($R/L_T \sim 2.6$), the GS2 curve peaks near its ITG maximum range of $k_y\rho_i = 0.5$, while the trial function curve does not turn over until near $R/L_T \sim 5.2$. Overall, as with the shaping scans, improvements in the trapped particle model may be needed to enhance quantitative agreement near the transition from TEM to ITG.

5.4.2 Electromagnetic Results

Benchmarks with GS2 have also been performed with the inclusion of electromagnetic dynamics. The parameters for this test case are: $r/a = 0.001$, $R/a = 1.00$, $\partial_r R_0 = -0.0$, $q = 4.472$, $\hat{s} = 3.00$, $\partial_{r/a}\beta = -0.0$, \hat{s} - α geometry, $R/L_{ni} = R/L_{ne} = 5.0$, $R/L_{Ti} = 12.5$, $R/L_{Te} = 10.0$, $T_{0i} = T_{0e}$. (Here a is not the minor radius but the normalizing length used internally in the code; such as when reporting the growth rate normalized with respect to v_{ti}/a .) Note that the non-trapping limit is used for simplicity since the effects of particle trapping were explored in the electrostatic benchmarks and here we focus more narrowly on the effects of electromagnetic dynamics. Also, note that $\partial_{r/a}\beta$ is not varied as β is varied. (In gyrokinetics, $\partial_{r/a}\beta$ enters in as an equilibrium parameter related to the gradient of the Shafranov shift, while β is a dynamical parameter and thus each can be varied independently. Here we keep $\partial_{r/a}\beta$ constant to focus on the dynamical effect of β while maintaining a

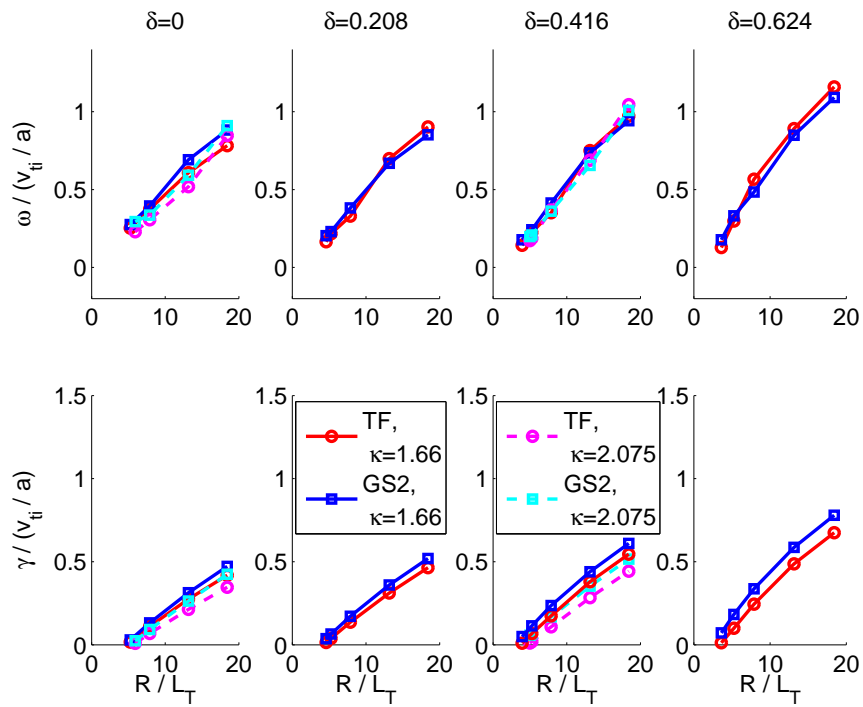


Figure 5.17: Real frequency and linear growth rate vs. temperature gradient length scale for generic test case parameters with adiabatic electrons for various δ and κ comparing results from GS2 with the trial function code. The reported results are maximized over a scan of $k_y \rho_i$ ranging from 0.1 to 1.0.

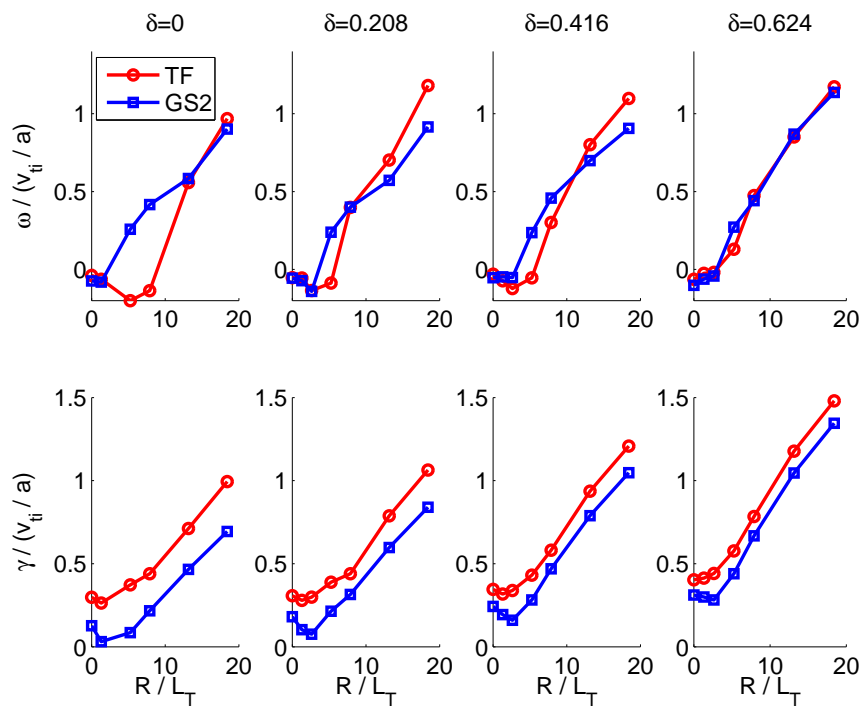


Figure 5.18: Real frequency and linear growth rate vs. temperature gradient length scale for generic test case parameters including gyrokinetic electrons for various δ at constant $\kappa = 1.66$ comparing results from GS2 with the trial function code. The reported results are maximized over a scan of $k_y \rho_i$ ranging from 0.1 to 1.0.

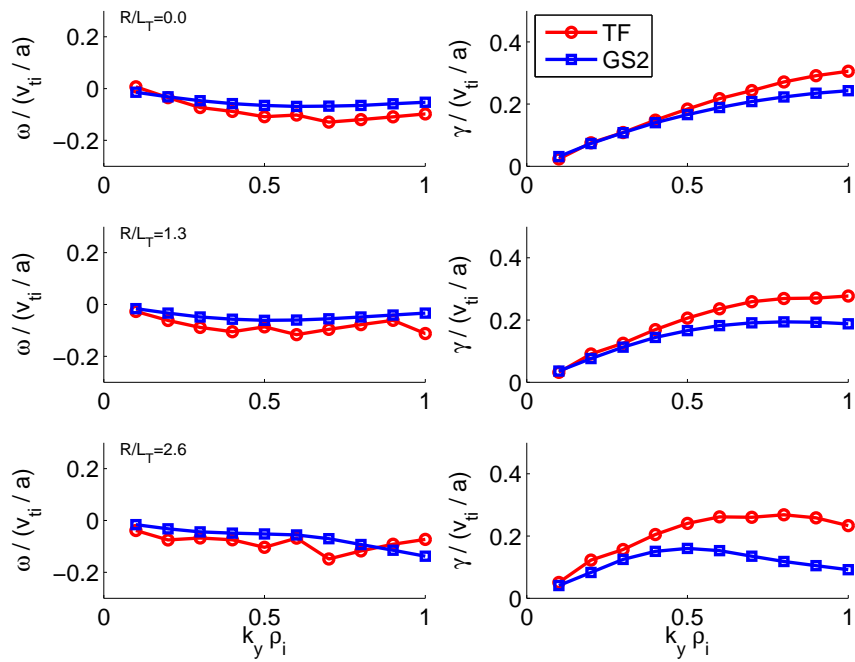


Figure 5.19: Real frequency and linear growth rate vs. $k_y \rho_i$ for generic test case parameters at $\kappa = 1.66$ and $\delta = 0.416$ including gyrokinetic electrons for various low values of the temperature gradient length scale comparing results from GS2 with the trial function code.

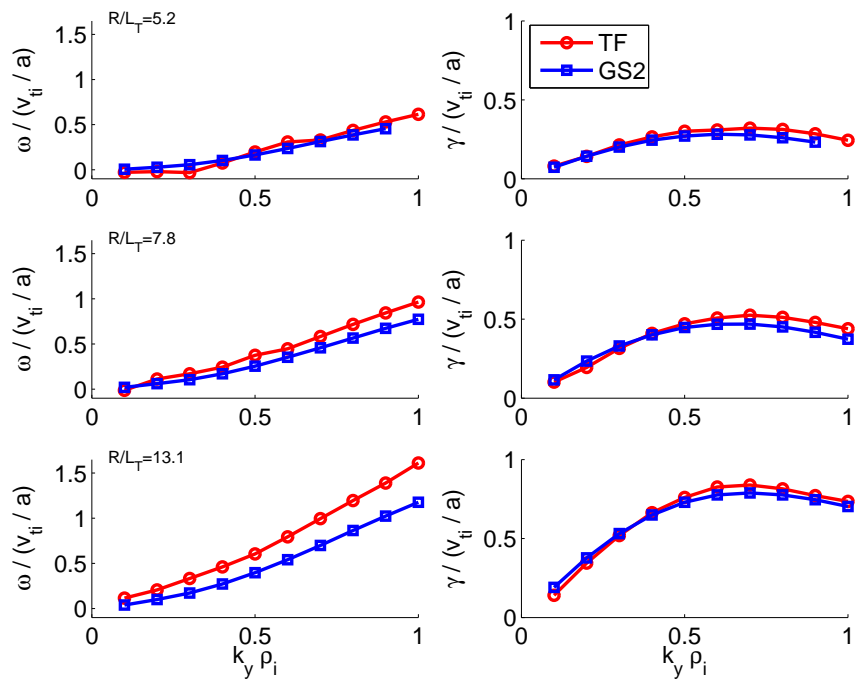


Figure 5.20: Real frequency and linear growth rate vs. $k_y \rho_i$ for generic test case parameters at $\kappa = 1.66$ and $\delta = 0.416$ including gyrokinetic electrons for various high values of the temperature gradient length scale comparing results from GS2 with the trial function code.

fixed equilibrium.)

Figure 5.21 shows the variation of the real frequency and linear growth rate with $k_y \rho_i$. In the electrostatic limit ($\beta = 0$), we find good agreement between the trial function code and GS2. However, with the inclusion of electromagnetic dynamics with a high value of β ($\beta_i = \beta_e = 2\%$), while the trial function code is able to follow the destabilization of finite β effects at high $k_y \rho_i$, at low $k_y \rho_i$ the trial function completely misses the strong destabilization due to the kinetic ballooning mode, showing instead a continuation of the high $k_y \rho_i$ mode.

The failure of the trial function code to represent the physics of the kinetic ballooning mode is further explored in figure 5.22. This figure shows a scan of the linear growth rate over β in both the low and high $k_y \rho_i$ regimes. It has been shown previously that the general trend with β for gyrokinetics is that the ITG mode dominates at low β (i.e. $\beta < \beta_c$, where β_c is the threshold for the kinetic ballooning instability) and is stabilized with increased β ; for $\beta > \beta_c$, the kinetic ballooning mode then dominates and is further destabilized with increased β [KIM *et al.*, 1993]. (However, 2nd stability at higher β can occur if the $\partial_r/a\beta$ effects on the equilibrium are included.) This trend is seen in the GS2 results for both $k_y \rho_i = 0.1$ and 0.7, with β_c relatively downshifted shifted for the $k_y \rho_i = 0.1$ case, above which the kinetic ballooning mode is very strongly unstable. The trial function code is able to follow GS2 in the regime of both the ITG mode and the kinetic ballooning mode for the $k_y \rho_i = 0.7$ case. However, for the $k_y \rho_i = 0.1$ case, the trial function results agree with GS2 only in the low β ITG regime. The trial function code does see a shift to a new dominant mode at high β , though its transition point β_c is too high ($\beta_c \sim 1.4\%$ rather than 0.4%) and it greatly underpredicts the growth rate of the kinetic ballooning mode, barely increasing as β is increased. Thus,

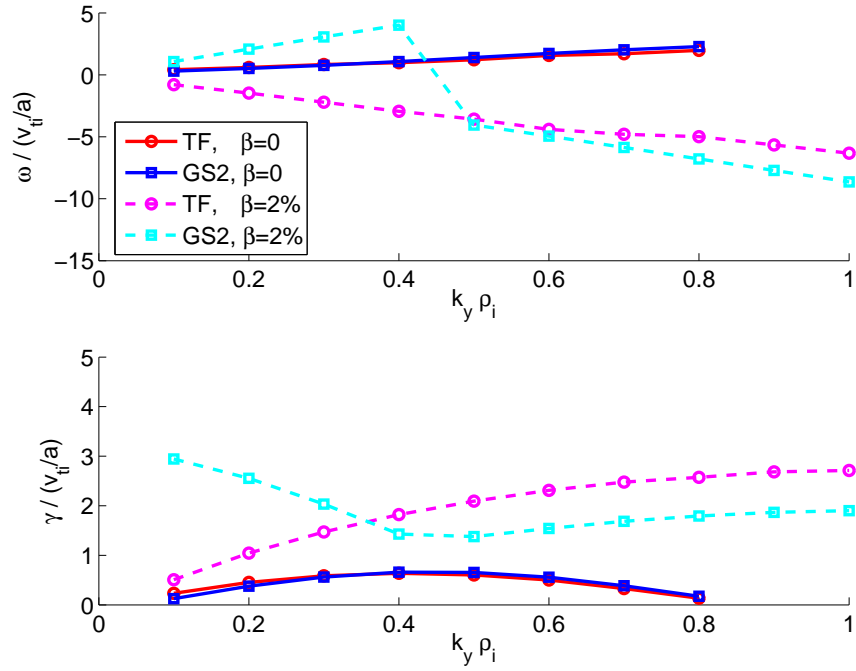


Figure 5.21: Real frequency and linear growth rate vs. $k_y \rho_i$ for generic test case parameters including electromagnetic dynamics comparing results from GS2 with the trial function code.

while benchmarks with GS2 were successful for the ITG mode both electrostatically and electromagnetically, these results show that extensions to include magnetic fluctuations and accurately recover the kinetic ballooning β limit are more difficult and may require extending the trial function model to include coupling to higher-order Hermite basis functions. This extension is explored in the next section.

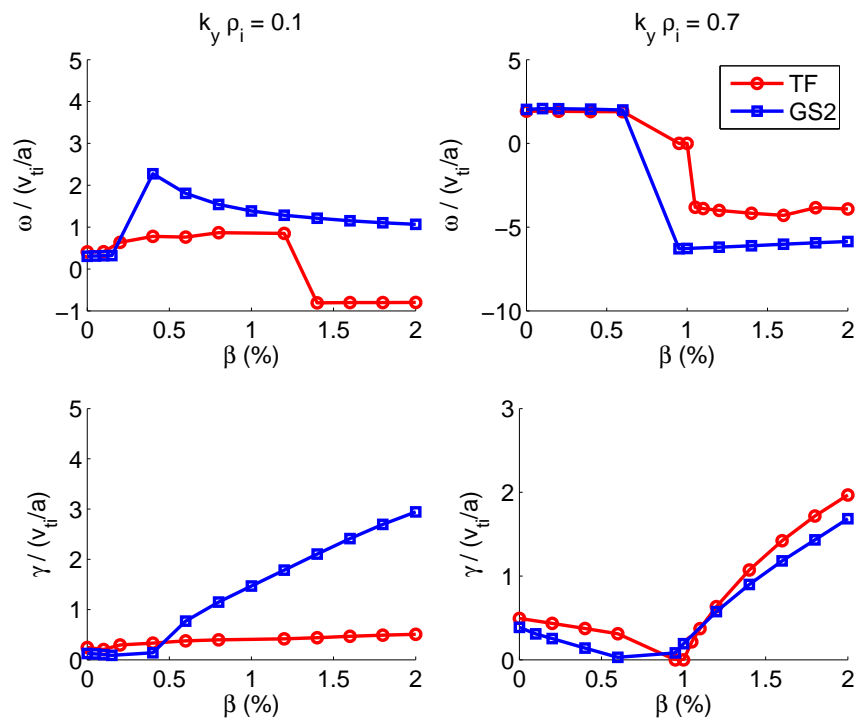


Figure 5.22: Real frequency and linear growth rate vs. $\beta_i = \beta_e \equiv \beta$ for generic test case parameters including electromagnetic dynamics comparing results from GS2 with the trial function code.

5.5 Higher-Order Models

The trial function model is more generally based on an expansion of the distribution function in terms of normalized Hermite polynomials, i.e.

$$h(\theta, v_{\parallel}, t) = e^{-\theta^2/4\sigma^2} \sum_{n=0}^{\infty} H_n \left(\frac{\theta}{\sqrt{2}\sigma} \right) h_n(v_{\parallel}, t) \quad (5.35)$$

where $H_n(x) = e^{x^2} \frac{d^n}{dx^n} e^{-x^2} \frac{(-1)^n}{\pi^{1/4} 2^{n/2} \sqrt{n!}}$. Here we discuss the extension of the trial function model to higher-order and a more natural derivation of the parallel loss term as a closure model for this expansion.

We consider the extended Hermite expansion in the simplified gyrokinetic equation

$$\frac{\partial h}{\partial t} + \frac{v_{\parallel}}{qR} \frac{\partial h}{\partial \theta} = \langle L(h) \rangle \quad (5.36)$$

where $L(h)$ is the general linear operator consisting of the rest of the terms in the full linear gyrokinetic equation, i.e.

$$\langle L(h_s) \rangle = -i \langle \omega_{dv} \rangle h_s + \left(\frac{\partial}{\partial t} + i\omega_{*T} \right) \frac{Z_s e F_M}{T_{0s}} \langle J_{0s} \rangle \left(\Phi - \frac{v_{\parallel}}{c} A_{\parallel} \right) \quad (5.37)$$

In general, a Hermite basis expansion of the terms represented by $L(h)$ is also necessary for an exact treatment of the gyrokinetic equation. However, we are not interested in developing a full Hermite expansion model, such as that used in the kinetic FULL code [REWOLDT *et al.*, 1982; REWOLDT *et al.*, 1987] or developed by Staebler for the gyro-Landau-fluid-based GLF23 code [STAEBLER *et al.*, 2005]. Rather, here we explore the significance of the various terms in the expansion model and develop a higher-order approximation to our original trial function model based on this analysis.

Thus, to begin, we consider only a higher-order Hermite basis transformation of the $v_{\parallel} \hat{b} \cdot \nabla$ term, which is generally dominant, particularly for electron dynamics. Using the expansion for h given by Eq. (5.35) in Eq. (5.36), the new trial function-based gyrokinetic equation becomes

$$\frac{\partial h_m}{\partial t} + \frac{v_{\parallel}}{2\sigma q R} \left[(\sqrt{m+1}) h_{m+1} - (\sqrt{m}) h_{m-1} \right] = \langle L(h_m) \rangle \quad (5.38)$$

for $m = 0, 1, 2, \dots$. Note that the scaling of the constant factor for the v_{\parallel} term matches the trial function-averaged $\sqrt{\langle k_{\parallel}^2 \rangle}$ of the original trial function model, given in Eq. (5.8). For closure of the system of equations, we consider a model of the form

$$h_{m,f+1}(v_{\parallel}, t) = C_0 h_{m,f-1}(v_{\parallel}, t) + C_1 \text{sgn}(v_{\parallel}) h_{m,f}(\theta, v_{\parallel}) \quad (5.39)$$

The closure constants C_0 and C_1 are determined by minimizing the error $\epsilon^2 = \int_0^{\infty} dt |h_{m,f+1,exact} - h_{m,f+1,closure}|^2$, where h_{exact} refers to the exact solution of the simplified gyrokinetic equation as given by Eq. (5.36) with $\langle L(h_m) \rangle = 0$ for a specific initial condition, i.e.

$$h_{exact}(\theta, v_{\parallel}, t) = F_M(v_{\parallel}) e^{-(\theta - v_{\parallel} t / qR)^2 / 4\sigma^2} \quad (5.40)$$

or, expanding this solution in Hermite basis functions,

$$h_{m,exact}(v_{\parallel}, t) = \frac{\pi^{1/4}}{\sqrt{m!}} \left(\frac{v_{\parallel} t}{2\sigma q R} \right)^m e^{-v_{\parallel}^2 t^2 / (8\sigma^2 q^2 R^2)} \quad (5.41)$$

We consider the closure equation in both a single constant form, where ϵ^2 is minimized only with respect to $C_1 \equiv C$ and we set $C_0 = 0$, as well as in a two constant form, where ϵ^2 is minimized with respect to both C_0 and C_1 . For these cases, we

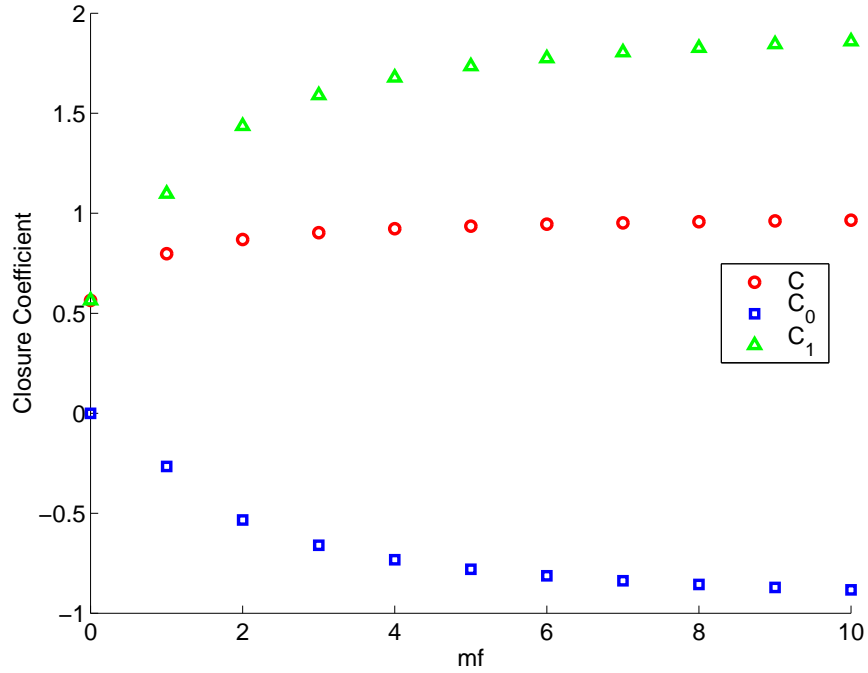


Figure 5.23: Closure coefficients for the Hermite-based trial function equations vs. final order of the expansion. C is the coefficient for the single constant closure model: $h_{mf+1} = C \operatorname{sgn}(v_{\parallel}) h_{mf}$. C_0 and C_1 are the coefficients for the two constant closure model: $h_{mf+1} = C_0 h_{mf-1} + C_1 \operatorname{sgn}(v_{\parallel}) h_{mf}$.

find that, for a general final order m ,

$$C = \frac{1}{\sqrt{m+1}} \frac{\Gamma(m+1)}{\Gamma(m+1/2)} \quad (5.42)$$

$$C_0 = \frac{m^{-1/2} [\Gamma^2(m+1/2) - \Gamma(m)\Gamma(m+1)]}{\sqrt{m+1} [\Gamma(m+1/2)\Gamma(m-1/2) - \Gamma^2(m)]} \quad (5.43)$$

$$C_1 = \frac{[\Gamma(m+1)\Gamma(m-1/2) - \Gamma(m)\Gamma(m+1/2)]}{\sqrt{m+1} [\Gamma(m+1/2)\Gamma(m-1/2) - \Gamma^2(m)]} \quad (5.44)$$

Figure 5.23 shows the variation of the closure constants with m .

Implementation of the above Hermite model is done analogously compared with

the original trial function mode, by rewriting the equations in terms of $h_{s,m} \rightarrow g_{s,m} + \frac{Z_s e F_M}{T_{0s}} \langle J_{0s} \rangle \left(\Phi_m - \frac{v_{\parallel}}{c} A_{\parallel,m} \right)$. Discretization is also done as before, treating the distribution function terms implicitly and the field terms explicitly with a 2nd order Adams-Bashforth scheme. Thus, the Hermite-based gyrokinetic equations can be solved independently for each particular species at each velocity grid point for all specified Hermite orders as a series of $n_{species} n_{vel}$ simple tri-diagonal matrix equations using standard Gaussian elimination with backsubstitution.

Note that the original trial function model given by Eq. (5.9) is equivalent to the 0th order Hermite-based equation with the addition of an $i\sqrt{\langle k_{\parallel}^2 \rangle} v_{\parallel} h_s$ term on the RHS. The value of the closure constant for the trial function model ($C_{\parallel} = 0.13$) is also smaller than the value for the 0th order Hermite-based model given by figure 5.23 ($C = 0.564$). However, while the higher-order model is designed to improve the trial function model in the more general electromagnetic description, it is anticipated that the original trial function model will perform better than the 0th order Hermite model with electromagnetic dynamics. The reason for this is that the 0th order Hermite equation does not have any terms involving g_s which are dependent on the sign of v_{\parallel} . This means that the only $sgn(v_{\parallel})$ dependence in the gyrokinetic equation is in the A_{\parallel} term, indicating that the Poisson equation, which picks out only the part of g_s which is symmetric in v_{\parallel} , will not be influenced by the effect of A_{\parallel} on g_s in the gyrokinetic equation. This likewise applies to the Ampere equation, which picks out the part of g_s which is antisymmetric in v_{\parallel} . Thus, the electrostatic and electromagnetic dynamics are completely decoupled. The effect of this is that the growth rate obtained from the 0th order Hermite-based equation is exactly the same (and gives the electrostatic value) regardless of the value of β . Thus, the 0th order equation is not extendable to the electromagnetic description.

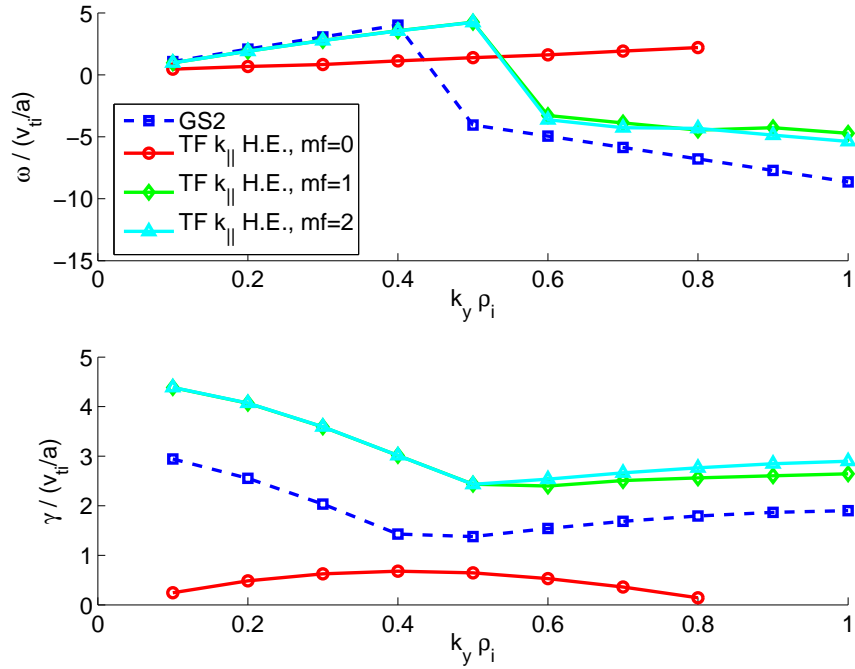


Figure 5.24: Real frequency and linear growth rate vs. $k_y \rho_i$ for generic test case parameters including electromagnetic dynamics comparing results from GS2 with the trial function code based on a Hermite basis transformation of the $k_{\parallel} v_{\parallel}$ term. The expansion is done to order mf and a single constant closure model is applied.

Results from the use of the higher-order Hermite basis transformation of the $k_{\parallel} v_{\parallel}$ term with the single constant closure is shown in figure 5.24. As expected, the original trial function model results (shown in figure 5.21) yield better agreement than the 0th order Hermite model for the high $k_y \rho_i$ mode, though both models fail to find the transition in the fastest growth mode at low $k_y \rho_i$ to the kinetic ballooning instability. However, with the retention of just two Hermite orders, the trial function model is able to capture the physics of the kinetic ballooning instability and, furthermore, shows good agreement with GS2 in both the low and high $k_y \rho_i$ regimes.

Figure 5.25 shows the results using the two constant closure model. Comparing these results with those in figure 5.24 for the higher-order models, we find that the

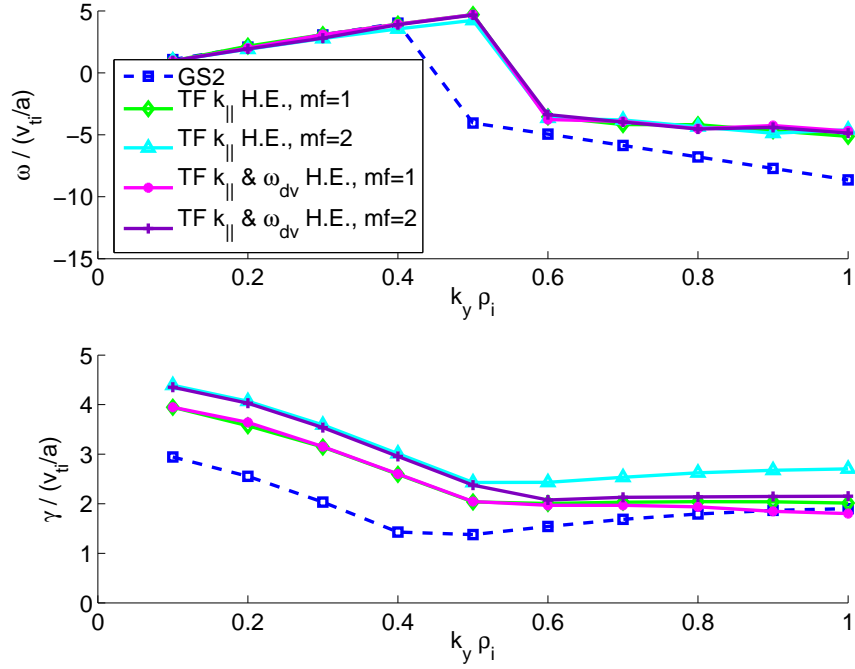


Figure 5.25: Real frequency and linear growth rate vs. $k_y \rho_i$ for generic test case parameters including electromagnetic dynamics comparing results from GS2 with the trial function code based on a Hermite basis transformation of 1) just the $k_{\parallel} v_{\parallel}$ term and 2) the $k_{\parallel} v_{\parallel}$ term and the ω_{dv} term. The expansion is done to order mf and a two constant closure model is applied.

two constant closure model is more accurate than the single constant closure model, particularly in the high $k_y \rho_i$ regime. Though the overall effect is small, we adopt the two constant closure for the rest of our studies, since the form of the equations is tri-diagonal with either model and no significant additional computation is required for this model.

To achieve better improvement, higher-order Hermite basis expansions of all of the terms in the gyrokinetic equation (not just the $k_{\parallel} v_{\parallel}$ term) must also be considered. This generally leads to a coupling between various m -th order moments which can be considered numerically. Here we present an extension of the Hermite-based model by also considering the expansion of the curvature and ∇B drift terms

in addition to the $k_{\parallel}v_{\parallel}$ term. Specifically, the Hermite expansion of h is considered in the following simplified gyrokinetic equation:

$$\frac{\partial h}{\partial t} + \frac{v_{\parallel}}{qR} \frac{\partial h}{\partial \theta} + i\omega_{dv}(\theta)h = \langle \tilde{L}(h) \rangle \quad (5.45)$$

where

$$\langle \tilde{L}(h_s) \rangle = \left(\frac{\partial}{\partial t} + i\omega_{*T} \right) \frac{Z_s e F_M}{T_{0s}} \langle J_{0s} \rangle \left(\Phi - \frac{v_{\parallel}}{c} A_{\parallel} \right) \quad (5.46)$$

This yields the following set of coupled equations for h_m :

$$\begin{aligned} & \frac{\partial h_m}{\partial t} + \frac{v_{\parallel}}{2\sigma qR} \left[\sqrt{m+1} h_{m+1} - \sqrt{m} h_{m-1} \right] \\ & + i \sum_0^{\infty} h_n \int_{-\infty}^{\infty} dx e^{-x^2} H_m(x) H_n(x) \omega_{dv}(\sqrt{2}\sigma x) = \langle L(h_m) \rangle \end{aligned} \quad (5.47)$$

As a closure for the ω_{dv} term, we terminate the summation at the last full Hermite order which is retained. This is unlike the $k_{\parallel}v_{\parallel}$ term closure, where an approximation for the next order is made, since a fully analytic form for the closure coefficients is not available upon inclusion of the term $+i\omega_{dv}(\theta)h_{m,exact}$ in the exact equation.

Comparing Eq. (5.47) with the original trial function model, note that the ω_{dv} term in Eq. (5.47) yields higher-order moments of the original Gaussian trial function averages. Since $\omega_{d,\parallel}$ and $\omega_{d,\perp}$ are symmetric in θ for an axisymmetric tokamak (assuming up-down symmetry and for modes with $k_x = 0$), only even orders of this term are nonzero for m even and likewise odd orders for m odd. Thus, the 0th order equation is equivalent to the gyrokinetic equation using only the $k_{\parallel}v_{\parallel}$ term, i.e. Eq. (5.38), since the $(m = 0, n = 0)$ coupling yields the term $i \langle \omega_{dv} \rangle h_0$, while the $(m = 0, n = 1)$ coupling yields the term $(i/\sigma) \langle \theta \omega_{dv} \rangle h_1$ which is 0.

Figure 5.25 shows the results from inclusion of the ω_{dv} term in the Hermite

expansion for $m_f = 1$ and $m_f = 2$. Compared with the previous Hermite expansion model, a slight improvement is seen at high $k_y \rho_i$, while no significant improvement is seen at low $k_y \rho_i$. For further investigation, figure 5.26 shows the accuracy of the extended Hermite expansion model as β is varied at constant $k_y \rho_i$ in both the low and high $k_y \rho_i$ regimes, for comparison with the results from the original trial function model in figure 5.22. The Hermite models and the original trial function model produce similar results for the $k_y \rho_i = 0.7$ case, i.e. following the GS2 results in the low β ITG regime and continuing through the transition to the strongly destabilized kinetic ballooning mode. However, the significant difference in the models is seen in the $k_y \rho_i = 0.1$ results. Recall that the the original trial function model was unable to accurately predict the transition to the kinetic ballooning mode and furthermore greatly underpredicted its growth rate. In contrast, figure 5.26 shows that with just a 1st order expansion in the model, the rate of destabilization with increased β is accurately recovered, though the transition point is somewhat lower than it should be.

Future work may explore a more general formulation of the Hermite expansion model in Eq. (5.35), such as follows:

$$\hat{h}(\theta, v_{\parallel}, t) = e^{iS(\theta)} e^{-\theta^2/4\sigma^2} \sum_{n=0}^{\infty} H_n \left(\frac{\theta}{\sqrt{2}\sigma} \right) h_n(v_{\parallel}, t) \quad (5.48)$$

where $S(\theta)$ is any real function of theta. A natural choice might be $S(\theta) = k_{\parallel,0} q R \theta$, where $k_{\parallel,0} = \sqrt{\langle k_{\parallel}^2 \rangle}$. Considering this expansion model in the simplified gyrokinetic equation given by Eq. (5.36), we obtain:

$$\frac{\partial h_m}{\partial t} + \frac{v_{\parallel}}{2\sigma q R} \left[(\sqrt{m+1}) h_{m+1} - (\sqrt{m}) h_{m-1} \right] + i k_{\parallel,0} v_{\parallel} h_m = \langle L(h_m) \rangle \quad (5.49)$$

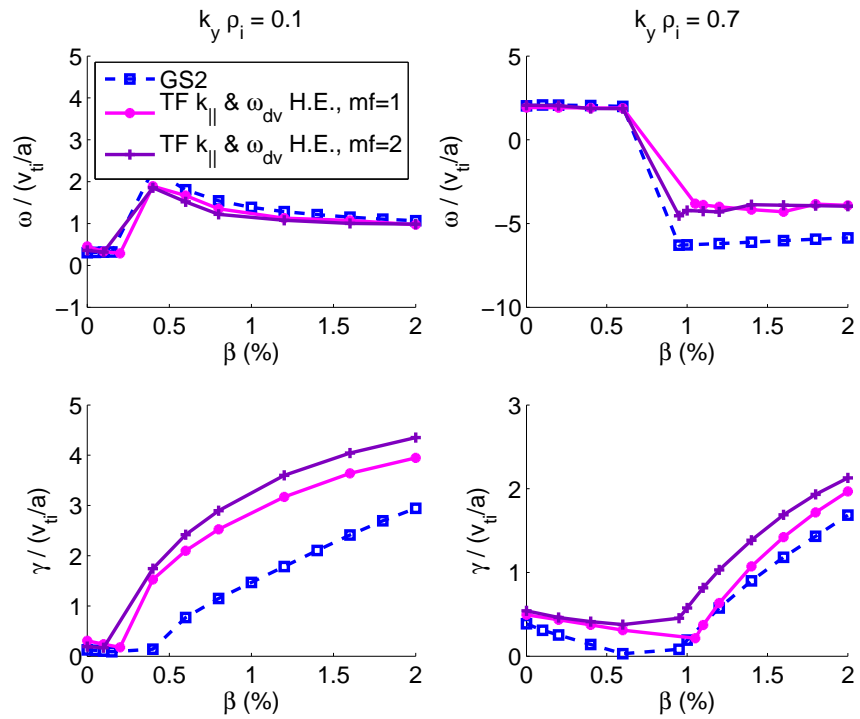


Figure 5.26: Real frequency and linear growth rate vs. $\beta_i = \beta_e \equiv \beta$ for generic test case parameters including electromagnetic dynamics comparing results from GS2 with the trial function code based on a Hermite basis transformation of the $k_{||}v_{||}$ term and the ω_{dv} term. The expansion is done to order mf and a two constant closure model is applied.

Note that using the closure model of Eq. (5.39) and again defining the closure coefficients to minimize the mean squared error, we find that the closure coefficients are independent of $k_{\parallel,0}$, i.e. we retain the closure constants given in Eqs. (5.42) - (5.44). The advantage of this model compared to the model in Eq. (5.38) is that it recovers the lowest order $m=0$ Hermite representation of the original trial function model in Eq. (5.9) and thus provides a more systematic derivation of the equations being used in the reduced-model. Future work could explore this higher-order expansion as an alternative.

Overall, the results presented here generally confirm the importance of higher-order Hermite terms in retaining the physical effects of electromagnetic dynamics. A Hermite closure model as we have described could be useful in existing full Hermite codes, which presently use just a simple truncation and retain more orders to compensate. This is also relevant for gyro-Landau-fluid-based models (such as the GLF23 model [STAEBLER *et al.*, 2005]), which carefully handle the closure problem for the fluid velocity-moment expansion but use simple truncation for the Hermite spatial expansion. One approach for improvement of such GLF models is to take fluid moments of the Hermite expansion of the gyrokinetic equation model that we have derived in this section and then apply closure approximations for the fluid moments in addition to the closure approximations for the Hermite expansion which we have already done. An alternative approach could be to instead begin with the gyro-Landau fluid equations in their present form with their existing closure approximations as already derived in k_{\parallel} space, transform them to a Hermite basis, and then re-derive the additional closures needed for the Hermite basis. These approaches may be explored as topics of future research.

5.6 Summary

A local linear gyrokinetic code has been developed to allow for fast scoping studies of gyrokinetic linear stability. This code includes models of the effects of plasma shaping, magnetic shear, and toroidal geometry by using representative values of k_{\parallel} , k_{\perp}^2 , ω_d , etc. averaged over a trial eigenfunction, using the same geometrical information available in the full GS2 gyrokinetic code (i.e. either a full numerical equilibrium or a local parameterized equilibrium). Simple models for trapped particles and for the parallel free streaming of particles out of the bad-curvature region are included.

The trial function code was successfully benchmarked with GS2 in the collisionless, electrostatic limit, with single and multiple gyrokinetic ion and electron species for a range of shaped flux surface equilibria. Overall, the trial function code was able to follow the same shaping trends as GS2 both in the adiabatic electron limit and with the inclusion of gyrokinetic electron dynamics, showing good agreement for both the ITG mode and the TEM. The code was also able to accurately find the critical temperature gradient, even in the presence of shaping. However, overprediction of the TEM growth rate in general has led to inaccuracies in the trial function code in some cases in predicting the transition from a dominant TEM mode to a dominant ITG mode, suggesting that a better model for trapped particles is needed. Furthermore, extensions to include magnetic fluctuations were found to be difficult. Specifically, with the addition of electromagnetic effects, while the trial function code was able to predict the stabilizing effects of β on the ITG instability, it was found that the inclusion of higher-order Hermite basis functions is necessary to accurately recover the kinetic MHD ballooning limit.

Overall, because of the reduced computational intensity of the trial function

model and its success in capturing the significant physics of gyrokinetic linear stability even in general geometry, such a code might be more practical than a full geometry code for optimization studies or for use in an iterative transport code, upon inclusion of collisional effect and a quasi-linear approximation or nonlinear effects with subgrid models.

Chapter 6

Conclusions

In this thesis work, advanced numerical algorithms for Eulerian/continuum gyrokinetic solvers were explored for more effective studies of plasma microturbulence. These algorithms focus specifically on the regime of ITG/TEM/KBM physics and are particularly designed for faster simulations with the inclusion of non-adiabatic electron dynamics and electromagnetic perturbations, which are necessary for accurate simulations of anomalous transport in core tokamak plasmas. In addition, advances were made in understanding the mechanisms leading to improved confinement in tokamaks via applications of gyrokinetic simulations to studies of the effects of flux surface shape on the gyrokinetic stability and transport of tokamak plasmas using the GS2 code and a new local linear trial function-based gyrokinetic code. The main results of this research and possible new continuing areas of research are summarized below.

6.1 Summary

6.1.1 Studies of Numerical Algorithms for Gyrokinetics

Several numerical algorithms for Eulerian gyrokinetic solvers were studied. These include semi implicit-explicit schemes, iterative implicit schemes, and an Alternating Direction Implicit (ADI) scheme. A semi implicit-explicit scheme, which treats the distribution function terms in the gyrokinetic equation implicitly while the field terms are treated explicitly, was explored in the context of GS2's 2nd order compact spatial differencing. Both single-step and two-step predictor corrector schemes were found to be numerically unstable at the highest k_{\parallel} modes (at the Nyquist limit) with the inclusion of gyrokinetic electrons. This result motivates the need for a more implicit treatment of the field dynamics, such as iterative implicit schemes.

An iterative implicit scheme for gyrokinetic simulations was developed based on “matrix free” iteration methods using numerical approximations to the plasma response as a preconditioner. This method was designed to reduce the long time needed to set-up implicit arrays, yet still have larger time step advantages similar to a fully implicit method. A numerical preconditioner was developed based on computing the response of simultaneously applied perturbations and refining the tail end using an extrapolation with the translation of a single exact response row. Implementation in GS2 and tests in the linear limit found that this preconditioner with a simple iteration algorithm works fairly well in the electrostatic limit, yet yields a strict time step restriction for convergence with electromagnetic dynamics of $(\Delta t)_{max} \sim (1/2r) * (n_{stride} \Delta z) * (k_y \rho_i / v_{te})$, where $n_{stride} \Delta z$ is the bandwidth of the response used for the preconditioner. It was found that more robust Krylov solvers, such as Bi-CGSTAB and non-restarted GMRES, are necessary for large time steps

with electromagnetic dynamics. This difficulty may be related to GS2's usage of Beam-Warming 2nd order compact finite differencing for the spatial derivatives, which introduces a high frequency Nyquist mode in the system at $k_{\parallel}qR\Delta\theta = \pi$ and $\omega\Delta t = \pi$. Thus, a more standard version of the compact finite differencing algorithm, which is usually implemented with 4th or 6th order accuracy, or even other non-compact finite differencing algorithms may be more effective and are a topic of future research. Overall, the original fully implicit algorithm of Kotschenreuther in GS2 may be best for moderate size nonlinear simulations which do not change the time step often (i.e. which require a minimal number of re-computations of the implicit response arrays). Otherwise, for example for inclusion of large-scale ExB effects via time-dependent shearing of the computational grid, simple iteration with a small time step or GMRES (or Bi-CGSTAB for large simulations with large storage requirements) may be advantageous.

The implementation of an ADI algorithm for a gyrokinetic problem was also explored. The resulting numerical stability properties for a test problem of a shear kinetic Alfvén wave at small $k_{\perp}\rho_i$ were studied. For this test case, we have focused on the time-advancement scheme and just Fourier transformed in the parallel spatial direction. A severe stability restriction on the time step of $(\Delta t)_{max} \sim 2|k_{\perp}\rho_s/(k_{\parallel}v_{te})|$ was found, even in the high $(\beta_e/2)/(m_i/m_e)$ regime, where the Alfvén wave is slower than the electron thermal speed and both the actual mode frequency of the Alfvén wave and the parallel electron motion time scale would appear to be very well resolved. This problem was also found in a partially implicit Adams-Bashforth scheme, which yielded a time step restriction which was twice as low as that found for the ADI algorithm. In fact, it was found that even

a fully explicit algorithm can be better at long wavelengths than these split operator algorithms. A further analysis of the ADI algorithm using a Landau-fluid approximation to the kinetic equation found that it is the splitting of the operators which yields the source of the numerical instability; for example, in the electrostatic limit, one of the split operators is nilpotent and not diagonalizable. Overall, these results suggest that an iterative implicit algorithm might be the best approach for extensions of core gyrokinetic simulations to edge kinetic formulations, where the fast dynamics of the Alfvén wave in the low β edge/scrape-off region cause most standard explicit algorithms to be numerically unstable.

6.1.2 Studies of the Effects of Shaping on Plasma Turbulence

As an application of gyrokinetic simulations, the effects of flux surface shape and other plasma parameters on the gyrokinetic stability and transport of tokamak plasmas were also studied. Studies of the scaling of nonlinear turbulence with shaping parameters were performed using the GS2 code, starting with an equilibrium based on a representative JET-like flux surface and artificially varying elongation, triangularity, and their radial gradients together using the Miller analytic equilibrium formalism to approach the circular limit via linear interpolation. Both linearly and nonlinearly, high elongation was found to be stabilizing on the ITG turbulence. Triangularity could be stabilizing when coupled with high κ or combined high α and \hat{s} , but was otherwise destabilizing at moderate κ or α . A scaling of the heat flux with elongation of $\chi \sim \kappa^{-1.5}$ or κ^{-2} (depending on the triangularity) was observed. While this scaling is consistent with previous gyrofluid simulations

[WALTZ and MILLER, 1999], it is not quite as strong as empirical experimentally-based elongation scalings. However, our results also show that high shaping results in a larger Dimits upshift of the nonlinear critical temperature gradient due to enhanced zonal flows. While this may help to explain much of the remaining of the empirical elongation scaling, the strong triangularity dependence observed in tokamaks most likely enters through edge boundary conditions for core turbulence and will be a topic of future research, particularly for recent initiatives to couple core tokamak simulations with edge kinetic formulations.

The effects of electromagnetic dynamics coupled with shaping were also presented. For electromagnetic runs, β was varied with shaping to keep the Troyon-normalized β fixed while also holding q_{95} fixed. Finite β was found to be a stabilizing influence on the linear ITG mode, and a scan over β found that shaping opens up access to a type of 2nd stability regime. However, nonlinear results show that finite β leads to large thermal electron transport, particularly for more circular plasmas, even well below the threshold for the linear kinetic ballooning instability.

Finally, a trial function-based local linear model for gyrokinetics was developed to aid in fast scoping studies of gyrokinetic linear stability, including shaping effects in particular. This model enhances the efficiency of flux tube-based simulations by using representative values of the equilibrium parameters averaged over a Gaussian trial eigenfunction, using the same geometrical information available in the full GS2 code. Simple models for trapped particles and for the parallel free-streaming of particles out of the bad-curvature region are also included. Benchmarks of the trial function code with GS2 in the ITG/TEM regime in the collisionless, electrostatic limit over a range of shaped flux surface equilibria were successful, even near the

critical temperature gradient. However, the trial function model generally overpredicted the TEM growth rate, leading to inaccuracies in the TEM to ITG transition and indicating that a better model for trapped particles is needed, such as based on a bounce-averaged (rather than a trial function-averaged) ω_{dv} . Furthermore, benchmarks with GS2 with the inclusion of electromagnetic dynamics found that, while the lowest-order model captures the stabilizing effects of β on the ITG mode, extensions of the trial function model to include coupling to higher-order Hermite basis functions are necessary to accurately recover the kinetic MHD ballooning limit.

6.2 Future Directions

The faster algorithms explored in this thesis allow for several new explorations in the study of plasma microturbulence. Such algorithms will be useful for multiscale initiatives, such as the development of a turbulent transport model based on an iterative coupling of a nonlinear gyrokinetic code and a macroscopic transport code, the coupling of core kinetic simulations to edge kinetic formulations, and the coupling of ETG physics with the ITG/TEM regime. In general, such future advanced applications of gyrokinetics rely on fast computations of the heat and particle fluxes from a gyrokinetic simulation. This can be achieved via advanced iterative implicit algorithms such as those explored in Chapter 2, from a trial function-based linear gyrokinetic code such as that explored in Chapter 5 with the additional inclusion of a quasi-linear model, or with the development of new reduced-order models such as subgrid models of turbulence. Subgrid models have been preliminarily tested in

GS2 as part of this on-going research. These results and ideas for improved models are described below. In addition, a near-term example of using fast iterative implicit algorithms to incorporate large-scale ExB shear effects in flux tube-based gyrokinetic codes is also discussed below. This application complements the studies of flux surface shape on gyrokinetic stability in Chapter 4 and could lead to a modified scaling which may be more applicable to cases with high sheared flows, such as at large $\rho_* = \rho/L_*$ (where ρ is the gyroradius and L_* is the scale length over which plasma gradients are changing) or near transport barriers.

6.2.1 Subgrid Models of Turbulence

Subgrid models of turbulence may be used to enhance the efficiency of nonlinear gyrokinetic simulations by reducing spatial resolution requirements. Subgrid models are widely used in large-eddy simulations (LES) of fluid turbulence. For a simulation in which only large spatial scales are resolved, a subgrid model provides a means of removing energy at the grid scale in a way that mimics the interactions that discarded modes would have had on fully resolved modes.

There is a large volume of literature of varying degrees of sophistication on subgrid models. But relatively simple subgrid models, even with a somewhat heuristic basis (such as hyperviscosity models with a Smagorinsky-like shearing rate scaling) have been found to be fairly effective. Reducing the resolution needed in a code by only a factor of 2 can lead to a factor of 16 improvement in performance (i.e. 2^3 for the spatial dimensions and another factor of 2 for the increase in the Courant-limited time step). One reason that simple subgrid models work fairly well is that, in the Kolmogorov picture of fluid turbulence at high Reynolds number, the behavior of the inertial range of scales is not very sensitive to the details of what

happens at small dissipative scales. A more challenging problem for LES simulations is handling boundary layers near fluid-solid interfaces, but this is not an issue for the homogeneous plasma turbulence simulations that we are considering here.

Typical subgrid models consist of an enhanced velocity-dependent turbulent hyperviscosity and can easily be applied to nonlinear gyrokinetic codes as described below. Here we follow the basic approach described in [SMITH, 1997]. Consider the following generic form of the gyrokinetic equation:

$$\frac{\partial f}{\partial t} = Lf + N(f) \quad (6.1)$$

where f is the perturbed particle distribution function and L and N are the linear and nonlinear operators respectively. The distribution function can be decomposed into a resolved part f_r and a subgrid part f_s . The filtered field evolution equation is then:

$$\frac{\partial f_r}{\partial t} = Lf_r + (N(f_r))_r + N_s \quad (6.2)$$

where the subgrid term is given by

$$N_s = (N(f))_r - (N(f_r))_r \quad (6.3)$$

A simple dissipative subgrid model for this term has the form:

$$N_{s,\vec{k}} \sim \nu_k |\vec{k}|^p f_{\vec{k}} \quad (6.4)$$

where ν is the turbulent viscosity/hyperviscosity and p is an integer.

Previous recent work related to plasmas has involved the incorporation of the Smagorinsky eddy viscosity ($p = 2$ in Eq. (6.4)) and, separately, a hyperviscosity

model ($p > 2$) in a 2D drift-wave turbulence code [SMITH, 1997]. The code used in this work is based on the model of Hasegawa and Mima, which contains the ExB drift advection nonlinearity, with the addition of the “ $i\delta$ ” equations to model linear instability and a 1-moment model of Landau damping which provides the primary means of dissipation. Both p and a scaling factor C in the hyperviscosity model were computed as parameterizations of the cutoff wavenumber using results from a direct numerical simulation of the eddy viscosity over a range of parameters and resolutions. Accurate results were obtained with the parameterized hyperviscosity model if the cutoff wavenumber was at least 4 times larger than the characteristic wavenumber of the advecting velocity. The Smagorinsky eddy viscosity model, on the other hand, required at least a factor of 8 difference for the same accuracy.

We have already incorporated a 2D Smagorinsky-like hyperviscosity ($p = 4$) subgrid model into GS2. In this model, the damping is applied only to the non-adiabatic part of the distribution function as $e^{-D_{hv}S\Delta t(\tilde{k}_\perp^4/\tilde{k}_{\perp,max}^4)}$, where D_{hv} is an arbitrary constant coefficient, $\tilde{k}_\perp^2 \equiv k_x^2 + k_y^2$, and S is the x-y averaged shearing rate, defined in terms of the ExB drift velocity $\vec{v} = (c/B)\hat{b} \times \nabla\Phi$ as:

$$\begin{aligned} S^2(\theta) &= \left\langle \left(\frac{\partial v_x}{\partial x} \right)^2 + \left(\frac{\partial v_y}{\partial y} \right)^2 + \frac{1}{2} \left(\frac{\partial v_x}{\partial y} + \frac{\partial v_y}{\partial x} \right)^2 \right\rangle \\ &= \sum_{k_x} \sum_{k_y} \tilde{k}_\perp^4 \frac{c}{B} |\Phi|^2 \end{aligned} \quad (6.5)$$

Preliminary results of χ_i as a function of R/L_{Ti} using the Cyclone DIII-D base case parameters [DIMITS *et al.*, 2000] are shown in figure 6.1. The equilibrium parameters for this test case use \hat{s} - α unshifted circular geometry with: $r/R = 0.18$, $q = 1.4$, $\hat{s} = 0.786$, $\partial_{r/R}\beta = -0.0$. A single ion species is used with $R/L_{ni} = 2.222$ and $T_{0i} = T_{0e}$ and the electron species is assumed adiabatic. The GS2 simulation

domain for these studies has fixed $L_x = 76.33\rho_i$ and $L_y = 62.83\rho_i$ with varying number of grid points in the perpendicular directions, i.e. varying resolution Δx and Δy . In spectral space, nonzero modes are resolved in the range $0.082 \leq |k_x\rho_i| \leq 0.082(nk_x - 1)/2$ and $0.10 \leq k_y\rho_i \leq 0.10(nk_y - 1)$. The domain along the field line has length $L_z = 2\pi qR = 8.79R$, with $N_\theta = 32$ grid points per 2π in θ . The velocity grid has $N_E = 16$ total energy grid points and $N_\lambda = 37$ pitch angle grid points ($\lambda = \mu/E$). Runs were performed as typical with time-centering parameter $r = 0.55$ and slight upwind diffusion (spatial-centering parameter $s = 0.55$). A value of $D_{hv} = 0.075$ was chosen for the constant coefficient in the subgrid model based on an optimization scan for the $R/L_{Ti} = 6.92$ case at low resolution ($7 k_x$ modes $\times 3 k_y$ modes).

Overall, the results in figure 6.1 show that, for low resolution runs, addition of a subgrid model significantly improves the accuracy, particularly at high R/L_{Ti} . In fact, with the subgrid model, a resolution of $11k_x$ modes $\times 3k_y$ modes ($=33$ total \tilde{k}_\perp modes) gives approximately equivalent accuracy to cases with twice as many modes ($15 \times 4 = 60$ total \tilde{k}_\perp modes). Thus, these results indicate that such a subgrid model may be a valuable tool in the future in performing more time efficient gyrokinetic simulations.

Future work will focus on improvements of this subgrid model. For example, these results in figure 6.1 show that the subgrid model overall consistently overpredicts χ_i , indicating that the damping rate may not be large enough. Fine-tuning some of the coefficients of the subgrid model might lead to further improvements. Another way to improve the model might be to use a more realistic form for the k -dependence of the eddy damping rate (instead of just a simple polynomial $|\vec{k}|^p$) [SMITH and HAMMETT, 1997], perhaps based on work by Kraichnan

[KRAICHNAN, 1976]. Disparate scale expansions of statistical turbulence theories [KROMMES and KIM, 2000] may also provide guidance for an improved subgrid model. Furthermore, a 3D subgrid model, i.e. essentially a 2D model with the addition of a parallel damping term which is proportional to the parallel shear $\nabla_{\parallel} v_{ExB}$ enhanced by a factor of $|\vec{k}_{\perp}|/k_{\parallel}$, may lead to more accurate results. A 3D model would account for the shearing of eddies to unresolved large parallel wavenumbers due to small deflections in the ExB velocity at different points along a field line. Previous results by [SMITH, 1997] show that inclusion of a 3D hyperviscosity model in a toroidal gyrofluid code can reduce the parallel resolution requirements by a factor of 2.

Overall, upon development of an improved 2D or 3D hyperviscosity subgrid model, implementation in a nonlinear version of the trial function-based code (in place of a quasi-linear approximation) would provide an accurate, yet still relatively computationally inexpensive, calculation of the heat transport coefficient and thus may be particularly useful for the development of an iteratively coupled gyrokinetic-based transport code.

6.2.2 Equilibrium-Scale ExB Shear Effects

Equilibrium-scale ExB shear flows are believed to be important in describing the formation of internal transport barriers. Nonlinear gyro-Landau-fluid simulations have shown that the ITG turbulence is suppressed when the shearing rate γ_{ExB} exceeds the maximum ITG linear growth rate in the absence of flow shear [WALTZ *et al.*, 1995]. More recent nonlinear gyrokinetic simulations with GYRO have also confirmed this “quenching rule” [KINSEY *et al.*, 2005]. Furthermore, gyrokinetic simulations have more generally shown the importance of ExB shear effects in

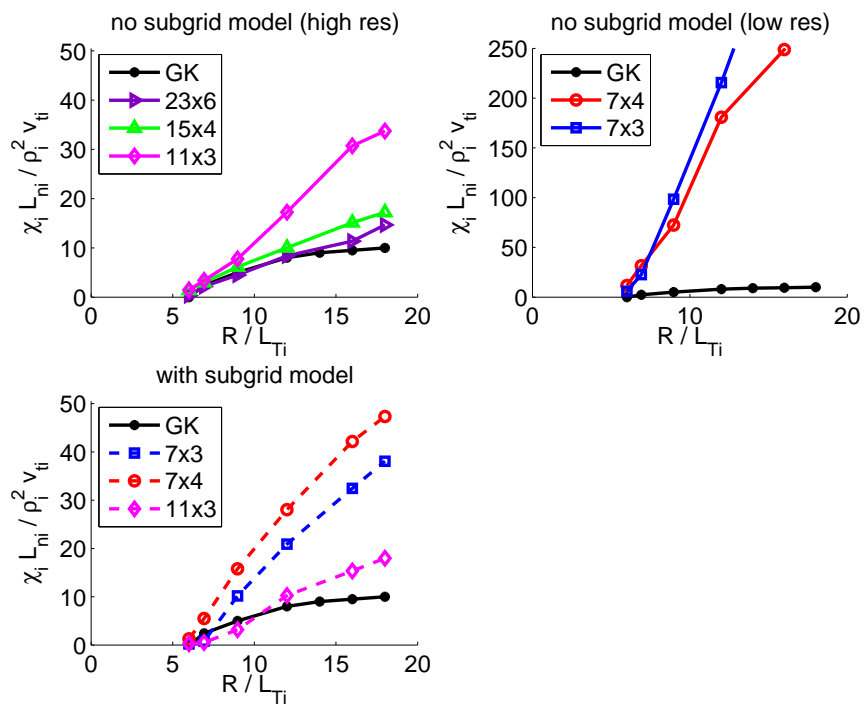


Figure 6.1: Ion heat flux vs. temperature gradient length scale for Cyclone DII-D base case parameters, comparing various grid resolutions (num k_x modes) \times (num k_y modes). “GK” refers to the high resolution results from the PG3EQ code of Dimits et al. The lower plot uses a hyperviscosity-based subgrid model.

modeling the Bohm-like scaling of low confinement L-mode discharges [CANDY and WALTZ, 2003b]. Thus, accurate core tokamak plasma simulations must include these shear flows.

While equilibrium-scale ExB shear effects are straightforward to implement in a global gyrokinetic code, implementation in a standard flux tube code, such as GS2, requires some re-consideration of the ballooning representation of the gyrokinetic equation due to its assumption of radially periodic boundary conditions. Equilibrium-scale ExB flows enter as a new LHS term in the gyrokinetic equation: $\vec{v}_{ExB}^{(0)} \cdot \nabla h$, where $\vec{v}_{ExB}^{(0)} = (c/B)\vec{E}_r^{(0)} \times \hat{b}$ has a radial gradient and is not periodic. A first approach in implementing radial ExB shear flows is to make GS2's Fourier-transformed radial coordinate k_x time dependent such that it shears at the ExB shearing rate, i.e. $k'_x = k_x + \dot{k}_x t$. This leaves the radial derivatives invariant, yet introduces an additional term from the time derivative of $\dot{k}_x(\partial f / \partial k'_x)$. (Other approaches for the coordinate transformation can also be used, such as that presented in [WALTZ *et al.*, 1994] or [BEER *et al.*, 1999], which shear the new coordinates in the poloidal direction so as to keep the flux tube aligned with the magnetic field.) The gyrokinetic equation in these time-dependent coordinates can then be solved by applying an iterative scheme, such as those explored in this thesis work, using GS2's present computation of the exact implicit response matrices for $k_x = \text{constant}$ as the preconditioner. Later, as a second approach, implementation of radially non-periodic boundary conditions could be explored so that the effects of diamagnetic velocity shear can be studied as well.

Appendix A

The GS2 Algorithm

Here we outline the implementation in GS2 of the implicit algorithm described in [KOTSCHENREUTHER *et al.*, 1995a] and in this thesis in section 2.1.1 in Chapter 2. The primary difference in the GS2 implementation is that it uses a predictor-corrector type format, rather than computing the inhomogeneous and homogeneous distribution function solutions directly. The precomputed response matrices are also reformulated. Denoting the standard response matrices as defined in Eqs. (2.18)-(2.21) as M_K , the GS2 response matrices are defined as:

$$M_{GS2,ij}^1 \equiv M_{K,ij}^1 - \sum_s \frac{n_{0s} e^2 Z_s^2}{T_{0s}} (1 - \Gamma_{0s,i}) \delta_{ij} \quad (\text{A.1})$$

$$M_{GS2,ij}^2 \equiv M_{K,ij}^2 \quad (\text{A.2})$$

$$M_{GS2,ij}^3 \equiv M_{K,ij}^3 \quad (\text{A.3})$$

$$M_{GS2,ij}^4 \equiv M_{K,ij}^4 - \frac{c}{4\pi} k_{\perp}^2 \delta_{ij} \quad (\text{A.4})$$

Subsequent solutions of the gyrokinetic equation then are found with the following steps:

1. Compute f_*^{n+1} from the gyrokinetic equation using f^n , Φ^n , A_{\parallel}^n , $\Phi^{n+1} = \Phi^n$, and $A_{\parallel}^{n+1} = A_{\parallel}^n$.
2. Solve a modified form of the Poisson-Ampere equations for the difference between the new and old fields using f_*^{n+1} :

$$\sum_s \frac{n_{0s} e^2 Z_s^2}{T_{0s}} (1 - \Gamma_{0s,i}) \Phi_i^n = \rho_{dens,i}(f_*^{n+1}) + M_{GS2,ij}^1 \Phi_{*,j}^{n+1} + M_{GS2,ij}^2 A_{\parallel,*j}^{n+1} \quad (\text{A.5})$$

$$\frac{c}{4\pi} k_{\perp,i}^2 A_{\parallel,i}^n = \rho_{curr,i}(f_*^{n+1}) + M_{GS2,ij}^3 \Phi_{*,j}^{n+1} + M_{GS2,ij}^4 A_{\parallel,*j}^{n+1} \quad (\text{A.6})$$

3. Sum to get the new fields:

$$\Phi^{n+1} = \Phi^n + \Phi_*^{n+1} \quad (\text{A.7})$$

$$A_{\parallel}^{n+1} = A_{\parallel}^n + A_{\parallel,*}^{n+1} \quad (\text{A.8})$$

4. Compute f_*^{n+1} from the gyrokinetic equation using f^n , Φ^n , A_{\parallel}^n , Φ^{n+1} , and A_{\parallel}^{n+1} .

This is a predictor-corrector like algorithm since the intermediate parameter f_*^{n+1} is a result of solution of the gyrokinetic equation in an explicit form, i.e. using the value of the fields at the old time step as a guess for the value of the fields at the new time step. Solution of the Poisson-Ampere equations produces, in essence, the residual error of this guess. The second gyrokinetic solve is then like a corrector step using the updated values (which are the true values in this case) of the future-time fields.

However, though this algorithm presents itself in the same format as a predictor-corrector scheme, it is not an approximation. To see this, we show the derivation of

the intermediate field equations from the inhomogeneous/homogeneous equations. We start with the standard Poisson-Ampere equations in terms of M_K , from Eqs. (2.14)-(2.17):

$$\sum_s \frac{n_{0s} e^2 Z_s^2}{T_{0s}} (1 - \Gamma_{0s,i}) \Phi_i^{n+1} = \rho_{dens,i}(f_{inhomo}^{n+1}) + M_{K,ij}^1 \Phi_j^{n+1} + M_{K,ij}^2 A_{\parallel,j}^{n+1} \quad (\text{A.9})$$

$$\frac{c}{4\pi} k_{\perp,i}^2 A_{\parallel,i}^{n+1} = \rho_{curr,i}(f_{inhomo}^{n+1}) + M_{K,ij}^3 \Phi_j^{n+1} + M_{K,ij}^4 A_{\parallel,j}^{n+1} \quad (\text{A.10})$$

Substituting M_{GS2} into these equations gives

$$0 = \rho_{dens,i}(f_{inhomo}^{n+1}) + M_{GS2,ij}^1 \Phi_j^{n+1} + M_{GS2,ij}^2 A_{\parallel,j}^{n+1} \quad (\text{A.11})$$

$$0 = \rho_{curr,i}(f_{inhomo}^{n+1}) + M_{GS2,ij}^3 \Phi_j^{n+1} + M_{GS2,ij}^4 A_{\parallel,j}^{n+1} \quad (\text{A.12})$$

Introducing the intermediate field parameters Φ_*^{n+1} and $A_{\parallel,*}^{n+1}$ and using the relationship between M_{GS2} and M_K , we can write that

$$\begin{aligned} \sum_s \frac{n_{0s} e^2 Z_s^2}{T_{0s}} (1 - \Gamma_{0s,i}) \Phi_i^n &= M_{GS2,ij}^1 \Phi_{*,j}^{n+1} + M_{GS2,ij}^2 A_{\parallel,*}^{n+1} \\ &+ \left[M_{K,ij}^1 \Phi_j^n + M_{K,ij}^2 A_{\parallel,j}^n + \rho_{dens,i}(f_{inhomo}^{n+1}) \right] \end{aligned} \quad (\text{A.13})$$

$$\begin{aligned} \frac{c}{4\pi} k_{\perp,i}^2 A_{\parallel,i}^n &= M_{GS2,ij}^3 \Phi_{*,j}^{n+1} + M_{GS2,ij}^4 A_{\parallel,*}^{n+1} \\ &+ \left[M_{K,ij}^3 \Phi_j^n + M_{K,ij}^4 A_{\parallel,j}^n + \rho_{curr,i}(f_{inhomo}^{n+1}) \right] \end{aligned} \quad (\text{A.14})$$

We would like to rewrite these equations in terms of f_*^{n+1} rather than f_{inhomo}^{n+1} by finding an equivalence relation using the gyrokinetic equation. To do this, we first

expand out the terms in brackets as:

$$M_{K,ij}^1 \Phi_j^n + M_{K,ij}^2 A_{\parallel,j}^n + \rho_{dens,i}(f_{inhomo}^{n+1}) = \sum_s eZ_s \int d^3v J_{0s,i} L_i \quad (\text{A.15})$$

$$M_{K,ij}^3 \Phi_j^n + M_{K,ij}^4 A_{\parallel,j}^n + \rho_{curr,i}(f_{inhomo}^{n+1}) = \sum_s eZ_s \int d^3v v_{\parallel} J_{0s,i} L_i \quad (\text{A.16})$$

where

$$L_i \equiv \frac{\delta f_i^{n+1}}{\delta \Phi_j^{n+1}} \Phi_j^n + \frac{\delta f_i^{n+1}}{\delta A_{\parallel,j}^{n+1}} A_{\parallel,j}^n + f_{inhomo,i}^{n+1} \quad (\text{A.17})$$

Consider the generic finite difference form of the gyrokinetic equation as given in Eq. (2.13). Ignoring the θ grid index for simplicity, the gyrokinetic equation becomes

$$Cf^n + Df^{n+1} = F\Phi^n + G\Phi^{n+1} + HA_{\parallel}^n + KA_{\parallel}^{n+1} \quad (\text{A.18})$$

The inhomogeneous gyrokinetic equation and the plasma response functions as derived from this equation are given in Eqs. (2.22), (2.24), and (2.25). Using these relation, we expand L in operator format as

$$L = D^{-1} [(F + G)\Phi^n + (H + K)A_{\parallel}^n - Cf^n] \quad (\text{A.19})$$

Note then that $L \equiv f_*^{n+1}$, i.e. Eq. (A.19) is just the solution of the gyrokinetic equation with $\Phi^{n+1} = \Phi^n$ and $A_{\parallel}^{n+1} = A_{\parallel}^n$. Thus, substituting f_*^{n+1} into Eqs. (A.13) and (A.14), the Poisson and Ampere equations become Eqs. (A.5) and (A.6). Once Φ_*^{n+1} and $A_{\parallel,*}^{n+1}$ are computed (and thus ultimately Φ^{n+1} and A_{\parallel}^{n+1}) from these equations, f^{n+1} can be computed directly from the gyrokinetic equation as in Step 4. Thus, we have shown that solution of the gyrokinetic-Poisson-Ampere equations in GS2 with this predictor-corrector like form of Kotschenreuther's algorithm is

equivalent to his original published algorithm in [KOTSCHENREUTHER *et al.*, 1995a].

Appendix B

Templates of Iterative Algorithms

Templates for the iterative algorithms discussed in Chapter 2 are presented here. We consider solution of a general linear system of equations $A\vec{x} = \vec{b}$, where A is a square nonsingular complex matrix, with left-preconditioning, i.e. $MA\vec{x} = M\vec{b}$, where M is the preconditioner which is assumed to be precomputed. The algorithms are presented in “matrix-free” form and thus it is not necessary that the elements of A be computed since the only necessary operations involving A are matrix-vector multiplications $A\vec{v}$, which can be defined implicitly. The templates given below for the steepest descent/conjugate gradient and bi-conjugate gradient stabilized (Bi-CGSTAB) algorithms are adapted from [BARRETT *et al.*, 1994]. The template for the restarted generalized minimal residual (GMRES(m)) algorithm is adapted from [SAAD and SCHULTZ, 1986] and [SAAD, 2003] using implementation of the Arnoldi algorithm through the modified Gram-Schmidt orthogonalization process and using the stopping conditions as defined in [FRAYSSE *et al.*, 2003].

B.1 Simple Iteration

Given an initial guess x^0 , compute the residual $r^0 = b - Ax^0$.

FOR $i = 0, 1, 2, \dots$

$$z^i = M^{-1}r^i$$

$$x^{i+1} = x^i + z^i$$

$$r^{i+1} = b - Ax^{i+1}$$

Check convergence; continue if necessary.

END

B.2 Steepest Descent and Conjugate Gradient

Given an initial guess x^0 , compute the residual $r^0 = b - Ax^0$.

FOR $i = 0, 1, 2, \dots$

$$z^i = M^{-1}r^i$$

IF $i = 0$ or steepest descent algorithm,

$$p^{i+1} = z^i$$

ELSE

$$\beta_i = \frac{\langle r^i | z^i \rangle}{\langle r^{i-1} | z^{i-1} \rangle}$$

$$p^{i+1} = z^i + \beta_i p^i$$

ENDIF

$$q^{i+1} = Ap^{i+1}$$

$$\alpha_{i+1} = \frac{\langle r^i | z^i \rangle}{\langle p^{i+1} | q^{i+1} \rangle}$$

$$x^{i+1} = x^i + \alpha_{i+1} p^{i+1}$$

$$r^{i+1} = r^i - \alpha_{i+1} q^{i+1}$$

Check convergence; continue if necessary.

END

B.3 Bi-CGSTAB

Given an initial guess x^0 , compute the residual $r^0 = b - Ax^0$.

Choose \tilde{r} (e.g. $\tilde{r} = r^0$).

FOR $i = 0, 1, 2, \dots$

(IF $\langle \tilde{r} | r^i \rangle = 0$, METHOD FAILS)

IF $i = 0$,

$$p^{i+1} = r^i$$

ELSE

$$\beta_i = \frac{\langle \tilde{r} | r^i \rangle}{\langle \tilde{r} | r^{i-1} \rangle} \omega_i$$

$$p^{i+1} = r^i + \beta_i (p^i - \omega_i v^i)$$

ENDIF

$$\hat{p} = M^{-1} p^{i+1}$$

$$v^{i+1} = A \hat{p}$$

$$\alpha_{i+1} = \frac{\langle \tilde{r} | r^i \rangle}{\langle \tilde{r} | v^{i+1} \rangle}$$

$$s = r^i - \alpha_{i+1} v^{i+1}$$

Check convergence wrt s :

IF s is small enough,

$$\text{Set } x^{i+1} = x^i + \alpha_{i+1} \hat{p}$$

STOP

ENDIF

$$\hat{s} = M^{-1} s$$

$$t = A \hat{s}$$

$$\omega_{i+1} = \frac{\langle t | s \rangle}{\langle t | t \rangle}$$

$$x^{i+1} = x^i + \alpha_{i+1} \hat{p} + \omega_{i+1} \hat{s}$$

$$r^{i+1} = s - \omega_{i+1} t$$

Check convergence; continue if necessary.

(for continuation, it is necessary that $\omega_{i+1} \neq 0$)

END

B.4 GMRES(m)

Given an initial guess x^0 , compute the residual $r^0 = M^{-1}(b - Ax^0)$.

Initialize $v_1 = \frac{r^0}{\|r^0\|_2}$

FOR $p = 0, 1, 2, \dots$

Construct a basis using the Arnoldi process:

FOR $j = 1, \dots, m$

$$w_j = M^{-1} A v_j$$

FOR $i = 1, \dots, j$

$$h_{ij} = \langle w_j | v_i \rangle$$

$$w_j = w_j - h_{ij} v_i$$

END

$$h_{j+1,j} = \|w_j\|_2$$

$$v_{j+1} = w_j / h_{j+1,j}$$

Define the $N \times j$ matrix $V_j = [v_1 \dots v_j]$

Define the $(j+1) \times j$ matrix $\bar{H}_j = h_{ik} 1 \leq i \leq j+1, 1 \leq k \leq j$

Compute y_j by solving the least squares problem:

$$\min_{\bar{y}_j \in C^m} \left\| \left(\|r^0\|_2 e_1 - \bar{H}_j y_j \right) \right\|_2, \text{ where } e_1 = (1, 0, 0, \dots, 0)^T \in C^j.$$

Check convergence of the Arnoldi-computed residual:

$$\rho^j = \left\| \left(\|r^0\|_2 e_1 - \bar{H}_j y_j \right) \right\|_2$$

IF ρ^j is small enough,

 Check convergence of the true residual:

$$x^j = x^0 + V_j y_j$$

$$r^j = M^{-1}(b - Ax^j)$$

 IF r^j is small enough, STOP

 ELSE continue

ENDIF

END

IF $j > m$,

 Restart:

$$\text{Set } x^0 = x^j = x^0 + V_m y_m$$

$$\text{Set } r^0 = r^j = M^{-1}(b - Ax^m)$$

$$\text{Re-initialize } v_1 = \frac{r^0}{\|r^0\|_2}$$

 Return to basis construction loop.

ENDIF

END

Appendix C

Unsaturated Transport in Finite β GS2 Simulations

Studies of the effects of shaping on nonlinear ITG turbulence with electromagnetic dynamics presented in section 4.4.2 in Chapter 4 found that β strongly negatively affects the electron transport. It was noted that unsaturated transport was observed for some cases, particularly as β increases and shaping decreases. Here we address these cases.

The results presented in section 4.4.2 were performed for $\beta < \beta(\kappa)$, where $\beta(\kappa)$ is given by Eq. (4.7), i.e. varying with shaping to keep the Troyon-normalized β fixed while also holding q_{95} fixed. In a scan over β for the shaped plasmas, unsaturated transport was observed for:

- $\kappa = 1.00$, as low as $\beta = \frac{1}{3}\beta(\kappa)$
- $\kappa = 1.20$, as low as $\beta = \frac{1}{2}\beta(\kappa)$
- $\kappa = 1.46$ and $\kappa = 1.80$, as low as $\beta = \beta(\kappa)$

As shown in the time evolution plots of the heat flux in figure C.1 for the $\kappa = 1.00$ circular case at $\beta = \frac{1}{3}\beta(\kappa)$, these cases look like typical well-resolved simulations, with the heat flux reaching an apparent steady state phase for a while. However, eventually the heat flux blows up, rising first and most rapidly in the magnetic flutter contribution to the electron transport.

Future work will focus on more comprehensive studies of these cases to address whether the observed unsaturated transport is a numerical problem. With the electrostatic results, numerical convergence studies were done with varying spatial resolution. However, with the electromagnetic cases, it is computationally difficult to do very high resolution runs. While diagnostics tools, such as analysis of the spectral components of the heat fluxes, were used to set the simulation domain within the constraints of computational intensity (which essentially limits the number of k_x and k_y modes that can be resolved) and to verify that the heat flux is well-resolved in spectral space, more exploration of the possibility of numerical issues could be done.

For example, similar results of unsaturated transport have been seen in electromagnetic GS2 simulations of high β spherical torus plasmas [APPLEGATE *et al.*, 2006], but they recently found that adding a modest amount of damping of very high k_\perp modes due to classical collisional electron diffusion (with a damping rate $\propto \nu_{ei}\rho_e^2 k_\perp^2$) was sufficient to prevent these cases from blowing up and the steady state phase was then maintained. This seems in line with the fact that, in the recently published GYRO electromagnetic results of [CANDY, 2005], initial convergence studies note the difficulties of accurately resolving, in particular, the magnetic component of χ_e in spectral content at high β_e . Furthermore, we note

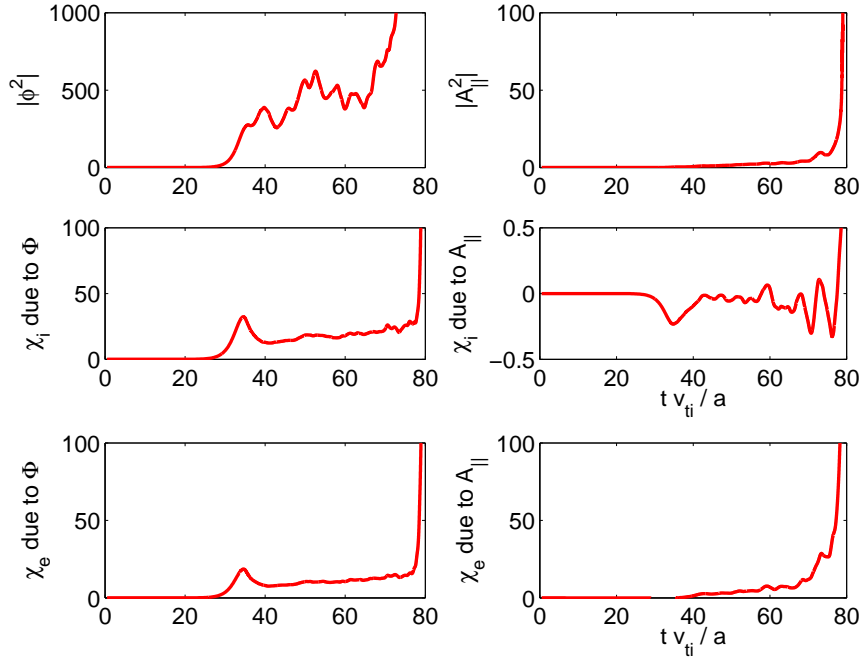


Figure C.1: Time evolution of the perturbed fields (top plots) and the electrostatic and electromagnetic components of the ion and electron heat flux (in units of $\chi_{iter,s} L_{mi} / (\rho_i^2 v_{ti})$) for the JET-based circular case at $\beta = \frac{1}{3}\beta(\kappa)$. Note that χ reaches an apparent steady state phase for a while, but eventually blows up.

that our particular JET-based cases may be even more challenging than usual because of their steeper temperature gradient ($R/L_T = 10.81$) and stronger magnetic shear ($\hat{s} = 1.62$) than a typical tokamak plasma. Thus, near future work will focus on more comprehensive studies of these unsaturated transport results, specifically first exploring the impact of a classical Coulomb diffusion term, such as that used by [APPLEGATE *et al.*, 2006], on turbulence in the standard tokamak regimes we have been focusing on. The use of subgrid models of turbulence, such as those discussed in section 6.2.1 in Chapter 6, can also be used to aid in spatial resolution convergence studies, without increasing the computational intensity.

Bibliography

Antonsen, T. M. and B. Lane (1980). Kinetic Equations for Low Frequency Instabilities in Inhomogeneous Plasmas. *Phys. Fluids* **23**, 1205.

Antonsen, T. M., J. F. Drake, P. N. Guzdar, A. B. Hassam, Y. T. Lau, C. S. Liu, and S. V. Novakovskii (1996). Physical Mechanism of Enhanced Stability from Negative Shear in Tokamaks: Implications for Edge Transport and the L-H Transition. *Phys. Plasmas* **3**, 2221.

Applegate, D. J., R. J. Hastie, and W. Dorland (2006). Private communication.

Arnoldi, W. E. (1951). The Principle of Minimized Iteration in the Solution of the Matrix Eigenvalue Problem. *Quart. Appl. Math.* **9**, 17.

Balay, S., K. Buschelman, V. Eijkhout, W. Gropp, D. Kaushik, M. Knepley, L. C. McInnes, B. Smith, and H. Zhang (2005). *PETSc Users Manual*. ANL-95/11 - Revision 2.3.0, Argonne, IL.

Barrett, R., M. Berry, T. F. Chan, J. Demmel, J. Donato, J. Dongarra, V. Eijkhout, R. Pozo, C. Romine, and H. Van der Vorst (1994). *Templates for the Solution of Linear Systems: Building Blocks for Iterative Methods*, 2nd Edition. SIAM, Philadelphia, PA.

- Bateman, G., A. H. Kritz, J. E. Kinsey, and A. J. Redd (1998). Predicting Temperature and Density Profiles in Tokamaks. *Phys. Plasmas* **5**, 1793.
- Beam, R. M. and R. F. Warming (1976). An Implicit Finite-Difference Algorithm for Hyperbolic Systems in Conservation-Law Form. *J. Comput. Phys.* **22**, 87.
- Beer, M. A. (1995). *Gyrofluid Models of Turbulent Transport in Tokamaks*. Ph.D. thesis, Princeton University.
- Beer, M. A., S. C. Cowley, and G. W. Hammett (1995). Field-aligned Coordinates for Nonlinear Simulations of Tokamak Turbulence. *Phys. Plasmas* **2**, 2687.
- Beer, M. A., R. V. Budny, C. D. Challis, G. Conway, C. Gormezano, G. Rewoldt, A. C. C. Sips, F. X. Soldner, B. J. D. Tubbing, and M. Von Hellerman (1999). Turbulence Suppression by ExB Shear in JET Optimized Shear Pulses. In *Proc. of the 26th EPS Conf. on Contr. Fusion and Plasma Physics*, ECA **23J**, 1669.
- Belli, E. A. and G. W. Hammett (2005). A Numerical Instability in an ADI Algorithm for Gyrokinetics. *Comput. Phys. Commun.* **172**, 119.
- Biglari, H., P. H. Diamond, and M. N. Rosenbluth (1989). Toroidal Ion-Pressure-Gradient-Driven Instabilities and Transport Revisited. *Phys. Fluids B* **1**, 109.
- Bourdelle, C., X. Garbet, G. T. Hoang, J. Onega, and R. V. Budny (2002). Stability Analysis of Improved Confinement Discharges: Internal Transport

Barriers in Tore Supra and Radiative Improved Mode in TEXTOR. *Nuclear Fusion* **42**, 892.

Bourdell, C., W. Dorland, X. Garbet, G. W. Hammett, M. Kotschenreuther, G. Rewoldt, and E. J. Synakowski (2003). Stabilizing Impact of High Gradient of β on Microturbulence. *Phys. Plasmas* **10**, 2881.

Brizard, A. J. (1992). Nonlinear Gyrofluid Description of Turbulent Magnetized Plasmas. *Phys. Fluids B* **4**, 1213.

Brizard, A. J. and T. S. Hahm (2006). Foundations of Nonlinear Gyrokinetic Theory. Submitted to *Review of Modern Physics*, PPPL-4153.

Candy, J. and R. E. Waltz (2003). An Eulerian Gyrokinetic-Maxwell Solver. *J. Comput. Phys.* **186**, 545.

Candy, J. and R. E. Waltz (2003). Anomalous Transport Scaling in the DIII-D Tokamak Matched by Supercomputer Simulation. *Phys. Rev. Lett.* **91**, 045001.

Candy, J., R. E. Waltz, and W. Dorland (2004). The Local Limit of Global Gyrokinetic Simulations. *Phys. Plasmas* **11**, L25.

Candy, J. (2005). Beta Scaling of Transport in Microturbulence Simulations. *Phys. Plasmas* **12**, 072307.

Catto, P. J., W. M. Tang, and D. E. Baldwin (1981). Generalized Gyrokinetics. *Plasma Phys. Controlled Fusion* **23**, 639.

Chen, Y. and S. E. Parker (2001). A Gyrokinetic Ion Zero Electron Inertia Fluid Electron Model for Turbulence Simulations. *Phys. Plasmas* **8**, 441.

- Chen, Y. and S. E. Parker (2003). A δf Particle Method for Gyrokinetic Simulations with Kinetic Electrons and Electromagnetic Perturbations. *J. Comput. Phys.* **189**, 463.
- Cheng, C. Z. and G. Knorr (1976). The Integration of the Vlasov Equation in Configuration Space. *J. Comput. Phys.* **22**, 330.
- Cheng, C. Z. and H. Okuda (1977). New Three-Dimensional Simulation Models for Cylindrical and Toroidal Plasmas. *J. Comput. Phys.* **25**, 133.
- Cohen, B. I., A. M. Dimits, W. M. Nevins, Y. Chen, and S. E. Parker (2002). Kinetic Electron Closures for Electromagnetic Simulation of Drift and Shear-Alfvén Waves. I. *Phys. Plasmas* **9**, 251.
- Cohen, B. I., A. M. Dimits, W. M. Nevins, Y. Chen, and S. E. Parker (2002). Kinetic Electron Closures for Electromagnetic Simulation of Drift and Shear-Alfvén waves. II. *Phys. Plasmas* **9**, 1915.
- Colella, P. (1990). Multidimensional Upwind Methods for Hyperbolic Conservation Laws. *J. Comput. Phys.* **87**, 171.
- Connor, J. W. and H. R. Wilson (1994). Survey of Theories of Anomalous Transport. *Plasma Phys. Controlled Fusion* **36**, 719.
- Cordey, J. G., K. Thomsen, A. Chudnovskiy, O. J. W. F. Kardaun, T. Takizuka, J. A. Snipes, M. Greenwald, L. Sugiyama, F. Ryter, A. Kus, J. Stober, J. C. DeBoo, C. C. Petty, G. Bracco, M. Romanelli, Z. Cui, Y. Liu, D. C. McDonald, A. Meakins, Y. Miura, K. Shinohara, K. Tsuzuki, Y. Kamada, H. Urano, M. Valovic, R. Akers, C. Brickley, A. Sykes, M. J. Walsh, S. M.

Kaye, C. Bush, D. Hogewei, Y. Martin, A. Cote, G. Pacher, J. Ongena, F. Imbeaux, G. T. Hoang, S. Lebedev, and V. Leonov (2005). Scaling of the Energy Confinement Time with β and Collisionality Approaching ITER Conditions. *Nuclear Fusion* **45**, 1078.

Cowley, S. C., R. M. Kulsrud, and R. Sudan (1991). Considerations of Ion-Temperature-Gradient-Driven turbulence. *Phys. Fluids B* **3**, 2767.

Dannert, T. and F. Jenko (2004). Vlasov Simulation of Kinetic Shear Alfvén Waves. *Comput. Phys. Commun.* **163**, 67.

Dimits, A. M., J. A. Byers, T. J. Williams, B. I. Cohen, X. Q. Xu, R. H. Cohen, J. A. Crotinger, and A. E. Shestakov (1994). Gyrokinetic and Global Fluid Simulations of Tokamak Microturbulence and Transport. In *Proc. of the 15th International IAEA Conference on Plasma Physics and Controlled Nuclear Fusion Research*, IAEA-CN-60/D-P5, Seville, Spain.

Dimits, A. M., T. J. Williams, J. A. Byers, and B. I. Cohen (1996). Scalings of Ion-Temperature-Gradient-Driven Anomalous Transport in Tokamaks (1996). *Phys. Rev. Lett.* **77**, 71.

Dimits, A. M., G. Bateman, M. A. Beer, B. I. Cohen, W. Dorland, G. W. Hammett, C. Kim, J. E. Kinsey, M. Kotschenreuther, A. H. Kritz, L. L. Lao, J. Mandrekas, W. M. Nevins, S. E. Parker, A. J. Redd, D. E. Schumaker, R. Sydora, and J. Weiland (2000). Comparisons and Physics Basis of Tokamak Transport Models and Turbulence Simulations. *Phys. Plasmas* **7**, 969.

Dorland, W. (1992). *Gyrofluid Models of Plasma Turbulence*. Ph.D. thesis, Princeton University.

Dorland, W., M. Kotschenreuther, Q. P. Liu, M. A. Beer, and G. W. Hammett (1996). 3D Simulations of Tokamak Plasma Turbulence: Experimental Tests and Predictions. In *Proc. of the Joint Varenna-Lausanne International Workshop on the Theory of Fusion Plasmas*, Varenna, Italy. Editrice Compositori, Societa Italiana di Fisica, Bologna, Italy (1997), 185.

Dorland, W., F. Jenko, M. Kotschenreuther, and B. N. Rogers (2000). Electron Temperature Gradient Turbulence. *Phys. Rev. Lett.* **85**, 5579.

Douglas, J. and H. H. Rachford, Jr. (1956). On the Numerical Solution of Heat Conduction Problems in two and three Space Variables. *Trans. Amer. Math. Soc.* **82**, 421.

Dubin, D. H. E., J. A. Krommes, C. Oberman, and W. W. Lee (1983). Non-linear Gyrokinetic Equations. *Phys. Fluids* **26**, 3524.

Durran, D. R. (1998). *Numerical Methods for Wave Equations in Geophysical Fluid Dynamics*. Springer Verlag Press, New York, NY.

Ernst, D. R., B. Coppi, S. D. Scott, M. Porkolab, and TFTR Group (1998). Unifying Role of Radial Electric Field Shear in the Confinement Trends of TFTR Supershot Plasmas. *Phys. Rev. Lett.* **81**, 2454.

Ernst, D. R., P. T. Bonoli, P. J. Catto, W. Dorland, C. L. Fiore, R. S. Granetz, M. Greenwald, A. E. Hubbard, M. Porkolab, M. H. Redi, J. E. Rice, K. Zhurovich, and Alcator C-Mod Group (2004). Role of Trapped Electron Mode Turbulence in Internal Transport Barrier Control in the Alcator C-Mod Tokamak. *Phys. Plasmas* **11**, 2637.

Ferron, J. R., M. S. Chu, G. L. Jackson, L. L. Lao, R. L. Miller, T. H. Osborne, P. B. Snyder, E. J. Strait, T. S. Taylor, A. D. Turnbull, A. M. Garofalo, M. A. Makowski, B. W. Rice, M. S. Chance, L. R. Baylor, M. Murakami, and M. R. Wade (2000). Modification of High Mode Pedestal Instabilities in the DIII-D tokamak. *Phys. Plasmas* **7**, 1976.

Ferron, J. R., T. A. Casper, E. J. Doyle, A. M. Garofalo, P. Gohil, C. M. Greenfield, A. W. Hyatt, R. J. Jayakumar, C. Kessel, J. Y. Kim, T. C. Luce, M. A. Makowski, J. Menard, M. Murakami, C. C. Petty, P. A. Politzer, T. S. Taylor, and M. R. Wade (2005). Optimization of DIII-D Advanced Tokamak Discharges with respect to the β Limit. *Phys. Plasmas* **12**, 056126.

Fletcher, R. (1975). Conjugate Gradient Methods for Indefinite Systems. In *Proc. of the Dundee Biennial Conference on Numerical Analysis*, G. Watson, ed., Springer Verlag Press, New York, NY.

Fraysse, V., L. Giraud, S. Gratton, and J. Langou (2003). *A Set of GMRES Routines for Real and Complex Arithmetics on High Performance Computers*. CERFACS Technical Report TR/PA/03/3, Toulouse, France.

Friedman, A., A. B. Langdon, and B. I. Cohen (1981). A Direct Method for Implicit Particle-in-Cell Simulation. *Comments on Plasma Phys. Controlled Fusion* **6**, 225.

Frieman, E. A. and L. Chen (1982). Nonlinear Gyrokinetic Equations for Low-Frequency Electromagnetic Waves in General Plasma Equilibria. *Phys. Fluids* **25**, 502.

-
- Gear, C. W. (1971). *Numerical Initial Value Problems in Ordinary Differential Equations*. Prentice-Hall Inc., Englewood Cliffs, NJ.
- Gear, C. W. and I. G. Kevrekidis (2003). Projective Methods for Stiff Differential Equations: Problems with Gaps in Their Eigenvalue Spectrum. *SIAM J. Sci. Comput.* **24**, 1091.
- Gear, C. W. and I. G. Kevrekidis (2003). Telescopic Projective Methods for Parabolic Differential Equations. *J. Comput. Phys.* **187**, 95.
- Golub, G. H. and C. F. Van Loan (1983). *Matrix Computations*. John Hopkins University Press, Baltimore, MD.
- Hahm, T. S. and L. Chen (1985). Theory of Semicollisional Kinetic Alfvén Modes in Sheared Magnetic Fields. *Phys. Fluids* **28**, 3061.
- Hahm, T. S., W. W. Lee, and A. Brizard (1988). Nonlinear Gyrokinetic Theory for Finite-Beta Plasmas. *Phys. Fluids* **31**, 1940.
- Hahm, T. S. and W. M. Tang (1989). Properties of Ion Temperature Gradient Drift Instabilities in H-mode Plasmas. *Phys. Fluids B* **1**, 1185.
- Hammett, G. W., W. Dorland, and F. W. Perkins (1992). Fluid Models of Phase Mixing, Landau Damping, and Nonlinear Gyrokinetic Dynamics. *Phys. Fluids B* **4**, 2052.
- Hammett, G. W., M. A. Beer, W. Dorland, S. C. Cowley and S. A. Smith (1993). Developments in the Gyrofluid Approach to Tokamak Turbulence Simulations. *Plasma Phys. Controlled Fusion* **35**, 973.

Hammett, G. W. (1997). Private communication. Based on *Status of Studying Rosenbluth and Hinton's Neoclassical Rotation Issues in Gyrofluid Equations*, informal notes available at <http://w3.pppl.gov/~hammett/work/rotneo/>.

Hammett, G. W. and F. Jenko (2001). Private communication. Based on *Thoughts on Continuum Algorithms*, notes from The Plasma Microturbulence Project Meeting at General Atomics, San Diego, CA, available at <http://w3.pppl.gov/~hammett/talks/2001/continuum-alg.pdf>.

Hawryluk, R. J. (1980). An Empirical Approach to Tokamak Transport. In *Physics of Plasmas Close to Thermonuclear Conditions*, vol. 1, B. Coppi, et al, ed., Commission of the European Communities, Brussels, Belgium.

Hestenes, M. R. and E. Stiefel (1952). Methods of Conjugate Gradients for Solving Linear Systems. *J. Research Nat. Bur. Standards* **49**, 409.

Hindmarsh, A. C., P. N. Brown, K. E. Grant, S. L. Lee, R. Serban, D. E. Shumaker, and C. S. Woodward (2003). *SUNDIALS: Suite of Nonlinear and Differential/Algebraic Equation Solvers*. UCRL-JP20037, Livermore, CA.

Horton, W. (1999). Drift Waves and Transport. *Rev. Mod. Phys.* **71**, 735.

Howes, G. G., S. C. Cowley, W. Dorland, and G. W. Hammett (2006). Astrophysical Gyrokinetics: Basic Equations and Linear Theory. Submitted to *Astrophys. J.*, arXiv:astro-ph/0511812.

Hua, D. D., X. Q. Xu, and T. K. Fowler (1992). Ion-Temperature-Gradient Modes in Noncircular Geometry. *Phys. Fluids B* **4**, 3216.

Hundsdoerfer, W. (1998). A Note on Stability of the Douglas Splitting Method. *Math. Comput.* **67**, 183.

ITER Physics Expert Group on Confinement and Transport, ITER Physics Expert Group on Confinement Modelling and Database, and ITER Physics Basis Editors (1999). Chapter 2: Plasma Confinement and Transport. *Nuclear Fusion* **39**, 2175.

Jardin, S. C., C. E. Kessel, C. G. Bathke, D. A. Ehst, T. K. Mau, F. Najmabadi, T. W. Petrie, and The ARIES Team (1997). Physics Basis for a Reversed Shear Tokamak Power Plant. *Fusion Engin. and Design* **38**, 27.

Jardin, S. C., C. E. Kessel, T. K. Mau, R. L. Miller, F. Najmabadi, V. S. Chan, M. S. Chu, R. LaHaye, L. L. Lao, T. W. Petrie, P. Politzer, H. E. St. John, P. Snyder, G. M. Staebler, A. D. Turnbull, and W. P. West (2005). Physics Basis for the Advanced Tokamak Fusion Power Plant ARIES-AT. Submitted to *Fusion Engin. and Design*, PPPL-3878.

Jenko, F. (2000). Massively Parallel Vlasov Simulation of Electromagnetic Drift-Wave Turbulence. *Comput. Phys. Commun.* **125**, 196.

Jenko, F., W. Dorland, M. Kotschenreuther, and B. N. Rogers (2000). Electron Temperature Gradient Driven Turbulence. *Phys. Plasmas* **7**, 1904.

Jenko, F., W. Dorland, and G. W. Hammett (2001). Critical Gradient Formula for Toroidal Electron Temperature Gradient Modes. *Phys. Plasmas* **8**, 4096.

Jenko, F. and W. Dorland (2002). Prediction of Significant Tokamak Turbulence at Electron Gyroradius Scales. *Phys. Rev. Lett.* **89**, 225001.

- Jenko, F., T. Dannert, and C. Angioni (2005). Heat and Particle Transport in a Tokamak: Advances in Nonlinear Gyrokinetics. *Plasma Phys. Controlled Fusion* **47**, B195.
- Kendl, A. and B. D. Scott (2006). Flux-Surface Shaping Effects on Tokamak Edge Turbulence and Flows. *Phys. Plasmas* **13**, 012504.
- Kessel, C., J. Manickam, G. Rewoldt, and W. M. Tang (1994). Improved Plasma Performance in Tokamaks with Negative Magnetic Shear. *Phys. Rev. Lett.* **72**, 1212.
- Kim, J. Y., W. Horton, and J. Q. Dong (1993). Electromagnetic Effect on the Toroidal Ion Temperature Gradient Mode. *Phys. Fluids B* **5**, 4030.
- Kinsey, J. E., R. E. Waltz, and J. Candy (2005). Nonlinear Gyrokinetic Turbulence Simulations of ExB Shear Quenching of Transport. *Phys. Plasmas* **12**, 062302.
- Kinsey, J. E. (2005). GLF23 Modeling of Turbulent Transport in DIII-D. *Fusion Sci. Tech.* **48**, 1060.
- Kotschenreuther, M., G. Rewoldt, and W. M. Tang (1995). Comparison of Initial Value and Eigenvalue Codes for Kinetic Toroidal Plasma Instabilities. *Comput. Phys. Commun.* **88**, 128.
- Kotschenreuther, M., W. Dorland, M. A. Beer, and G. W. Hammett (1995). Quantitative Predictions of Tokamak Energy Confinement from First Principles Simulations with Kinetic Effects. *Phys. Plasmas* **2**, 2381(1995).

- Kraichnan, R. H. (1976). Eddy Viscosity in two and three Dimension. *J. Atmos. Sci.* **33**, 1521.
- Krommes, J. A. and C.-B. Kim (2000). Interactions of Disparate Scales in Drift-Wave Turbulence. *Phys. Rev. E* **62**, 8508.
- Kruskal, M. D. and R. M. Kulsrud (1958). Equilibrium of a Magnetically Confined Plasma in a Toriod. *Phys. Fluids* **1**, 265.
- Kupfer, K., R. W. Harvey, O. Sauter, M. J. Schaffer, and G. M. Staebler (1996). Kinetic Modeling of Scrape-off Layer Plasmas. *Phys. Plasmas* **3**, 3644.
- Lazarus, E. A., M. S. Chu, J. R. Ferron, F. J. Helton, J. T. Hogan, A. G. Kellman, L. L. Lao, J. B. Lister, T. H. Osborne, R. Snider, E. J. Strait, T. S. Taylor, and A. D. Turnbull (1991). Higher Beta at Higher Elongation in the DIII-D Tokamak. *Phys. Fluids B* **3**, 2220.
- Lee, W. W. (1983). Gyrokinetic Approach in Particle Simulation. *Phys. Fluids* **26**, 556.
- Lee, W. W. (1987). Gyrokinetic Particle Simulation Model. *J. Comput. Phys.* **72**, 243.
- LeVeque, R. J. (2002). *Finite Volume Methods for Hyperbolic Problems*. Cambridge University Press, Cambridge, U. K.
- Lin, Z. and L. Chen (2001). A Fluid-Kinetic Hybrid Electron Model for Electromagnetic Simulations. *Phys. Plasmas* **8**, 1447.
- McKee, G. R., C.C. Petty, R.E. Waltz, C. Fenzi, R.J. Fonck, J.E. Kinsey, T.C. Luce, K.H. Burrell, D.R. Baker, E.J. Doyle, X. Garbet, R.A. Moyer, C.L.

Rettig, T.L. Rhodes, D.W. Ross, G.M. Staebler, R. Sydora and M.R. Wade (2001). Non-dimensional Scaling of Turbulence Characteristics and Turbulent Diffusivity. *Nuclear Fusion* **41**, 1235.

Mercier, C. and N. Luc (1974). *Lectures in Plasma Physics*. Technical Report No. EUR-5127e 140, Commission of the European Communities, Brussels, Belgium.

Mikkelsen, D. R., G. Bateman, D. Boucher, J. W. Connor, Yu. N. Dnestrovskij, A. Fukuyama, M. J. Greenwald, W. A. Houlberg, S. M. Kaye, J. E. Kinsey, A. H. Kritz, M. Marinucci, Y. Ogawa, D. Schissel, H. Shirai, P. M. Stubberfield, M. F. Turner, G. Vlad, R. E. Waltz, and J. Weiland (1998). Test of 1-D Transport Models and Their Predictions for ITER. In *Proc. of the 17th International IAEA Conference on Fusion Energy*, IAEA-CN-69/ITERP1/08, Yokohama, Japan.

Mikkelsen, D. R., W. Dorland, D.W. Ross, M. Greenwald, S. Wolfe, P. Bonoli, C. Fiore, A. Hubbard, J. Irby, E. Marmor, D. Mossessian, J. Rice, G. Taylor, J. Terry (2002). Nonlinear Simulations of Drift-Wave Turbulence in Alcator C-Mod. In *Proc. of the 19th International IAEA Conference on Fusion Energy*, IAEA-CN-94/EX/P5-03, Lyon, France.

Miller, R. L., M. S. Chu, J. M. Greene, Y. R. Lin-Liu, and R. E. Waltz (1998). Noncircular, Finite Aspect Ratio, Local Equilibrium Model. *Phys. Plasmas* **5**, 973.

Nevins, W. M., E. Bringa, B. I. Cohen, R. H. Cohen, M. Dorr, G. Gilmer, A. Kubota, J. Hittinger, G. Kerbel, C. Mundy, T. D. Rognlien, X. Q. Xu, and J.

Verboncoeur (2004). Kinetic Simulation of Boundary Plasma Transport. In Bull. Am. Phys. Soc. **49**, FP1.116, Savannah, GA.

Ongena, J., M. Evrard, and D. McCune (1998). Numerical Transport Codes. *Trans. Fusion Tech.* **33**, 181.

Ongena, J., W. Suttrop, M. Becoulet, G. Cordey, P. Dumortier, Th. Eich, L. C. Ingesson, S. Jachmich, P. Lang, A. Loarte, P. Lomas, G. P. Maddison, A. Messiaen, M. F. F. Nave, J. Rapp, G. Saibene, R. Sartori, O. Sauter, J. D. Strachan, B. Unterberg, M. Valovic, B. Alper, Ph. Andrew, Y. Baranov, J. Brzozowski, J. Bucalossi, M. Brix, R. Budny, M. Charlet, I. Coffey, M. De Baar, P. De Vries, C. Gowers, N. Hawkes, M. von Hellermann, D. L. Hillis, J. Hogan, G. L. Jackson, E. Joffrin, C. Jupen, A. Kallenbach, H. R. Koslowski, K. D. Lawson, M. Mantsinen, G. Matthews, P. Monier-Garbet, D. McDonald, F. Milani, M. Murakami, A. Murari, R. Neu, V. Parail, S. Podda, M. E. Puiatti, E. Righi, F. Sartori, Y. Sarazin, A. Staebler, M. Stamp, G. Telesca, M. Valisa, B. Weysow, K-D. Zastrow and EFDA-JET workprogramme contributors (2001). Recent Progress on JET Towards the ITER Reference Mode of Operation at High Density. *Plasma Phys. Controlled Fusion* **43**, A11.

Osbourne, T. H., J. R. Ferron, R. J. Groebner, L. L. Lao, A. W. Leonard, M. A. Mahdavi, R. Maingi, R. L. Miller, A. D. Turnbull, M. Wade, and J. Watkins (2000). The Effect of Plasma Shape on H-mode Pedestal Characteristics on DIII-D. *Plasma Phys. Controlled Fusion* **42**, A175.

Parker, S. E., W. W. Lee, and R. A. Santoro (1993). Gyrokinetic Simulation of Ion Temperature Gradient Driven Turbulence in 3D Toroidal Geometry. *Phys. rev. Lett.* **71**, 2042.

- Parker, S. E., C. Kim, and Y. Chen (1999). Large-scale Gyrokinetic Turbulence Simulations: Effects of Profile Variation. *Phys. Plasmas* **6**, 1709.
- Parker, S. E., Y. Chen, and W. Wan (2004). Electromagnetic Gyrokinetic Simulations. *Phys. Plasmas* **11**, 2494.
- Peaceman, D. W. and H. H. Rachford, Jr. (1955). The Numerical Solution of Parabolic and Elliptic Differential Equations. *J. SIAM* **3**, 28.
- Petty, C. C., T. C. Luce, K. H. Burrell, S. C. Chiu, J. S. deGrassie, C. B. Forest, P. Gohil, C. M. Greenfield, R. J. Groebner, R. W. Harvey, R. I. Pinsky, R. Prater, and R. E. Waltz (1995). Nondimensional Transport Scaling in DIII-D: Bohm versus Gyro-Bohm Resolved. *Phys. Plasmas* **2**, 2342.
- Qin, H., W. M. Tang, and W. W. Lee (2000). Gyrocenter-Gauge Kinetic Theory. *Phys. Plasmas* **7**, 4433.
- Rewoldt, G., W. M. Tang, and M. S. Chance (1982). Electromagnetic Kinetic Toroidal Eigenmodes for General Magnetohydrodynamic Equilibria. *Phys. Fluids* **25**, 480.
- Rewoldt, G., W. M. Tang, and R. J. Hastie (1987). Collisional Effects on Kinetic Electromagnetic Modes and Associated Quasilinear Transport. *Phys. Fluids* **30**, 807.
- Rewoldt, G. and W. M. Tang (1990). Toroidal Microinstability Studies of High-Temperature Tokamaks. *Phys. Fluids B* **2**, 318.
- Rogers, B. N., W. Dorland, and M. Kotschenreuther (2000). Generation and Stability of Zonal Flows in Ion-Temperature-Gradient Mode Turbulence. *Phys.*

Rev. Lett **85**, 5336.

Romanelli, F. (1989). Ion Temperature-Gradient-Driven Modes and Anomalous Ion Transport in Tokamaks. *Phys. Fluid B* **1**, 1018.

Romanelli, F. and S. Briguglio (1990). Toroidal Semicollisional Microinstabilities and Anomalous Electron and Ion Transport. *Phys. Fluids B* **2**, 754.

Rosenbluth, M. N. and F. L. Hinton (1998). Poloidal Flow Driven by Ion-Temperature-Gradient Turbulence in Tokamaks. *Phys. Rev. Lett* **80**, 724.

Ross, D. W. and W. Dorland (2002). Comparing Simulation of Plasma Turbulence with Experiment. II. Gyrokinetic Simulations. *Phys. Plasmas* **9**, 5031.

Saad, Y. and M. H. Schultz (1986). GMRES: A Generalized Minimal Residual Algorithm for Solving Nonsymmetric Linear Systems. *SIAM J. Sci. Stat. Comput.* **7**, 856.

Saad, Y. (2003). *Iterative Methods for Sparse Linear Systems*, 2nd Edition. SIAM, Philadelphia, PA.

Smith, S. A. (1997). *Dissipative Closures for Statistical Moment, Fluid Moments, and Subgrid Scales in Plasma Turbulence*. Ph.D. thesis, Princeton University.

Smith, S. A. and G. W. Hammett (1997). Eddy Viscosity and Hyperviscosity in Spectral Simulations of 2D Drift Wave Turbulence. *Phys. Plasmas* **4**, 978.

Snyder, P. B. (1999). *Gyrofluid Theory and Simulation of Electromagnetic*

Turbulence and Transport in Tokamak Plasmas. Ph.D. thesis, Princeton University.

Sonneveld, P. (1989). CGS: A Fast Lanczos-type Solver for Nonsymmetric Linear Systems. *SIAM J. Sci. Stat. Comput.* **10**, 36.

Staebler, G. M., J. E. Kinsey, and R. E. Waltz (2005). Gyro-Landau Fluid Equations for Trapped and Passing Particles. *Phys. Plasmas* **12**, 102508.

Stallard, B. W., C. M. Greenfield, G. M. Staebler, C. L. Rettig, M. S. Chu, M. E. Austin, D. R. Baker, L. R. Baylor, K. H. Burrell, J. C. DeBoo, J. S. deGrassie, E. J. Doyle, J. Lohr, G. R. McKee, R. L. Miller, W. A. Peebles, C. C. Petty, R. I. Pinsker, B. W. Rice, T. L. Rhodes, R. E. Waltz, L. Zeng, and the DIII-D Team (1999). Electron Heat Transport in Improved Confinement Discharges in DIII-D. *Phys. Plasmas* **6**, 1978.

Sydora, R. D., V. K. Decyk, and J. M. Dawson (1996). Fluctuation-induced Heat Transport Results from a Large Global 3D Toroidal Particle Simulation Model. *Plasma Phys. Controlled Fusion* **38**, A281.

Tang, W. M. (1978). Microinstability Theory in Tokamaks. *Nuclear Fusion* **18**, 1089.

Tang, W. M., G. Rewoldt, and L. Chen (1986). Microinstabilities in Weak Density Gradient Tokamak Systems. *Phys. Plasmas* **29**, 3715.

Troyon, F., R. Gruber, H. Saurenmann, S. Semenzato, and S. Succi (1984). MHD-Limits to Plasma Confinement. *Plasma Phys. Controlled Fusion* **26**, 209.

Turnbull, A. D., Y. R. Lin-Liu, R. L. Miller, T. S. Taylor, and T. N. Todd (1999). Improved Magnetohydrodynamic Stability Through Optimization of Higher Order Moments in Cross-Section Shape of Tokamaks. *Phys. Plasmas* **6**, 1113.

Uckan, N. A. (1990). *ITER Physics Design Guidelines*. ITER Doc. Series, No. 10, IAEA, Vienna, Austria.

Valovic, M., J. Rapp, J. G. Cordey, R. Budny, D. C. McDonald, L. Garzotti, A. Kallenbach, M. A. Mahdavi, J. Ongena, V. Parail, G. Saibene, R. Sartori, M. Stamp, O. Sauter, J. Strachan, W. Suttrop and contributors to the EFDA-JET Workprogramme (2002). Long Timescale Density Peaking in JET. *Plasma Phys. Controlled Fusion* **44**, 1911.

Van der Vorst, H. A. (1992). Bi-CGSTAB: A Fast and Smoothly Converging Variant of Bi-CG for the Solution of Nonsymmetric Linear Systems. *SIAM J. Sci. Stat. Comput.* **13**, 631.

Waltz, R. E., G. D. Kerbel, and J. Milovich (1994). Toroidal Gyro-Landau Fluid Model Turbulence Simulations in a Nonlinear Ballooning Mode Representation with Radial Modes. *Phys. Plasmas* **7**, 2229.

Waltz, R. E., G. D. Kerbel, J. Milovich, and G. W. Hammett (1995). Advances in the Simulation of Toroidal Gyro-Landau-Fluid Model Turbulence. *Phys. Plasmas* **2**, 2408.

Waltz, R. E., G. M. Staebler, W. Dorland, G. W. Hammett, M. Kotschenreuther, and J. A. Konings (1997). A Gyro-Landau-Fluid Transport Model. *Phys. Plasmas* **4**, 2482.

- Waltz, R. E., R. L. Dewar, and X. Garbet (1998). Theory and Simulation of Rotational Shear Stabilization of Turbulence. *Phys. Plasmas* **5**, 1784.
- Waltz, R. E. and R. L. Miller (1999). Ion Temperature Gradient Turbulence Simulations and Plasma Flux Surface Shape. *Phys. Plasmas* **6**, 4265.
- Waltz, R. E. (2005). Private communication. Based on *Comparative Technical History of GYRO*, informal notes available at http://fusion.gat.com/comp/parallel/samples/gyro_tech_hist.pdf.
- Wang, W. X., Z. Lin, W. M. Tang, W. W. Lee, S. Ethier, J. L. V. Lewandowski, G. Rewoldt, T. S. Hahm, and J. Manickam (2006). Gyrokinetic Simulation of Global Turbulent Transport Properties in Tokamak Experiments. Submitted to *Phys. Rev. E*, PPPL-4142.
- Wendroff, B. (1960). On Centered Difference Equations for Hyperbolic Systems. *J. SIAM* **8**, 549.
- Xu, X. Q., R. H. Cohen, T. D. Rognlien, and J. R. Myra (2000). Low-to-High Confinement Transition Simulations in Divertor Geometry. *Phys. Plasmas* **7**, 1951.